

Dissertation

Structurally modified two-dimensional materials for membrane applications

von

Lukas Madauß
geboren in Essen

zur Erlangung des Grades
Doktor der Naturwissenschaften
(Dr. rer. nat.)

vorgelegt der Fakultät für Physik
der Universität Duisburg-Essen

Duisburg, März 2021



UNIVERSITÄT
DUISBURG
ESSEN

Offen im Denken

1. Gutachterin: Prof. Dr. Marika Schleberger
2. Gutachterin: Prof. Dr. Christina Trautmann
3. Gutachter: Prof. Dr. Heiko Wende

Datum der Einreichung: 04. März 2021

Datum der Disputation: 03. November 2021

Abstract

Membranes are an essential part of our lives and are constantly being improved with respect to their physical and chemical properties as well as their filtration performances. Nevertheless, it is advisable to search for new membrane materials that may outperform current ones, reduce costs of production, and eliminate hazardous chemicals involved in fabrication processes.

This thesis addresses recently emerged membrane materials and investigates their suitability as such. The first part involves carbon-based materials with a focus on graphene and graphene oxide. Graphene is an atomically thin and two-dimensional material which was discovered by A. Geim and K. Novoselov in 2004. Its applicability as a membrane has been addressed in various research articles - a trend which continues to grow. The handling of large-area graphene however, poses several challenges impeding both membrane fabrication processes as well as fundamental research experiments. This issue is addressed by developing a surface engineering technique which increases the mechanical stability of graphene allowing safe and improved handling of graphene.

Chemical modifications of graphene, *e.g.*, graphene oxide, have been investigated as a promising membrane material in recent years as well. Even though the synthesis of graphite oxide is well known since 1859, the possibility of exfoliating individual graphene oxide sheets to form layered membranes has opened doors for new applications. Here, graphene oxide laminates are characterized with respect to their functionality as proton conducting membranes. Hydronium and hydroxide ions are generated via photocatalytic water splitting and their mobility through a graphene oxide membrane is studied, revealing a promoted diffusion transport of hydronium ions owing to an energetically favored transport mechanism.

The second part of the thesis shifts the focus towards the material molybdenum disulfide. The suitability of swift heavy ion and highly charged ion irradiation as a tool to perforate suspended single-layer molybdenum disulfide is investigated. Both pore sizes and defect creation efficiencies can be well adjusted via the potential energy in case of highly charged ion irradiation and the energy loss per track length when dealing with swift heavy ions. The irradiation conditions described in this thesis result in pore sizes of a half to eight nanometers in diameter. Upon further adjustments of ion types and properties larger and smaller pore diameters are expected to be attainable as well.

Simulations have forecasted for the chemical stoichiometry of the edges of molybdenum disulfide pores to play an important role in membrane applications. Therefore, defects induced by swift heavy ion and highly charged ion irradiation are investigated with respect to their chemical composition revealing a depletion of sulphur and an accumulation of molybdenum atoms close-by the ion modification which is also shown to be beneficial for catalytic reactions.

The last part addresses the influence of a substrate and the thickness of molybdenum disulfide on the defect formation initiated by swift heavy ion irradiation. The presence of a substrate is found not to be a prerequisite for defect formation. Further, not only do the defect structures change for increasing layer numbers but so do the defects experience a transition from continuous material modifications to discontinuous ones.

Kurzzusammenfassung

Membranen stellen einen essentiellen Bereich des täglichen Lebens dar. Es verwundert daher wenig, dass physikalische und chemische Eigenschaften aktueller Membranmaterialien fortlaufend verbessert werden, um noch effizientere und präzisere Filtermembranen zu realisieren. Unabhängig davon umfassen Forschungsvorhaben aber auch neuartige Materialien, welche unter Umständen bessere Ergebnisse liefern, Produktionskosten verringern und den Herstellungsprozess umweltfreundlicher gestalten können.

Die vorliegende Arbeit thematisiert erst kürzlich entdeckte Materialien, deren Eigenschaften sich für Anwendungen im Bereich der Membrantechnik empfehlen. Die erste Hälfte der Arbeit umfasst die kohlenstoffbasierten Materialien *Graphen* und *Graphenoxid*. Graphen wurde erstmalig im Jahr 2004 von A. Geim und K. Novoselov entdeckt und ist aufgrund seiner atomaren Dicke ein für hochpermeable und zugleich selektive Membrananwendungen ein prädestinierter Kandidat. Der Umgang mit großflächigem Graphen birgt allerdings einige Herausforderungen. Es wird daher eine Methode vorgestellt, mit welcher sich die mechanischen Eigenschaften Graphens modifizieren lassen und dadurch einen qualitativ verbesserten Umgang ermöglichen.

Neben Graphen in seiner unmodifizierten Form erfährt auch die oxidierte Variante, Graphenoxid, steigende Popularität. Obwohl die Synthese Graphitoxids schon seit 1859 bekannt ist, ermöglicht insbesondere die Aufschichtung einzelner Graphenoxidlagen hin zu Laminaten echte Anwendungen in der Membrantechnik. Vor diesem Hintergrund wird hier deren Nutzbarkeit als protonenleitfähige Membranen untersucht. Mittels photokatalytischer Wasserspaltung werden Hydronium- und Hydroxidionen generiert und deren Diffusionsmechanismen durch das Graphenoxid untersucht. Der Transport von Hydroniumionen erweist sich dabei als energetisch favorisiert und resultiert in einer erhöhten Beweglichkeit der Ladungsträger.

Der zweite Teil dieser Arbeit fokussiert die Aufmerksamkeit auf das Material Molybdändisulfid. Zunächst wird die Möglichkeit adressiert, einlagiges Molybdändisulfid mittels hochgeladener Ionen sowie schneller Schwerionen zu perforieren. Generierte Lochgrößen sowie Effizienzen der Defektgenerierung skalieren mit der potenziellen Energie hochgeladener Ionen bzw. dem Energieverlust pro Einheitslänge schneller Schwerionen. Die hier untersuchten Parameter ermöglichen die Erzeugung von Poren mit einem kontrollierbaren Durchmesser von einem halben bis acht Nanometer.

Da der chemischen Stöchiometrie der Porenränder im Molybdändisulfid ein starker Ein-

fluss auf die Leistungsfähigkeit als Membran zugesagt wird, soll diese folglich genauer untersucht. Durch schnelle Schwerionen bzw. hochgeladene Ionen hervorgerufene Defekte weisen in unmittelbarer Umgebung eine Verarmung an Schwefelatomen auf, was neben dem positiv prognostizierten Effekt für Filteranwendungen nachweislich auch für katalytische Reaktionen genutzt werden kann.

Zuletzt wird der Einfluss des Substratmaterials sowie der Schichtdicke des Molybdändisulfids kontrolliert variiert, um auch deren Auswirkungen auf die Wechselwirkung mit schnellen Schwerionen zu untersuchen. Es kann gezeigt werden, dass sich Defektformen mit steigender Lagenanzahl strukturell verändern und einen Übergang von kontinuierlichen zu diskontinuierlichen Modifikationen erfahren.

Contents

1	Introduction	1
2	Fundamentals	5
2.1	Membrane Technology	5
2.1.1	Pressure-Driven Filtration	5
2.1.2	Electrodialysis	8
2.2	Improvement of State-of-the-Art Membranes - a Two-Dimensional Approach	8
2.3	2D Materials	13
2.3.1	Graphene	14
2.3.2	Graphene Oxide	18
2.3.3	Molybdenum Disulfide	22
2.4	Synthesis of 2D Materials	26
2.4.1	Micromechanical Exfoliation	26
2.4.2	Chemical Vapor Deposition	27
3	Defect Generation and Characterization Techniques	31
3.1	Ion Beams	31
3.1.1	Swift Heavy Ions - Electronic Stopping	32
3.1.2	SHI Irradiation Facilities	35
3.1.3	Highly Charged Ions	37
3.1.4	Classical Over-Barrier Model	37
3.2	Electronic Excitation in Solids and Energy Transfer Mechanisms	43
3.3	Characterization Techniques of Material Modifications	47
3.3.1	Types of Microscopy	47
3.3.2	Atomic Force Microscopy Imaging Modes	48
3.3.3	Raman Spectroscopy	50
3.3.4	Raman Spectrum of Graphene	50
3.3.5	Raman Spectrum of MoS ₂	53
4	Surface Engineering of Graphene	55
5	Graphene Oxide Membranes: Selective Proton Transport for Hydrogen Generation	69

6	Electronic Excitation and Perforation of Single-Layer MoS ₂	79
7	Chemical Structure of SHI Irradiated MoS ₂ for Catalytic Applications	91
7.1	Investigation of the Mo-S Stoichiometry of SHI Induced Defects in Single-Layer MoS ₂	92
7.2	Hydrogen Evolution Reaction of SHI Generated Defects in Single-Layer MoS ₂	97
8	Defect Engineering of MoS ₂	101
8.1	Tuning Defect Modifications in Single-Layer MoS ₂ via SHI Irradiation Conditions	102
8.2	Thickness Dependent Defect Types in MoS ₂ : From Rifts to Hillocks	105
8.3	Formation of Hillocks and Blisters in Bulk MoS ₂	107
9	Summary & Outlook - Future of 2D Membranes	113
	Bibliography	117

1 Introduction

A membrane is characterized by its ability to retain atoms, molecules, ions or other particles due to its physical and/or chemical properties while letting other species pass at the same time. It acts as a separating agent to spatially isolate a certain type of particle from a larger ensemble. The diversity of membrane types and applications has long made them indispensable in fields of medicine [1–3], water purification [4], food industry [5,6], automobile sector [7,8] as well as in newly emerging fields of renewable energy sources [9,10].

The rapidly increasing number of applications calling for further improvement of the mechanical stability, chemical durability, and separation efficiency of current state-of-the-art membranes is equally accompanied by the demand of minimizing fabrication costs and has therefore prompted membrane research to also investigate other materials than polymers and ceramics which currently form the backbone of membrane industry. Especially the thickness of a membrane sets an intrinsic limit for realizable permeability values of the fluid which is supposed to be filtered. For cylindrical shaped membrane pores in, *e.g.*, track-etched polymer membranes, the Hagen-Poiseuille equation dictates an inverse proportional relation between the volumetric flow rate and the membrane thickness assuming a laminar flow of the fluid [11]. With respect to this issue, atomically thin, large-area, and robust membranes with an adjustable pore size distribution would certainly be a good starting point for solving this issue [12]. It is therefore of little surprise that two-dimensional (2D) materials have been heavily investigated as potential membrane materials since the discovery of the only one-carbon-atom-thick crystal, named graphene, by A. Geim and K. Novoselov in 2004 [13,14]. In the early days, it was produced via exfoliation technique yielding highly crystalline graphene layers of the best quality at the expense of reproducibility and with no option of up-scaling. More advanced synthesis growth procedures have quickly solved these problems and adapted to industrial standards. Yet, there is only a restricted number of suitable growth substrate materials making safe handling and a defect-free transfer often inevitable.

1. The aim of chapter 4 *Surface Engineering of Graphene* is to present and investigate a universal technique to increase the mechanical stability of large-area single-layer graphene sheets during transfer without having to rely on the usual polymer support materials which are prone to induce defects in graphene and leave contaminants once removed

again. The transferred graphene layer is analyzed afterwards by various spectroscopical techniques characterizing the crystallinity and cleanliness of its surface.

Aside from graphene, which certainly still ranks among the most heavily investigated 2D materials, chemical modifications of it have been experiencing growing attention as well. Especially graphene oxide (GO), the oxidized form of graphene, has shown exceptional properties in terms of water permeability and filtration characteristics when used as a membrane laminate. It offers a great deal of adjustable properties allowing it to cover a wide range of applications [15–18]. Only recently it was suggested to act as a proton conductor with the possibility of replacing perfluorinated polymer membranes as the current undisputed top dog in this field [19, 20].

2. To address the possibility of utilizing GO as potential proton conducting membranes, elements of photocatalytic water splitting and proton transport through an ion selective membrane are combined. GO oxide is employed in form of a membrane laminate and used to spatially separate hydronium and hydroxide ions after photocatalytic water splitting with the help of titanium dioxide nanoparticles. The transport mechanism of both hydronium and hydroxide ions through a GO membrane is studied in chapter 5 *Graphene Oxide Membranes: Selective Proton Transport for Hydrogen Generation* revealing possibilities for proton diffusion comparable to those of commercially available perfluorinated polymer membranes.

Unless 2D materials or 2D laminates already display intrinsic filtration characteristics due to their fabrication process, other techniques to adjust their properties are required. Ion irradiation ranks among the most efficient and frequently applied techniques for material modification. In the semiconductor industry it is an extremely important technique to artificially implant dopants into another material for increasing the overall electrical conductivity [21, 22]. Ions used in this process typically have a kinetic energy in the keV-regime. Even though keV-ions can offer exceptional spatial accuracy during irradiation and are by far the most often encountered ion type in research laboratories, the amount of energy each ion can deposit into a target material per unit track length is strongly limited. The reason for this lies in the interaction mechanism of the ion and the target atoms which simply does not permit the deposition of high energy densities [23, 24]. This is even more critical for very thin materials and peaks for 2D materials where only a minimum of energy can be deposited. Hence, obtainable material modifications and defects are limited in size which again confines the range of applications. It is therefore necessary to look for other ion types and irradiation techniques.

Swift heavy ions (SHI) and *highly charged ions* (HCI) may solve this problem as their interaction with matter is fundamentally different to keV-ion irradiation allowing the deposition of much higher energy densities [23, 25]. The characteristic property of a HCI is its large amount of potential energy stored in form of a high charge state. On the contrary, ions are referred

to as SHIs when their striking property lies in their kinetic energy. A detailed description of the characteristics of a HCI and SHI as well as the phenomena occurring during SHI and HCI irradiation of solids are presented in chapter 3 *Ion Irradiation of Solids*. SHI irradiation in particular is a well-known technique to modify bulk materials and is also applied for fabrication of track-etched membranes [26, 27]. The large kinetic energy allows the ions to penetrate bulk materials at a nearly constant energy loss contributing to uniform and deep reaching material modifications [28]. Recent work has shown that SHI may also be used to modify substrate supported 2D materials by altering their surface morphology leading to pores [29], slits [30] or foldings [31, 32] within the material whose geometries and sizes are adjustable by adapting irradiation conditions. This applies for graphene but other 2D materials as well including molybdenum disulfide (MoS_2), which is arguably the most famous representative of the group of transition metal dichalcogenides (TMDCs). Two planes of sulphur atoms (S) encapsulate a molybdenum (Mo) layer forming the thinnest obtainable MoS_2 crystal. Even though a S-Mo-S monolayer is a three-atom thick material, it is still referred to as a 2D material. It displays very intriguing properties including catalytic qualities and a direct band-gap allowing applications in (opto-)electronic devices. By modifying MoS_2 with the help of ion irradiation its already interesting properties may be improved even further or expanded such that completely new fields of application become accessible, *e.g.*, membrane science. The second part of the thesis deals with the material MoS_2 and focuses on SHI and HCI induced modifications relevant for membrane applications.

3. The intend of chapter 6 *Electronic Excitation and Perforation of Single-Layer MoS_2* is to investigate and compare the suitability of SHI and HCI irradiation for pore creation in suspended single-layer MoS_2 with a clear focus on pore diameters between one and ten nanometers. In this regard, the characterizing properties of each ion type (*i.e.*, the potential energy E_{pot} for HCIs and the energy loss per track length dE/dx for SHIs) are varied and their implications on defect sizes and creation efficiencies in MoS_2 are studied.

After establishing irradiation conditions for controllable defect creation, the chemical structure of these ion induced defect is studied motivated by a predicted significant impact on membrane related applications affecting both water and gas permeabilities [33, 34]. Aside from modeling the chemical structure of SHI irradiated MoS_2 , catalytic reactions, *e.g.*, the hydrogen evolution reaction, will be used as well to characterize the defect chemistry and stoichiometry of given defects.

4. The aim of chapter 7 *Chemical Structure of SHI Irradiated MoS_2 for Catalytic Applications* is to develop a deeper understanding about the changes of the chemical stoichiometry of single-layer MoS_2 in close vicinity to a SHI impact. By combining surface sensitive characterization methods with theoretical predictions and by probing catalytic properties,

information about otherwise hardly accessible chemical changes in the MoS₂ due to ion irradiation is investigated.

While perpendicular SHI irradiation is a suitable choice for introducing defects and pores into single-layer MoS₂, the situation may behave differently when dealing with substrate supported layers or with samples which are thicker than just one layer. It is therefore imperative to understand the influence of the substrate and layer number during defect formation caused by ion irradiation and debate how the structure of defects changes when such irradiation conditions or material properties are varied.

5. Chapter 8 *Defect Engineering of MoS₂* discusses the implications of the underlying substrate on the defect modifications originating from SHI irradiation. Layer-thickness dependent studies are discussed to investigate possible limitations of perforating multi-layered MoS₂ via SHI irradiation. To visualize differences in morphology arising from a change of substrate or layer thickness and not risk overseeing them in case their are formed within the bulk of multi-layered MoS₂, grazing incidence irradiation is applied to guarantee modifications being located close the surface.

2 Fundamentals

Chapter 2 gives an overview of different membranes classes, their classification according to their filtration characteristics, and important values characterizing the properties of membranes. Subsequently, the limitations of 3D membranes in terms of permeability are demonstrated and a recently emerged material class referred to as 2D materials will be introduced. Due to their unique physical properties, 2D materials have the potential to be utilized as next-generation membranes for various applications.

2.1 Membrane Technology

2.1.1 Pressure-Driven Filtration

Approaches in engineering aiming to manipulate the transport of commonly gaseous and/or liquid streams between two fractions with the help of (semi-)permeable membranes are commonly referred to as membrane technology. The simplest model of a membrane can be understood as a black box shown in Fig. 2.1. The feed solution containing the unfiltered liquids/gases interacts with a membrane such that certain species of the initial feed are removed and a filtered solution (permeate) is obtained. Parts of the feed solution that are retained by the membrane or feed solution which is yet unfiltered are referred to as retentate [35].

Even though the driving force in all filtration processes is a difference in the electrochemical potential across the membrane due to gradients in concentration, pressure, temperature, and/or electrical potential, one certainly has to differentiate between membranes of different pore sizes and the filtration technique itself. The four main pressure-driven membrane separation methods are i) micro-, ii) ultra-, iii) nano-filtration, and iv) reverse osmosis. A schematic of these four filtration classes with exemplary filtrates, their respective operating pressures, and typical membrane pore sizes are presented in Fig. 2.2. Microfiltration is operated at the lowest trans-membrane pressure gradient among the four filtration regimes mentioned above and allows the removal of larger species or bacteria. While the necessary pressure gradually increases for the remaining filter grades, the respective pore diameters of the membranes and

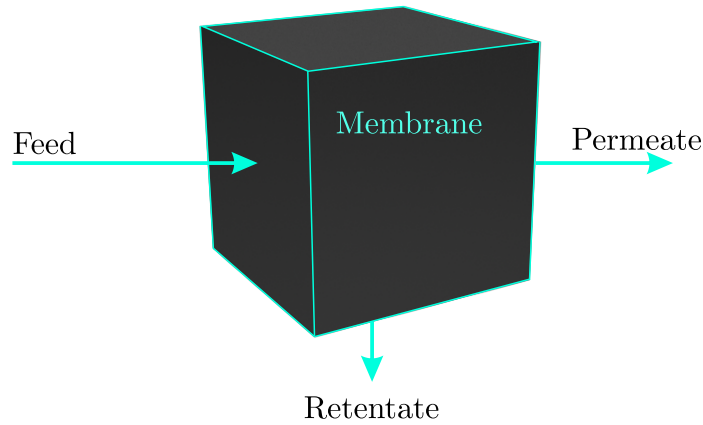


Figure 2.1: Schematic of a membrane. The feed solution is split into the permeate which represents the already filtered product and the retentate which contains refrained particles and yet unfiltered feed. The requirements set for the permeate with respect to, *e.g.*, particle size and flux are strongly influenced by the membrane and its properties.



Pressure [bar]	0.1 - 2	0.1 - 5	3 - 20	5 - 120
Pore sizes [nm]	10 - 10000	2 - 100	0.5 - 2	< 0.5
Filtered species	bacteria, larger particles	proteins, viruses, macro-molecules	small organic molecules, multivalent ions	monovalent ions

Figure 2.2: Schematic of different pressure driven filtration processes including micro-, ultra-, and nanofiltration as well as reverse osmosis. Pressure ranges, membrane pore sizes, and common filter applications are given (examples in bold are typical retentates of that specific filtration class and shown in the respective schematic).

sizes of the filtered particles decrease likewise. Hence, filtration based on reverse osmosis requires pressure differences of more than 100 bar but also allows the removal of smallest particles, *e.g.*, monovalent ions during desalination applications. It is important to note that not only do the respective membrane structures differ but so does the transport mechanism. Micro-, ultra-, and (to some extent) nanofiltration can be described with the pore-flow model which assumes convective flow of the fluid passing through pores that are much larger than the feed particles themselves [36]. According to the Hagen-Poiseuille equation 2.1, which applies well for cylindrical pores in track-etched membranes [11], the total flow per unit membrane area J can be described with the number of pores N , the pore diameter d , the viscosity of the liquid μ , the thickness of the membrane l , and the trans-membrane pressure difference Δp :

$$J_{\text{HP}} = N \frac{\pi d^4}{128 \mu l} \cdot \Delta p \quad (2.1)$$

Often, the permeability p_{HP} is referred to, which represents a normalized membrane flux with respect to the pressure gradient and is given by eq. 2.2.

$$p_{\text{HP}} = J_{\text{HP}} / \Delta p = N \frac{\pi d^4}{128 \mu l} \quad (2.2)$$

However, it is worth noting that the pore-flow model does not apply for all membranes types. For instance, reverse osmosis polymer membranes are dense materials and described best by the solution-diffusion model. Here, separation of the different species of the feed solution relies on their varying solubilities and diffusivities inside the membrane [37].

The selectivity S of a membrane is another important characteristic aside from the aforementioned permeability p_{HP} [38]. It refers to the ability of a membrane to retain certain substances and is defined as the ratio of an easily permeating substance S_{eps} and of the retained substance S_{rs} . Both S_{eps} and S_{rs} are defined as their respective concentration ratios in the permeate and feed solution. Assuming a negligible change in concentration of the easily permeating substance, the overall selectivity S is simply given by the inverse of S_{rs} according to eq. 2.3.

$$S = \frac{S_{\text{eps}}}{S_{\text{rs}}} \approx \frac{1}{S_{\text{rs}}} = \frac{c_{\text{rs,feed}}}{c_{\text{rs,permeate}}} \quad (2.3)$$

2.1.2 Electrodialysis

Another industrially used and highly developed process is electrodialysis, which relies on electrically charged membranes and an electrical potential gradient in contrast to the aforementioned pressure-driven filtration processes. Generally, charged functional groups are attached to the polymer chains of the membrane material which reduce or even fully prohibit transport of ions which are equally charged as the functional groups but allow passage of ions of opposite charge. One differentiates between cationic membranes which carry negatively charged functional groups and allow cations to pass and anionic membranes with fixed positive charges that suppress cationic transport and permit anionic movement. Fig. 2.3 shows an exemplary electrodialysis module made up of alternating layers of anionic (A) and cationic (C) membranes which may be used for desalination processes. Two electrodes are positioned across the stack of membrane layers to accelerate the dissolved ions in the solution. Initially, all interspaces are filled with a feed and a pick-up solution. Due to the restricted movement of anions (cations) through the cationic (anionic) layers, every second membrane interlayer space is gradually depleted of ions while the adjacent ones (those of the pick-up solutions) are enriched with ions. The concentrated and demineralized products are then extracted separately [39].

Even though polymer membranes do not play an important role in this thesis, the filtration principle of electrodialysis can be adapted to the still fairly new graphene oxide membrane laminates which will be discussed in section 2.3.2 on p. 18 in more detail. Actual filtration measurements relying on the mechanisms of electrodialysis are presented in chapter 5 on p. 69.

2.2 Improvement of State-of-the-Art Membranes - a Two-Dimensional Approach

Currently, polymer-based membranes cover a wide range of applications in fields of micro-, ultra-, nano-filtration, reverse osmosis, electrodialysis, gas separation, and many more [40–42]. A variety of requirements are imposed on a filtration membrane including a high permeability and selectivity, both of which are directly correlated with each other as shown for ultrafiltration measurements of the protein bovine serum albumin (BSA) in Fig. 2.4 [38]. A high permeability is usually accompanied by a low selectivity and vice versa. Simply increasing the permeability by reducing the thickness of the material without altering other properties might only work up to a certain extent before compromising the mechanical stability of the membrane.

2D materials may present a solution to this problem. Their outstanding mechanical strength [43, 44] compared to many polymers (*e.g.*, free-standing, large-area graphene with an experimentally verified elastic Young modulus and equibiaxial strength of 1000 GPa and

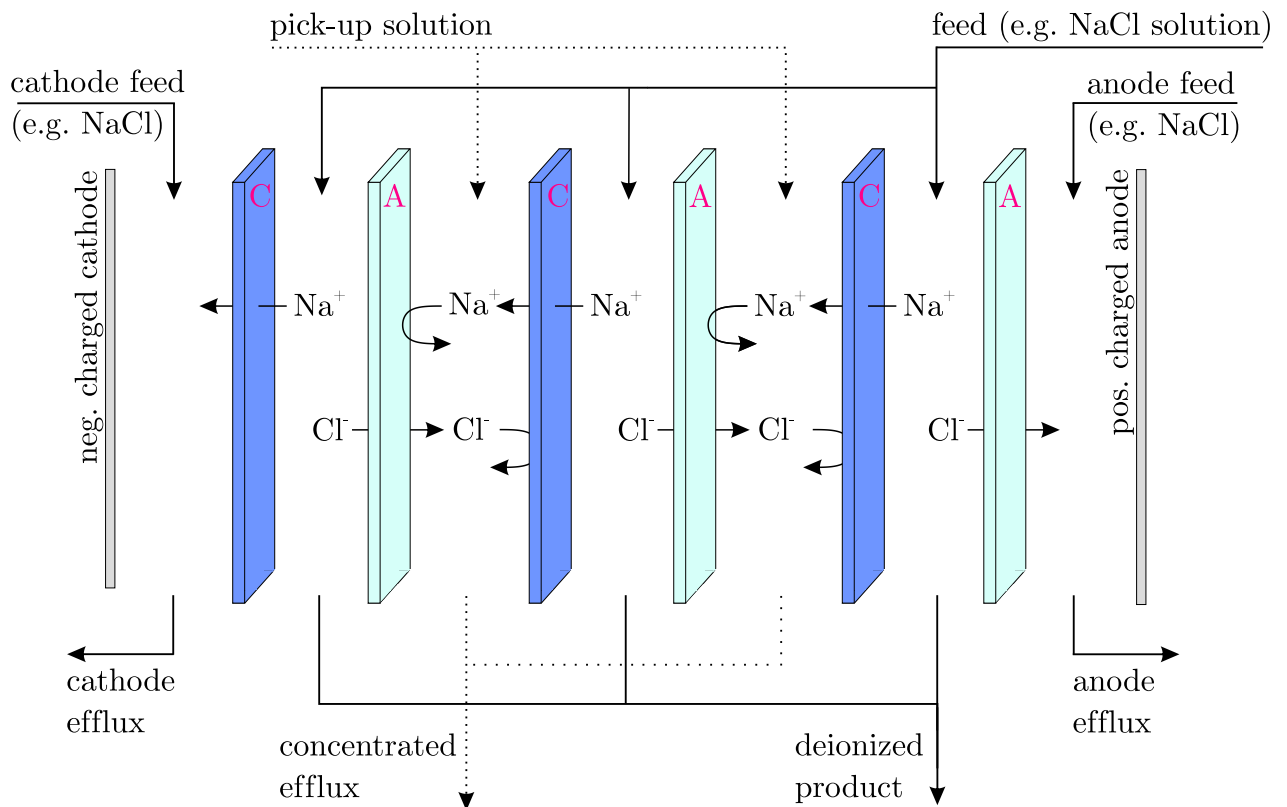


Figure 2.3: Schematic of an electrodesalination process. Stacks of alternating cationic and anionic exchange membranes and an electrical potential gradient across the module allow the deionization of liquids [39].

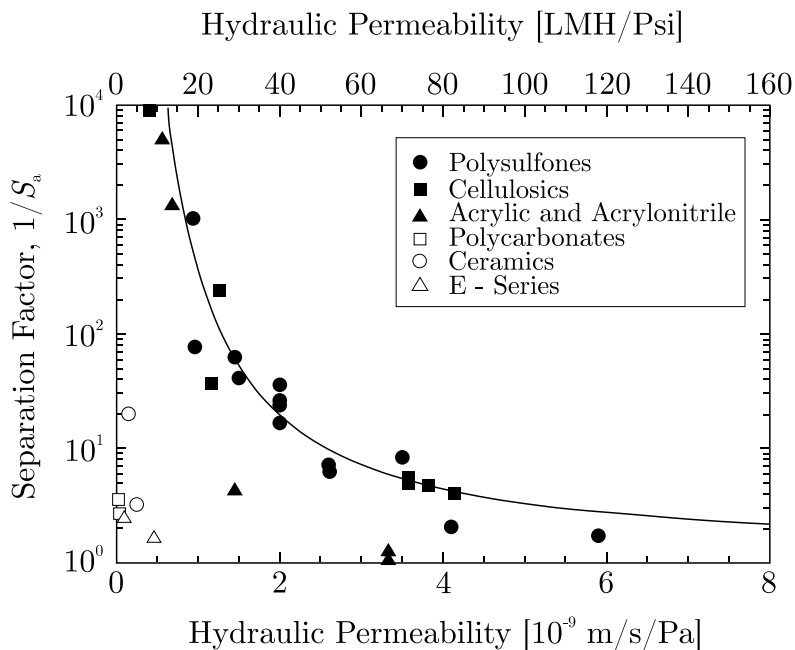


Figure 2.4: Trade-off between separation factor $1/S_a$ and hydraulic permeability for different ultrafiltration membranes and BSA as the filtered proteins. Reproduced with permission. Copyright © 2005 Elsevier B.V. [38].

100 GPa, respectively, compared to polystyrol with a Young modulus of 3.1 GPa and a tensile strength of 0.05 GPa [44–46]) and chemical resistance [47, 48] make them attractive candidates as future membrane materials (the exact values of their mechanical properties may differ depending on their defect density and fabrication method [44]). Still, they display sufficient mechanical strength and chemical resistance to withstand high pressure differences and many chemicals during filtration processes. Their selling point in multiple ways, however, is their atomic thickness. Because they are *de facto* all-surface, any modification (*e.g.*, adsorption of stabilizing agents, defects or contact to other 2D materials) will have a disproportionately large impact compared to 3D materials whose majority of atoms/molecules are shielded within the bulk material.

Layered 2D materials have been experiencing growing interest for the last years as well and have been used as membranes in various configurations and modifications. Especially graphene oxide laminates, which are stacks of multiple individual graphene oxide sheets, have shown intriguing filtering properties not at least because of their functional groups located on the basal planes and edges of the crystallites. In ref. [15] R. Joshi *et al.* performed one of the first filtration experiments with a graphene oxide membrane of only few μm thickness. Some of the measurements are reproduced in Fig. 2.5 showing the possibility of ionic and molecular filtration using graphene oxide membranes. Larger molecules (*e.g.*, glycerol) were successfully removed while smaller ions (*e.g.*, K^+ , Mg^{2+}) could pass.

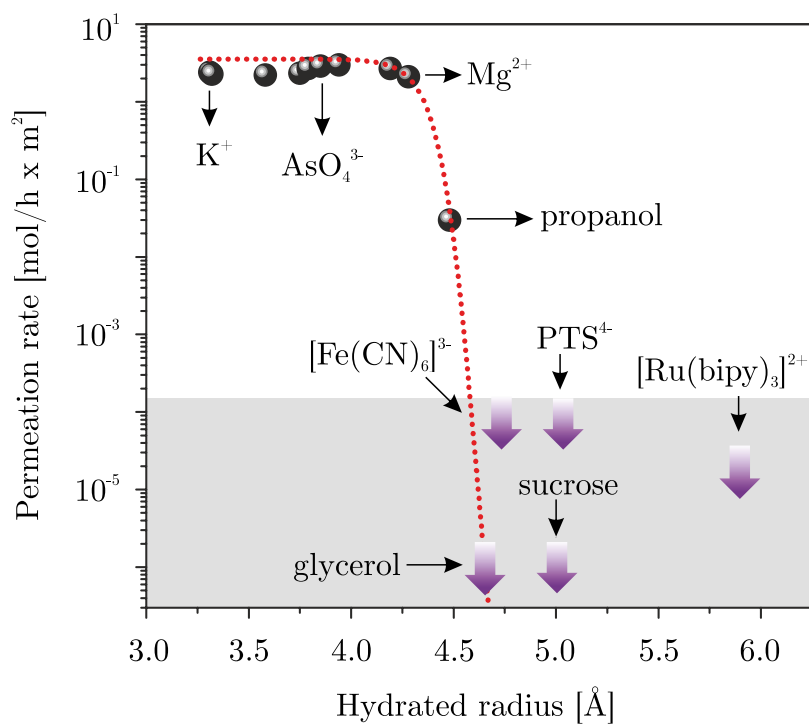


Figure 2.5: Permeation rates through a 5 μm thick graphene oxide membrane were normalized per 1 M feed solution. No permeation was detected for the solutes located in the grey area. The thick arrows indicate the detection limit, which depends on the solute. Copyright © 2014, American Association for the Advancement of Science [15].

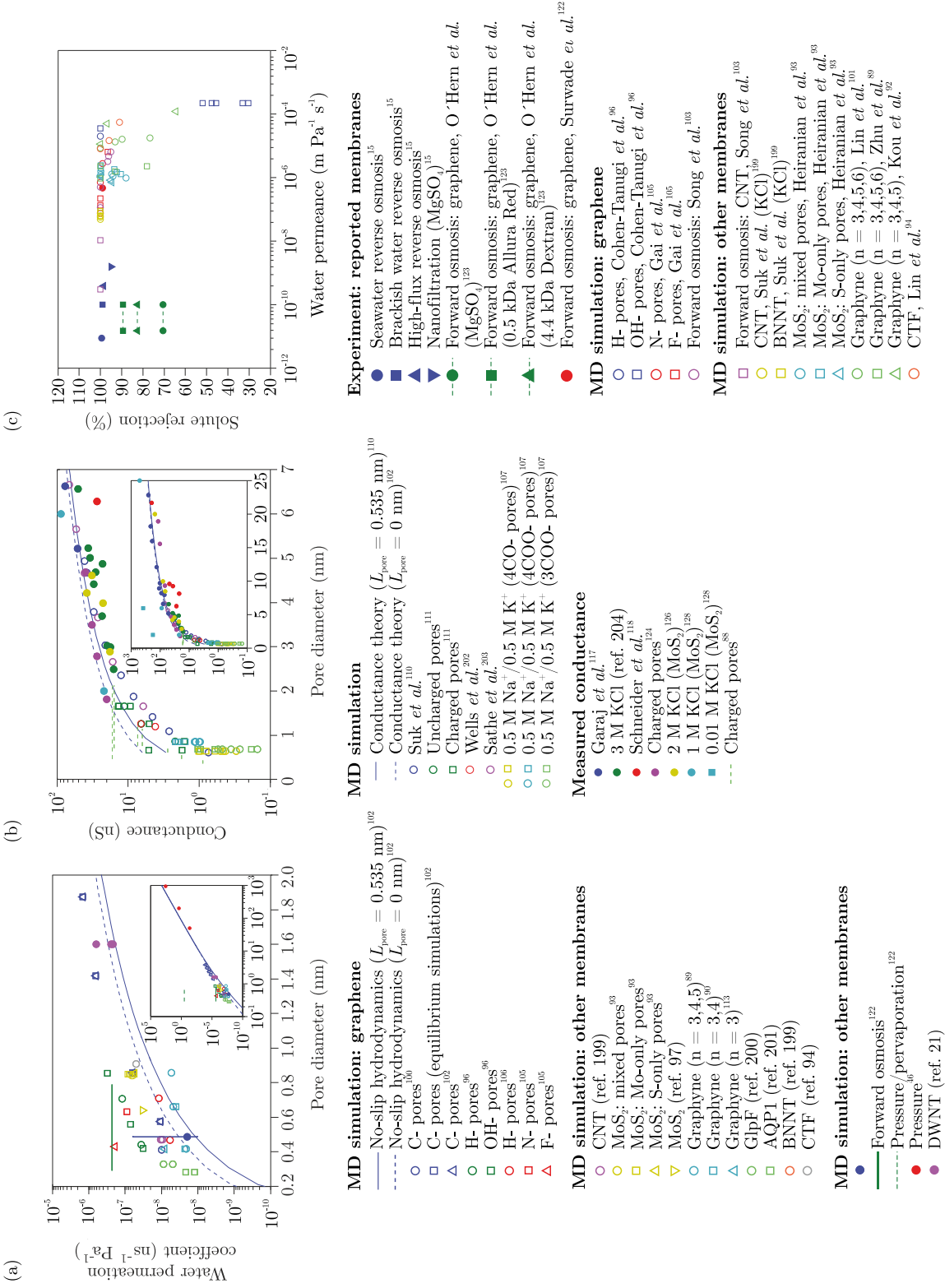


Figure 2.6: Theoretical and experimental data on (a) water permeance, coefficient, (b) conductance, and (c) salt rejection of nanoporous atomically thin membranes. References within the figure correspond to the bibliography of the publication by Wang *et al.*. Reproduced with permission. Copyright © 2017, Nature Publishing Group [12].

Even more evident than the impact adsorbed materials or functional groups have on individual 2D materials or laminates of 2D materials are the advantages of porous atomically thin layers (*e.g.*, single-layer graphene, single-layer MoS₂, etc.) when utilized as a membrane. Here, their minimal thickness can be fully exploited in form of a highly reduced flow resistance of the fluid when passing through the porous membrane. Numerous theoretical and experimental studies have been dedicated to study water permeation (Fig. 2.6 (a)), ion conductance (Fig. 2.6 (b)), and salt rejection (Fig. 2.6 (c)) through atomically thin materials driven by pressure [33, 49–52], osmosis [53, 54], or electrical potential gradients [55, 56]. Certainly, what stands out is the high number of publications investigating different pore edge terminations which were shown to influence water transport by de-/increasing transport energy barriers [33, 51]. Further, pore functionalization and pore charges were shown to alter the ionic conductance through atomically thin membranes allowing the realization of, *e.g.*, cation/anion selectivity [57]. Desalination has been another highly investigated topic where 2D membranes have been employed. Various perforated and modified 2D materials have shown an exceptionally high water flux with a salt rejection close to 100 % [12, 33, 51].

Despite the multitude of experiments and creativity of material modifications associated with them, there is barely (if not none experiment at all) demonstrating measurements with large-area 2D materials exhibiting artificially generated pores sizes between two and ten nanometer in diameter with a clear emphasis on a controllable defect creation or synthesis technique. Only a few approaches have been presented which come close to this pore size regime and with an option of scalability [58, 59]. If the focus of an experiment that has been published as a research article lies on a precise pore size, perforation is usually achieved with help of a focused electron/ion beam which is in no way scalable and restricts experiments to small-area devices [60–62]. In case of large-area membrane measurements, keV-ion irradiation followed by plasma or chemical etching is usually the method of choice, which however is limited in accuracy with respect to pore size distribution [63–65]. It is therefore imperative to find new modification techniques which allow a large-area perforation of 2D materials with a narrow pore size distribution - especially in the pore size regime of ultrafiltration.

2.3 2D Materials

Two-dimensional (2D) materials had long been thought of as thermodynamically unstable and had only been theoretically investigated. Especially the work of R. E. Peierls and L. D. Landau [66–68] and later of N. D. Mermin and H. Wagner [69, 70] demonstrated the instability of low-dimensional materials due to atomic displacements caused by thermal fluctuations. Their extent would be comparable to interatomic distances, hence tearing low-dimensional materials apart and prohibiting their existence. Due to this, it was an even bigger surprise when A. Geim and

K. Novoselov successfully isolated a one-atom thick layer of hexagonally oriented carbon atoms in 2004, followed by many other 2D materials, both substrate supported or fully suspended [13, 14, 71, 72]. The interest in this new class of materials has drastically grown ever since. Due to their versatile intrinsic properties, material specific characteristics, and the possibility to create almost completely new materials when combining them (by simply stacking them on top of or next to each other as schematically shown in Fig. 2.7) both academia and industry show great interest in this material class trying to exploit their properties in fields of (opto-)electronics [73, 74], membrane science [75, 76], catalysis [77, 78], mechanical engineering [79, 80], and many more. Three representatives of the class of 2D materials and/or their chemical modifications will be presented in the following. Intrinsic properties as well as their utilization as a membrane will be elucidated and still debated and troubling problems discussed.

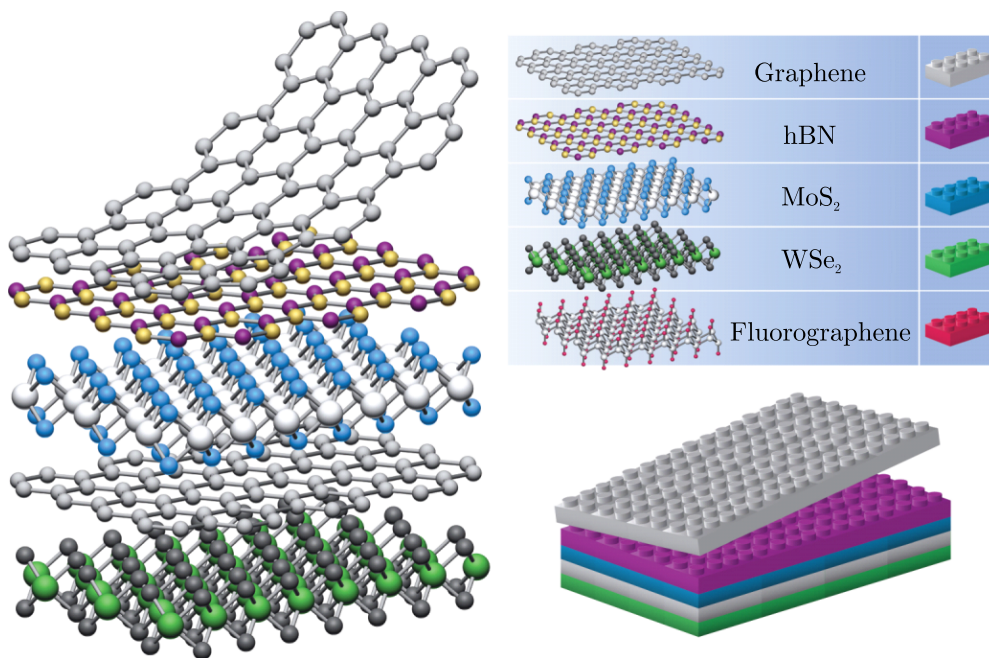


Figure 2.7: Schematic of stacked various 2D materials yielding fundamentally new material properties. Reproduced with permission. Copyright © 2013, Nature Publishing Group [81].

2.3.1 Graphene

Almost two decades after the discovery of 2D materials and the successful synthesis of countless variations, the most famous representative of the 2D material class remains graphene, which can nowadays easily be produced at wafer-scale dimensions and remains the only true 2D material that has been used as large cm²-scaled membranes so far [63, 82, 83]. An optical image

of a 4" Cu wafer fully covered with single-layer graphene is shown in Fig. 2.8 (a). Graphene is a single-atom thick sheet of carbon atoms arranged in a hexagonal, sp^2 -hybridized lattice structure, as illustrated in Fig. 2.8 (b). Each carbon atom shares a strong σ -bond with its three direct neighbors. The fourth electron of each atom occupies the $2p_z$ orbital whose orientation is perpendicular to the lattice. This electron along with one electron from all the other carbon atoms overlap and form a delocalized π -system which is mainly responsible for the outstanding electronic properties of graphene [71, 84]. Its unit cell is defined by its lattice vectors \vec{a}_1 and \vec{a}_2 :

$$\vec{a}_1 = \frac{a}{2}(3, \sqrt{3}), \quad \vec{a}_2 = \frac{a}{2}(3, -\sqrt{3}), \quad (2.4)$$

where a denotes the carbon-carbon distance of 0.142 nm. The three nearest neighbors of each atom can be described with δ_1 , δ_2 , and δ_3 :

$$\delta_1 = \frac{a}{2}(1, \sqrt{3}), \quad \delta_2 = \frac{a}{2}(1, -\sqrt{3}), \quad \delta_3 = -a(1, 0) \quad (2.5)$$

It becomes evident that the lattice is split into two individual sub-lattices A and B , whose atoms are highlighted in yellow and blue in Fig. 2.8 (b), respectively. Depending on the direction along the crystal lattice, one distinguishes between the zigzag (marked in green) and armchair (marked in blue) orientation. Fig. 2.8 (c) shows the first Brillouin zone of graphene's reciprocal lattice with its unit vectors \vec{b}_1 and \vec{b}_2 :

$$\vec{b}_1 = \frac{2\pi}{3a}(1, \sqrt{3}), \quad \vec{b}_2 = \frac{2\pi}{3a}(1, -\sqrt{3}) \quad (2.6)$$

Even though first experiments focused on graphene's extraordinary electrical properties, while usually being fully supported by a substrate material, its utilization in suspended form, *e.g.*, as a pressure sensor or filtration membrane, quickly found interest. Only recently it was shown by I. E. Roslon *et al.* that graphene pores may be used as a precise and low-cost gas effusion sensor. By sudden pumping of gas through perforated graphene using optothermal forces and closely monitoring its varying frequency response, the authors were able to differentiate between several gases due a different oscillating behavior of graphene resulting from a varying molecular weight of the effusing gas [85]. Even more prominent and obvious are actual graphene-based filtration membranes. Experiments include desalination measurements [64] with a high fouling resistance [86], gas separation modeling [59], and even investigate graphene's suitability for DNA sequencing [87]. Just as any other 2D material, graphene too needs some

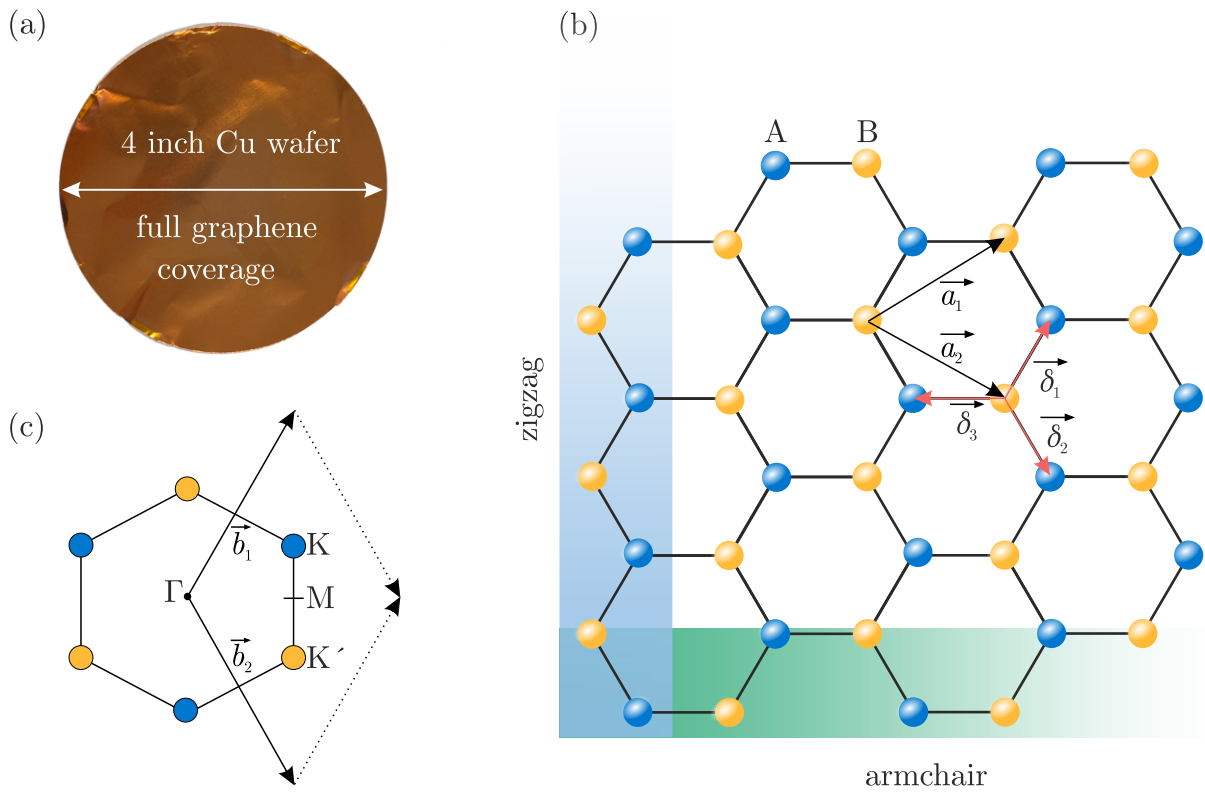


Figure 2.8: (a) 4" copper wafer fully covered with graphene. (b) Top view of graphene's crystal lattice with unit vectors \vec{a}_1 and \vec{a}_2 . The edges are referred to as zigzag or armchair depending on their orientation. Nearest-neighbor vectors are $\vec{\delta}_1$, $\vec{\delta}_2$, and $\vec{\delta}_3$. (c) First Brillouin zone of graphene's reciprocal lattice with reciprocal unit vectors \vec{b}_1 and \vec{b}_2 and high-symmetry points Γ , K, K', and M [84].

sort of support material when used for membrane applications. Often a porous polymer support is utilized with pores that are small enough to provide sufficient mechanical support but also too large to significantly affect the overall resistance of the composite membrane. The necessity of a support requires a transfer of the graphene layer from the growth material onto the support material at some point. With respect to this, E. S. Polsen *et al.* and S. Bae *et al.* have reported advanced roll-to-roll growth [88] as well as roll-to-roll transfer [89] processes of single-layer graphene onto flexible substrates which certainly proves the possibility of industrial up-scaling. Fig. 2.9 shows a schematic of the growth (a), (b) and transfer line (c) used by E. S. Polsen *et al.* and S. Bae *et al.* for high-throughput growth and transfer of graphene, respectively.

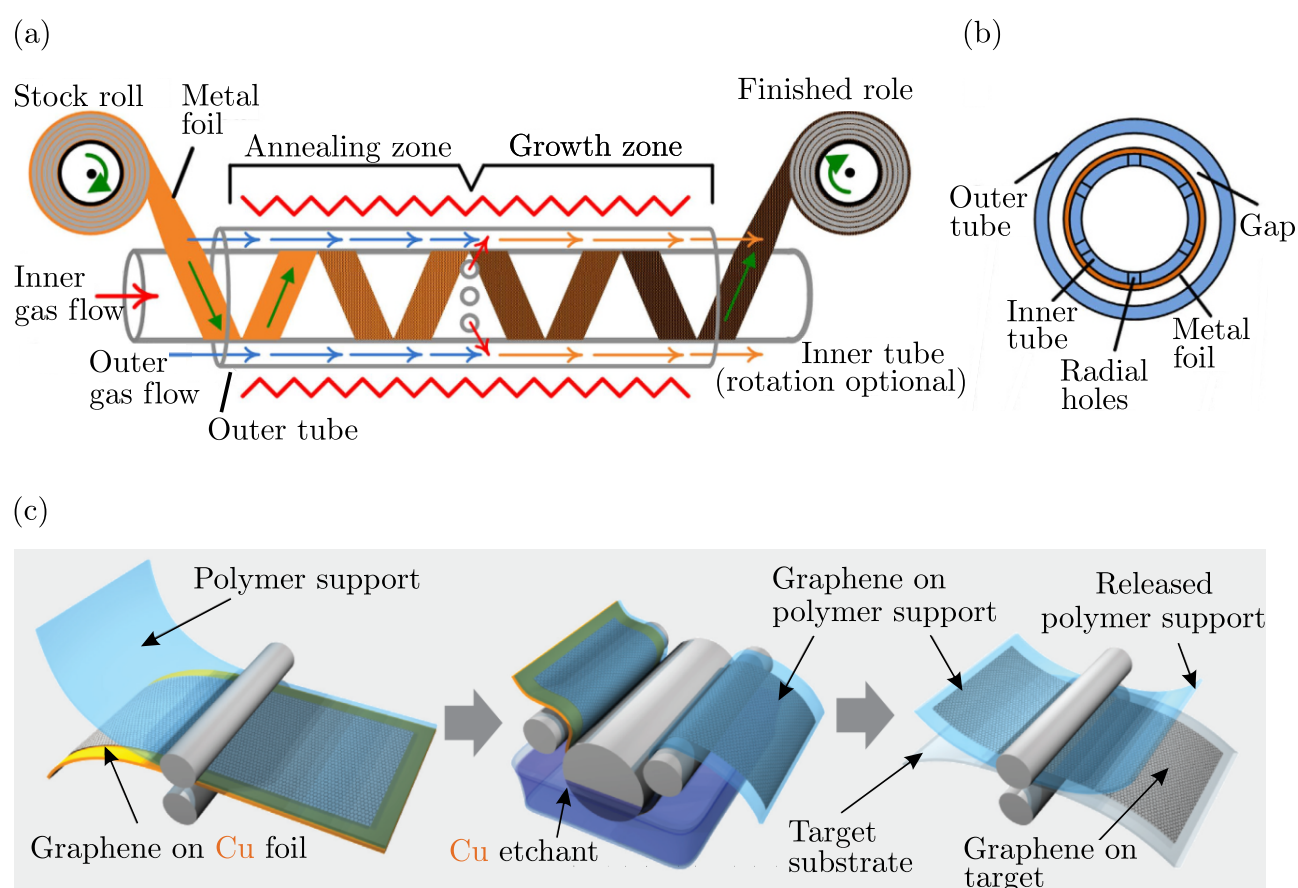


Figure 2.9: (a)-(b) High-throughput CVD growth of single-layer graphene on flexible copper substrates. Reproduced with permission. Copyright © 2015, the authors of ref. [88]. (c) Automatic roll-to-roll transfer system of graphene onto flexible substrates. Reproduced with permission. Copyright © 2010, Nature Publishing Group [89].

However, for lab-scale experiments where smaller samples are sufficient or those requiring a rigid or non roll-to-roll compatible substrate other transfer techniques are necessary. In order to move the focus away from the familiar polymer-based transfer, which is actually notorious

for unintentional defect creation, a polymer-free transfer without the restriction to certain substrates is desirable [90–93]. A common transfer of graphene with help a polymer support layer is presented in Fig. 2.10. After the growth step of graphene on a thin Cu foil (a), a stabilizing and sacrificial polymer layer is deposited onto the 2D material (b) which provides mechanical support during the etching step of the Cu (c). Finally, the polymer/graphene stack is transferred onto the target material and the polymer film is dissolved again.

Chapter 4 addresses this issue and introduces a transfer method which is based on a surface energy engineering approach of the graphene layer prior to the transfer. The modified graphene can be handled without any support layer which again results in much cleaner and defect-free graphene.

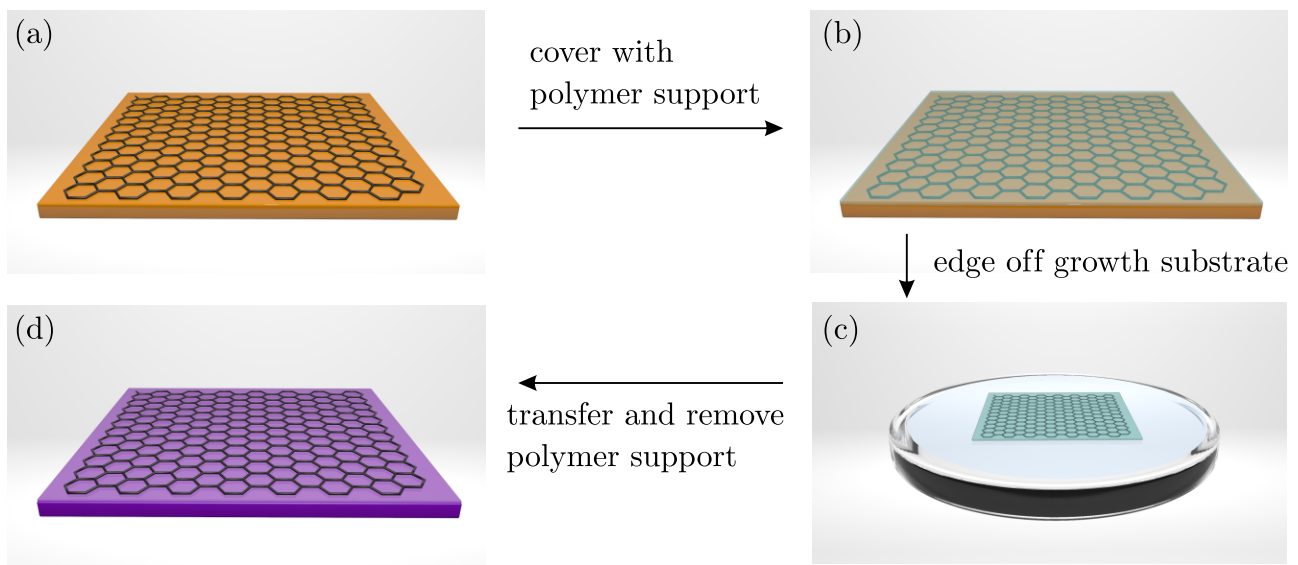


Figure 2.10: Schematic of polymer-based transfer of single-layer graphene. (a) As grown graphene on Cu substrate. (b) The sacrificial polymer layer is deposited onto the substrate. (c) Growth substrate is etched off and (d) polymer/graphene stack is transferred onto target material. The polymer is then dissolved with suitable solvents.

2.3.2 Graphene Oxide

Graphene-based composites and material modifications of graphene have been experiencing equally much attention as its unmodified form. Especially graphene oxide (GO) is heavily investigated due to the versatile possibilities of using it in fields of environmental science, *e.g.*, using GO as an environmentally friendly electrical capacitor [94, 95], a storing device for hydrogen gas [96], or as a chemical catalyst [97]. The interest in GO, however, was initiated by its unique performance as a filtration membrane [15]. Originally synthesized by Benjamin

Collins Brodie in 1858 as graphite oxide by a method later known as the *Brodie method*, several other procedures for synthesizing it have emerged over the years (*e.g.*, Staudenmaier [98] or Hummers and Offeman method [99]) all of which include a concentrated acid with an oxidizing agent. In this work, GO has been prepared according to the Hummers method, which include the oxidation of natural graphite with potassium permanganate. Followed by sonication to exfoliate the graphite flakes into single- and bi-layer and refinement via centrifugation, the GO flakes can be deposited onto a porous polymer support subsequently which allows the fabrication of GO membranes as shown in Fig. 2.11 (a).¹ Optical and scanning electron microscopy images of a polyvinylidene fluoride (PVDF) supported GO membrane and of the laminated structure of GO are presented in Fig. 2.11 (b) and (c), respectively.

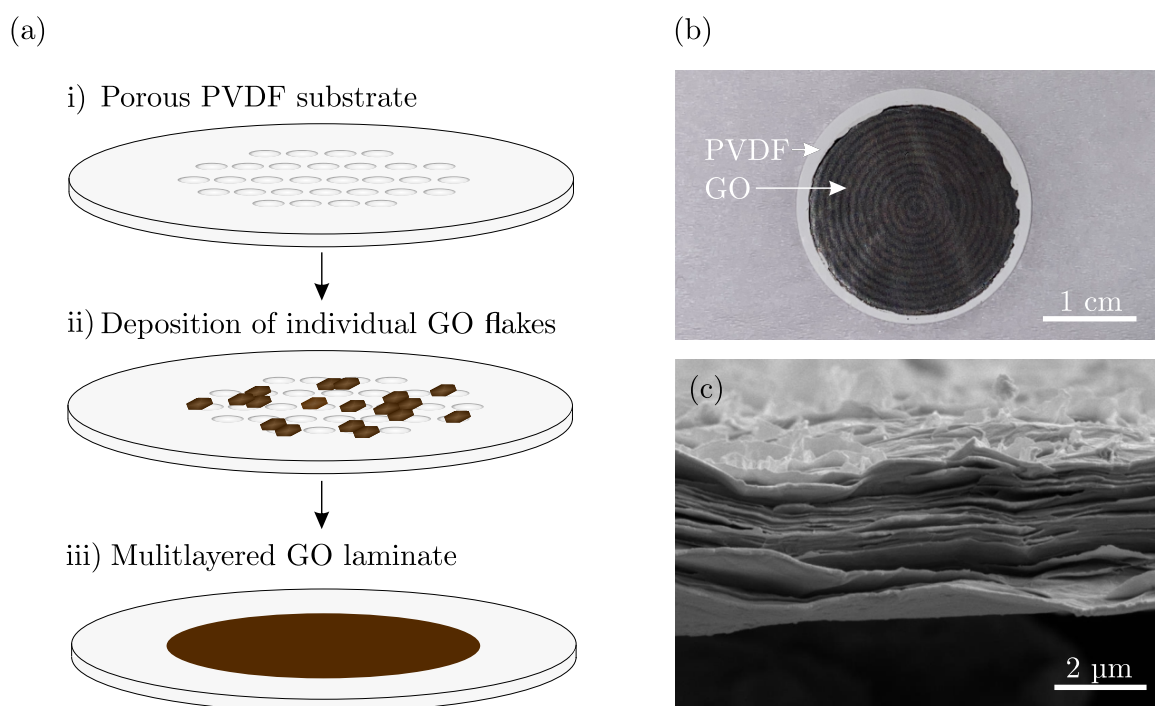


Figure 2.11: (a) Schematic of preparation process of GO membranes. (b) Optical image of a GO membrane supported by a porous polymer substrate. (c) Cross-section SEM image of GO. Reproduced with permission. Copyright © 2020, American Chemical Society [100].

The chemical structure of GO and reduced GO (rGO) is schematically illustrated in Fig. 2.12 showing sp^3 -hybridized carbon atoms that form the backbone of the material [101]. In contrast to graphene, GO features oxygen and hydrogen containing functional groups, *i.e.*, hydroxyl- (-OH), epoxy- (=O), and carboxyl- (-COOH) groups, that are attached to the basal

¹GO membrane fabrication was performed by Prof. Dr. Rakesh Joshi and Mr. Tobias Foller - School of Materials Science and Engineering, University of New South Wales, Kensington, New South Wales 2052, Australia

planes and edges of the GO sheets. These functional groups are of particular interest as their presence causes a hydrophilic behaviour of GO and also governs the interlayer distance of individual GO laminates. Reducing GO and hence partially removing its functional groups leads to a more and more hydrophobic behavior and a decreased interlayer spacing, which can be explained with the functional groups acting as spacers preserving a certain distance between adjacent GO flakes. It is due to this behavior that filtration properties have mainly been tuned by altering the degree of reduction of GO [102, 103]. In this regard, Fig. 2.13 illustrates the general water transport and filtration mechanism through (a) GO and (b) rGO, respectively. Before reduction, the interlayer spacing d_{GO} is large enough that, *e.g.*, both water molecules and hydrated ions or natural organic molecules (NOMs) can pass through the channels. rGO, however, shows a decreased interlayer spacing ($d_{rGO} < d_{GO}$) such that larger hydrated ions or NOMs are retained making the interlayer spacing a critical property for filtration. However, adapting GO's properties only by tuning d_{GO} hardly applies when dealing with particles of almost identical size within the feed solution. One possible solution is not to rely on d_{GO} but on the electrostatic interaction with its natural functional groups and the transport mechanisms within the water filled channels as has been done for the spatial separation of hydronium and hydroxide ions in chapter 5 *Graphene Oxide Membranes: Selective Proton Transport for Hydrogen Generation*.

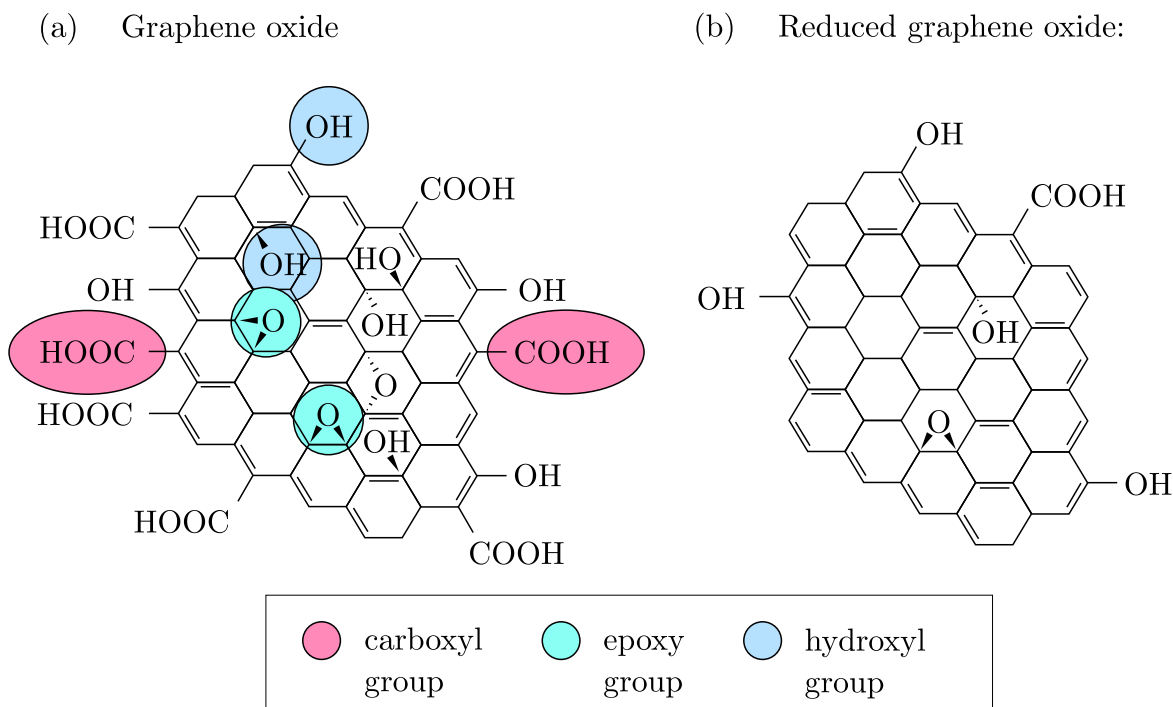


Figure 2.12: (a) Schematic of the chemical structure of GO and rGO. GO contains hydrophilic functional groups that are a direct result from the preparation process. Reducing the GO again removes these functional groups. The extend of this process determines how many of its functional groups will be left afterwards.

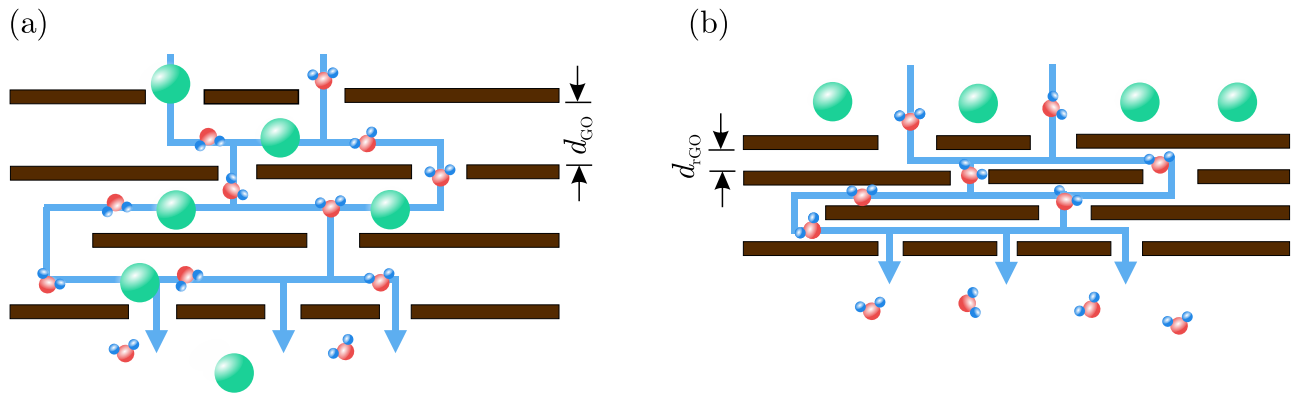


Figure 2.13: Schematic of water and particle, *e.g.* ions or NOMs, transport through (a) GO and (b) rGO. Oxygen and hydrogen atoms are represented by red and blue spheres, respectively. Other particles are shown as green spheres.

2.3.3 Molybdenum Disulfide

Molybdenum disulfide (MoS_2) is arguably the second most famous 2D material, but certainly the most investigated 2D material among the family of 2D transition-metal dichalcogenides (TMDCs) [104,105]. Not only does it exist in form of a van-der-Waals 3D bulk crystal similar to graphene with the possibility of being thinned down to a single-layer, but it may also be synthesized via several deposition techniques routinely performed by the semiconductor industry, *e.g.*, chemical vapor deposition (CVD) [106,107], metal-organic chemical vapor deposition (MOCVD) [108,109] or molecular beam epitaxy (MBE) [110,111]. Even though various crystal structures are potentially viable, most of them are thermodynamically highly instable. The by far most stable atomic arrangement is the hexagonal(H)-form shown in a (a) top- and (b) side view in Fig. 2.14. The lattice vectors \vec{a}_1 and \vec{a}_2 of 1H- MoS_2 and some exemplary less stable crystal forms of MoS_2 , *e.g.*, 1T-, 1T', and 1T'', are presented in Fig. 2.15 [112–114].

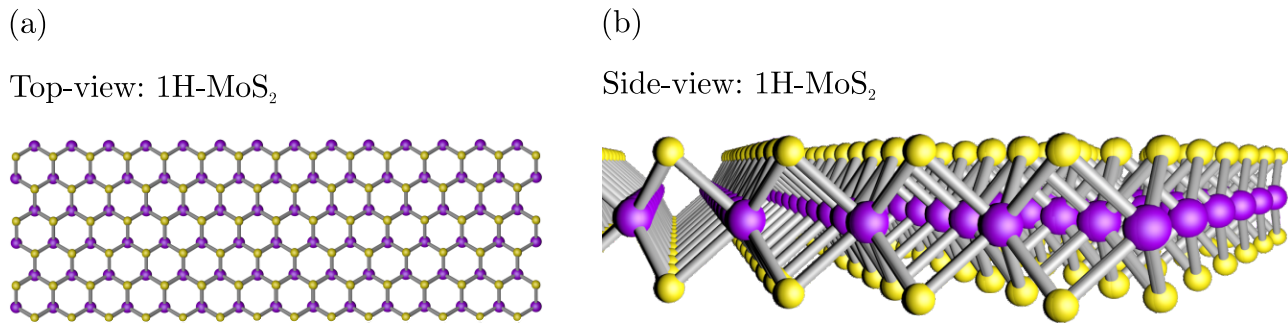


Figure 2.14: Schematic of 1H- MoS_2 crystal lattice shown in a (a) top- and (b) side-view. S and Mo atoms are represented by yellow and purple spheres, respectively.

Current MoS_2 -based membrane research mainly covers fields of desalination and pore sizes associated with nano- and reverse osmosis filtration [116–118]. Following the preparation procedure of GO membranes from individual crystalline flakes, comparable membrane laminates made of MoS_2 are synthesized as shown in Fig. 2.16. Micropollutants and sodium chloride can be retained by $> 90\%$ and 87% , respectively and by controlling the surface chemistry and the interlayer spacing further applications become possible [115]. Even though this approach is perfectly scalable and performs well within its filtration regime, it is hardly applicable for ultrafiltration.

Other membrane fabrication approaches focus on electrochemical defect creation [119,120]. By slowly increasing a trans-membrane voltage intrinsic defects were widened into 2-3 nm large MoS_2 pores. Exemplary measurements from ref. [119] are shown in Fig. 2.17 (a). By measuring current-voltage curves an increase in current is related to an extension of the MoS_2 pore.

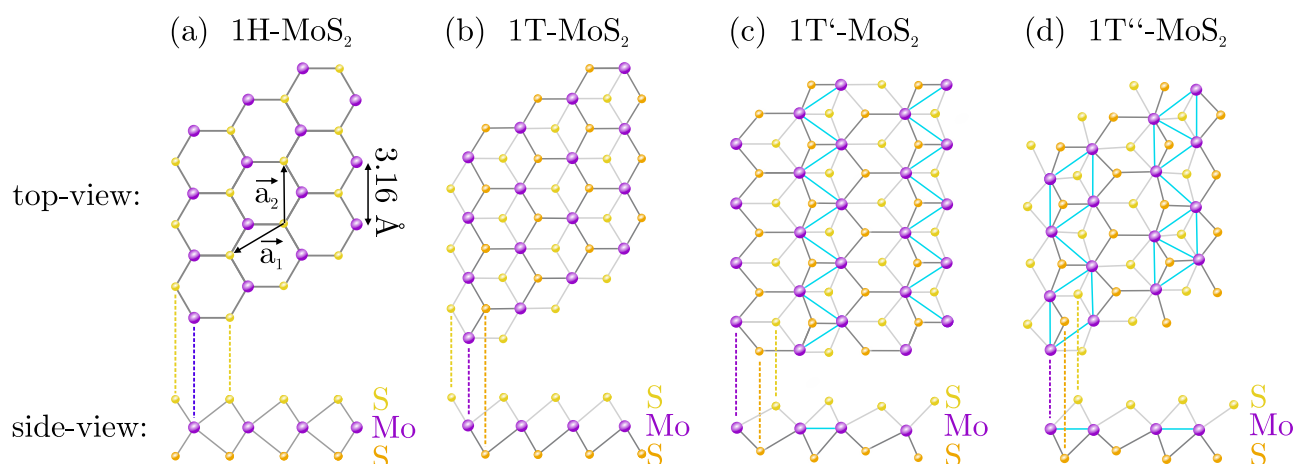


Figure 2.15: Schematic of obtainable single-layer MoS₂ crystal structures as top- and side-view. The only thermodynamically stable form under ambient conditions is the semi-conducting 1H form (a). The metallic 1T form (b) is less stable and degrades due to oxidation. 1T' (c) and 1T'' (d) are highly unstable. Upper and lower S atoms are represented by yellow and orange spheres, respectively. Mo atoms are shown in purple.

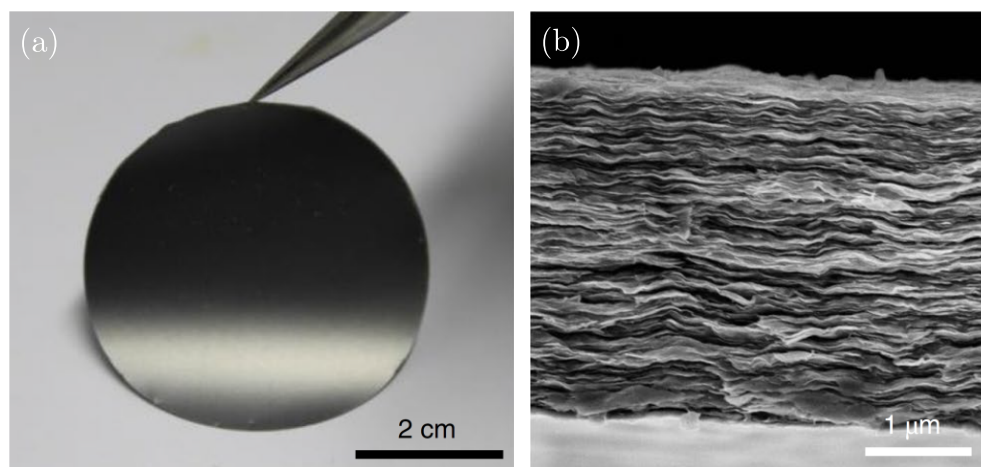


Figure 2.16: MoS₂ laminates serving as filtration membranes with a comparable structure than GO membranes. (a) Optical and (b) cross section SEM image of MoS₂ laminate membrane. Reproduced with permission. Copyright © 2019, the authors of ref. [115].

However, J. Feng *et al.* observed that this process only sets in once reaching a critical voltage V_{crit} . This approach certainly offers many advantages, *e.g.*, scalability and little restriction to pore sizes. Still, the practicability and accuracy of this method is arguable. First, initial defects are required for the process to take place making an additional defect creation process, *e.g.*, keV-ion irradiation, necessary. Second, the actual pore opening is described as a successive polygon removal process due to oxidation of MoS₂ as indicated in (b), where four exemplary stages are presented. With increasing pore size, the proposed mechanism will accelerate due to an increasing pore area questioning the accuracy when fabricating larger nanopores (note that only the initial intrinsic defect size, *i.e.* point defect, was imaged and following sizes were calculated based on experimental conditions and data).

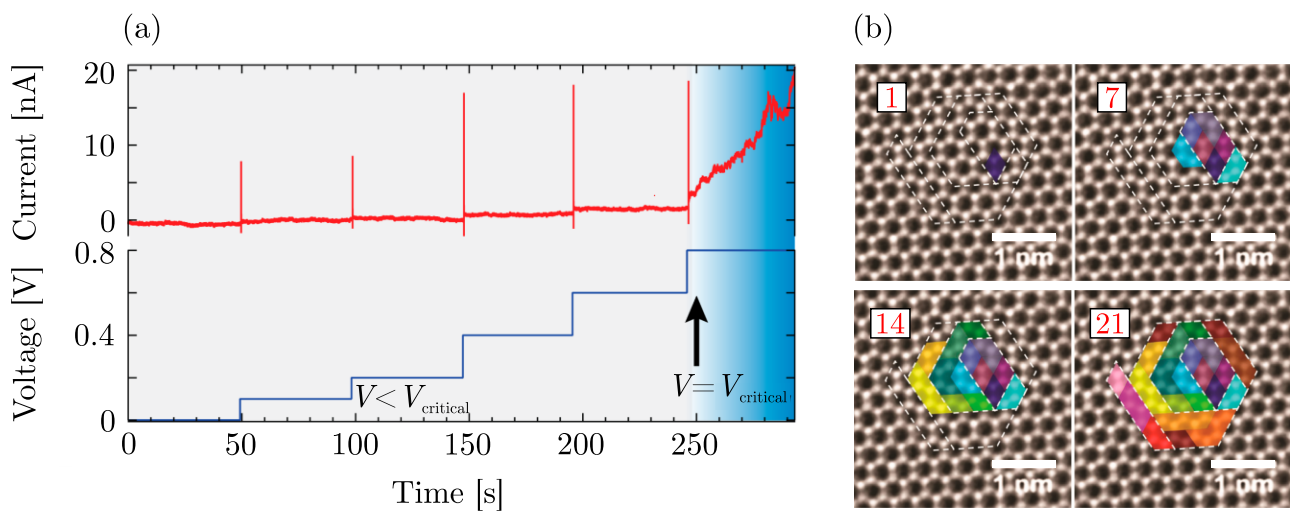


Figure 2.17: (a) Electrochemical pore creation in a MoS₂ membrane using a trans-membrane voltage. (b) Four exemplary stages (labeled as 1, 7, 14, and 21) of expected pore geometry. Reproduced with permission. Copyright © 2015, American Chemical Society [119].

Still, the most often used defect engineering method of 2D materials including MoS₂ remains ion irradiation as it offers a quick and precise tool to introduce a well-defined number of defects [34, 63, 121]. Especially the possibility of non-stoichiometric defect creation, *i.e.*, preferential removal of S or Mo atoms, has initiated research to theoretically investigate the influence of pore termination on the water permeability through MoS₂ pores. Fig. 2.18 presents molecular dynamics (MD) simulations comparing different edge configurations in (a) and their influence on water permeability in (b). Clearly all MoS₂ edge termination perform well and even outperform calculated water permeability of graphene nanopores of similar size. However, MoS₂ pores with Mo edge termination show the highest water flux compared to mixed or S-only edges resulting from both a higher water density and flow velocity within a Mo only pore. The reason for this lies in the higher hydrophilicity of Mo over S and MoS₂ [122, 123], as well as in a reduced energy barrier that a water molecule has to overcome to enter the pore [33]. This

finding is of particular interest as it will be shown later in the experimental result chapters 6 *Electronic Excitation and Perforation of Single-Layer MoS₂* and chapter 7 *Chemical Structure of SHI Irradiated MoS₂ for Catalytic Applications* that SHIs and HCIs are suitable to not only perforate MoS₂ but also evoke such promotive pore terminations.

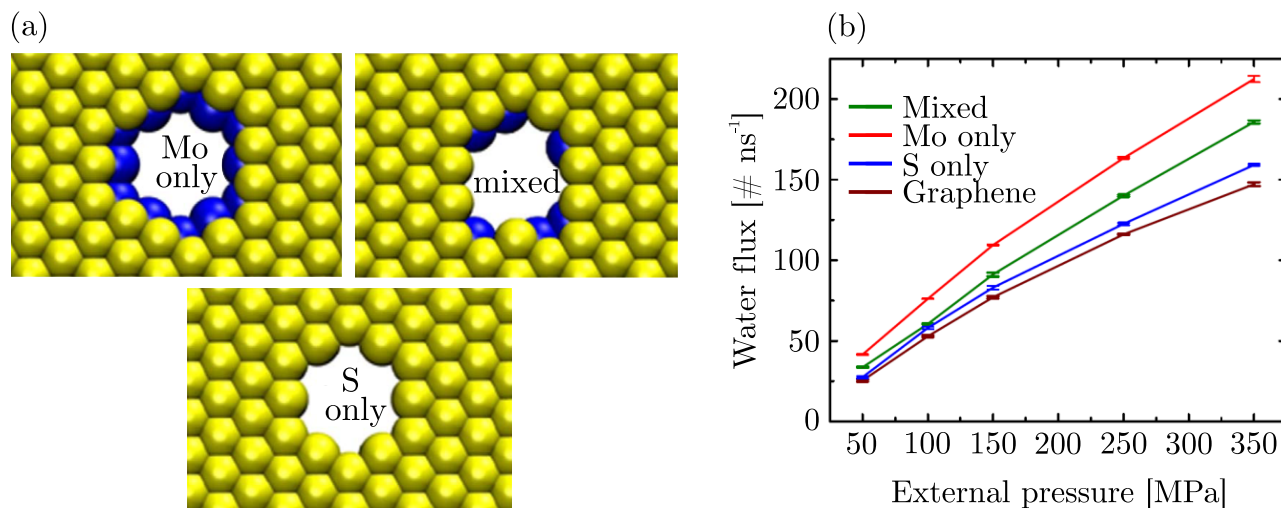


Figure 2.18: (a) Different edge termination of MoS₂ pores. (b) Calculated water permeability through porous MoS₂ depending on edge types shown in (a) and through graphene for comparison. All pores have approximately equivalent accessible pore areas. Reproduced with permission. Copyright © 2015, the authors of ref. [33].

2.4 Synthesis of 2D Materials

2.4.1 Micromechanical Exfoliation

To study and eventually apply 2D materials as membranes, they first have to be produced or synthesized via appropriate fabrication techniques. The most frequently used methods for 2D material production are the mechanical exfoliation and chemical vapor deposition (CVD). The exfoliation technique gained a tremendous amount of attention after A. Geim and K. Novoselov used it to isolate 2D crystals and it still is unrivaled when it comes to crystallinity and cleanliness of the produced samples as well as simplicity of handling and execution [14]. The exfoliation technique exploits weak vdW forces between adjacent planes of vdW crystals so that layers can easily be peeled off from a 3D bulk crystal as shown in Fig. 2.19 (a) for peeled-off MoS₂. The material can then be pressed onto and removed again from a target wafer causing smaller crystals to adhere to the substrate as shown in Fig. 2.19 (b)-(d). The convenience of this technique as well as its universal applicability to nearly every vdW material and target substrate makes it a still highly appreciated method of sample preparation.

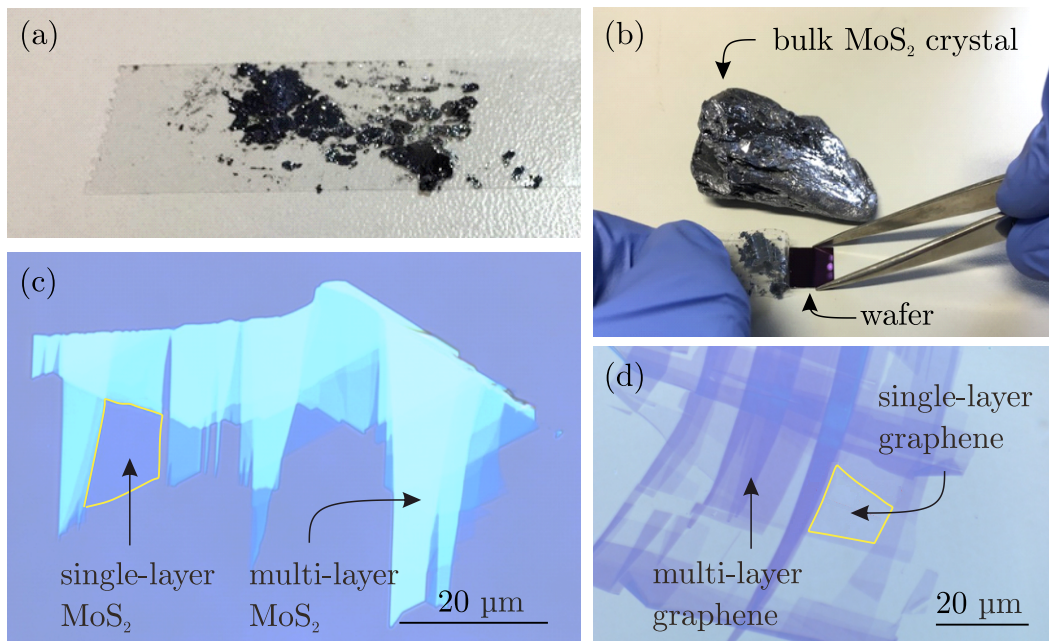


Figure 2.19: Process of exfoliating ultrathin layers of vdW crystals. (a) Scotch tape is used to peel off layers from a bulk crystal which are (b) pressed onto and removed again from a target wafer of choice (here Si/SiO₂). Individual flakes with varying thicknesses adhere to the substrate. Optical images of exfoliated (c) MoS₂ and (d) graphene, respectively.

A decisive drawback, however, is the lacking possibility for up-scaling and reproducibility making this approach uninteresting for industrial applications where often continuous and cm^2 large-area films are required. Therefore, other techniques (mainly adapted from the semiconductor industry) have been applied to synthesize 2D materials with the advantage of being able to tune the size [106], thickness [124], growth location [125], orientation [126], as well as electrical and optical properties of the grown 2D materials [127, 128]. Especially, the chemical vapor deposition (CVD) has proven its reliability and is most often used for growth processes.

2.4.2 Chemical Vapor Deposition

CVD describes a process which is particularly useful for growing 2D materials as exemplary shown in Fig. 2.20 for the growth of MoS_2 . Solid chemical reactants (sulphur - yellow spheres, molybdenum oxide - purple spheres) are evaporated (step 1) and transported via an inert carrier gas towards a growth substrate (step 2). After adsorption onto the heated substrate (step 3) and chemical reaction to form the final reaction product (step 4) according to the reaction $2\text{MoO}_3 + 7\text{S} \rightarrow 2\text{MoS}_2 + 3\text{SO}_2$, the material is allowed to diffuse on the substrate and rearrange to form a crystalline lattice (step 5). Gaseous by-products of the reaction are removed from the system (step 6).

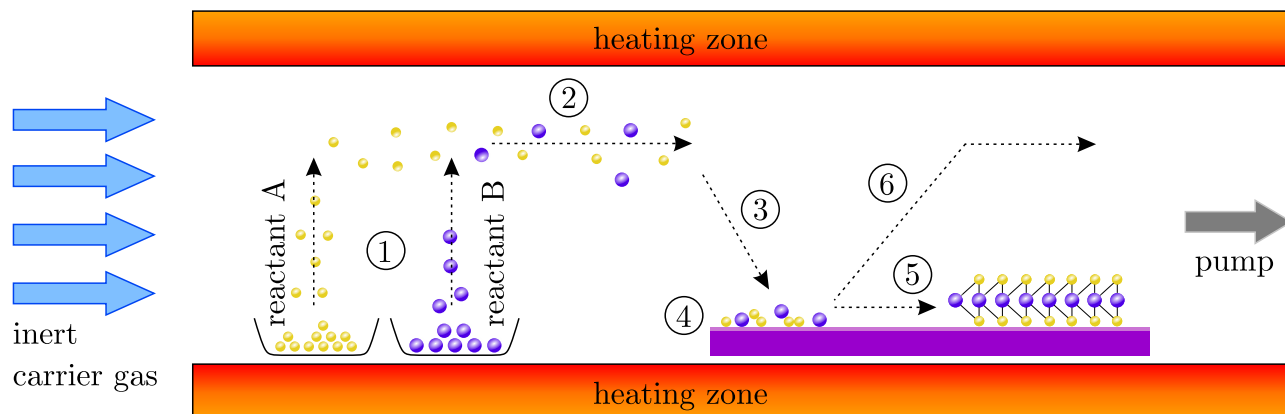


Figure 2.20: Principle of CVD process exemplary shown for growth of 2D MoS_2 . Reactants are evaporated and transported to the growth substrate where they adsorb, react, and form the desired material. Gaseous by-products are removed from the system.

A sketch of the growth oven set up used during this thesis is presented in Fig. 2.21. A 3-zone split tube furnace (ThermConcept GmbH, Bremen, Germany, model ROK 70/750/12-3z) was used to conduct all growth experiments of MoS_2 layers. Two thermally isolated zones (1), (2) are heated separately to evaporate sulphur (3) and molybdenum oxide powder (4),

each located in a separate ceramic crucible and heating zone. The crucibles are placed in a 30 mm quartz glass tube. Argon gas is used to purge the tube prior to the growth process in order to remove oxygen gas and during the growth to transport evaporated chemical reactants towards the growth substrates that are also positioned in the second heating zone (5). Fig. 2.21 (b)-(d) present some of the different growth result that can be obtained, depending on the growth parameters and substrate pre-treatment. Randomly oriented and triangular (b) as well as locally defined (c) MoS₂ flakes or even continuous single-layer films MoS₂ (d) are obtainable.

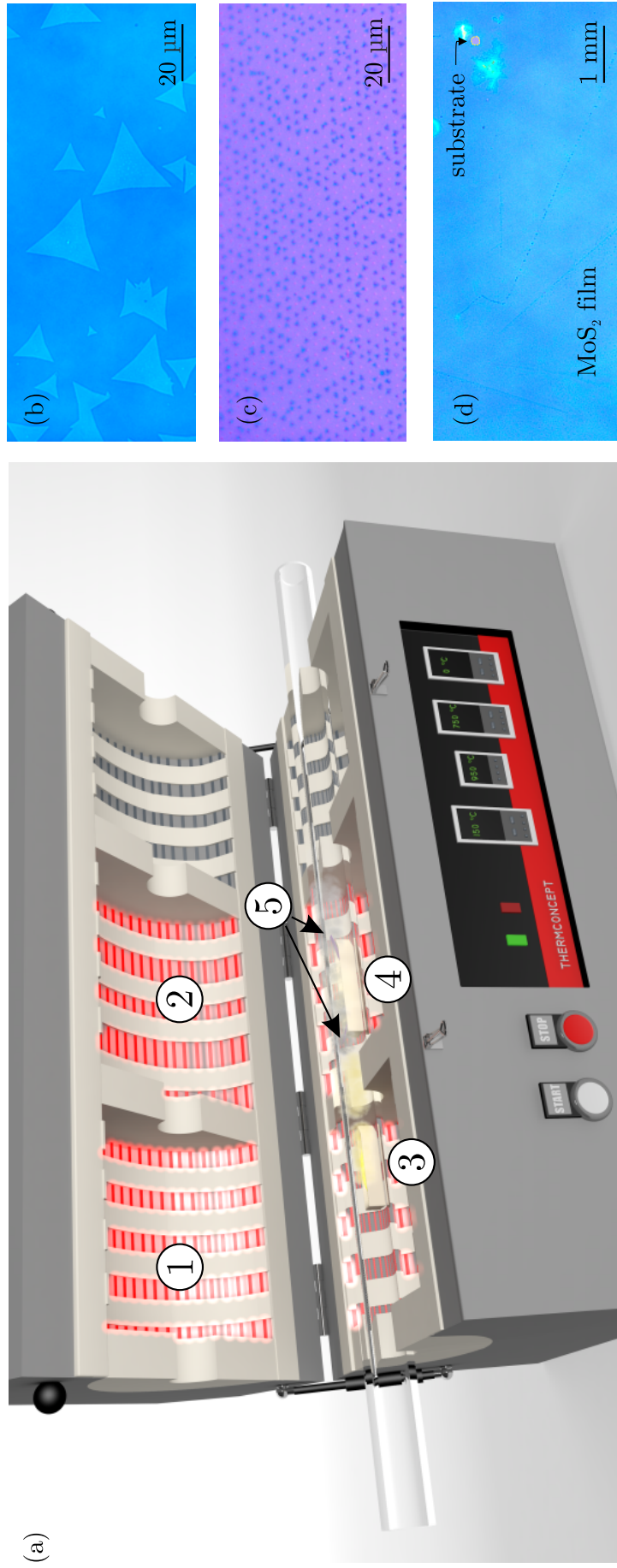


Figure 2.21: (a) Schematic of CVD tube furnace used in this thesis for growth of 2D TMDCs. Chalcogenides (here sulphur) and transition metals (here molybdenum oxide) sources are placed in separate zones and heated until reaching their respective evaporation temperature. An inert carrier gas (here argon) transports the reactants towards the target wafer on which growth of the 2D TMDCs begins. Optical images of CVD grown single-layer MoS₂ on SiO₂ as (b) individual flakes, (c) individual flakes at predetermined positions, (d) a continuous film.

3 Defect Generation and Characterization Techniques

The vast majority of state-of-the-art devices require precisely tailored materials to increase efficiency and boost performance. A well-known and commonly applied technique for material modification is ion irradiation. Areas of applications extend across the semiconductor industry, where both electrical and optical material properties may be altered by ion implantation [21,129] and can even cover certain parts of membrane science where it plays a crucial role in the fabrication of track-etched membranes [26,27,130,131].

First experiments date back to the beginning of the 20th century when Ernest Rutherford and colleagues observed scattering events of alpha particles shot through a thin gold foil [132]. Just as the theoretical understanding of ion-solid irradiation has grown ever since, new questions about the interaction mechanism have emerged. This chapter aims to give a basic understanding of different ion types, their properties, and their interaction principles with solids. The ion types that will be presented are suitable for defect engineering of 3D and 2D materials as will be shown in later chapters. To visualize and quantify ion induced material modifications, two frequently used characterization techniques (atomic force microscopy² and Raman spectroscopy³) will be addressed as well.

3.1 Ion Beams

Ions can be created by adding or removing an electron from initially electrically neutral particles. They are sensitive to electric and magnetic fields which may be used to manipulate their velocity and trajectory. When an accelerated ion enters a material, it undergoes a variety of interaction and scattering processes. Along its trajectory the ion loses its energy through different energy deposition mechanisms whose exact nature depend on the amount and kind of energy initially stored in the ion [23,25,133]. Generally, one distinguishes between a nuclear stopping force

²Bruker Dimension Icon with SCANASYST-AIR tips using the PeakForce Tapping[®] mode

³Renishaw inVia Raman microscope

dE_n/dx , in the following denoted as *nuclear stopping*, and an electronic stopping force dE_e/dx , in the following denoted as *electronic stopping* (note that literature usually refers to it as a stopping power and uses the abbreviation of S_n and S_e for the nuclear and electronic part, respectively, but for clarity and since it does not carry the physical unit of *power*, this thesis refers to it as a force). In the former case, momentum of the incident ion is transferred elastically to the target atoms causing the ion to decelerate and leading to collision cascades as well as atomic displacements in the target material [134, 135]. The latter term applies for inelastic scattering events, *e.g.*, electronic excitation, ionization, and charge exchange mechanisms, which are often accompanied by large deposited energy densities along the ion track causing phase changes and structural modifications of the target material [136–140]. The differential energy loss dE per unit track length dx of the ion can be described as $dE/dx = -n \cdot dE(E)/dx$ with the atomic density n and the total atomic collision cross section $dE(E)/dx$ [141]. As nuclear and electronic differential cross sections are found to be statistically independent of each other, dE/dx can be described by two separate contributions: the nuclear energy loss dE_n/dx and the electronic energy loss dE_e/dx [142]. Both contribute simultaneously to the overall energy deposition such that the formula for the combined deposited energy per unit track length reads:

$$S = S_n + S_e = dE/dx = -dE_n/dx - dE_e/dx \quad (3.1)$$

However, depending on the ion's properties, *i.e.*, its kinetic energy E_{kin} , potential energy E_{pot} , and atomic mass Z_{ion} , as well as the target material's properties, *i.e.*, its atomic mass Z_{target} , the total values and individual contributions of dE_n/dx and dE_e/dx may differ significantly. The focus of this thesis lies on material modifications initiated by electronic stopping. In the following, *swift heavy ions* and *highly charged ions* will be introduced and their interaction with solids will be explained.

3.1.1 Swift Heavy Ions - Electronic Stopping

Swift Heavy Ions (SHI) represent a special group of ions. Their name already indicates that only *heavy* and *swift* ions belong to this ion class. Neither of the two attributes however is really specified giving room for interpretation what an SHI is. Usually, ions heavier than carbon and with a kinetic energy greater than 0.1 MeV/u can be considered as a SHI. One aspect all of them have in common though is how they interact with matter and how they deposit their energy. Fig. 3.1 (a) shows a calculation of dE_n/dx (red line) and dE_e/dx (blue line) for a xenon (Xe) ion with varying E_{kin} interacting with MoS₂. It becomes obvious that the contribution of dE_n/dx

to the total energy loss is negligible for E_{kin} greater than 10 MeV. The electronic stopping force on the contrary is barely evident for E_{kin} below 10 MeV but constitutes almost 100 % of the total energy deposition for higher energies. After reaching the point of maximal energy deposition (Bragg-peak), the total dE/dx decreases again for further growing E_{kin} . Both the absolute value of dE/dx and the position of the Bragg-peak shift to larger values for heavier ions as illustrated in Fig. 3.1 (b) for hydrogen (^1H - inset), nickel (^{58}Ni - dotted curve), xenon (^{129}Xe - solid curve), and uranium (^{238}U - dashed curve).

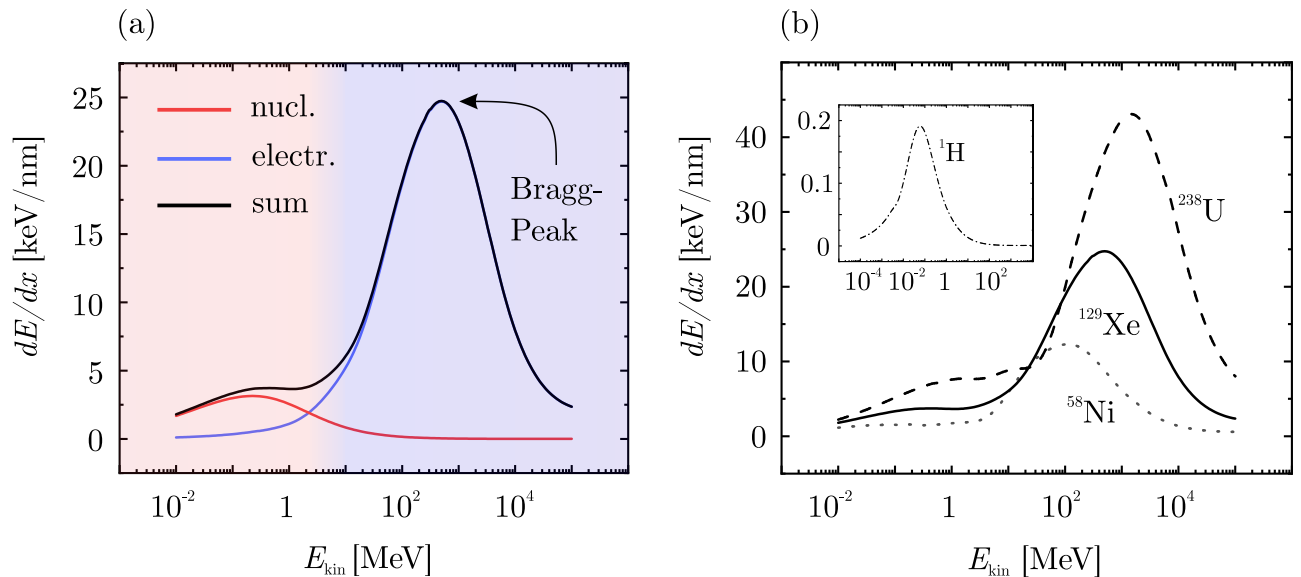


Figure 3.1: (a) Calculation of nuclear and electronic energy losses per nm track length of a xenon ion penetrating through molybdenum disulfide. Nuclear and electronic stopping regimes are highlighted with a red and blue background, respectively. (b) Comparison of total energy loss with respect to their kinetic energy of different ions penetrating through molybdenum disulfide. Calculations have been performed with the SRIM 2013 software [143].

The electronic stopping regime for SHI can be divided into three regions: (i) the left flank of the energy deposition curve where dE/dx increases for higher E_{kin} , (ii) the Bragg-peak, and (iii) the right flank where dE/dx decreases again for higher E_{kin} .

- (i) The first regime can be described by the theory of Lindhard-Scharff-Schiott (LSS) where the stopping force that decelerates the ion can be understood as a friction force. The energy loss is given by eq. 6.1.

$$dE_e/dx = 8\pi\zeta\epsilon^2 a_0 \frac{Z_1 Z_2 v}{Z^{2/3} v_0} \quad (3.2)$$

Z denotes the atomic number of the ion, v and v_0 represents the velocity of the ion

and the Bohr velocity, respectively. ζ equals $Z_1^{2/3}$, where Z combines the atomic masses of the ion and target atom according to $(Z_1^{2/3} + Z_2^{2/3})^{3/2}$. ϵ is dimensionless and in the order of 1-2. It is evident from Fig. 3.1 and can be derived from eq. 6.1 that the electronic energy loss dE_e/dx is proportional to v or $\sqrt{E_{\text{kin}}}$ for $v < v_{\text{Bragg}}$, with v_{Bragg} corresponding to the velocity of the ion at the Bragg-peak.

Additionally, after entering the solid the ion experiences a constant loss and gain of electrons from its surroundings. Up to a velocity of $v = v_0 * Z_1^{2/3}$, its equilibrium charge state Q_{eq} changes according to $Q_{\text{eq}} = Z_1^{1/3} * v/v_0$, with v and Z_1 being the ion's velocity and atomic mass, respectively. Charge state equilibrium is usually obtained after approximately ten nm penetration depth [139, 144].

- (ii) The Bragg-peak represents the point of maximum energy loss and at the same time separates the electronic energy loss regime into two almost symmetrical regions. Even though an SHI is per definition a high-velocity particle, the regimes left and right to the Bragg-peak will be referred to as *low energy regime* and *high energy regime* in this work and are highlighted in Fig. 3.2 by the light and dark blue area, respectively. An important consequence resulting from this curve symmetry is demonstrated in Fig. 3.2. Even though the same dE/dx can be obtained with different E_{kin} , the material modification may change significantly - an effect known as the *velocity effect* [145, 146]. Generally, the following rule applies: the larger the difference in E_{kin} of ions with the same dE/dx , the greater the difference in material modification. Even though the ion deposits most of its energy in a very narrow (a few nm) core track, secondary particles (*i.e.*, ions, electrons, and especially δ -electrons), whose energies scale with the ion's E_{kin} , distribute their energy in much larger distances of up to one μm . This in turn leads to smaller energy densities close to the core track but affects and may damage further distanced areas at the same time.

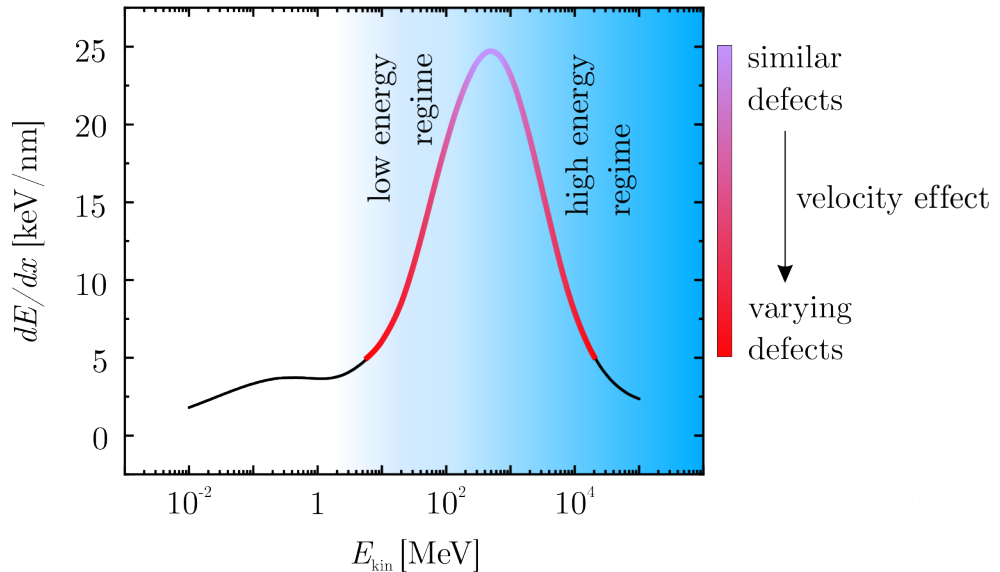


Figure 3.2: Principle of the velocity effect. A larger difference in E_{kin} of two ions with the same energy loss per track length dE/dx lead to stronger varying material modifications compared to ions with slightly varying E_{kin} and identical dE/dx .

- (iii) The third regime cannot be described by the LSS theory as it does not account for relativistic effects or bremsstrahlung which both become important when operating with ions in the *high energy regime*. Bethe and Bloch however managed to develop a quantum mechanical theory allowing the calculation of dE_e/dx according to eq. 3.3 under the assumption that the mass and velocity of the ion are much larger than those of the target atoms [137, 138].

$$dE_e/dx = \frac{4\pi e^4 m_e Z_p^2 N_e}{2\beta^2} \ln \left[\frac{2\gamma^2 \beta^2 c^2 m_e E_{\text{max}}}{I^2} \right] - \phi \quad (3.3)$$

Here, γ represents the Lorentz term which is $\gamma = (1 - \beta^2)^{-\frac{1}{2}}$ and $\beta = v/c$. I and E_{max} symbolize the ionization energy and the maximum energy transfer, respectively, and ϕ accounts for atomic excitations and density fluctuations. Unlike to the first regime, the energy loss dE/dx scales with $\ln(E_{\text{kin}})/E_{\text{kin}}$.

3.1.2 SHI Irradiation Facilities

SHI irradiations that were performed as part of this thesis predominantly took place at the Grand Accélérateur National d'Ions Lourds (GANIL) in Caen (France), at the Ruđer Bošković Institute (RBI) in Zagreb (Croatia), and the GSI Helmholtzzentrum für Schwerionenforschung

GmbH in Darmstadt (Germany) as shown in Fig. 3.3.⁴ Due to the different types of ion accelerators, irradiations with a large range of different E_{kin} could be performed. Fig. 3.3 (a) gives an overview of the typical ion energy range each beamline operates within. SHI experiments performed at the RBI (b) typically involve ions with a $E_{\text{kin}} < 30$ MeV, ions at the IRRSUD beamline at the GANIL (c) reach E_{kin} of ca. 100 MeV, and the SME beamline at the GANIL (d) or the X0 beamline at the GSI allow ion irradiations with energies of 1,000 MeV or more.

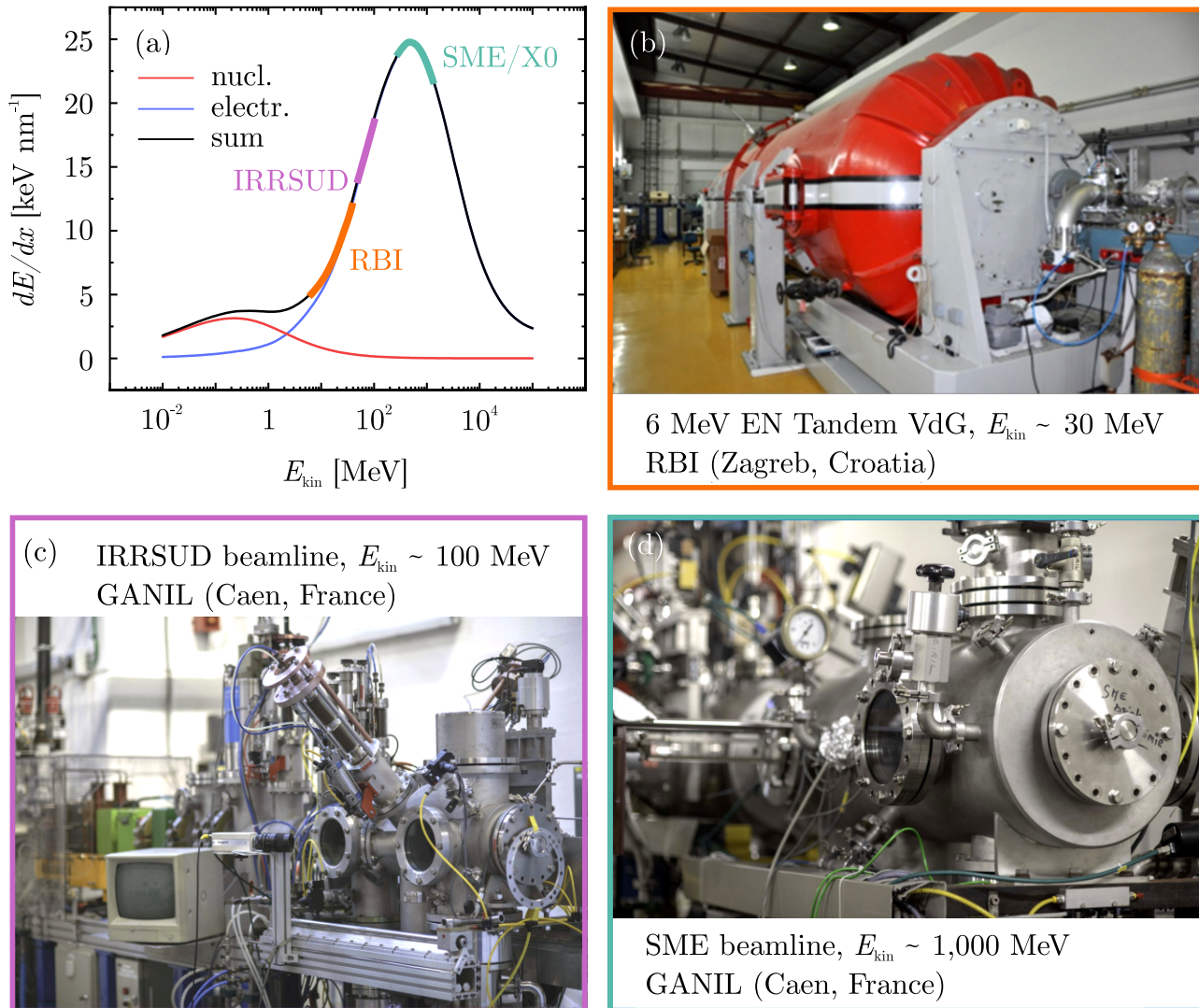


Figure 3.3: (a) SHI facilities and with typical ion energies. (b) 6 MV EN Tandem Van de Graaff accelerator allowing irradiation with up to ca. 30 MeV kinetic energy [147]. (c) Ions at the IRRSUD beamline typically have 1 MeV/u energy (total of 100 MeV). (d) Ions at the SME beamline reach 10 MeV/u (total of 1,000 MeV) or more. [148].

⁴Due to the complexity of each irradiation beamline and the experience it takes to operate them, researchers, engineers, technicians, any many more were involved and contributed to the irradiations presented in following chapters.

3.1.3 Highly Charged Ions

The next class of ions that will be addressed are *highly charged ions* (HCI) whose initial properties are fundamentally different to those of a SHI. While a SHI carries nearly all of its energy as kinetic energy, a HCI's characteristic property is its high potential energy E_{pot} compared to a rather minor E_{kin} (< 25 keV/u). To ionize a neutral atom ionization energy has to be provided as any deviation from its neutral charge state is energetically unfavorable. Once an atom is already singly-charged every further ionization requires more energy than the previous step as the positive charge of the atom's core is less screened and interacts stronger with the remaining electrons. Hence, the total potential energy of an ion is the sum of each individual ionization step according to eq. 3.4.

$$E_{\text{pot}}(q) = \sum_{i=1}^N E_I^i \quad (3.4)$$

Fig. 3.4 correlates the potential energy of a Xe atom (turquoise) with its charge state q as well as the required energy input for each ionization step (blue). Especially when an electron from a new, fully occupied atom shell (*i.e.*, N-, M-, L- or K-shell) is supposed to be removed an overly larger portion of ionization energy is necessary as shown with a logarithmic plot of E_{pot} in the inset of Fig. 3.4.

3.1.4 Classical Over-Barrier Model

The *classical over-barrier model* (COB) describes the interaction and charge transfer of a charged particle (*e.g.*, an ion) that is approaching a conducting surface [150, 151]. Generally, the potential landscape of a charge in front of surface at a distance R can be described with the concept of mirror charges. Here, the initial charge of the ion Q induces an accumulation of oppositely charged particles on the surface that again further accelerate the ion. Their contribution to the overall potential can be modeled as if a charge $-Q$ is located inside the conductor with a distance of $2R$ to the initial ion ($-R$ with respect to the surface). The overall potential for an electron leaving the surface and located at position z can be calculated according to eq. 3.5 [151, 152] and is plotted in Fig. 3.5 with respect to z . Here, the surface is located at $z = 0$, the ion is positioned at $z = R$ (dashed, vertical line), and energy barriers are represented in red.

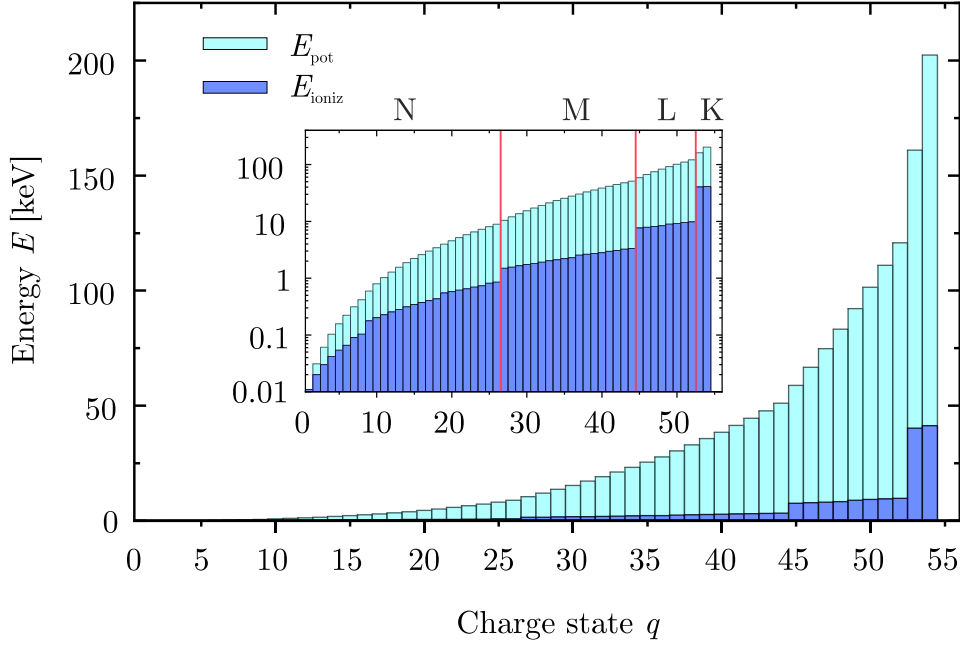


Figure 3.4: E_{pot} of a Xe ion with respect to its charge state q shown in blue and necessary energy for each ionization step in turquoise. Logarithmic representation of the ionization energy (inset) emphasizes the disproportionately large amount of ionization energy that is required when the first electron of a fully occupied atom shell is removed. Data taken from [149].

$$V(z, R, Q) = V_{\text{HCl}} + V_{\text{HCl}}^{\text{Image}} + V_{\text{electron}} = -\frac{Q}{|z - R|} + \frac{Q}{|z + R|} - \frac{1}{4z} \quad (3.5)$$

As long as the distance of the ion to the surface is too large, *i.e.*, for $R > R_{\text{crit}}$ (Fig. 3.5 (a)), the electron located at the Fermi energy E_{F} (dotted, horizontal line) of the material at $z = 0$ would have to overcome an energy barrier ΔE_{B} to fill an empty atomic state of the ion. With decreasing distance of the ion to the surface, however, the energy barrier gradually decreases until it reaches a value of zero corresponding to a critical distance R_{crit} (Fig. 3.5 (b)). At this point, first *resonant neutralization* (RN) processes of the charged ion with electrons of the solid are likely to occur which reduce the charge of the ion to $Q-n$, with n being the number of electrons [151, 153]. This in turn reduces R_{crit} again resulting into a steplike neutralization process of the ion. For distances $R < R_{\text{crit}}$ the energy barrier has further decreased followed by a swift neutralization of the ion as shown in Fig. 3.5 (c). R_{crit} can be calculated with eq. 3.6 for varying work functions W of the surface and charge states Q .

$$R_{\text{crit}} = \sqrt{2Q/W_{\text{A}}} \quad (3.6)$$

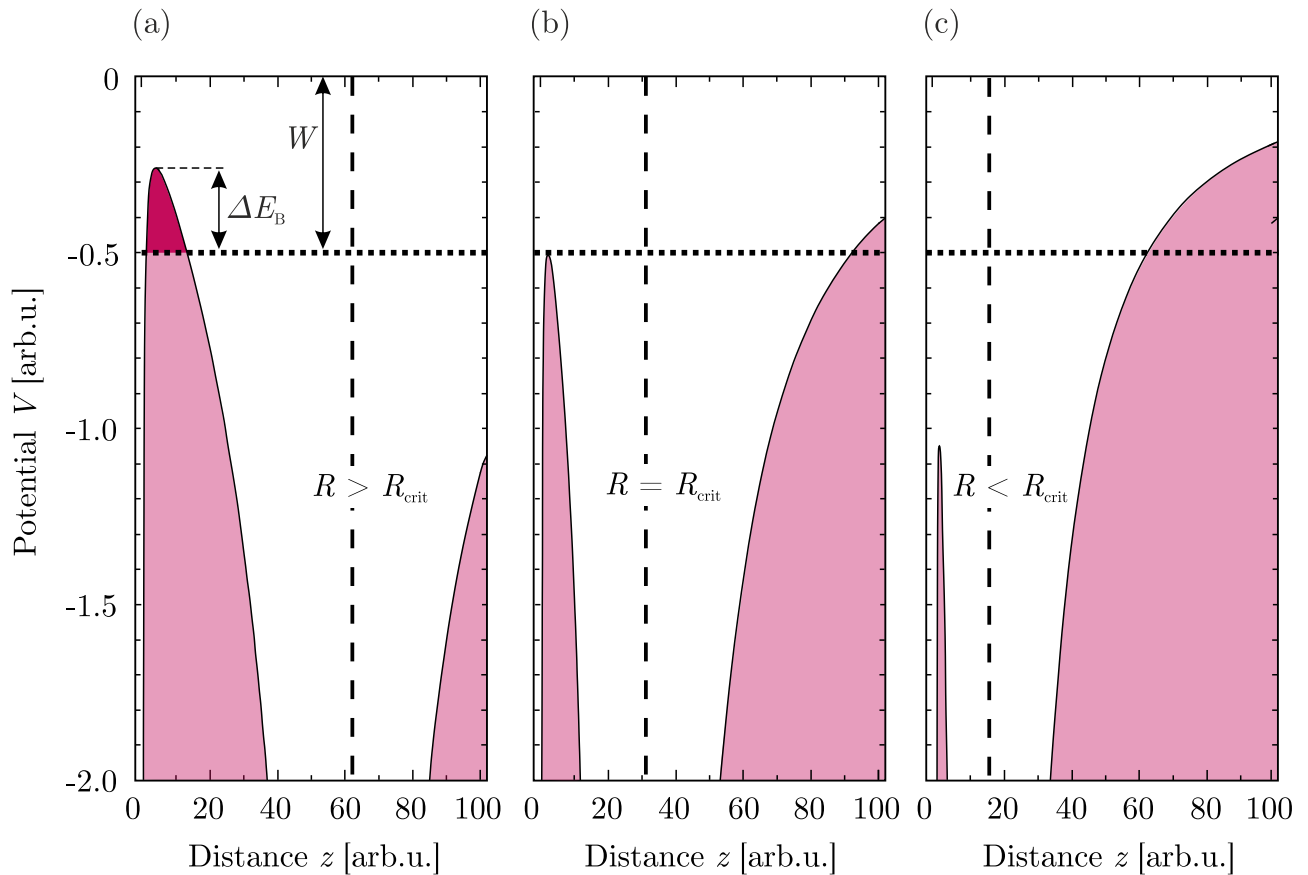


Figure 3.5: Classical over-barrier model when an ion located at R (dashed, vertical line) approaches and interacts with a surface. (a) For ion-surface distances larger than the critical distance R_{crit} , electrons in the material face an energy barrier ΔE_B which usually prohibits a charge transfer. (b) For $R = R_{\text{crit}}$ the barrier has shrunk to zero which allows a resonant charge transfer. (c) Distance R is now smaller than R_{crit} leading to a swift neutralization of the ion. Reproduced from ref. [154].

Even when the HCI has been neutralized to a great extent by the electrons of the surface, it is far off its energetic equilibrium. This is due to the fact that the collected electrons occupy high *Rydberg*-states of the ion in the beginning which are however less energetically favorable than those close to the core. In this particular state the atom is often referred to as a *hollow atom* (HA), as outer states are occupied by electrons while inner ones with high binding energies are completely or to a great extent unoccupied depending on the initial charge state of the ion [155, 156]. In the following, several neutralization but also further ionization mechanisms of the HA take place allowing the HA to fill its ground states in order to reach energetic equilibrium eventually. Schematics of the respective processes are presented in Fig. 3.6.

i) Auger neutralization

The Auger neutralization (Fig. 3.6 (a)) describes a process where an electron of the surface fills an unoccupied and low Rhydberg-state of the HA under the premise that the energy gained from filling this low-energetic state is at least as large as the required work function W of the material. If this holds energy is transferred to another electron of the surface which can then be emitted from the solid. The ion does reduce its overall charge state during this process [157, 158].

ii) Auger deexcitation

The Auger deexcitation (Fig. 3.6 (b)) refers to relaxation processes that lead to a occupation of energetically favored atomic states of the HA with at least two electrons being involved. The Auger deexcitation can be further divided into an *indirect* and *direct* Auger deexcitation process. The former one describes a procedure where an electron transits from the solid into a low-energetic *Rhydberg*-state state while transmitting its energy to another electron located in a high-energy state causing it to emit from the HA [159].

The direct deexcitation often also referred to as *interatomic coulombic decay* process is opposite to the former one such that a high-energetic electron transitions into a low-energetic state. The excess energy is transferred to an electron inside the surface instead and may lead to its emission. A prerequisite that holds for both processes is that the difference in energy of the transitioning electrons' initial and final state is larger than the respective work function such that both cases allow an emission of an electron into the vacuum. The ion does not change its overall charge state [159–161].

iii) Radiative deexcitation

In case of the radiative deexcitation (Fig. 3.6 (c)), a high-energetic *Rhydberg*-electron relaxes into a energetically lower atomic state. The difference in energy is now released in form of a photon [162].

iv) Quasi-resonant deexcitation

The Quasi-resonant deexcitation (Fig. 3.6 (d)) describes a process leading to a reduction of the charge state of the ion. For small distances of HCI and surface, low-energetic orbitals of the ion and surface form a collective molecular orbital which allows charge transfer between the ion and the surface [163–165].

v) Auger ionization

Aside from deexcitation processes leading to a reduction of the charge state of the HCI and/or a relaxation of electrons from high-energetic Rhydberg-states into energetically lower ones, additional ionization processes may also occur causing a further increase of the charge state of the ion. The Auger ionization (Fig. 3.6 (e)) outlines a process involving the relaxation of an electron from a high- into a low-energetic state. The difference in energy is transferred to another electron located in one of the higher energy states so that it is emitted into the vacuum.

vi) Resonant ionization

The resonant ionisation (Fig. 3.6 (f)) considers transitions of electrons from the HCI to the surface leading to an additional ionization of the ion.

Which interaction mechanism between ion and surface actually occurs depends on the interaction time as well as the relative positions of the energy levels of ion and surface material. The interaction time τ can be calculated according to eq. 3.7 and allows a first estimate which mechanism might take place by considering the time scale on which these processes occur. Especially for HCI irradiation of two-dimensional (2D) materials τ reaches values of 10^{-15} s.

$$\tau = \sqrt{\frac{Q \cdot m}{E_{kin} \cdot W_A^2}} \quad (3.7)$$

The radiative deexcitation process, for instance, takes considerably longer (*i.e.*, 10^{-9} s) than the ion interacts with the surface [162]. Processes such as the Auger neutralization, indirect Auger deexcitation, and Auger ionization have been shown to occur within 10^{-12} s, which is still 1000-times longer than τ . The quasi-resonant deexcitation on the other hand allows fast electron transfers due to the overlapping atomic orbitals of the HA and surface atom in form of shared molecular orbitals. However, the efficiency of charge transition via this process is limited if the atomic numbers Z of the ion and target material differ too much. The reason for this lies in an energetic misalignment of the individual orbitals such that an efficient electron transfer is prohibited. This consideration may play an insignificant role when irradiating graphene (${}_6\text{C}$), but surely has to be taken into consideration when working with MoS_2 (${}_{42}\text{Mo}$, ${}_{16}\text{S}$) and highly charged xenon (${}_{54}\text{Xe}$) ions. Recent experiments investigating charge transfer and deexcitation processes of fully suspended single-layer graphene and MoS_2 during highly charged Xe ion irradiation identified the direct Auger deexcitation (or interatomic coulombic decay) as the most efficient mechanism occurring on a time scale of only 10^{-15} s [161, 167, 168]. It should be noted though that despite the mechanism's pace, the ions could not be fully neutralized within the time span they interacted with the material.

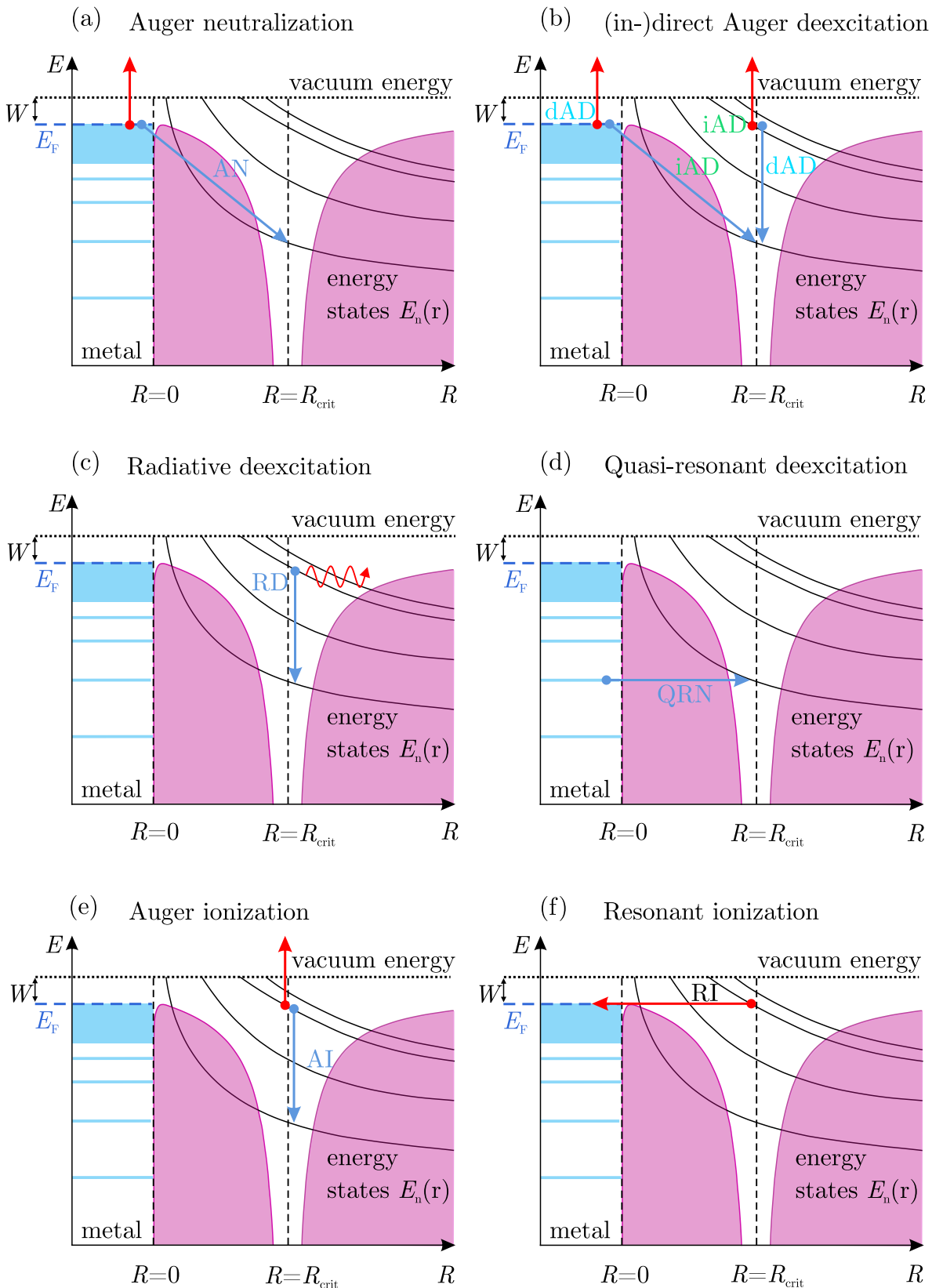


Figure 3.6: Different interaction mechanisms of a HCI and a surface. The processes shown in (a)-(c) lead to an occupation of lower energy levels while preserving the ion's charge state. (d) An electron fills an electronic state, hence reducing the charge state. (e)-(f) lead to further ionization of the ion, while filling low energetic levels simultaneously for the process in (e). Reproduced from ref. [166].

3.2 Electronic Excitation in Solids and Energy Transfer Mechanisms

The energy transfer of ions interacting with a surface follows two independent processes as stated before: i) nuclear stopping dE_n/dx , which results in transfer of momentum from the ion to the lattice and causing collision cascades inside the solid and ii) electronic stopping dE_e/dx , which excites the electronic system of the target material. Nuclear stopping is the dominant mechanism for singly charged ions with energies in the keV regime. Electronic excitation induced by SHI and HCI irradiation, however, is fundamentally different and shall be explained in the following. Fig. 3.7 (a) and (b) present simulation results which give insight into the distribution and spread of energy inside SiO_2 after irradiation with a 11.4 MeV/u Ca ion [25, 169]. Almost immediately after ion impact in Fig. 3.7 (a) ($t = 0.5$ ps) a super-heated core track along the trajectory of the ion is formed whose radius rapidly grows as temperature spreads within the material, shown in Fig. 3.7 (b) ($t = 10$ ps). A. Chatterjee *et al.* proposed two equations to calculate the energy density at a given distance r from the ion track. Eq. 3.8 describes the energy distribution in the core track, which is independent on r , whereas eq. 3.9 considers the energy density of the halo which is mainly affected by δ -electrons and shows a r^{-2} -dependency.

$$\rho_{\text{core}} = \frac{dE_e/dx}{2\pi r_c^2} \left(1 + \frac{1}{2\ln(\sqrt{e}r_p/r_c)}\right) \quad \text{for } r \leq r_c \quad (3.8)$$

$$\rho_{\text{halo}} = \frac{dE_e/dx}{4\pi r^2} \frac{1}{\ln(\sqrt{e}r_p/r_c)} \quad \text{for } r_c < r \leq r_p, \quad (3.9)$$

In eqns. 3.8 and 3.9 dE_e/dx represents the electronic energy loss, r_c describes the core radius of the ion track and r_p the radius of the penumbra. \ln refers to the natural logarithm and e to its basis [170]. Due to its high E_{kin} , the penetration depth may reach values of several mm depending on its mass and that of the target material [143, 171].

The energy distribution of a solid that is excited by a HCI behaves very differently as shown for a CaF_2 crystal irradiated with a Xe^{33+} ion in Fig. 3.7 (c) and (d) [25, 169]. The energy is deposited almost completely within a depth of 1-2 nm with respect to the impact of the ion leading to a highly excited and spatially localized electronic system close to the surface. The penetration depth of the ion and hence the volume in which energy is distributed still depends on its E_{kin} but is negligibly small compared to a SHI. A slow HCI as the one shown in Fig. 3.7 (c) ($E_{\text{kin}} = 0.15$ q keV) will not penetrate as far into the bulk material as a swift HCI will with a larger E_{kin} as shown in 3.7 (d) ($E_{\text{kin}} = 10$ q keV). The respective energy density within the material will therefore be higher for the former case.

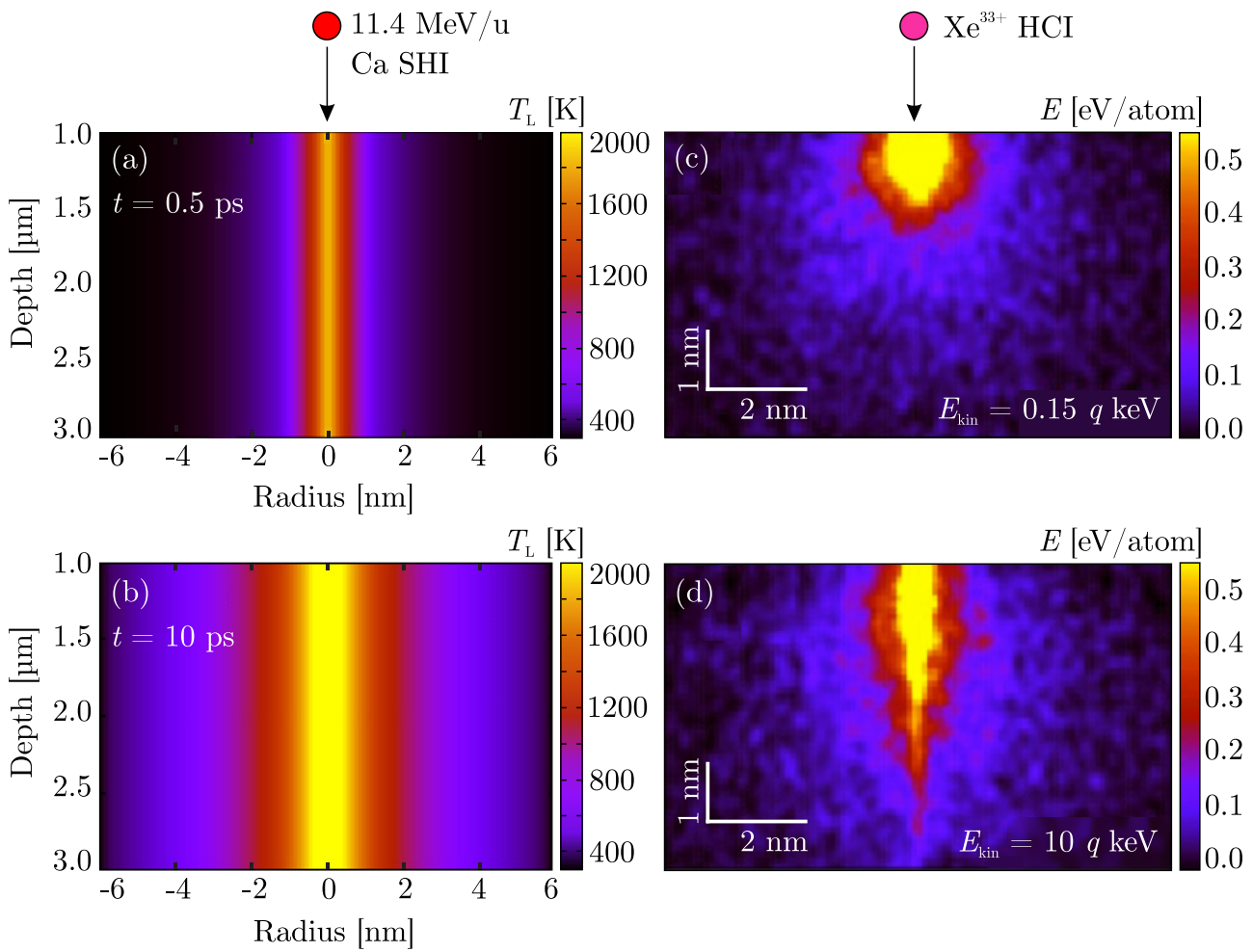


Figure 3.7: (a), (b) Time-dependent temperature distribution inside of SiO_2 after 11.4 MeV/u Ca-ion impact. A super-heated core track evolves around the ion trajectory which spreads over time. The energy loss of SHIs in matter is almost constant over a considerably long distance and penetration depths may reach values of several mm depending on the properties of the ion and target material. Reproduced with permission. Copyright © 2011, IOP Publishing [25]. (c), (d) Energy distribution inside a CaF_2 crystal after highly charged Xe^{33+} ion impact. The energy is deposited close to the surface. Depending on E_{kin} the depths in which energy is deposited may vary slightly. Reproduced with permission. Copyright © 2008, American Physical Society [169].

Despite the striking differences of SHIs and HCIs with respect to their E_{kin} , they very much evoke a similar response in the electronic system of the irradiated material. Since both ion types have been used in this thesis for material modifications, the three main mechanisms of how an electronic system responds to a strong electronic excitation after ion impact shall be presented in the following. The term *ion* refers to both SHI and HCI unless noted otherwise.

The Coulomb-Explosion Model

The electronic system of the material undergoes an almost immediate transition into an excited state within a 10^{-17}s to 10^{-13}s timeframe after ion impact. The large amount of deposited energy per unit track length is further spatially located within in few nm-large radius leading to a highly ionized system densely concentrated to a small volume. The *Coulomb-Explosion* model of R. L. Fleischer [172] predicts a rapid and dynamic repulsion of the ionized atoms. The model, however, presumes certain necessities so that the ionic repulsion in fact can take place.

- (i) Electrostatic forces have to outweigh the binding energies in order to create permanent material modifications and prevent recrystallization processes. The following relation has to hold: $n^2 > \epsilon_0^4 Y / (10e^2)$, with n being the averaged ionization, ϵ representing the dielectric constant, and a_0 and Y describing the atomic distance and Young modulus, respectively. e denotes the elementary charge.
- (ii) The charge carrier density and mobility have to meet additional requirements, which all ensure that a swift deexcitation of the ionized volume is prevented. Atomic dynamics typically set in 10^{-13} s after ion impact. To ensure an explosion due to electrostatic repulsion the number of ionized atoms n_a has to be larger than the number of freely moving electrons n_e for each atomic plane, such that the maximum density of free electrons can be calculated according to $n_e < en_a / \pi a_0 \mu_e k_B T t$, with a_0 being the averaged atomic distance, μ_e being the electron mobility, k_B representing the Boltzmann constant, T and t describing the temperature and the electrons' diffusion time, respectively. Aside from requirements set for the electrons, the model also outlines that the holes inside the ionized volume must not repel each other too quickly, hence their mobility μ_h has to be limited to $\mu_h < a_0^2 e / k_B t T$.

Considering the requirements of the Coulomb-Explosion Model one can speculate that this mechanism hardly applies to well conducting materials, *e.g.*, metals or graphene (unless the Fermi energy E_F lies just between valence and conductance band), where both high charge carrier densities and mobilities are given. However, this model should be taken into consideration when dealing with insulators or semiconductors like MoS_2 .

The Thermal Spike Model

The central elements of the *Thermal Spike Model* are two coupled differential eqns. 3.10 and 3.11. One of them describes the change of temperature of the electronic system over time while the second one refers to the temperature of the phononic system. F. Seitz and J. S. Köhler contributed to the development of this model by treating the electron propagation within an integrated continuum approximation [173]. M. Toulemonde and A. Meftah established the assumption of primarily excitation of the electrons due to ion irradiation and the subsequent transfer into the phononic system [174–177]. After ion impact the electronic system experiences an almost immediate excitation in form of ionization processes on a 10^{-15} s timescale. Via electron-phonon coupling according to the aforementioned eqns. 3.10 and 3.11, the energy is transferred to the phononic system leading to a strong and localized increase in temperature within 10^{-13} - 10^{-10} s after ion impact, which may prevent the formation of defects in some cases.

$$C_e(T_e) \frac{\partial T_e}{\partial t}(\vec{r}, t) = \nabla \cdot (\kappa_e(T_e) \nabla T_e(\vec{r}, t)) - g \cdot (T_e(\vec{r}, t) - T_p(\vec{r}, t)) + S(\vec{r}, t) \quad (3.10)$$

$$C_p(T_p) \frac{\partial T_p}{\partial t}(\vec{r}, t) = \nabla \cdot (\kappa_p(T_p) \nabla T_p(\vec{r}, t)) + g \cdot (T_e(\vec{r}, t) - T_p(\vec{r}, t)) \quad (3.11)$$

In 3.10 and 3.11 $C(T)$ represents the heat capacity, $T(\vec{r}, t)$ is the temperature and κ the thermal conductivity. $S(\vec{r}, t)$ denotes the energy input by the ion. The indices e and p represent the electronic and phononic system, respectively. The elevated temperature may lead to melting, sublimation, and phase transition processes resulting in permanent material modifications [178, 179]. Thermal equilibrium is reached for times later than 10^{-10} s after ion impact.

Materials with a high thermal conductivity (*e.g.*, graphene with 5000 W/mK at room temperature [180]) are likely to be less sensitive and therefore less affected than those with a low thermal conductivity (*e.g.*, single-layer MoS₂ with only 20-130 W/mK at room temperature [181–183]). Compared to MoS₂, graphene is more capable of quickly distributing the arising thermal spike.

3.3 Characterization Techniques of Material Modifications

Visualization and quantification of ion induced defects in 2D materials has become increasingly important. One of the most common surface characterization techniques which has also been used in this thesis for imaging SHI modifications of MoS₂ is Atomic Force Microscopy. The principles as well as a fairly new imaging mode of this method will be presented in the following. For materials with intrinsic or artificially induced defects that are difficult to image by conventional scanning probe microscopy methods or where the underlying substrate simply does not permit highly resolved measurements other approaches have to be followed. Here, Raman spectroscopy will be used to quantify intrinsic properties and material modifications of graphene which would be impossible to access otherwise.

3.3.1 Types of Microscopy

The lower resolution limit Δx of regular optical microscopy (Stimulated Emission Depletion (STED) microscopy excluded [184, 185]) is ultimately restricted by the Abbe diffraction limit according to $\Delta x = \lambda/(2NA) = \lambda/(2n\sin(\theta))$, where λ represents the wavelength of light, NA is the numerical aperture, n and θ corresponds to the refractive index of the surrounding medium (typically air with $n_{\text{air}}=1$) and half the aperture angle of the objective lens, respectively [186, 187]. Due to values of NA in the range of 1.3-1.6 and a limited sensitivity of the human retina restricted to wavelengths within the optical spectrum of light ($380 \text{ nm} < \lambda < 780 \text{ nm}$), optical microscopy cannot be used to analyze nm-small material modifications. The need for new imaging methods initiated the development of other microscopical approaches that do not rely on the wavelength of light. Many of these new techniques rely on a scanning sensor being in close proximity to the sample's surface such that interactions between the sensor and sample can be detected. G. Binnig and H. Rohrer were honored with the Nobel Prize in physics in 1986 for their invention of the first *Scanning Tunneling Microscope* (STM) which allows imaging conducting surfaces with atomic resolution [188]. In 1986 they introduced the first *Atomic Force Microscope* (AFM) enabling to also image non-conducting surfaces with sub-nm resolution [189].

3.3.2 Atomic Force Microscopy Imaging Modes

Atomic Force Microscopy (AFM) relies on interacting forces between a sensor and surface atoms of the investigated sample [190]. The nature of these interactions depends on the distance between sensor and surface, resulting in either attractive or repulsive forces. Fig. 3.8 (a) is a graphical plot of the Lennard-Jones potential which illustrates the interaction between a pair of neutral atoms or molecules depending on their distance. The Lennard-Jones potential comprises both attractive van-der-Waals (vdW) forces that dominate for larger distances (due to the formation of spontaneous dipoles in sensor and surface) and repulsive Pauli forces that become crucial for smaller distances (due to overlapping atomic/molecular orbitals of sensor and surface). The potential $V(r)$ can be expressed by eq. 3.12.

$$V(r) = 4V_0 \left(\left(\frac{R_a}{r} \right)^{12} - \left(\frac{R_a}{r} \right)^6 \right), \quad (3.12)$$

with V_0 being the depth of the potential well, R_a representing the distance at which V is zero, and r being the distance between the interacting species.

The respective sensor that interacts with the sample is a nm-sized tip located at the end of a cantilever as shown in Fig. 3.8 (b). A laser beam is directed onto the back side of the cantilever right above the tip and refracted towards a position sensitive photodiode (PSD). The cantilever is then moved across the sample causing the tip to experience either attractive or repulsive forces at each position. Depending on the mode of operation this again can be used to monitor, *e.g.*, changes of the i) bending of the cantilever (applies for contact mode measurements during static AFM), which results from a *direct contact* of tip and sample leading to a static deflection of the cantilever (repulsive force regime) or ii) amplitude and phase of oscillation (applies for amplitude modulated measurements during dynamic AFM), which in contrast to the former mode is based on a *contactless* interaction of tip and surface (attractive regime) and involves an oscillating cantilever. Here, frequency shifts of the oscillating cantilever due to force-tip interactions result in a measurable change of amplitude, as illustrated in Fig. 3.9 (a) (note that other operational AFM modes do exist [191, 192] and the reason for introducing the former two techniques being their partial analogy to the measurement method used in this thesis and described in the following).

The intermittent mode (or TappingModeTM) combines elements of the repulsive and attractive force regime by using an oscillating cantilever whose amplitude involves tip-surface distances associated with nearly zero but also very strong interactions. As the name suggests, the tip taps on the surface during each oscillation. Similar to the previous AFM mode, the measured quantity of TappingModeTM AFM is the amplitude of oscillation which is influenced by the tip-surface interaction and therefore depends on the distance on the tip-surface distance.

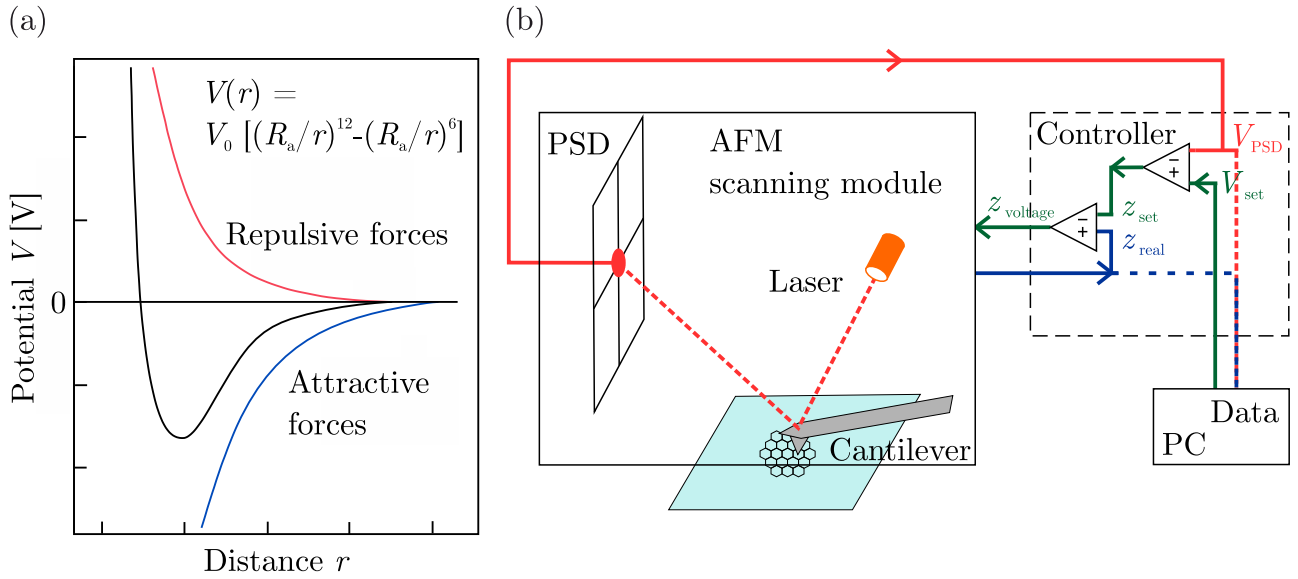


Figure 3.8: (a) Lennard-Jones potential describing the changes in potential V of two electrically neutral atoms/molecules (here atoms of cantilever's tip and surface atoms) in dependency on their distance. (b) Schematic AFM setup. The tip-surface interactions result in a change of the cantilever's properties (bending, frequency and/or phase of oscillation) which is detected by a PSD after the beam is reflected from the cantilever's back. A feedback electronic compares the momentary value to the setpoint and restores the value set initially. Reproduced from ref. [193].

PeakForce Tapping[®], a technique developed by the company Bruker[®] and mostly used in this thesis, represents a special type of TappingModeTM. Here, the indentation force which the tip applies on the surface is an additional control parameter and can be adjusted. Full force-distance curves between tip and sample are recorded at each position (pixel) of the measured area. An exemplary force-distance curve and schematics of the cantilever at each significant event during the cycle are shown in Fig. 3.9 (b). (1) The cantilever approaches the surface from a distance where no significant forces between tip and surface are present. At position (2) attractive forces outweigh the cantilever's spring constant and cause the tip to attach to the surface - often referred to as *snap-in*. The applied force is now gradually increased until the cantilever's deformation corresponds to the set peak-force (3)-(5). Reducing the applied force eventually leads to the detachment of the tip from the sample (5)-(6) to complete one cycle. Aside from gathering information about the topography of the measured surface (similar to regular tapping mode) additional material properties (*i.e.*, points A, B, C in Fig. 3.9 (b)) may be deduced from the force-distance curves. Point X, for instance, corresponds to the adhesion between tip and sample and takes larger values for stickier surfaces, Y correlates with the sample's deformation, and Z is the energy dissipation.

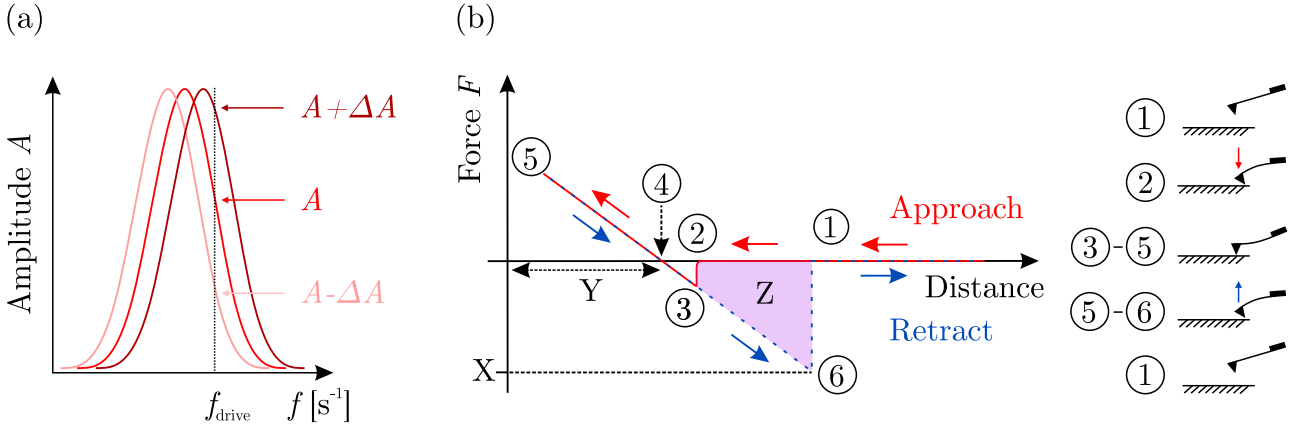


Figure 3.9: (a) Change in oscillating amplitude A due to shift in resonance curve originating from attractive and repulsive forces during, for instance, during dynamic amplitude modulated AFM measurements. (b) Force-distance relation for PeakForce Tapping[®] measurements.

3.3.3 Raman Spectroscopy

Raman spectroscopy describes a spectroscopical approach to probe the vibration characteristics of matter by investigating its inelastic scattering processes with light. This in turn allows to draw conclusions about its structural properties and chemical bindings. The effect was observed by Sir Chandrasekhara Venkata Raman for the first time in 1928 and is based on a temporal variation of a dipole moment evoked in the investigated material when illuminated with light [194]. It has become increasingly important for the characterization of solids, gases, liquids, and especially 2D materials. For the latter case, it is now applied routinely to characterize various properties which are otherwise hard to quantify. To name a few properties of 2D materials, which can be probed by Raman spectroscopy: defect densities [195, 196], charge carrier concentrations [197, 198], strain [199], and layer number [200].

3.3.4 Raman Spectrum of Graphene

The Raman spectrum of graphene contains a multitude of information about, *e.g.*, the number of graphene layers, presence of defects, strain, and doping [196, 201, 202]. Four exemplary scattering events causing the four most prominent Raman modes of graphene are shown in Fig. 3.10 and will be discussed in the following. All processes are based on three subsequent mechanisms: (i) charge carrier excitation (indicated by green arrows), (ii) (in-)elastic phonon scattering (indicated by dashed, black arrows), and (iii) charge carrier recombination (indicated by red arrows).

G-mode:

The graphite(G)-mode can be observed in all sp^2 -hybridized carbon materials and corresponds to a stretching motion of the hexagonal lattice structure as shown in Fig. 3.10 (e). Among the modes listed here, it is the only one requiring just one phonon that is located in the Brillouin-zone center at the Γ -point, hence carrying a momentum q of zero. The respective Raman process of the G-mode is presented in Fig. 3.10 (a). It is noteworthy that neither the layer thickness nor the excitation energy causes a shift of the mode, whereas both electrical doping and strain change its position [196].

2D-mode:

The 2D-mode, often also referred to as G' -mode, describes a "breathing"-mode of the hexagonal lattice as shown in Fig. 3.10 (f) and originates from two scattering events. Momentum conservation is satisfied as the involved phonons located at the K-point have wave vectors of opposite direction (see Fig. 3.10 (b)). The peak width (full width at half maximum - FWHM) varies when increasing the layer number. For instance, bi-layer graphene's 2D-mode consists of four individual phonons all with slightly different energies. The envelope of these modes is broader than for single-layer graphene. The 2D-mode's FWHM is compared in Fig. 3.10 (g) between for single-, bi-layer graphene, and bulk graphite and increases from 28 cm^{-1} to 60 cm^{-1} for single-layer graphene and graphite, respectively. The 2D-mode is strongly affected by strain, electrical doping, layer number, and excitation energy [203].

D-mode:

The defect(D)-mode of graphene is, as the 2D-mode, an inter-valley process connecting the K- and K' -point of the Brillouin zone as shown in Fig. 3.10 (c). The motion of the lattice is associated to an oscillating movement similar to that of the 2D-mode shown in Fig. 3.10 (f) even though with only half of the 2D-mode's frequency. In striking contrast to the former two kinds of phonons, the D-mode is only observable if the lattice is defective. Charge carriers can then scatter elastically to satisfy conservation of momentum. Hence, the presence and intensity of the D-mode can be used to quantify the defect density in graphene via Raman spectroscopy [195, 204, 205]. Fig. 3.10 (h) presents an exemplary Raman spectrum of defective graphene (blue curve) with a large D-mode located at 1350 cm^{-1} .

 D' -mode:

The D' -mode is to some extent similar to the D-mode as it also a defect-initiated process. The respective intra-valley Raman process is presented in Fig. 3.10 (d). The D' -mode is located in close proximity to the G-mode, as shown in Fig. 3.10 (h) (blue curve) [206].

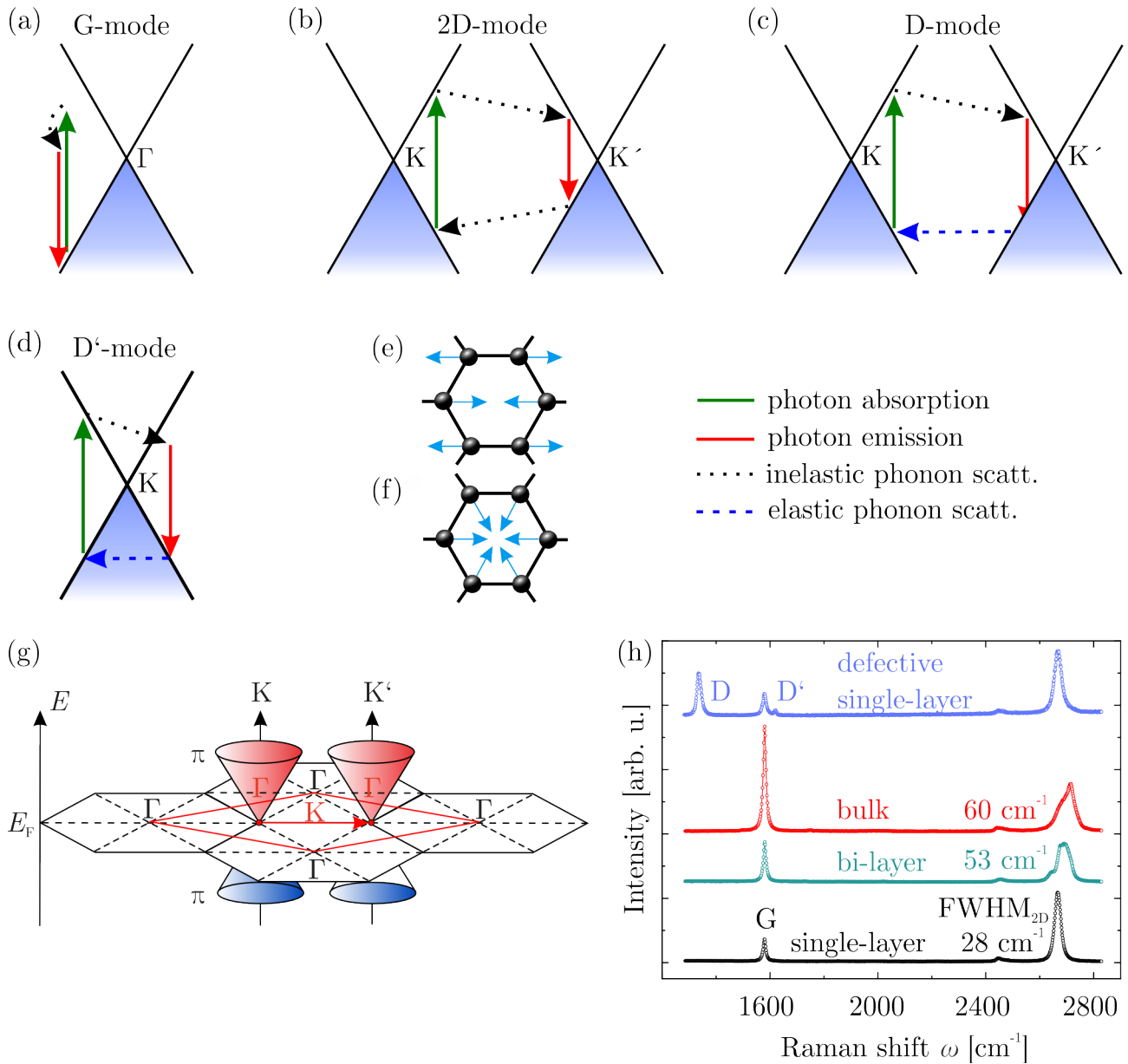


Figure 3.10: Raman scattering mechanisms in single-layer graphene. Electron dispersion (solid, black lines), occupied states in valence band (blue colored), photon absorption or emission (green and red arrows), elastic or inelastic phonon scattering (blue and black dashed lines). (a) G-mode is caused by a one-phonon process located in at the Γ point in the center of the Brillouin-zone. (b) 2D-mode is an intervalley process with two phonons of opposite momentum connecting the K- and K'-point of the Brillouin-zone. (c)-(d) Only in presence of defects can the D-mode and D'-mode be observed as charge carriers may scatter elastically at the defects to satisfy conservation of momentum. (e)-(f) Schematic of lattice vibrations associated with G- and D/2D-mode, respectively. (g) Electronic Brillouin zones of graphene (black hexagons), the first-phonon Brillouin zone (red rhombus), and schematic of electronic dispersion (red and blue colored Dirac cones). The phonon wave vectors connecting electronic states in different valleys are labelled in red. Reproduced with permission. Copyright © 2013, Nature Publishing Group [196]. (h) Raman spectra of single-layer graphene (black), bi-layer graphene (green), bulk graphite (red), and defective single-layer graphene (blue).

3.3.5 Raman Spectrum of MoS₂

Four Raman active modes contribute to the Raman spectrum of bulk 2H-MoS₂. Two of those, however, are not observable due to selection rules for the scattering geometry that was used here (E_{1g} -mode) [207] and due to limited suppression of the Rayleigh scattered radiation (E_{2g}^2 -mode) [208]. The remaining E_{2g}^1 - and A_{1g} -mode are shown in Fig. 3.11 (a). They are located at a Raman shift of approx. 385 cm^{-1} , corresponding to an out-of-plane, optical (ZO) phonon, and approx. 403 cm^{-1} , corresponding to an in-plane, transverse, optical phonon (iTO). It has been found that the position of the modes is influenced by the presence of additional layers of MoS₂. Fig. 3.11 (b) shows the dependence of each mode's position as well as their frequency difference on the layer number [200]. The E_{2g}^1 -mode shows a blueshift to lower Raman shifts for increasing layer thickness, whereas the A_{1g} -modes shifts to larger frequencies. Their frequency difference increases and can therefore be used as a first indicator for the layer thickness. It is worth noting though that C. Lee *et al.* acquired these data with exfoliated MoS₂ crystals, hence the results should not be applied to differently prepared MoS₂ heedlessly but certainly can be used for a first estimate.

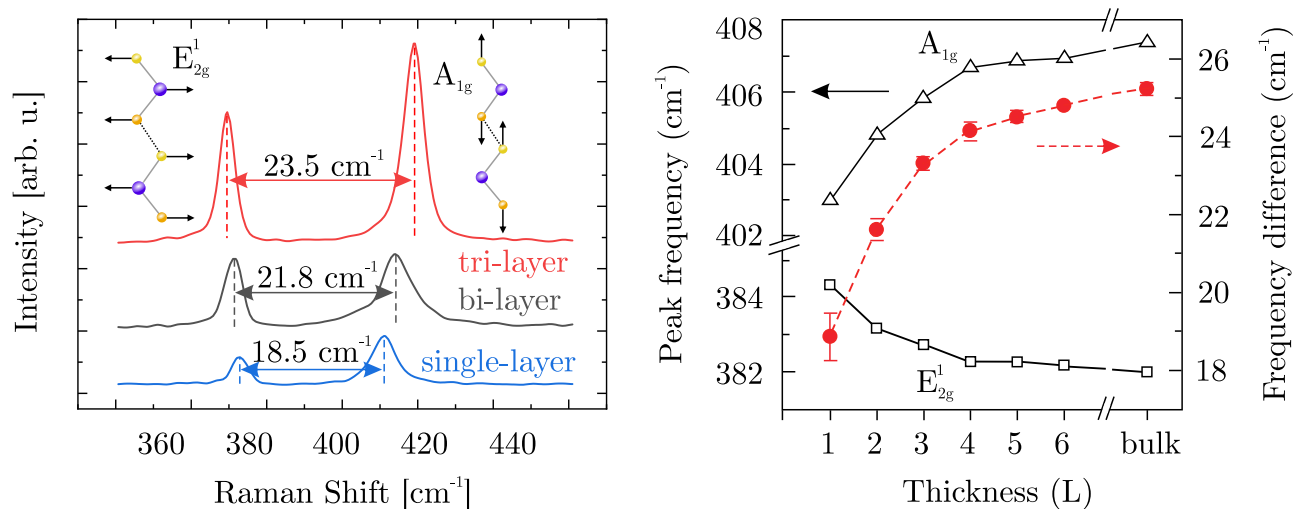


Figure 3.11: (a) Raman spectra of single-, bi-, and tri-layer MoS₂. The lattice vibrations of the E_{2g}^1 and A_{1g} modes are shown as insets. (b) Peak frequency and frequency difference of the E_{2g}^1 and A_{1g} modes dependent on the layer thickness. Increasing layer number causes the modes' frequencies to shift away from each other. Reproduced with permission. Copyright © 2010, American Chemical Society [200].

4 Surface Engineering of Graphene

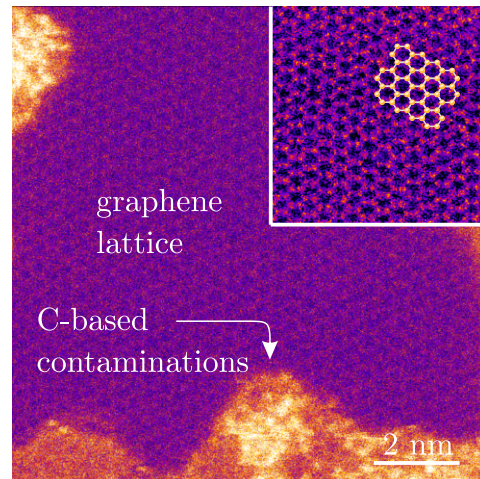
Abstract - The following chapter puts the focus on the 2D material *graphene*. A method is presented which allows to increase graphene's intrinsic mechanical stability, hence solving issues and difficulties while handling the one-atom thick layer. Despite current efforts to synthesize single-layer graphene on arbitrary substrates via CVD process directly, the material of choice remains copper (Cu) due to its catalytic properties during synthesis. This limitation of restricted number of suitable growth substrates often implicates the necessity to transfer graphene from the growth substrate onto another desired material. Even though the quality of CVD grown single-layer graphene on Cu substrates has largely improved over the years, transferring it without introducing unintentional defects and suffering from a contaminated graphene surface after transfer still poses a challenge. Optimizing the transfer itself or developing effective post-transfer cleaning steps are typical approaches, which in the best case only conceal the problem.

This chapter presents a pre-treatment of monolayer graphene on copper (referred to as Gr/Cu in the following) to improve the quality and reproducibility of the transfer process itself. A negligible amount of functional acetate groups acting as a stabilizer during wet-chemical transfer is reliably attached to graphene by pressing an ethylene-vinyl acetate copolymer foil onto the monolayer graphene prior to transfer. The general opinion that crumbling of graphene without a support layer in a H₂O environment is caused due to differences in surface energy, is refuted by demonstrating that this behavior is rather caused by the polar interactions between graphene and water. Suppressing these interactions minimizes the risk of graphene rupture and permits an extremely clean transfer yielding a high graphene coverage and a minimal number of defects.

Parts of the following chapter are an adaptation of ref. [209] and have been reprinted with permission from Madauß, L. *et al.*, A swift technique to hydrophobize graphene and increase its mechanical stability and charge carrier density. *npj 2D Mater. Appl.* **4**, 11 (2020), <https://doi.org/10.1038/s41699-020-0148-9>. Copyright © 2020, the authors of ref. [209]. Text passages that are reproduced literally are set in quotation marks.

As mentioned in previous chapters, different methods exist to perforate graphene to use it as a membrane afterwards. The majority of such research publications dealing with graphene membranes, however, considers the defect creation mechanism as a means to an end and often uses less precise or non-scalable perforation methods as other arguably better suited techniques are less common or accessible. SHI irradiation for instance does not bear such disadvantages, still there is lack of experimental information about which ion type and ion properties to use for generating a certain defect size in graphene [210,211]. One reason for this is the fact that a detailed pore size analysis of porous graphene, usually performed with a transmission electron microscope (TEM), poses several challenges. The main reason for this are carbon-based residues from a typical polymer-assisted transfer which, once adsorbed onto the graphene surface, are nearly impossible to remove and prevent further characterization of the pore sizes [212–214]. This is even more critical for graphene than for many other 2D materials as this type of microscopy relies on Rutherford-scattering, hence delivering best contrasts for materials with a high atomic number Z . Here, contaminations and graphene are practically of the same material (carbon), hence often prohibiting sufficient resolution of the graphene layer. An exemplary high-angle annular dark-field scanning transmission electron microscopy (HAADF-STEM) measurement of single-layer graphene is presented in Fig. 4.1⁵. The low atomic weight of graphene’s carbon atoms already complicates atomic resolution, but areas with large amounts of contaminations make a detailed analysis impossible (note that the non-usable part of a contaminated sample easily exceeds 99 % and that Fig. 4.1 purposely shows an area with clean and non-usable graphene for comparison). It is therefore imperative to find new transfer methods which not only are defect-free but also keep the amount of adsorbates to a minimum.

Figure 4.1: HAADF-STEM image of single-layer graphene. Carbon-based contaminations as a result of polymer-assisted transfer methods pose a severe challenge for imaging nm-sized defects. Inset shows a zoom of the crystal structure revealing the expected hexagonal structure.



Even though efforts are made towards the direct growth of graphene onto other materials in order to avoid transferring the 2D layer [215,216], copper (Cu) still remains the most frequently used material for CVD growth of graphene making a transfer often inevitable [217–222].

⁵STEM measurements were performed by Dr. Mukesh Tripathi, Faculty of Physics, University Vienna, 1090 Vienna, Austria

Consequently, a lot of attention has been devoted to improving either the transfer itself, *e.g.*, by using low molecular weight polymers which are shown to dissolve easier [89, 223–227], or post-transfer cleaning steps, *e.g.*, thermal annealing at 200 °C or more which again restricts the number of suitable target materials [228, 229]. Inspired by the idea of decorating graphene oxide membranes with surface charges, hence being able to control its cation/anion selectivity, "we apply a fast and straightforward approach to decorate the graphene with stabilizing functional carbon groups, which strongly increase the stability of our graphene sheet during transfer hence making all polymer-based sacrificial layer redundant." In contrast to the solutions discussed in literature, the approach presented in this thesis focuses on a pre-treatment of the graphene layer itself and only requires a commercially available vacuum bag sealing machine and ethylene-vinyl acetate copolymer (EVAC) as a bag material, see Fig. 4.2 (refer to Supporting Information Fig. 1 of ref. [209] for additional characterization of the bag material). The pre-treatment, etching, and transfer steps are schematically presented in Fig. 4.2. "Having flattened the complete Gr/Cu sample, we can place the Gr/Cu on an ammonium persulfate (APS) solution. After etching off the Cu and gradually diluting the APS solution with H₂O, a target substrate can be used to scoop out the graphene sheet. Note that the final transfer is performed in a pure H₂O environment where no supporting layer for stabilization is necessary once the flattening step had been applied." For the sake of compatibility with the majority of characterization techniques used in the following, SiO₂ was chosen as a target substrate. The transfer however is not restricted to this or rigid materials in general but may as well be used to cover porous wafers or polymers.

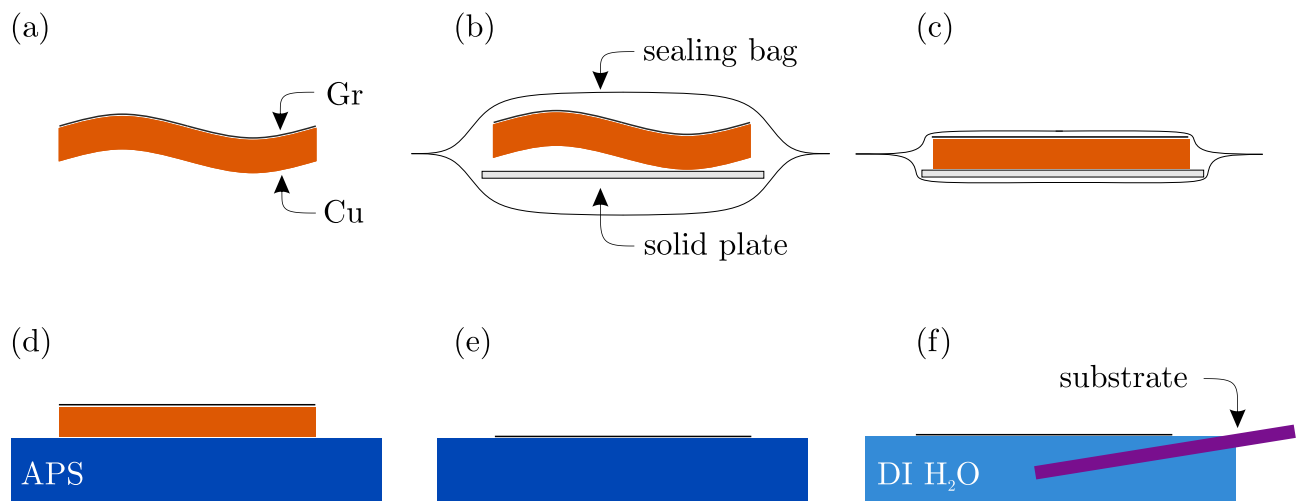


Figure 4.2: Process steps of flattening Gr/Cu using an ethylene-vinyl acetate copolymer foil. (a-c) Flattening of Gr/Cu is achieved by using a vacuum bag sealing machine. (d-f) An aqueous ammonium persulfate solution is used for etching the Cu. After diluting with DI H₂O, graphene can be scooped out with the target substrate. Reproduced with permission. Copyright © 2020, the authors of ref. [209].

"The effect of the flattening already becomes visible when looking at the non-supported graphene layer floating on the APS etching solution, shown in Fig. 4.3 (a). While the flattened graphene maintains its rectangular form determined by the shape of the initial Gr/Cu wafer, the non-treated graphene crumbles and rips. The same results are obtained once the graphene sheets have been transferred, see Fig. 4.3 (b) for regular graphene and Fig. 4.3 (c) for flattened graphene, respectively. The latter one shows a perfectly homogeneous coverage over the whole sample. The non-processed graphene, however, not only displays tens of μm^2 -sized uncovered regions, but even the covered parts show poor smoothness and countless wrinkles.

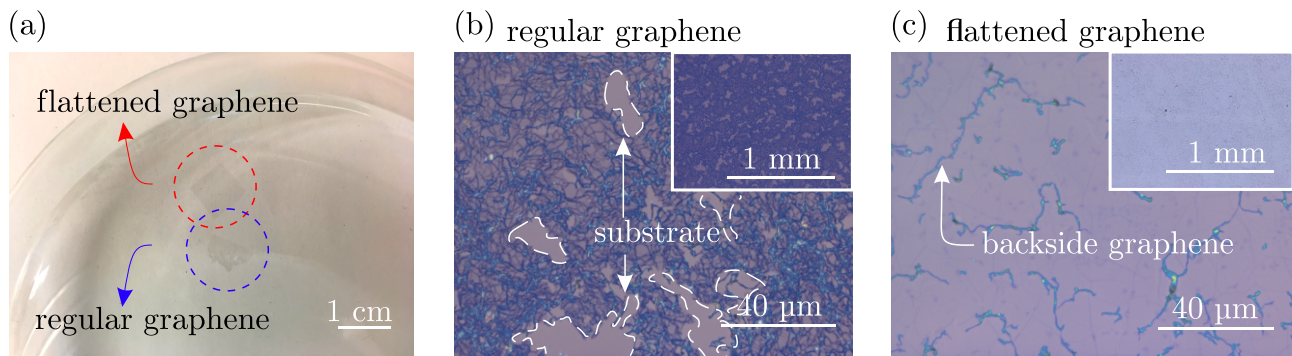


Figure 4.3: Optical images of regular and pre-treated graphene during and after transfer. (a) Flattened and regular graphene floating on an APS etching solution. (b) and (c) Optical microscopy images of non-flattened and flattened graphene transferred onto Si/SiO₂ substrates, respectively. Reproduced with permission. Copyright © 2020, the authors of ref. [209].

In order to evaluate the success of the transfer method presented here in terms of quality and coverage, we will compare the pre-flattened graphene with conventionally transferred graphene supported by a PMMA layer (in the following referred to as PMMA graphene) after transfer onto a SiO₂ substrate. For this, we have performed Raman mappings." Referring to the intensity ratio of graphene's Raman active defect(D)-mode and graphite(G)-mode is the usual approach to characterize the defect density in graphene [195,230]. Combining it with the x - and y -coordinates of the mapping area allows a spatial visualization of the defect density. "Raman measurements indeed confirm an extremely low defect density with an average A_D/A_G intensity ratio of ~ 0.04 for the flattened graphene compared to an intensity ratio of ~ 0.2 for the PMMA-assisted graphene transfer as shown in Fig. 4.4 (a) and (b) (note that neither of the samples have undergone any additional ethanol rinsing, heat treatment or similar). Aside from a highly crystalline graphene layer, we observe a considerably high charge carrier density in graphene induced by charge transfer as can be derived from the peak position of the G-mode in the Raman mappings, see Fig. 4.4 (c) and (d) for PMMA-transferred graphene and flattened graphene, respectively. Even though PMMA is known as a strong p-dopant for graphene, the

flattened graphene displays an even higher level of doping, most likely originating from the two oxygen atoms present in the side group (acetate) which will promote a charge transfer due to oxygen's strong electronegativity and presumably facilitated by the intimate contact at the interface between the rubbery EVAC and graphene and the weaker bond (C-O) between polymer main chain and side group (acetate), compared to glassy PMMA with a C-C bond to the side group (methyl ester) [...] - the mass spectroscopy analysis below will refer to and support this assumption. "Comparing the Raman shift of the G-mode (and I_{2D}/I_G intensity ratio, see Supporting Information Fig. 3 of ref. [209]) of the flattened graphene with the work of Bruna *et al.*, we can conclude that both transferred samples exhibit a p-doped behavior with a charge carrier concentration of approximately $5 \times 10^{12} \text{ cm}^{-2}$ for the PMMA-transferred and $1.5 \times 10^{13} \text{ cm}^{-2}$ for the flattened graphene [197]. The combination of an extremely low defect density and a high level of charge carriers in graphene is expected to be beneficial for a high charge carrier conductivity. The flattening step thus proves to be an effective and gentle way for doping graphene."

Aside from an extremely low defect density, which certainly becomes important for actual filtration measurement, the most crucial advantage of a polymer-free transfer for microscopical investigations is avoiding persistent polymer residues on graphene's surface as no dissolving step of any polymer support is required. How the different approaches will affect graphene's surface will be analyzed in the following by atomic force microscopy (AFM).⁶ Fig. 4.5 presents typical AFM measurements of graphene transferred with PMMA support in (a) and (b), without PMMA support and without a flattening pre-treatment in (c) and (d), and finally without PMMA but with a flattening step prior to the transfer in (e) and (f). Dense, nm-sized PMMA leftovers in (a) and (b) render all samples prepared this way useless for any microscopic analysis. The non-processed graphene transferred without PMMA in Fig. 4.5 (c) and (d) should in principle be the cleanest obtainable graphene. Even though one does not face the problem of polymeric residues, the large number of wrinkles, undefined numbers and positions of multi-layer graphene due regions of overlapping single-layer areas and its non-continuity do not allow utilization as a membrane or as a well-defined material for ion perforation/analysis experiments. Fig. 4.5 (e) and (f), however, illustrates graphene that had been treated with the previously discussed flattening step. The advantages of the PMMA-supported transfer in (a) and (b) (*i.e.*, small number of wrinkles and large parts of a continuous 2D layer) and those of the non-flattened transfer in (c) and (d) (*i.e.*, clean surface) could be combined yielding clean and smooth single-layer graphene in (e) and (f). If even fewer overlapping areas are required, the substrate may be cleaned with oxygen plasma or similar before transfer to increase its hydrophilicity [231] and prevent a bulge of water being trapped between substrate and graphene, which, once it evaporates, is the main reason for the few remaining graphene wrinkles in (e) and (f).

⁶AFM measurements were performed by Mr. Erik Pollmann, University of Duisburg-Essen, Faculty of Physics and CENIDE, 47057 Duisburg, Germany

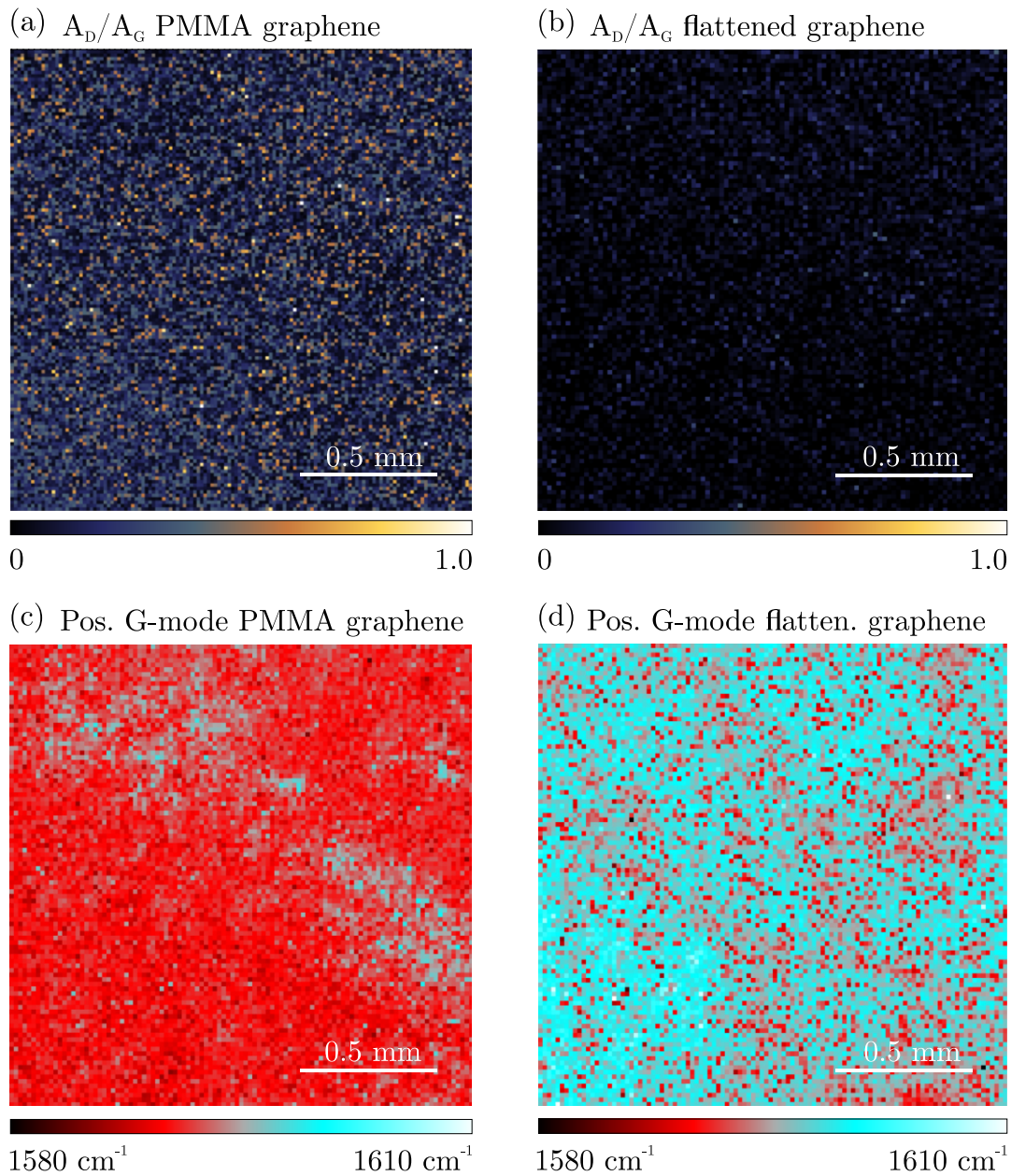


Figure 4.4: Raman spectroscopy maps of graphene transferred with and without PMMA. Intensity ratios of D- and G-mode of (a) PMMA transferred and (b) flattened graphene. Raman shift of graphene's G-mode is presented in (c) and (d) for PMMA transferred and flattened graphene, respectively. Neither of the samples had been treated by any means after the transfer. After scooping graphene out of the H_2O with a SiO_2/Si wafer, the samples were left to dry under ambient conditions. Reproduced with permission. Copyright © 2020, the authors of ref. [209].

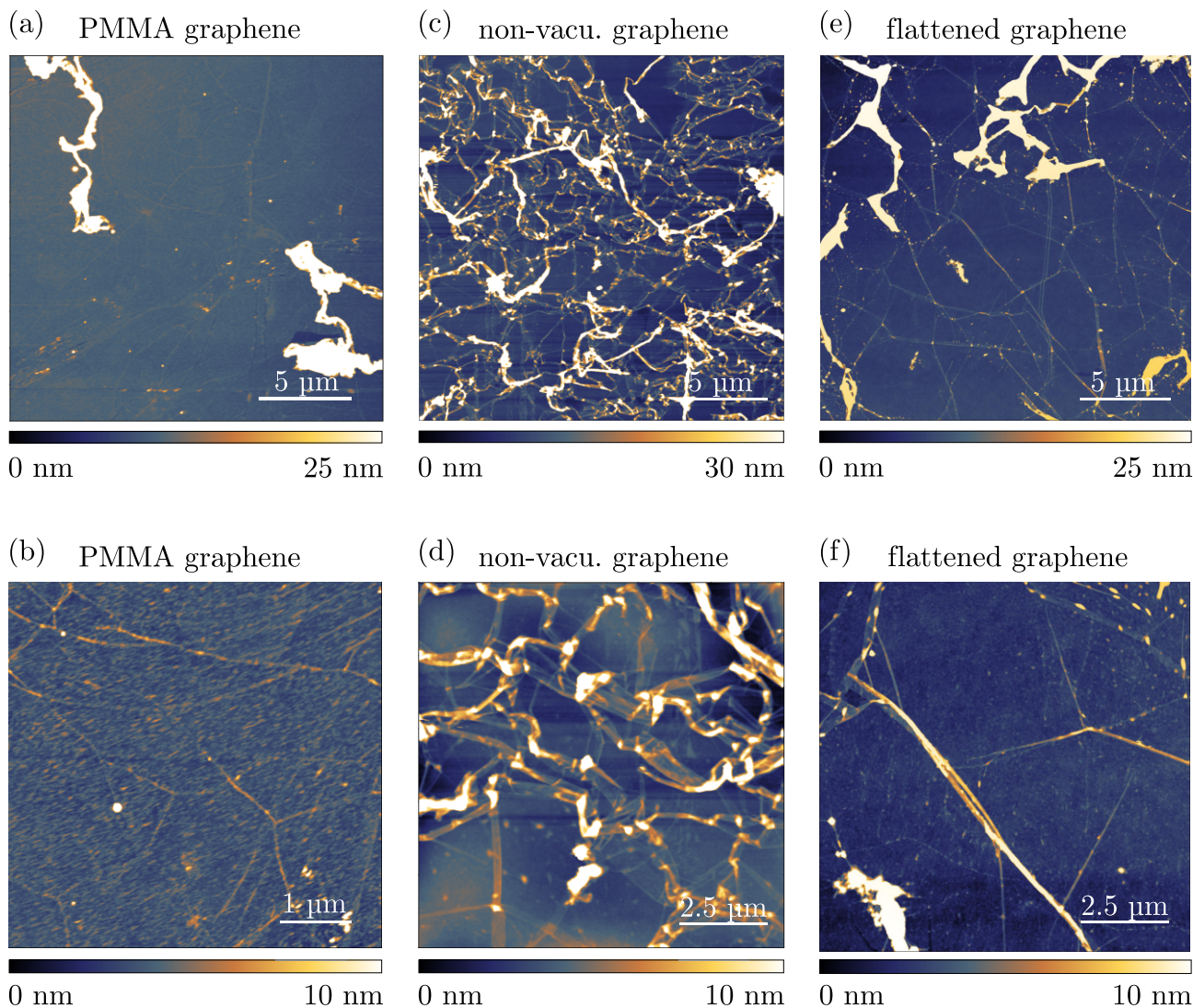


Figure 4.5: AFM images of transferred CVD graphene onto SiO_2 substrates with (a, c) and without (b, d) PMMA support. Graphene supported with PMMA during the transfer shows high density of nm-sized polymer residues after dissolving the PMMA layer, whereas the flattened graphene is nearly free of any contaminations. Note the different scale bars in (c) and (d), underlining the huge improvement in cleanliness. The bright spots in Fig. 4 (c) and (d) are no polymer residues from the flattening foil but overlapping graphene parts or wrinkles resulting from the drying process after scooping out graphene with a target wafer. Scale bar is $5 \mu\text{m}$ for (a, b), $1 \mu\text{m}$ for (c), and $2.5 \mu\text{m}$ for (d). Reproduced with permission. Copyright © 2020, the authors of ref. [209].

The following passages deal with the reason for the enhanced mechanical stability of graphene once it has undergone the flattening step. "Arguing that the copper itself has been flattened on a microscopic scale, hence providing a more uniform and smoother surface for the graphene is highly unlikely. SEM images shown in Fig. 4.6 (a) and (b) of regular and flattened CVD graphene on Cu, respectively, reveal no observable differences in terms of the smoothness of the Cu substrate (aside from a reduced dirt particle density for the flattened Gr/Cu). It is much more plausible that the very surface of graphene itself has been altered by our approach. In order to draw conclusions about the flattening step, the success rate of transfer, and the flattening time, we studied how graphene behaves during the transfer when varying the flattening time, the result of which is presented in Fig. 4.6 (c). We found that there is a clear dependency of the transfer success rate (corresponding to graphene not ripping/crumbling) and the flattening time. While we were practically never able to successfully transfer non-flattened graphene, we obtained a success rate of 100 % after just one day of flattening. Relating this observation with the change of the contact angle of a water droplet on the Gr/Cu surface, also shown in Fig. 4.6 (c), we can draw two important conclusions: (i) both the transfer success rate and the contact angle have their lowest values for non-treated Gr/Cu with values of 0 and 89.1° , respectively. After 1 day of flattening, the success rate and the contact angle has increased displaying values of 1 and 93.1° . (ii) Neither of the two values change when the flattening time is further increased indicating that the responsible mechanism during the flattening step has converged. Since a large contact angle between a water droplet and a surface typically indicates hydrophobic properties of the surface, we can conclude that the flattening increases the hydrophobicity of the graphene. A saturation of the contact angle most likely results from the fact that once the majority of graphene's surface has been decorated with adsorbates, additional molecules are less likely to attach to graphene as nearly all free adsorption sites have already been filled. Even if additional layers of adsorbates would remain on graphene's surface, the contact angle is not expected to change any more as it is predominantly governed by the layers in direct contact.

To further address this observation, we performed X-ray photoelectron spectroscopy (XPS) measurements to confirm the presence of additional adsorbates on graphene's surface.⁷ Owing to the surface sensitivity of XPS, the data we obtained can be correlated with surface modifications. Again, we have varied the flattening time from 0 s to 2 days as shown in Fig. 4.7 (a) and (b). The data reveals that initially almost all of the carbon present on the sample is sp^2 -hybridized. This is of no surprise since the electrons of pristine graphene form sp^2 -hybridized orbitals. With increasing flattening time, we observed a growing amount of sp^3 -hybridized as well as C-O bound carbon, which we explain by additional adventitious carbon from the EVAC-foil as a result of the flattening step [...] (Supporting Information Fig. 4 & 5 of ref. [209] show additional XPS data of flattened Gr/Cu). To estimate the amount of carbon residues

⁷XPS measurements were performed by Dr. Ulrich Hagemann (University of Duisburg-Essen, CENIDE, ICAN, 47057 Duisburg, Germany) using a VersaProbe II microscope (UlvacPhi) with a monochromatic Al K_α source

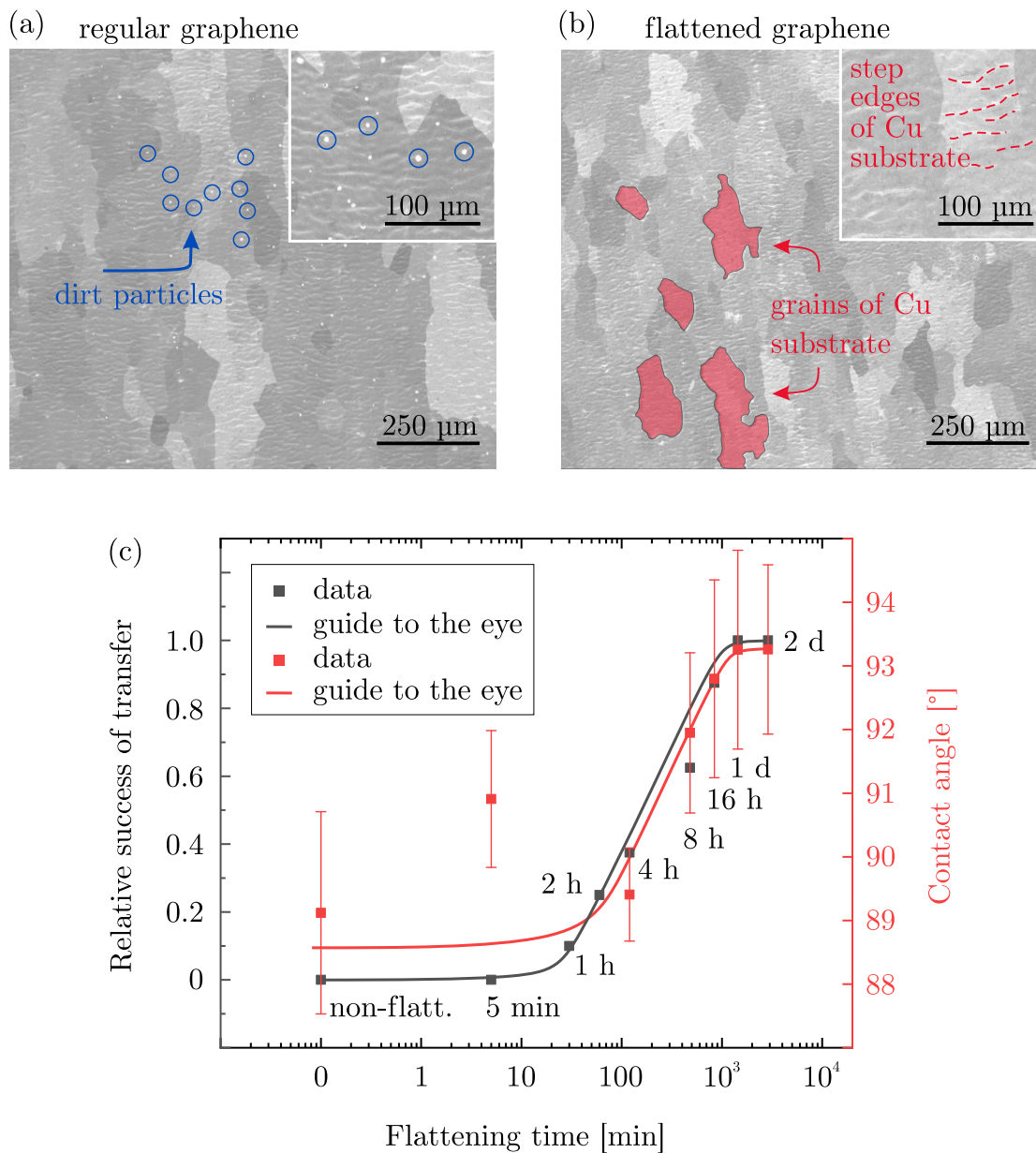


Figure 4.6: SEM images of (a) regular and (b) flattened Gr/Cu. Scale bars are 250 μm for main images and 100 μm for insets. (c) Dependency of the relative success of transfer and contact angle on flattening time of Gr/Cu. Error bars represent standard deviations. Reproduced with permission. Copyright © 2020, the authors of ref. [209].

on graphene after flattening, we compared the carbon signal originating from graphene to the overall carbon intensity, as presented in Fig. 4.7 (d) for EVAC and various other materials. Despite the direct contact to the EVAC-foil, graphene still contributes 48 % to the total C signal after being in contact with the EVAC foil for two days, which is a similar value when using other polymer-based materials or aluminum. Interestingly, similarly processed Gr/Cu samples flattened with a polycarbonate (PC) foil sometimes also allow successful transfers comparable to the EVAC-flattened samples. Notably, the XPS spectra of EVAC- and PC- flattened Gr/Cu are almost identical (see Supporting Information Fig. 6 of ref. [209]). Despite this, all other Gr/Cu samples flattened with, *e.g.*, polyethylene terephthalate (PET), aluminum or simply old Gr/Cu sample not only show a signal of hydrophilic adsorbates, *e.g.*, -COOH groups on graphene as presented for PET-flattened Gr/Cu in Fig. 4.7 (c), but also displayed the same ripping/crumbling behavior during the transfer as non-treated Gr/Cu."

Under consideration of the results obtained from contact angle and XPS measurements, it is reasonable to assume that minor fragments of the EVAC foil adsorb onto the graphene and improve its stability during transfer. Followingly, secondary ion mass spectroscopy (ToF-SIMS) measurements were performed to further investigate the surface chemistry (measurements were performed with a TOF.SIMS 5 from Ion-ToF and Bi³⁺ ions as projectiles).⁸ A first strong indicator stressing the presence of fragments of the flattening foil attached onto the graphene layer becomes evident when comparing the ToF-SIMS spectra for non-flattened and flattened Gr/Cu in Fig. 4.8 (a) and the bare polymer foil in (b). The intensity pattern in vicinity to a mass-charge ratio of 59 of flattened graphene and the foil is resembling and absent for untreated graphene. The mass-charge ratio of 59 can be attributed to acetate groups which form the side chains of the copolymer. However, it is not the case that a continuous polymer film is peeled off the EVAC-foil during the flattening step and would de-facto represent a hidden polymer support layer. ToF-SIMS spectra in Fig. 4.8 (c) and (d) show that some EVAC-foil characteristic mass-charge intensity patterns (marked in green) only appear when analyzing the bare foil, which cannot be observed for neither flattened nor non-flattened graphene. The improved properties during wet-chemical transfer are indeed expected to result from a selective deposition of only fragments of the copolymer including characteristic acetate groups.

A direct comparison of the sensitivities of XPS and ToF-SIMS allows a rough estimate of the amount of acetate groups that attach to a graphene layer. Since no characteristic fingerprint of the acetate groups was detectable during the XPS measurements (*e.g.*, a signal from C=O), but only the far more sensitive (ppb) ToF-SIMS measurements were able to detect their presence, the density of acetate groups has to be comparable to ≈ 0.2 monolayer or less which corresponds to the sensitivity of the XPS. With respect to the initial motivation of preparing contaminant-free, suspended graphene layers for easier TEM analysis of ion induced defects, the deduced 20 % graphene coverage by acetate adsorbates is likely to turn out even less.

⁸ToF-SIMS measurements were performed by Mr. Tobias Heckhoff, University of Duisburg-Essen, Faculty of Physics and CENIDE, 47057 Duisburg, Germany

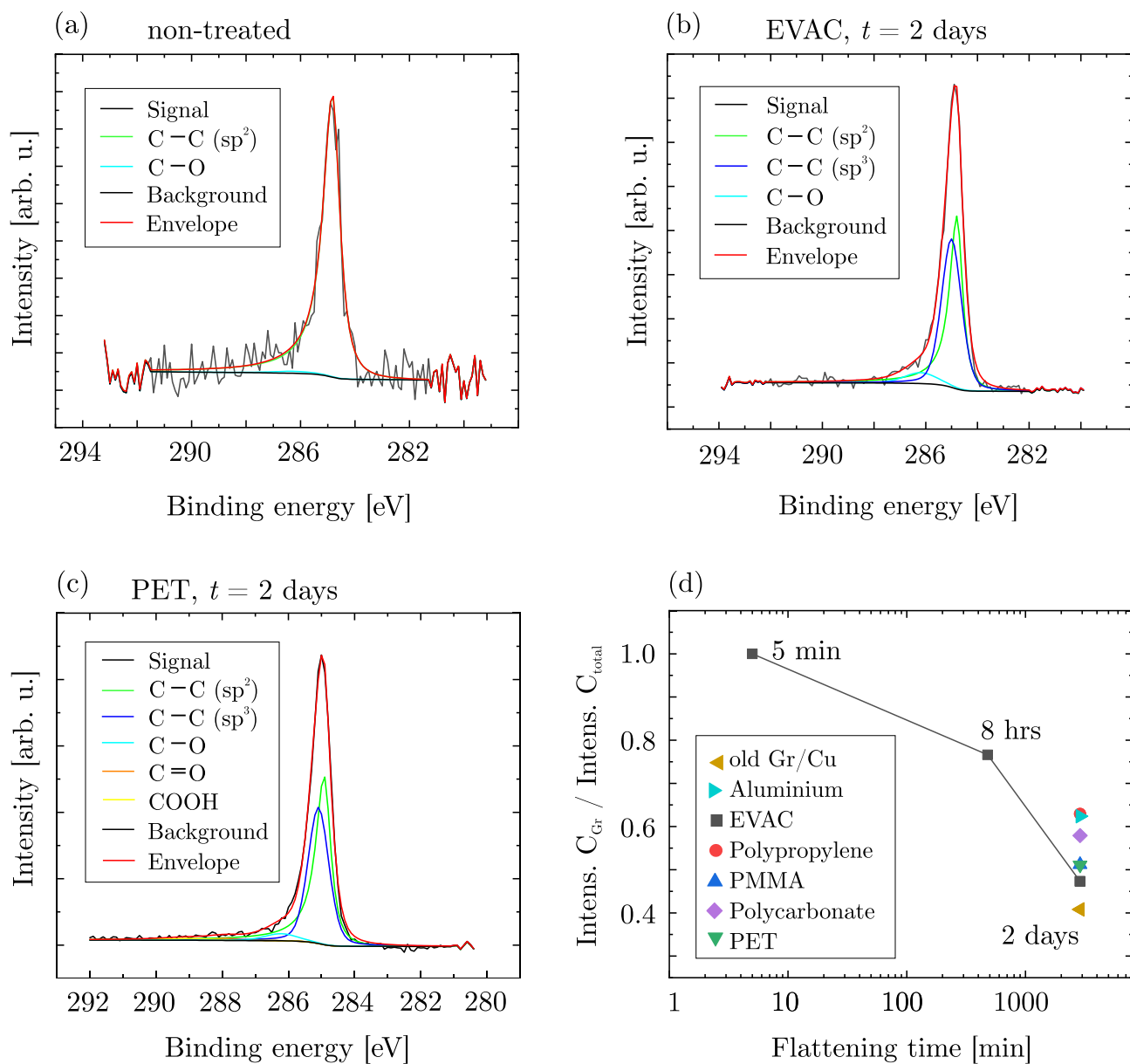


Figure 4.7: XPS measurements of Gr/Cu samples that have been flattened before with various materials. (a, b) With increasing flattening time of the EVAC-foil additional carbon residues are deposited on graphene. (c) XPS spectrum of Gr/Cu after two days of flattening using a polyethylene terephthalate (PET) foil. (d) Intensity ratio of carbon signal originating from graphene compared to the total carbon signal for differently treated Gr/Cu samples as a function of time. Reproduced with permission. Copyright © 2020, the authors of ref. [209].

Under worst circumstances only the acetate groups would adsorb, form a thin monolayer film, and cover the largest possible area, *i.e.*, covering 20 % of graphene. It is more likely that adsorbates form clusters or that larger parts of the carbon-rich polymer main chain occasionally adsorb, hence boosting the XPS intensity of the sp^3 -hybridized carbon signal while actually being located within a small area.

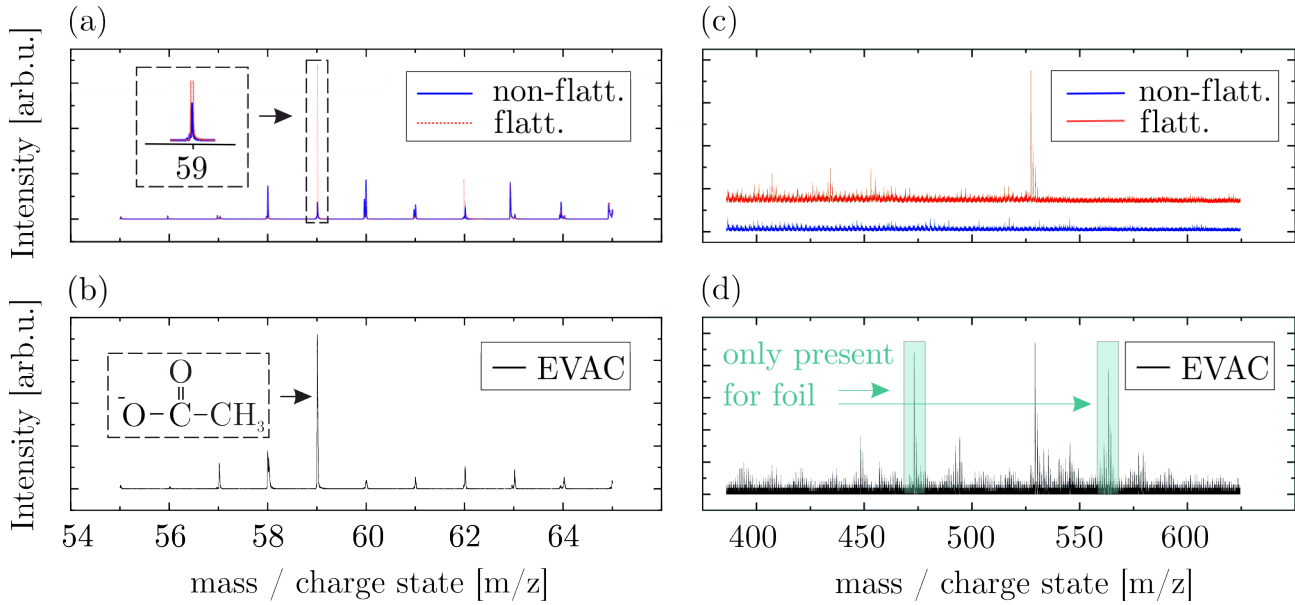


Figure 4.8: ToF-SIMS spectra of 1-day-flattened and non-flattened Gr/Cu in (a), (c) and bare EVAC-flattening foil in (b), (d). The data show the negatively charged ion spectrum of the ToF-SIMS measurements. Reproduced with permission. Copyright © 2020, the authors of ref. [209].

"A possible explanation for the increase of the mechanical stability after the EVAC-flattening step is based on lowering the difference in surface energy of graphene and the etching solution. If the difference in surface energy is small enough graphene would retain its shape allowing a successful transfer. In case of a large difference in surface energies between graphene and the etching solution, the system is expected to minimize its energy by reducing the surface area of graphene causing it to crumble" - similar to what is known as the Volmer-Weber [232] and Stranski-Krastanov [233] mechanisms during metal- and semiconductor thin film growth. "To test our hypothesis, we probed the contact angle of calibrated liquids with flattened and regular CVD graphene on copper. Generally, the interactions between a liquid and a solid depend on the chemical structure of the adsorbate and adsorbent and can be divided into polar and dispersive interactions. Polar interactions arise due to permanent or dipole-induced interactions, hence, strongly depend on the chemical structure of the investigated materials. Dispersive interactions on the contrary are caused by fluctuating electron densities and therefore are always present regardless of the chemical nature [234, 235]. Both the polar σ^p and dispersive σ^d interactions contribute to the total surface energy σ of a liquid (subscript L) or

solid (subscript S) and can be correlated according to the Owens-Wendt eq. 4.1 as:"

$$\frac{\sigma_L(\cos\theta + 1)}{2\sqrt{\sigma_L^d}} = \frac{\sqrt{\sigma_S^p}\sqrt{\sigma_L^p}}{\sqrt{\sigma_L^d}} + \sqrt{\sigma_S^d} \quad (4.1)$$

Probing the contact angles θ of regular and flattened graphene with test liquids of known polar and dispersive energy parts accesses the unknown surface energy contributions of graphene and allows their determination according to eq. 4.1. The respective surface energy parts of pure H₂O, non-treated Gr/Cu, and flattened Gr/Cu (EVAC and PET once) are illustrated in Fig. 4.9. The flattening pre-treatment does not match the surface energy contributions of Gr/Cu to the respective values of pure water, against former expectations, but even increases their difference (*e.g.*, σ decreases from 40.6 mJ cm⁻² to 37.8 mJ cm⁻² for PET-flattened and 34.5 mJ cm⁻² for EVAC-flattened Gr/Cu, respectively, compared to 72.8 mJ cm⁻² for water.) With this observation the general opinion, that it is the difference in surface tension which causes the graphene to rip, can be refuted [227, 236, 237].

Yet, it is unclear why EVAC-flattened graphene performs peerlessly better than unmodified graphene or PET-flattened graphene during transfer. Taking a closer look at the relative individual variations of σ^p and σ^d , it becomes more obvious why EVAC-flattened graphene performs best. σ^d decreases by only 8 % and 14 % for PET- and EVAC-flattened Gr/Cu, respectively. σ^p , however, is reduced by 29 % after PET- and even 76 % for EVAC-foil treatment. Taking into consideration that polar and dispersive interactions predominantly interact with their own kind and that σ^p constitutes 2/3 of water's total σ [238], the flattening step and with it the adsorbed acetate groups are believed to suppress especially the polar interaction between graphene and water and hence prevent the graphene from ripping and crumbling during transfer (refer to Supporting Information Fig. 8 of ref. [209] for individual measurements of the contact angle for water, diiodmethane, and glycerol as test liquids).

Conclusion of Chapter 4 and Outlook for Chapter 5

An inexpensive and scalable approach to increase the stability and simplify the issue of handling of single-layer graphene during wet-chemical transfer was presented. By decorating graphene's surface with functional acetate groups by reliably pressing an ethylene-vinyl acetate copolymer foil onto graphene using a vacuum bag sealer, polar interactions between graphene and water can be minimized and prevent the one atom thin layer from ripping and crumbling when brought in contact with water.

Even though wet-transfer techniques in general are hardly applicable for membrane production on an industrial scale, the investigated surface modification method can be used to

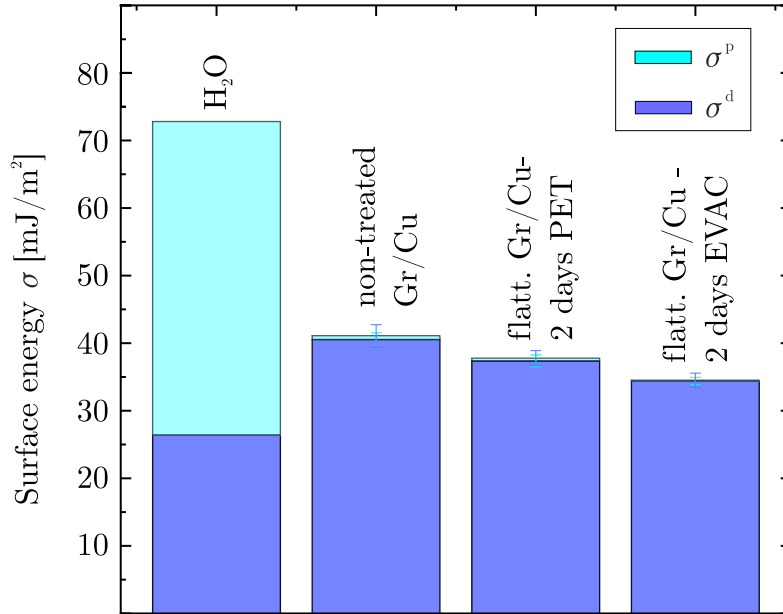


Figure 4.9: Surface energy measurements of flattened and regular Gr/Cu. Polar and dispersive parts of surface energy of water, regular Gr/Cu, PET-, and EVAC-flattened Gr/Cu substrates. Error bars represent standard deviations. Reproduced with permission. Copyright © 2020, the authors of ref. [209].

produce extremely clean and nearly defect-free lab-scale graphene without being restricted to only certain target materials during sample preparation. This again allows more precise and reproducible research on, *e.g.*, ion-graphene interaction by avoiding the aforementioned polymer residues and the problems that come with them during microscopy.

Altering materials via surface modifications, however, is in no way restricted to single-layer graphene even though its property of being nothing but surface surely increases the implications any surface modification has on its performance. Chemical variations of graphene, *e.g.* graphene oxide, owe part of their unique properties to its functional groups as well. It is therefore even more interesting to fabricate a 3D material out of individual 2D layers, all of which are chemically modified, to obtain a maximum of functional groups per volume while still preserving the nature of the 2D building blocks. With this intention, the suitability of graphene oxide fabricated as a membrane laminate and the influence of functional groups as well as its 2D-layered ground structure on selective proton transport through the membrane will be investigated in the following chapter 5 *Graphene Oxide Membranes: Selective Proton Transport for Hydrogen Generation*. Similarities and differences to classical polymer-based materials that are currently used in this energy-science relevant field of proton conducting membranes will be discussed as well.

5 Graphene Oxide Membranes: Selective Proton Transport for Hydrogen Generation

Abstract - Graphene oxide certainly ranks among the most intensively studied membrane materials in recent year and does not only share part of its name with 2D graphene, but also its ability of being used as a membrane. While one of the crucial drawbacks of 2D graphene membranes is its potential risk of ripping, hence forming a short-circuit at the breaking position and rendering the membrane useless, graphene oxide membranes are fabricated as μm -thick laminates and hence showing better mechanical stability. Numerous research articles have shown exceptional filtration characteristics of graphene oxide. By stacking multiple μm^2 -large ultrathin graphene oxide sheets on top of each other, full membranes of graphene oxide can be fabricated, which (just by the fabrication process) already display filtration properties and do not require additional perforation steps. The vertical interlayer spacing of these layered sheets determines the cut-off size of filtered particles. The ability to tune the interlayer spacing further increases the number of possible applications. However, what has often been neglected are graphene oxides natural surface charges and functional groups which open the door for non-conventional ways of filtration. The following chapter investigates the suitability of regular, non-modified graphene oxide membranes for the spatial separation of hydronium and hydroxide ions revealing selective proton conducting properties of GO due by a combination of energetically favored transport mechanisms and reduced interaction with the GO itself.

Parts of the following chapter are an adaptation of ref. [100] and have been reprinted with permission from Madauß, L. *et al.*, Selective Proton Transport for Hydrogen Production Using Graphene Oxide Membranes. *J. Phys. Chem. Lett.* 2020, 11, 21, 9415-9420, <https://doi.org/10.1021/acs.jpcllett.0c02481>. Copyright © 2020 American Chemical Society. Text passages that are reproduced literally are set in quotation marks.

"The growing demand for energy and the urgency for clean and sustainable energy sources has shifted the focus of research towards environmentally friendly ways of energy harvesting. While new technologies and materials enable us to use green energy sources (*e.g.* sunlight, geothermal heat, and wind) more efficiently, a still highly investigated and yet unsolved issue remains the storage of energy for times of high demand [239, 240]. While electrical, electrochemical, and thermal energy storage offers advantages such as fast distribution and flexibility, it also causes problems, including low storage capacity, demand for cost effective materials, energy losses over time, and low conversion efficiencies [241, 242]. A very promising alternative lies in chemical energy storage in form of hydrogen (H_2). Not only does H_2 outmatch other technological approaches in terms of energy density, but it also offers one of the highest storage capacities and can be re-electrified in fuel cells or burned in combined gas power plants at any time [243, 244]. The most common methods for H_2 production rely on light hydrocarbons (*e.g.*, steam reforming of methane [245] and coal gasification [246]). Because of environmental regulations and the search for environmentally friendly alternatives for H_2 production, other approaches have developed, with the most popular ones being the fields of electrolysis [247, 248] and solar water splitting [249, 250]. Especially the field of photocatalytic water splitting has been gaining attention in recent years because, unlike electrolysis, it does not require electrical power and thus may present an easier and more direct source for generation of hydrogen.

In the following, we will apply TiO_2 nanoparticles as a well-known photocatalyst for splitting H_2O under light illumination into H^+ and OH^- ions [251, 252]. One of the main challenges of photocatalytic water splitting, however, is the spatial separation of the H^+ and OH^- ions. Ion separation by regular size exclusion using porous membranes poses a barely unbreachable obstacle due to the minimal size difference of 0.18 Å in their hydrated radii (2.82 Å for H_3O^+ and 3.00 Å for OH^- , respectively) [253]. Solely relying on proton-conducting polymer electrolyte membranes (PEMs) made of perfluorinated polymers (*e.g.*, Nafion[®] membranes) for ion separation involves economic drawbacks due to a high production price, toxic chemicals involved in the preparation process, and loss of its proton conductivity at higher temperatures [254–258].

[...] With the discovery of two-dimensional (2D) materials, the focus of membranes and PCM-based research has largely shifted towards this new class of materials [259–263]." While single-layer graphene was the first and only material in the focus of membrane related research in the beginning, other intriguing and promising materials as well as material modifications suitable for membrane fabrication have emerged and been studied intensively [264–269]. Especially graphene oxide (GO) membranes, fabricated by stacking individual GO sheets on top of each other to form arbitrarily large laminates, have shown promising characteristics for filtration [15, 17, 102, 270, 271]. Compared to truly 2D materials, GO membranes do not require additional perforation steps, as their ability to filter is already given by its as-prepared structure and largely governed by the interlayer spacing of adjacent individual GO sheets. "As their distance of ~0.8 nm for dry, non-reduced GO is strongly influenced by the presence of oxygen-containing groups (*e.g.*, carboxyl, hydroxyl, and epoxy groups), reducing the GO and hence

partially removing its functional groups enables tuning of the interlayer distance - an effect that one may use to tune the filtration characteristics of the membrane [19,103]. [...] This approach of filtration by classical size exclusion, however, is not applicable when the particle sizes barely differ or are even identical, as in the case of water's natural ions H_3O^+ and OH^- . Instead of altering the interlayer spacing or reducing GO, we operate with regular GO membranes that exhibit interlaying spacings much larger than the hydrated radii of the ions." Considering GO's negative surface charges [272], the importance of its functional groups and their electrostatic interaction with ions, unmodified GO may present a real alternative to classical polymer-based proton conducting materials. The cross-linked water cluster networks in current state-of-the-art perfluorinated PEMs are in striking resemblance to GO's laminated structure and its water filled channels, which could provide similar frame conditions for proton transport. Contemplating the chemistry of, *e.g.*, Nafion[®] membranes (with its hydrophobic perfluorinated backbone (PTFE) and perfluorovinyl ether side chains terminated with sulfonic acid groups (SO_3H)) and the proposed arrangement of these polar and charged acids groups as shown in Fig. 5.1 (a), proton transport within these water filled clusters throughout the polymer matrix is similar to the water transport mechanism in GO as shown in (b), where interlayer spacings too fill with water when exposed to water or humidity [273].

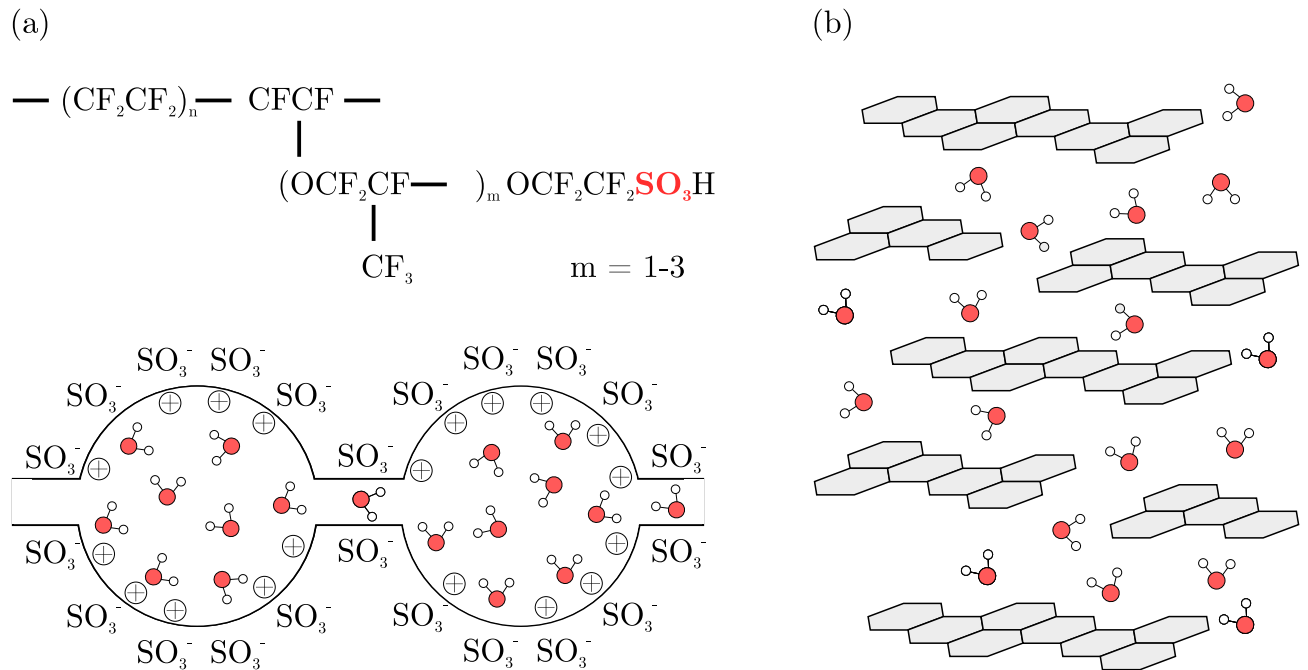


Figure 5.1: (a) Polymeric backbone and $-\text{SO}_3\text{H}$ terminated side chains of Nafion[®] membrane. Loosely bound hydrogen ions provide transport pathways for cations. Hydronium ions can also move via the Grotthuss mechanism through water filled clusters. (b) Water filled channels in GO membranes exhibiting a similar hydrogen bond network as in per-fluorinated sulfonic acid membranes.

Only recently it was shown by Mouhat *et al.* that GO acquires an average negative charge of -6.56 mC cm^{-2} when immersed in water [274], which not only promotes cation selectivity as the $-\text{SO}_3^-$ groups do in Nafion[®] membranes but also exceeds the cation exchange capacity (CEC) of those. The CEC is a measure of the capacity of a soil to hold exchangeable cations on its surface via electrostatic interaction. Values of $0.92 \frac{\text{mmol}(\text{charge})}{\text{g}}$ are typical for Nafion[®] membranes. Expanding the charge-area density for GO to a charge-volume density for comparison with Nafion[®] membranes, much larger values ($\times 10^4$) are obtained for GO (considering a thickness of graphene oxide of 0.34 nm and a wet interlayer spacing of 1.2 nm). In fact, Karim *et al.* reported proton conductivities of 10 S/m for pure GO [275], whereas Liu *et al.* even observed values as large as 56.4 S/m at 80 °C in aqueous solution along with good thermal stability for bismuth oxide/GO composite membranes [276]. Humidified Nafion[®] membranes for comparison operate at around 10 S/m and only rarely reach proton conductivities of 30 S/m [277].

The measurement setup used during this thesis is shown in Fig. 5.2 (a). "The central elements are (1) a light emitting diode (LED) of 385 nm wavelength, (2) & (5) two platinum (Pt) wires serving as electrodes for the transmembrane measurements, (3) a glass slide covered with TiO₂ (anatase) nanoparticles,⁹ (4) the GO membrane on a porous PVDF support attached onto a porous aluminum (Al) membrane for mechanical support, and (6) & (7) two additional Pt electrodes located in the chamber behind the membrane. The second set of Pt electrodes, (6) & (7), will later on be used exclusively in the experiment to characterize the conductance of the water after ions have passed through the GO membrane. The water inside the cell (18.2 MΩ cm resistance and 2 ppb organic contaminants) is replaced by fresh water after each measurement. H₃O⁺ and OH⁻ ions are created at the TiO₂ catalyst-water interface via photocatalytic water splitting. The overall standard potential of the cell adds up to -1.23 V meaning that the desired reaction is non-spontaneous and energy has to be delivered to the system." The 3.2 eV large band gap of the TiO₂ photocatalyst is accounted for by the 385 nm UV LED, which drives the chemical reactions according to $2\text{H}_2\text{O} \leftrightarrow \text{O}_2 + 4\text{H}^+ + 4\text{e}^-$ and $4\text{H}^+ + 4\text{e}^- \leftrightarrow 2\text{H}_2$ with potentials of -1.23 V and 0 V relative to the standard hydrogen electrode (SHE), respectively. "Also, to avoid instantaneous recombination of the H₃O⁺ and OH⁻ ions, we apply a small voltage of 1.1 V at the platinum electrodes (this voltage was chosen because it is sufficiently below the theoretical value of 1.23 V where electrolysis begins). Additionally, the applied bias forces either one of the ions through the membrane, and hence, by measuring the overall current between anode and cathode with varying polarity, we can obtain information on whether either one of the ions propagates more easily through the membrane. If the potential is negative on the right side in Fig. 5.2 (b), H₃O⁺ ions are forced through the membrane, and if the potential is positive, OH⁻ ions pass the membrane. Therefore, the measured current gives information about the mobility of the ions through the membrane.

⁹Preparation of the TiO₂ nanoparticles was done by Dr. Kirsten Dunkhorst - University of Duisburg-Essen, 47057 Duisburg, Germany. The particles had an average diameter of 50 nm.

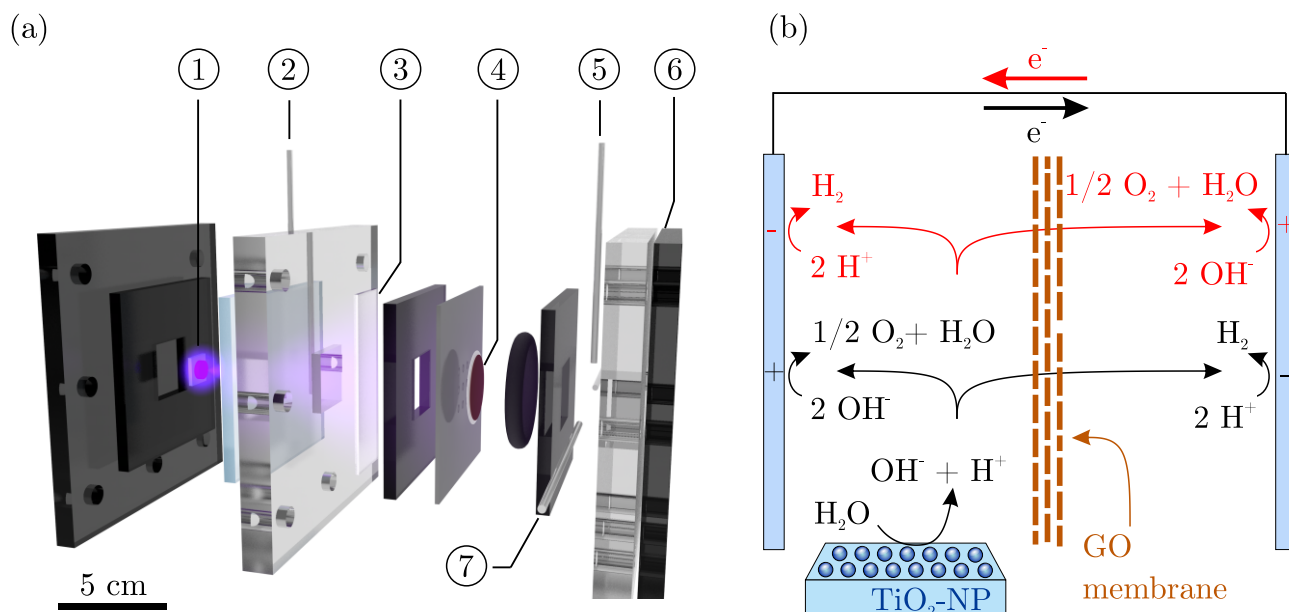


Figure 5.2: Experimental setup and diffusion principle of hydronium and hydroxide ions. a) Schematic drawing of the modified fuel cell used in this work. A GO membrane serves as the membrane element to spatially separate H⁺ and OH⁻ ions. b) Schematic of water splitting mechanism and half-cell reactions. H₂O is split into OH⁻ and H⁺ at the TiO₂ surface with the necessary energy for H₂O splitting being provided by excited charge carriers in the TiO₂. H⁺ and OH⁻ are then driven to the respective electrodes (H⁺ to negatively biased cathode to form molecular hydrogen and OH⁻ to positively biased anode to form H₂O and molecular oxygen). The GO membrane serves as an additional barrier for H⁺ or OH⁻ depending on the polarity of the electrodes. Reproduced with permission. Copyright © 2020, American Chemical Society [100].

The GO membranes were prepared by starting with the synthesis of graphite oxide as a starting material according to Hummer's method.¹⁰ Here, natural graphite is oxidized with a KMnO₄-to-graphite ratio of three by weight [278]. The solution was then sonicated to exfoliate the graphite flakes into mono- and few-layer graphene flakes. The solution was further refined by centrifugation. Finally, the GO solution was filtered through Millipore PVDF membranes with 0.22 μm pores in order to obtain supported GO membranes with a thickness of approx. 2.4 μm [15]" (Supporting Information Fig. S1 (a) of ref. [100] present exemplary SEM images).

The chemical and crystalline properties of the GO membranes were tested prior to the experiments. X-ray photoelectron spectroscopy (XPS) data presented in Fig. 5.3 (b) confirm a high number of hydroxyl-, epoxy-, and carboxyl-groups as expected for non-reduced GO. X-ray diffraction (XRD) measurements were used to determine the interlayer spacing of the GO membranes in the dry state as well as in the wet state, which amounted to 0.8 nm and

¹⁰GO membrane preparation was performed by Prof. Dr. Rakesh Joshi and Mr. Tobias Foller, School of Materials Science and Engineering, University of New South Wales, Kensington, New South Wales 2052, Australia

1.2 nm, respectively (refer to Supporting Information Fig. S1 (b) of ref. [100] for additional XRD data).

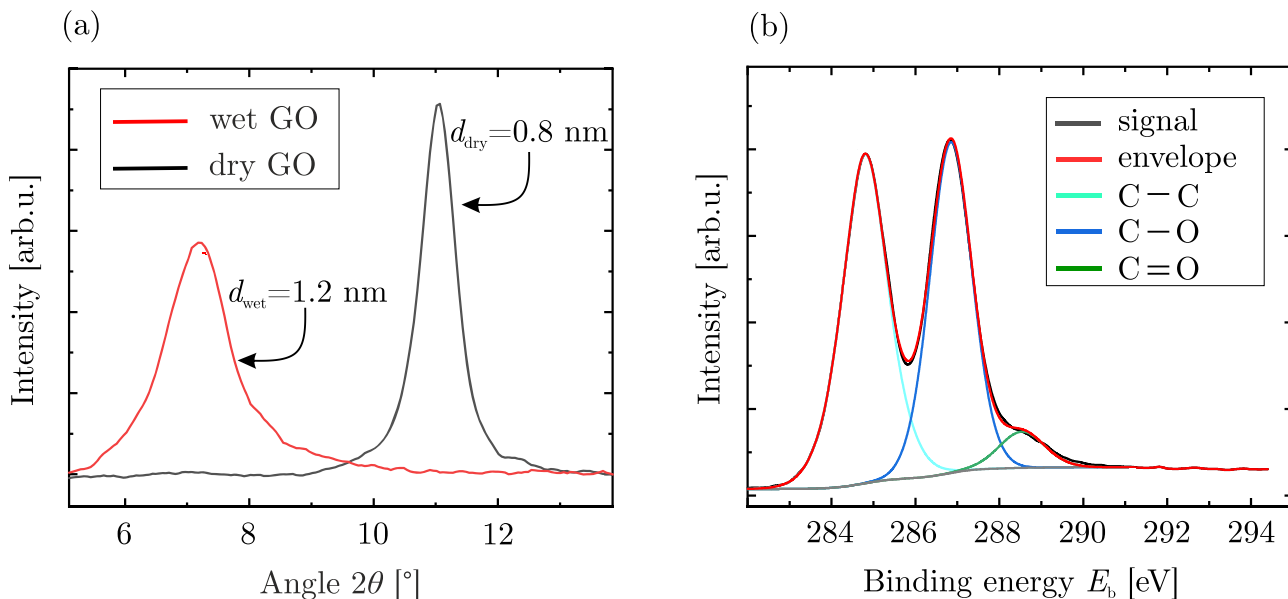


Figure 5.3: Characterization of interlayer spacing and chemical composition of GO membranes. a) XRD measurements of dry and wet GO membranes showing an increase in interlayer distance of GO laminates for the wet state. b) XPS measurements of the C1s peak of GO. Reproduced with permission. Copyright © 2020, American Chemical Society [100].

After establishing a suitable measurement setup and verifying GO's chemical stability when fully immersed in water for several days, diffusion experiments under the conditions described above were conducted. Fig. 5.4 (a) presents the evolution of the cell current I over time both for a polarization of the electrodes supporting H_3O^+ (red curve) and OH^- transport (blue curve) through the GO membrane. Even though an initial drop in current is observable during the first 30 min (which results from ionic residues still present in the water adsorbing at the electrodes, hence decreasing the overall conductivity - see Supporting Information of ref. [100] for additional characterization), two very different behaviors depending on the polarity can be observed: (i) after reaching equilibrium, the current is nearly four times higher when driving H_3O^+ ions through the GO membrane than for switched polarity and having OH^- ions move through the laminate, (ii) the evolution of current for both polarities differs, *i.e.*, a gradually increasing current is observable for H_3O^+ diffusion through the membrane, whereas the conductivity for the OH^- -favored polarity gradually decreases over time.

Even though the identical number of photocatalytically generated charge carriers are given at the same position within the setup, H_3O^+ diffusion through the GO membrane is clearly favored and leads to an overall smaller resistance of the cell supporting the initial hypothesis

of selective proton transport. These observations cannot be accounted for by a classical size exclusion mechanism as GO's interlayer spacing of 1.2 nm in the wet state is significantly larger than the hydrated radii of the respective ions. It is worth noting that the measured value of 1.2 nm is a very conservative estimate since considerably larger interlayer spacing of up to 6 nm have been measured when the GO is immersed in water for several hours [271,279]. Using a non-porous aluminum support as reference leads to a cell current close to zero (black curve in Fig. 5.4 (a)), which rules out any possibility of leakage current and verifies that the observations which have been made are due to a selective ion transport behavior of the GO membrane. Additional reference measurements without a GO membrane show an identical behavior of the current regardless of the electrodes' polarity under otherwise same measurement condition. The influence of the TiO₂ nanoparticles, their degradation over time, gradual adsorption of CO₂ and organic contaminations, and the influence of contaminated water are accessible in the Supporting Information of ref. [100] (Fig. S2, S3, S5, and S6). None of these external influences, however, contradict or falsify the measurements shown here.

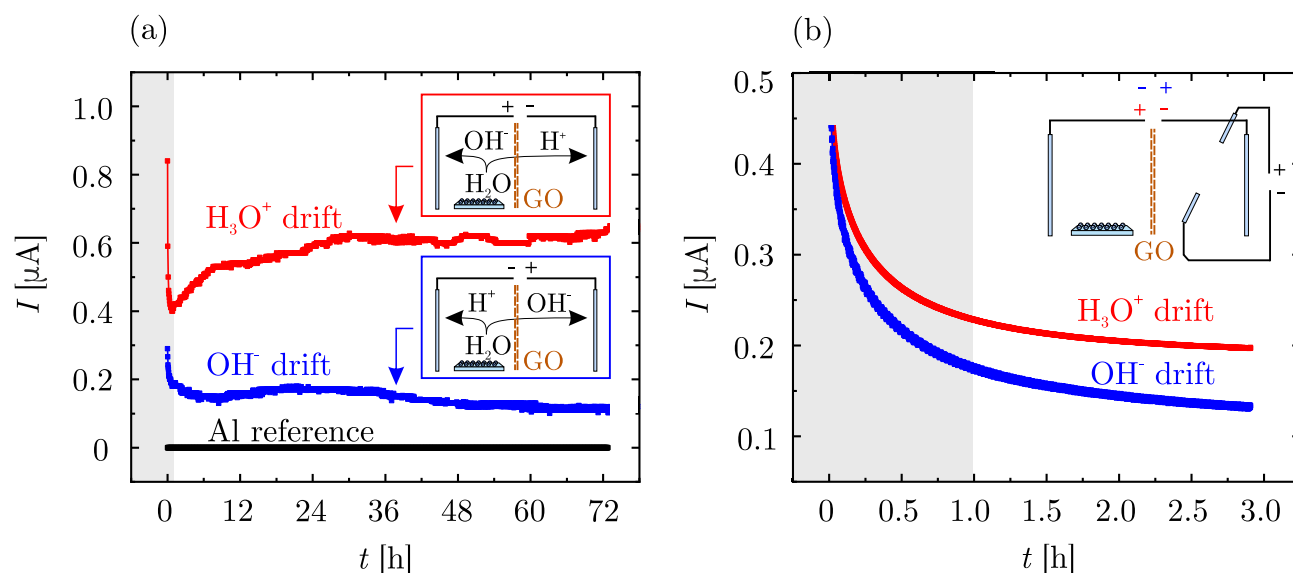


Figure 5.4: Cell-current measurement for different polarities. a) Current measurements over the cell for different polarities facilitating H_3O^+ drift (red) and OH^- drift (blue) through the GO membrane. Reference measurement with a non-porous Al plate instead of the GO membrane is shown in black. Each measurement is the mean of two independent measurements all conducted with the same GO membrane. b) Additional, independent measurement similar to a) except that current was now measured in the half-cell behind the GO membrane for different polarities facilitating H_3O^+ drift (red) and OH^- drift (blue) through the GO membrane. The current is always larger for H_3O^+ -drift polarity. Reproduced with permission. Copyright © 2020, American Chemical Society [100].

"Our results may be best explained by the negatively charged surface of GO. In fact, it has recently been shown by Zhang *et al.* that by manipulation of the charge of GO, controllable cation or anion transport (in their study, much larger ions were tested, *e.g.*, Mg^{2+} , Cl^- or SO_4^{2-}) through the GO can be realized [280]. The movement of ions inside the GO channels is strongly affected by the presence of GO functional groups and water molecules. Water molecules can attach to those hydrophilic groups and form a homogeneous hydrogen-bonding network that enables charge transport of the hydronium and hydroxide inside the GO according to the Grotthuss mechanism [281,282]."

To further verify the proposed suitability of GO laminates as proton selective membranes, the aforementioned second set of Pt electrodes is now added to the second chamber of the setup (parts (6) & (7) in Fig. 5.2), which allows to characterize the conductivity of water only in this half-cell. The measurement configuration and the acquired data are shown in Fig. 5.4 (b). Measurements are taken for a positive and negative trans-membrane voltage, enabling H_3O^+ and OH^- diffusion, by turns. Similarly to Fig. 5.4 (a), a voltage of 1.1 V was applied across the electrodes no. 2 & 5 first. After letting the system reach equilibrium electrodes no. 6 & 7 are biased in order to measure the current only within the half-cell after H_3O^+ and OH^- ions have already passed through the GO membrane. "In agreement with our previous measurements, we observe a permanently higher current when promoting H_3O^+ drift through the GO membrane (the current is approximately 50 % larger for H_3O^+ -favored polarity than for OH^- -favored polarity throughout the measurement). This analysis unambiguously shows that the contribution of H_3O^+ ions to the overall charge flow is significantly enhanced compared to the OH^- drift. [...]"

To compare our experimental findings and test the possibility of Grotthuss mechanism for ion diffusion, we carried out density functional theory (DFT) calculations to assess the hydronium and the hydroxyl ion diffusion processes through GO layers (see experimental and computational methods section in the Supporting Information of ref. [100]).¹¹ It is known that the space between GO layers consists of a network of water molecules that are attached to GO nanosheets through hydrogen bonding [283]. It is also known from previous experimental studies that GO primarily contains epoxy and hydroxyl functional groups [284]. With this information, we tested the diffusion of the two ions assisted by the interlayer water network (Fig. 5.5 (a) and (d)), hydroxyl (Fig. 5.5 (b) and (e)) and epoxy functional groups (Fig. 5.5 (c) and (f)). Previous *ab initio* molecular dynamic simulations have shown that the hydronium and the hydroxyl ions most frequently diffuse via H double jumps [285] as depicted in Fig. 5.5 (a) and (d) for example. Hence, we considered this diffusion behavior to compare their energetics.

¹¹DFT simulations were performed by Dr. Priyank V. Kumar - School of Chemical Engineering, University of New South Wales, Kensington, New South Wales 2052, Australia and Dr. Tiziana Musso - School of Materials Science and Engineering, University of New South Wales, Kensington, New South Wales 2052, Australia

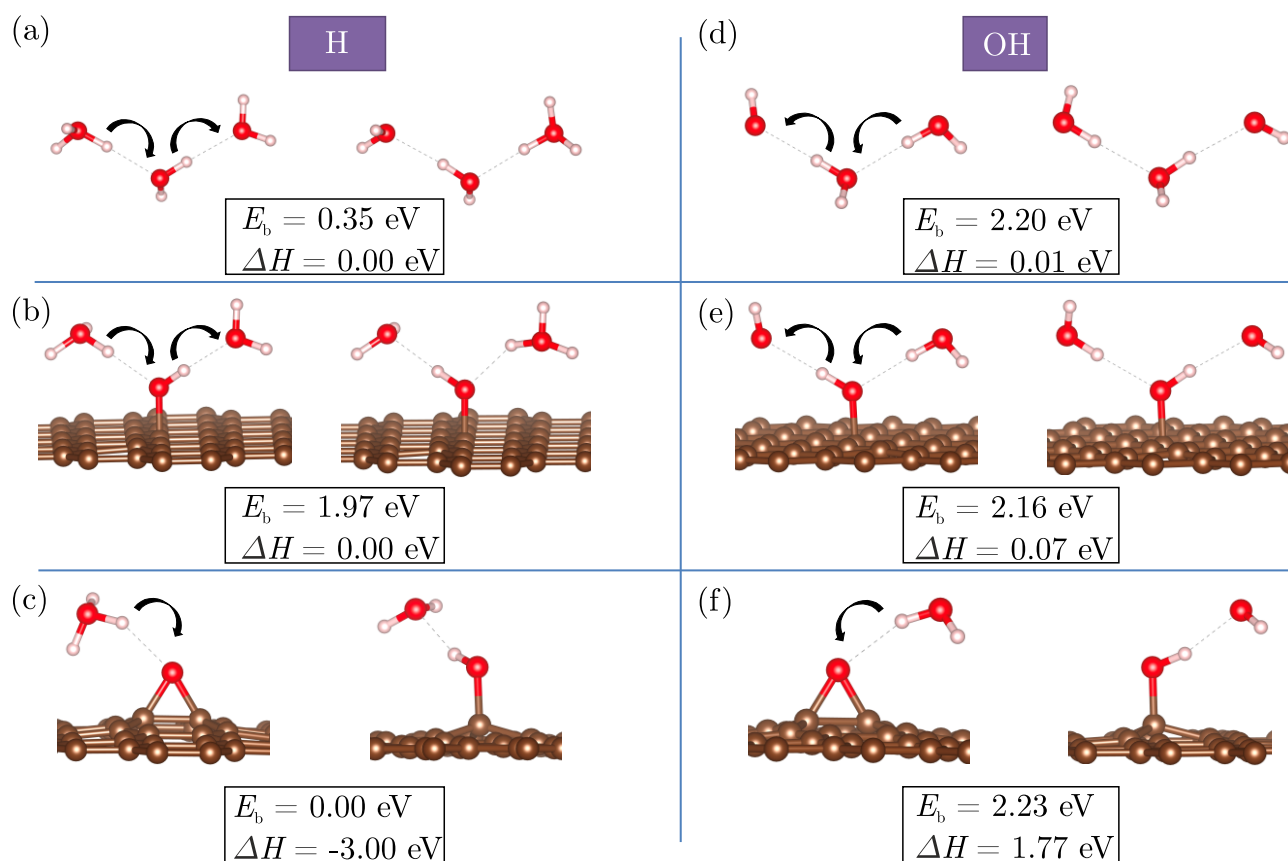


Figure 5.5: DFT calculations of the interaction of hydronium and hydroxide ions with GO. Structural configurations used to model the diffusion of a hydronium ion assisted by a) the water network present within the GO sheets, b) a hydroxyl functional group, and c) an epoxy functional group present in GO. Corresponding structural configurations for hydroxide ion diffusion are shown in d), e) and f), respectively. These diffusion processes occur through double (a, b, d, e) and single (c, f) H jumps as indicated by curved arrows. The activation barrier E_b and the enthalpy of the reaction ΔH are given for each diffusion process. C, O, and H atoms are represented by brown, red, and white spheres, respectively. Reproduced with permission. Copyright © 2020, American Chemical Society [100].

Clearly, our calculations show that the barrier for hydronium ion diffusion (0.35 eV) is much less than the barrier for hydroxide ion diffusion (2.20 eV) through the water network for a similar coordination structure. Similar calculations in the case of ion diffusion assisted by a hydroxyl functional group on GO reveal that the hydronium ion diffusion has a lower activation barrier (1.97 eV) than the hydroxide ion diffusion (2.16 eV). However, we note that this value is much higher than its corresponding value in the case assisted by water, thus making hydronium ion diffusion through water molecules more favorable than that assisted by hydroxyl groups. As for the case of ion diffusion assisted by the epoxy groups on GO, we consider only H single jumps since an epoxy group lacks a H atom. We find that the transfer of H from a

hydronium ion to the epoxy group leads to the formation of a very stable configuration that is 3 eV lower in energy. Therefore, it is unlikely that this transferred H would further hop onto a nearby water molecule, thereby making hydronium ion diffusion assisted by an epoxy group unfavorable. Similarly, a hydroxide ion would require a H jump from a nearby water molecule, and this process is found to be largely unfavorable, as a high activation barrier (2.23 eV) as well as an enthalpy increase of 1.77 eV needs to be overcome. [...] Taken together, our DFT results show that hydronium ion diffusion is more favorable than hydroxide ion diffusion and that this is most likely to happen through diffusion along the hydrogen-bonded water networks rather than being assisted by the oxygen functional groups of GO."

Conclusion of Chapter 5 and Outlook for Chapter 6

The suitability of regular, non-modified GO as a potential proton selective membrane material was investigated. By generating H_3O^+ and OH^- ions via photocatalytic water splitting and studying their transport behavior through a GO laminate by turns, a higher mobility of H_3O^+ ions over OH^- ions was observable and can be correlated with an energetically favored transport described by the Grotthuss mechanisms. GO's functional groups, however, were shown to influence the ions' transport only weakly.

GO laminates display intriguing properties and certainly have the potential of being used as a low-cost and efficient proton conducting material. Diffusion of H_3O^+ ions through a GO membrane may even be realized without applying external electrical fields provided that the gradient in ion concentration across the membrane is large enough. This indeed would be an extremely clean and sophisticated way for hydrogen ion generation, separation, and finally hydrogen gas production. Considering the fact that experimental conditions were chosen to meet requirements for a first proof of concept, hence giving much room for further improvement (*e.g.*, using a more efficient photocatalyst, optimizing catalyst-membrane distance, minimizing cell-volume, *etc.*), the idea of spatially separating hydronium and hydroxide ions with GO membranes may find industrial application in the future.

The following chapter 6 *Electronic Excitation and Perforation of Single-Layer MoS₂* shifts the focus of this thesis away from organic membrane materials and addresses an inorganic 2D material which originally received much attention due to its (opto-)electronic properties: Single-layer MoS₂. However, various research articles have also shown and predicted its superior performance over many other 2D materials when utilized as a porous membrane [33,115,286].

6 Electronic Excitation and Perforation of Single-Layer MoS₂

Abstract - Part of the reason why the interest in 2D materials is still growing is the idea to use them as filtration membranes. Their atomic thickness promises exceptionally high permeabilities outmatching current state-of-the-art membranes. Several techniques for perforation have been introduced - all of which either lack the ability of controlled defect creation or the possibility of up-scaling. The following chapter therefore investigates the suitability of ion irradiation of suspended single-layers MoS₂ for controllable and adjustable pore creation. To be more precise, defect creation is achieved by electronic excitation of the MoS₂ lattice after SHI and HCI irradiation mainly due to the possibility of depositing larger amounts of energy into the 2D material compared to regular keV ion bombardment. Various SHIs covering an energy loss range from 5 keV/nm to 32 keV/nm in MoS₂ were used for defect creation as well as highly charged Xe ions with a fixed E_{kin} of 180 keV and varying E_{pot} between 5 keV and 40 keV. In both cases, dependencies of the pore radius r on the energy loss dE/dx and charge state q for SHI and HCI, respectively, are observable. However, it is worth noting that despite an allegedly similar excitation mechanism of SHI and HCI a very different threshold behavior for defect creation and defect creation efficiency is found.

Experimental and theoretical data on HCI perforated MoS₂ can be found in ref. [287] and has been reprinted with permission from Kozubek, R. ... Madauß, L. *et al.*, Perforating Free-standing Molybdenum Disulfide Monolayers with Highly Charged Ions. *J. Phys. Chem. Lett.* 2019, 10, 5, 904-910, <https://doi.org/10.1021/acs.jpcllett.8b03666>, Copyright © 2019 American Chemical Society.

The majority of research publications addressing single-layer MoS₂ after discovering its thermodynamic stability under ambient conditions have focused on its exciting (opto-)electronic [104] and catalytic properties [288]. Its utilization as a membrane has been investigated only little even though the amount of attention dedicated to membrane applications is increasing. Those experiments investigating porous single-layer MoS₂, however, often deal with point-vacancies introduced by keV-ion irradiation [34], non-scalable approaches (*e.g.*, pore drilling via an electron beam) [60] or cover pore sizes way beyond 10 nm and therefore out of the scope of this thesis [289]. As has been shown in previous studies, SHIs and HCIs are both scalable and reliable tools for nanostructuring 2D materials and shall therefore be used to perforate single-layer MoS₂ and study its response to electronic excitation [31, 211, 290].

To fabricate suspended MoS₂, it is grown on a SiO₂ substrate via the CVD process discussed in chapter 2.4.2 first and subsequently transferred onto a transmission electron microscopy (TEM) mesh (QUANTIFOIL[®] Holey Carbon Gold Grids). A schematic of the transferred single-layer MoS₂ and an optical image of it is shown in Fig. 6.1 (a) and (b), respectively. The inset in (b) shows the porous structure of the support grid which allows TEM microscopy images to be taken of material suspended over 1.2 μm large holes.

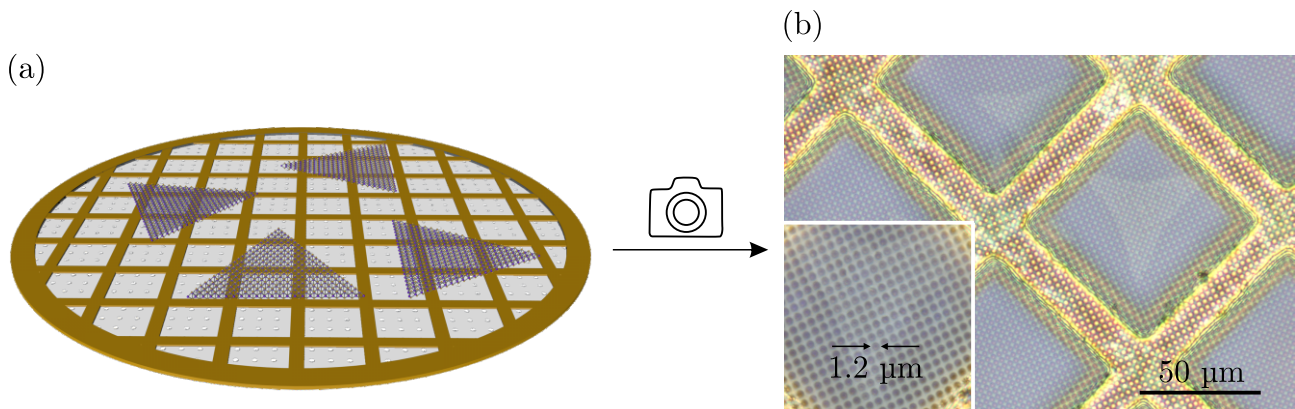


Figure 6.1: (a) Schematic and (b) optical image of single-layer MoS₂ on a porous TEM grid used for SHI and HCI irradiation experiments.

Representative data of pristine, HCI-, and SHI-irradiated layers are shown in Fig. 6.2. Images were recorded with a scanning transmission electron microscope (STEM) with a high-angle annular dark-field (HAADF) detector at the University of Vienna (aberration-corrected Nion UltraSTEM 100 microscope).¹² Pristine MoS₂ shows the expected hexagonal lattice with Mo and S atoms observable as brighter and darker spheres, respectively. An exemplary image is presented in Fig. 6.2 (a). No intrinsic defects are noticeable prior to irradiation. Following HCI irradiation, round shaped pores with a charge state dependent radius are induced into

¹²HAADF-STEM images were recorded by Assoc. Prof. Dr. Jani Kotakoski, Dr. Mukesh Tripathi, and Mr. Rajendra Singh - University of Vienna, Physics of Nanostructured Materials, Boltzmannngasse 5, 1090 Vienna, Austria

the MoS₂ as shown in Fig. 6.2 (b)-(d). Interestingly, for all HCl charge states, a residual polycrystalline structure is occasionally formed at the edges of a MoS₂ pore as exemplarily shown for Xe⁴⁰⁺ ions in (d) (refer to Supporting Information Fig. S4 & S5 of ref. [287] for additional information). Further investigation has shown that these are Mo clusters most likely formed from sputtered Mo atoms.

The situation behaves similar for SHI irradiated single-layer MoS₂. Again, ion impacts induce round shaped pores whose radii depend on the ions' initial properties. In contrast to HCl perforated MoS₂ where the Mo clusters occasionally appear at some pores (more or less independently on the ions' charge states), the process behaves differently for SHI irradiation. Fig. 6.3 demonstrates the appearance and disappearance of Mo clusters located at pore edges depending on the ions' properties. Clusters already form for ¹⁰⁹I 0.1 MeV/u ions - even though their number is quite small as shown in Fig. 6.3 (a). For ¹²⁹Xe 0.71 MeV/u ions, whenever a MoS₂ pore is created it shows at least one or even two Mo clusters. Exemplary images are presented in Fig. 6.3 (b). With an even higher energy loss, *e.g.*, by using ¹³⁶Xe 6.2 MeV/u ions the Mo cluster disappear completely leaving only pores behind without any Mo agglomerates. Though, it is not known yet whether the disappearance of these Mo cluster is a gradually occurring phenomenon, observable once exceeding the energy deposition of ¹²⁹Xe 0.71 MeV/u ions, or if a sharp threshold is involved.

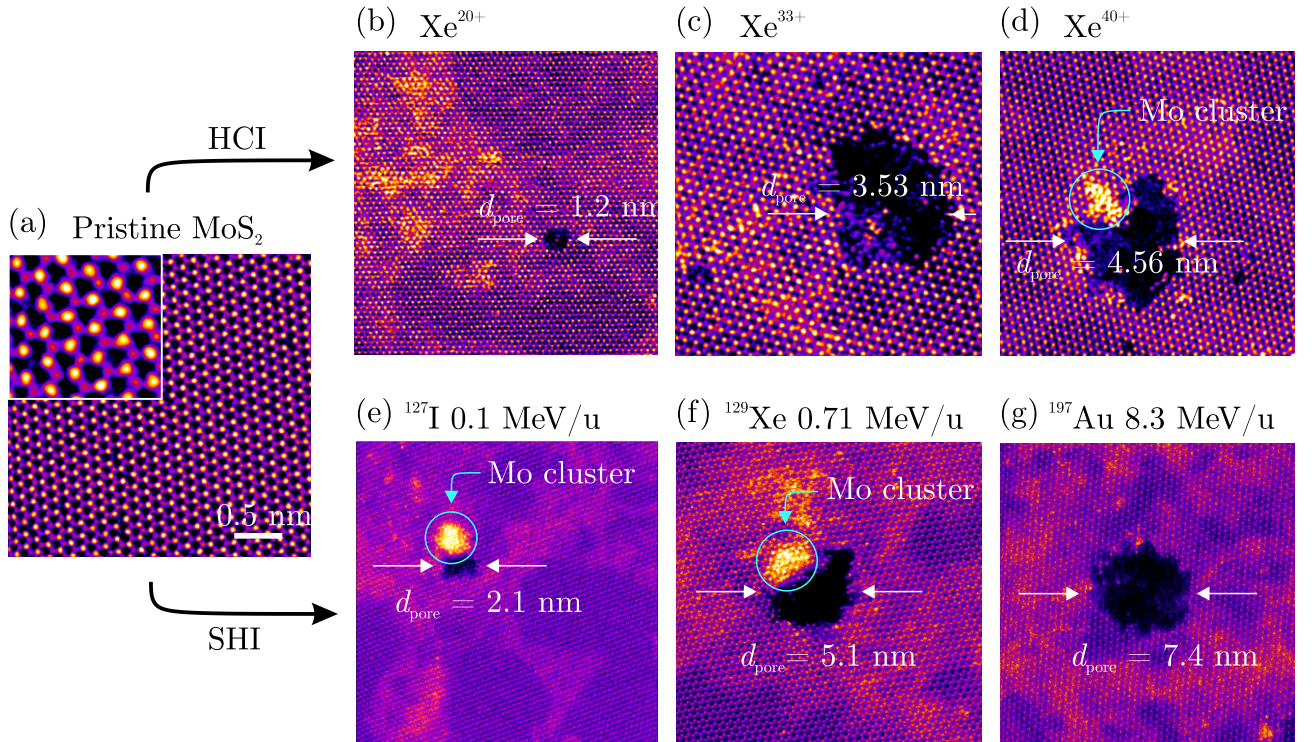


Figure 6.2: STEM image of (a) pristine single-layer MoS₂ showing its hexagonal atomic lattice. (b)-(d) HCl irradiation performed with Xe²⁰⁺, Xe³³⁺, and Xe⁴⁰⁺ on MoS₂ [287]. (e)-(g) SHI irradiation performed with ions of different energy loss. For both ion types, a dependency of the pore radius on their respective properties is observed.

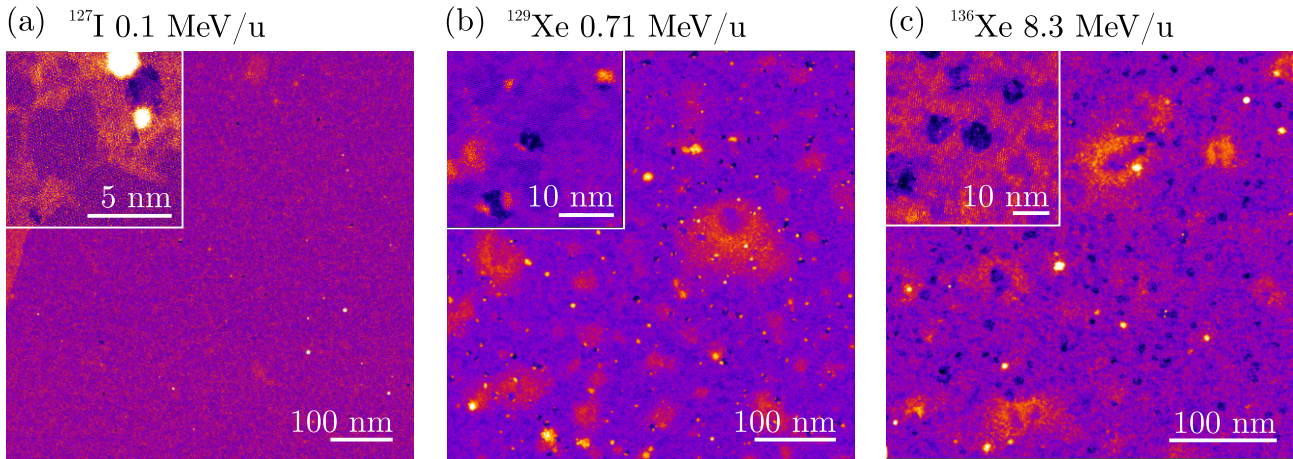


Figure 6.3: Formation of Mo cluster depending on the irradiation conditions. (a) SHI irradiation with ¹⁰⁹I 0.1 MeV/u occasionally results in the formation of Mo clusters. (b) ¹²⁹Xe 0.71 MeV/u practically always generate at least one Mo cluster at the pore edges. (c) MoS₂ pores generated with ¹³⁶Xe 8.3 MeV/u ions never show Mo clusters.

It is certainly interesting to compare the pore size histograms of HCI and SHI induced pores in single-layer MoS₂. Some of the pore size distributions from HCI and SHI perforated single-layer MoS₂ are shown in Fig. 6.4. Taking a closer look at the pore size histograms of HCI perforated MoS₂ in (a), distributions noticeably shift to larger a pore radius r and generally display a broader width for increasing charge states. A similar observation can be made for SHI perforated samples. As expected, a larger energy loss dE/dx of the ion (calculated with SRIM software [143]) results in a larger r and increasing distribution width.

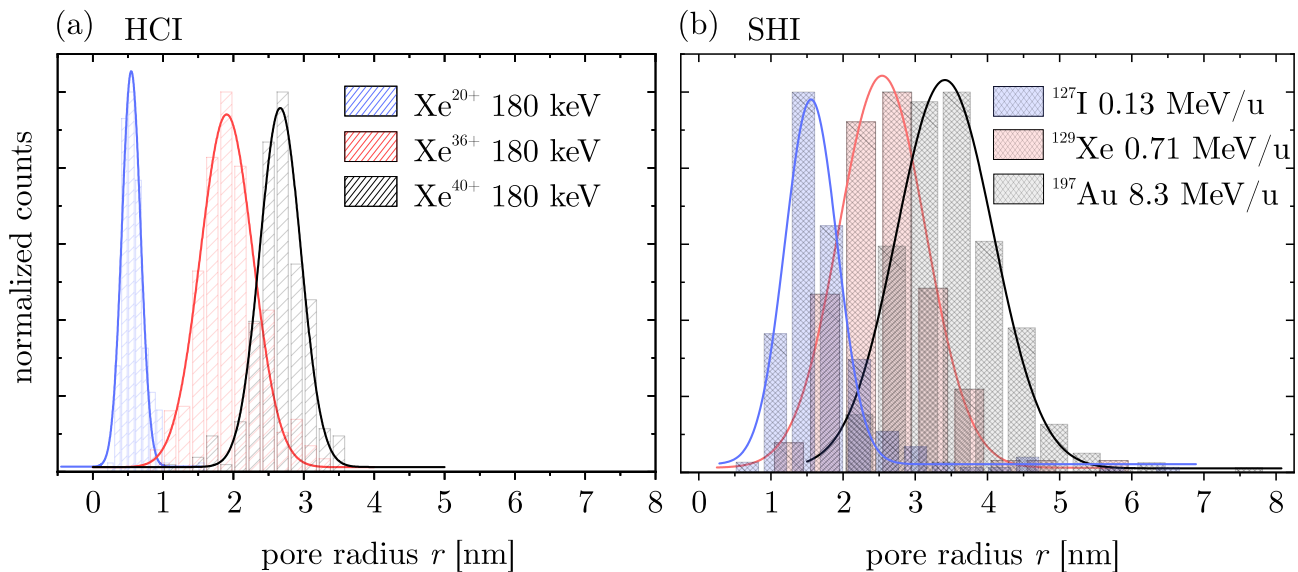


Figure 6.4: Pore size histograms of (a) HCI (Xe) and (b) SHI irradiated MoS₂. A minimum of 200 pores were evaluated for each HCI charge state and SHI dE/dx stopping force.

Note that HCI generated pores are more uniform than those generated by SHI irradiation which is reflected in a narrower pore size distribution. This even applies for those HCIs and SHIs that induce MoS₂ pores of comparable size (*e.g.*, Xe⁴⁰⁺ with a (2.67 ± 0.3) nm pore radius and ¹²⁹Xe 0.71 MeV/u with a (2.62 ± 0.69) nm pore radius). One may speculate what the reason for this observation is since both ion types predominantly interact with the electronic system of the target material. Comparing typical time scales of electronic polarization with the interaction time of a HCI and a surface, it becomes obvious that both processes operate on a 10^{-15} s timescale. Given the high potential energy of a HCI and its relatively low velocity, electrons within the MoS₂ have enough time to reposition themselves such that every HCI experiences a similar or at least comparable electron density during impact. SHI on the other hand are considerably faster which leads to a reduced interaction time with the 2D material. Due to spontaneous and induced dipoles, which are always present regardless of external fields and may alter the electron distribution of the material for a short amount of time, or simply due the equilibrium electron density distribution, a SHI could potentially encounter an electron-depleted MoS₂ region within its interaction time leading to a smaller pore radius whereas another SHI reaches an electron-accumulated position which allows much stronger interaction causing the formation of larger pores. With respect to this argumentation, a visualization of the charge density distribution of pristine single-layer MoS₂ (from the area highlighted in (b) with a black square), is given in Fig. 6.5 (a). The data underlines that electrons in monolayer MoS₂ are not evenly distributed, but that they tend to accumulate especially near the S atoms (and slightly less the Mo atoms), hence forming what is referred to as a *volcanic-cone-like* profile [291].

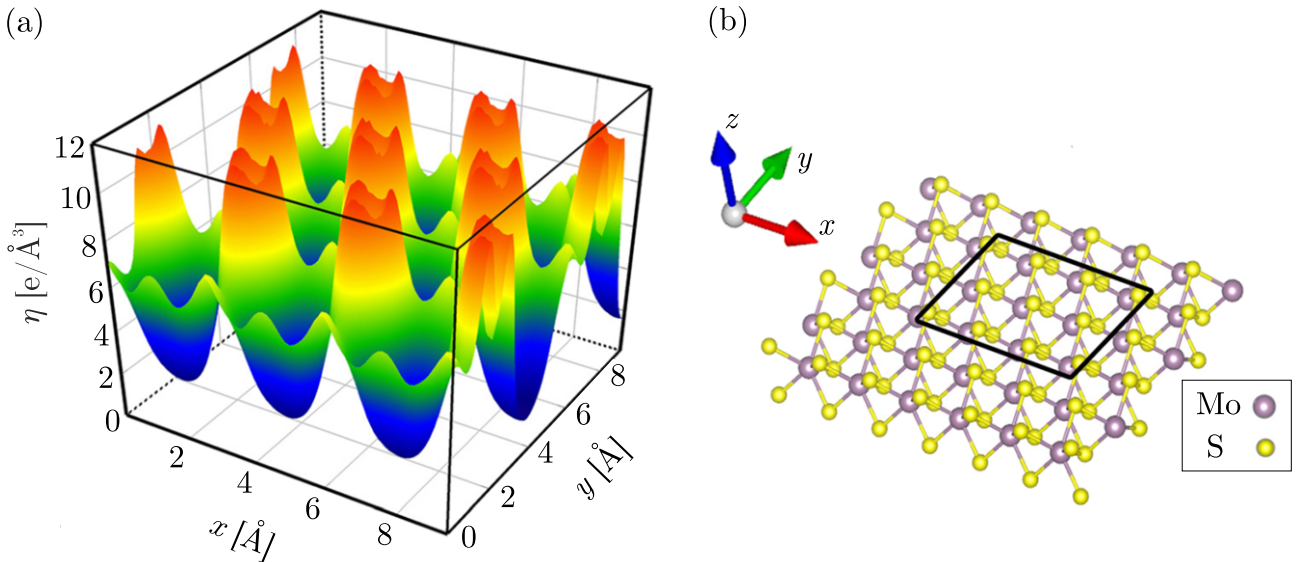


Figure 6.5: (a) Density profile of the intrinsic electric charge in an infinite pristine MoS₂ monolayer. (b) Atomistic structure of the monolayered MoS₂. The solid lines highlight the squared zone in which the charge density profile is depicted in (a). Reproduced with permission. Copyright © 2018, the authors of ref. [291].

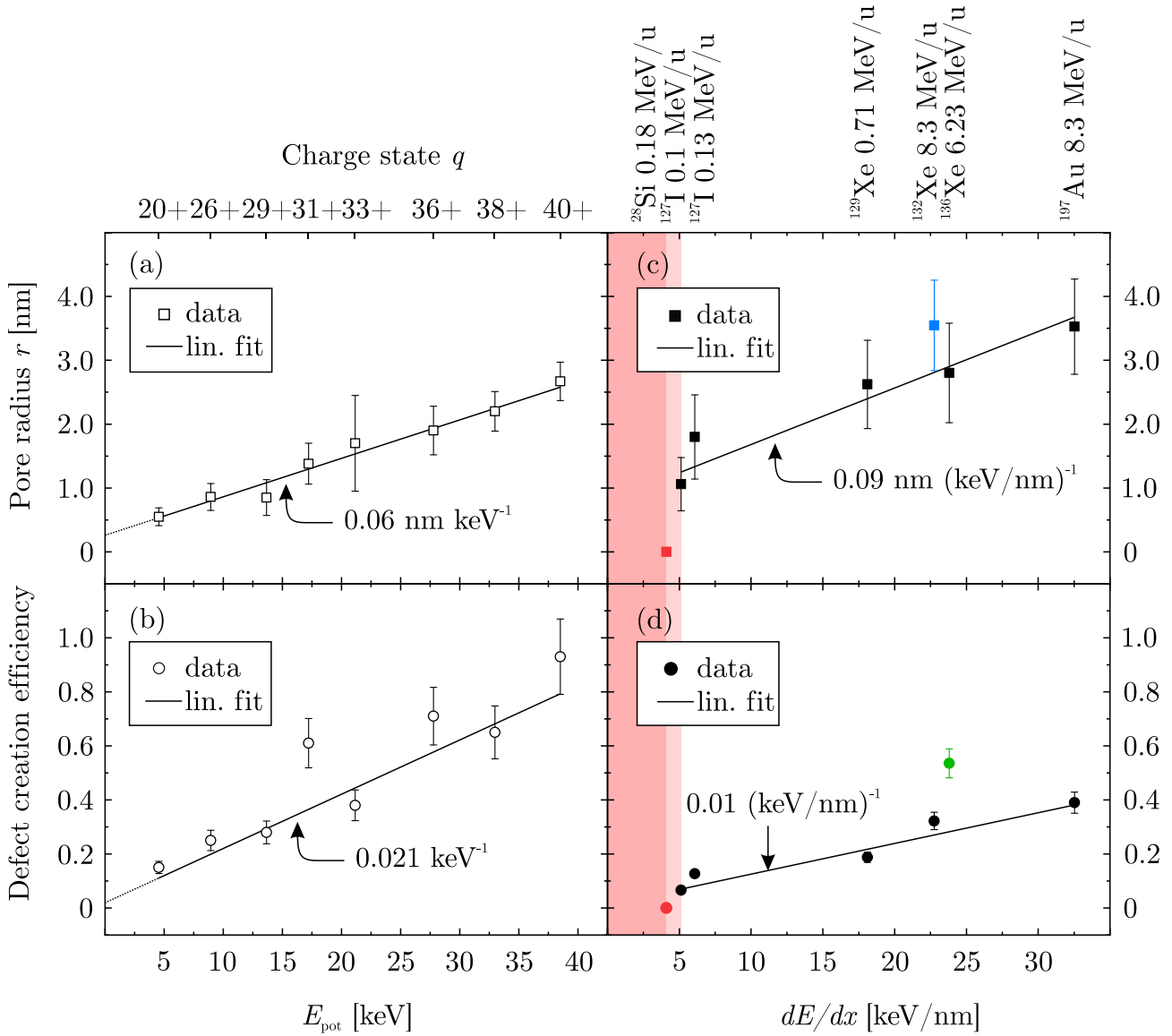


Figure 6.6: Comparison of pore radii r and pore creation efficiencies in single-layer MoS₂ after HCI and SHI irradiation. Efficiency error bars result from inaccuracies of ion fluence. Pore radii error bars represent standard deviations.

A more extensive analysis of pore sizes and pore creation efficiencies can be found in Fig. 6.6 for HCI generated pores in (a) and (b) as well as for SHI generated pores in (c) and (d). Starting with the perforation of single-layer MoS₂ by HCI irradiation, the pore radius r and efficiency is plotted as a function of the HCI's potential energy E_{pot} (lower x-axis) and the charge state q (upper x-axis) at a constant E_{kin} of 180 keV. r displays a linear dependency on E_{pot} with a slope of $(6.04 \pm 0.32) \cdot 10^{-2} \text{ nm/keV}$. Extrapolation to $q = 0$ yields an offset of $(0.27 \pm 0.06) \text{ nm}$ corresponding to the smallest size of a pore that would be induced into a MoS₂ monolayer after interaction with a neutral 180 keV E_{kin} Xe atom, which is in good agreement to theoretical predictions [292]. Similarly, the pore creation efficiency increases nearly linearly with larger q from below 20 % to almost 100 % for a charge state of 5+ and 40+, respectively.

Before comparing these results to SHI generated pore sizes, further attention should be paid to the defect creation mechanism during HCI irradiation. The total deposited energy E^{dep} can be described with eq. 6.1

$$E^{\text{dep}}(q) = \left(\frac{dE}{dx}\right)_n(q) + \left(\frac{dE}{dx}\right)_e(q) + E_{\text{pot}}^{\text{dep}}(q), \quad (6.1)$$

with $E_{\text{pot}}^{\text{dep}}(q)$ being the amount of potential energy introduced into the MoS₂ and $(\frac{dE}{dx})_{n,e}(q)$ representing a charge-state dependent nuclear and electronic stopping force, respectively. To address the importance of $(\frac{dE}{dx})_e(q)$ and $E_{\text{pot}}^{\text{dep}}(q)$ and especially their dependency on q , molecular dynamics (MD) simulations with a charge state-independent $(\frac{dE}{dx})_e(q)$ and without consideration of the ion's charge state were performed.¹³ Because sputtering is usually driven by nuclear stopping, defect creation with charge state dependent $(\frac{dE}{dx})_n(q)$ was used. The results are presented in Fig. 6.7 [287]. Even though a minimal increase in r is obtained due to a charge state dependent $(\frac{dE}{dx})_n(q)$ the discrepancy to the experiment stresses the importance of implementing both a charge state dependent $(\frac{dE}{dx})_e(q)$ and $E_{\text{pot}}^{\text{dep}}(q)$ into the simulations. This, however, is quite challenging since sufficient data is not available on this topic yet and only a few first results have been published so far addressing charge-state dependent transmission and interaction mechanisms of HCIs with graphene and single-layer MoS₂ [167, 168].

Nevertheless, a closer look at the atomic structure of HCI irradiated MoS₂, as shown in Fig. 6.7 (b) for two independent simulations, reveals similar results which have been made in the SHI related experiment as well. A clear accumulation of Mo atoms located next to the pores (red areas) are observable. As stated before in section 2.3.3 on p. 22, Mo-enriched pores in MoS₂ are highly beneficial and promise a higher water flux than regular pores.

We now turn to the dependency of the pore radius and creation efficiency for different SHIs with varying stopping forces dE/dx in suspended single-layer MoS₂, which is presented in Fig. 6.6 (c) and (d) next to the results of the HCI irradiation experiments.¹⁴ The first striking difference for SHI interaction with MoS₂, is the pore threshold behavior for small dE/dx values in (c). To be more precise, suspended single-layer MoS₂ does not show any signs of perforation after irradiation with ²⁸Si 0.18 MeV/u ions (corresponding to a dE/dx of 4.1 keV/nm) demonstrating that no pore creation is obtainable for stopping forces up to this value. This is very different to the results presented for HCI irradiation where no such threshold behavior was observed within the range of investigated E_{pot} and no indication hints towards a threshold for ions with a q smaller than 20+. A slightly larger dE/dx of 5.1 keV/nm, however,

¹³MD simulation where performed by Mahdi Ghorbani-Asl, Silvan Kretschmer, and Arkady V. Krashennnikov - Institute of Ion Beam Physics and Materials Research, Helmholtz-Zentrum Dresden-Rossendorf, 01328 Dresden, Germany

¹⁴Additional SHI data acquired after submission of the thesis suggest a different relation to the one shown here. A manuscript containing respective data will be submitted soon.

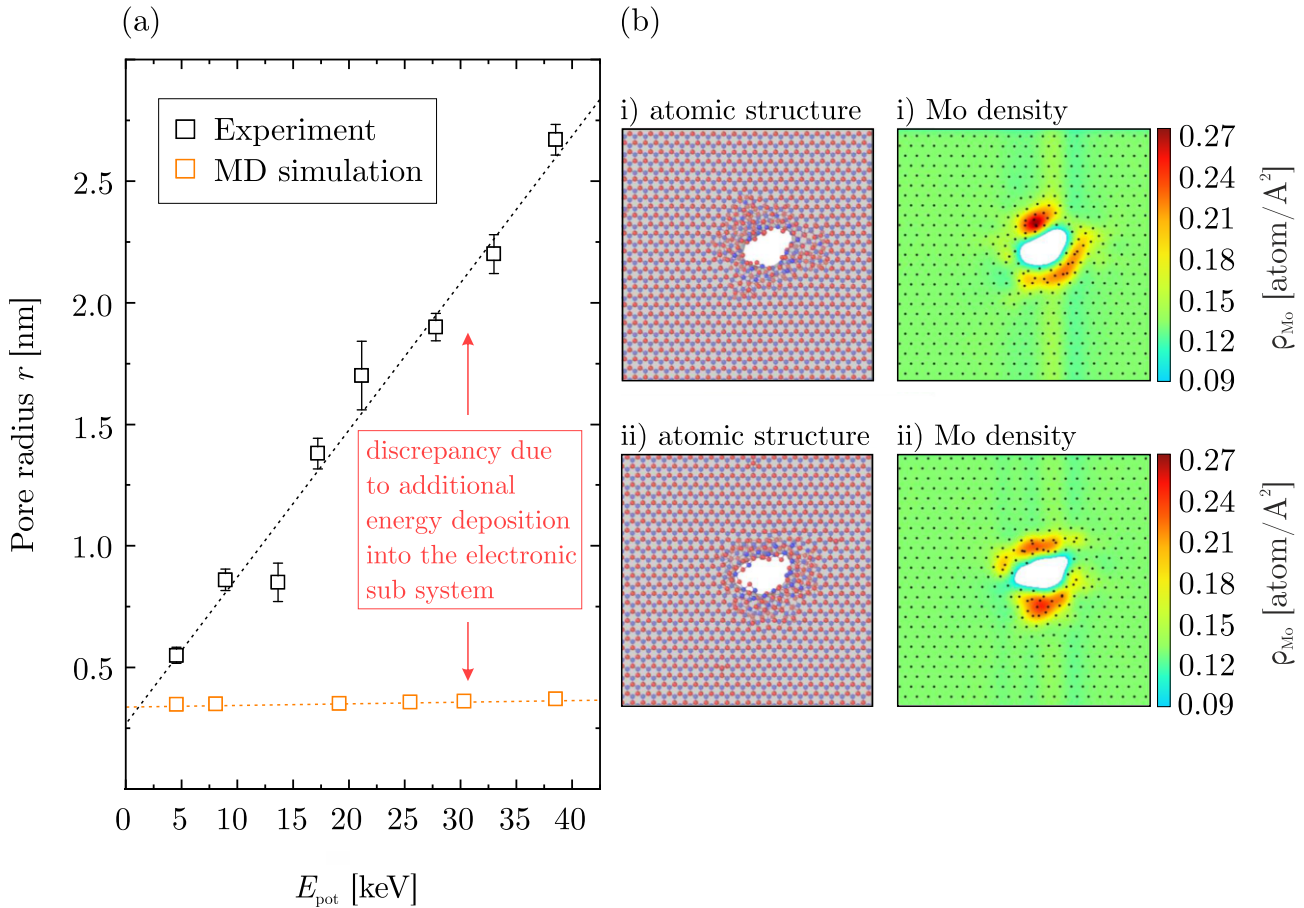


Figure 6.7: (a) Average pore radius in MoS₂ as function of the potential energy obtained by STEM measurements (black) and by MD simulations (orange). The discrepancy between the data sets decreases with decreasing E_{pot} until the extrapolated values at $E_{\text{pot}} = 0$ keV are nearly identical. Error bars represent standard deviations. (b) Two independent MD results of irradiated single-layer MoS₂ after simulating an impact of a Xe⁴⁰⁺ ion with a E_{kin} of 180 keV. Both the atomic structure and the density of Mo atoms are shown. Reproduced with permission. Copyright © 2019, American Chemical Society [287].

already leads to pores in single-layer MoS₂ with 1.1 nm radius. Considering the slope of only (0.09 ± 0.01) nm/(keV/nm) of the linearly fitted data points in Fig. 6.6 (c), it is highly unlikely not to expect a threshold located in between dE/dx values of 4.1 keV/nm and 5.1 keV/nm to justify the sudden increase in pore size. Stopping forces associated with a deposited energy below this certainly insufficient value of 4.1 keV/nm are highlighted in red in Fig. 6.6 (c). The actual threshold is expected to be located within the dE/dx range marked in light-red.

Another unexpected observation was made for the data point highlighted in blue (corresponding to ¹³²Xe 8.3 MeV/u). Due to the unique nature of the dependency of dE/dx on E_{kin} and the velocity effect associated with it, the linear fit shown here only considers ions whose dE/dx either lie on the left flank of their respective dE/dx - E_{kin} curve or in close vicinity to their respective Bragg-peak (*close vicinity* refers to a deviation of the ion's dE/dx of less than 3 % to its maximum). The data point marked in blue does not fulfill these requirements as it deviates by almost 10 % from its max. dE/dx . Still, the comparison of the blue marked data point (¹²⁶Xe 8.3 MeV/u, dE/dx of 22.75 keV/nm) with the one to slightly larger dE/dx (¹³⁶Xe 6.23 MeV/u, dE/dx of 23.8 keV/nm) illustrates the implications of the velocity effect and the radial distribution of energy after perpendicular SHI impact. Even though the calculated energy losses are almost identical deviating by less than 3 %, the respective pore radii differ by more than 20 %.

It is worth comparing the respective deposited energy densities e , which have been calculated in the following by taking the ratio of dE/dx normalized to the thickness of single-layer MoS₂ (0.65 nm) and the experimentally obtained pore radius r . Certainly, some assumptions have been made: i) all of the deposited energy is used for pore creation, ii) the deposited energy density is independent on the distance d of the ion impact, hence a constant radial energy loss distribution $dE/dx(r)$ is assumed. Especially the latter assumptions involve inaccuracies. Still the deposited energy densities give a first explanation for this observation and are summarized in table 6.1 along with various properties of the two aforementioned SHIs. The first column refers to the ions' properties, the second and third ones state their energy losses in MoS₂ and percentual differences to their max. energy loss, respectively (negative values describe dE/dx values located to the right of the Bragg-peak). The fourth column shows the pore radius r . With assumptions i) and ii) made, the final column shows the mean deposited energy density for the two ions. It is apparent that the ¹³²Xe 8.3 MeV/u ion disperses its energy over a larger area leading to a smaller energy density. In bulk materials this may lead to an insufficiently damaged core track [145], however, if the threshold for pore creation in 2D MoS₂ is exceeded nevertheless, every additional portion of energy distributed close to the ion impact is wasted as it does not contribute to an increase in pore size.

Finally, the pore creation efficiency for SHI irradiation shall be discussed and compared to HCI irradiation. While the efficiency for HCI irradiation reaches nearly 100 % for Xe⁴⁰⁺ ions with an increase in efficiency of 2.1 %/keV, considerably lower values are obtained for any SHI investigated so far. Even though a general dependency can be established and higher pore

Ion properties	dE/dx [keV/nm]	$\Delta(dE_{\text{Bragg}}/dx)$ [%]	r [nm]	e [keV/nm ²]
¹³² Xe 8.3 MeV/u	22.75	-8.0	3.55	0.37
¹³⁶ Xe 6.23 MeV/u	23.80	3.6	2.80	0.63

Table 6.1: SHI properties and energy loss density for pore creation in single-layer MoS₂.

creation efficiencies are obtained for increasing dE/dx with a slope of 1 %/(keV/nm), it is still surprising why efficiencies do not reach values comparable to those of HCI irradiation, even though pore sizes are the same or even larger. Similar to the previous discussion addressing why pore size distributions of SHI perforated MoS₂ tend to be broader than those of HCI irradiated MoS₂, SHI impact locations and the electron density of MoS₂ at those respective positions might be the reason once again. Following this hypothesis that a SHI whose trajectory points through the center or a region with a low electron density of the hexagonal lattice, it is expected to interact less with the electronic system of MoS₂. Due to its high velocity, the response time of surrounding electrons near the impact point is insufficiently short such that they are unable to react to the electric charge of the SHI and accumulate as they would do in case of a HCI with a considerably lower velocity.

The aforementioned efficiency-slope of 1 %/(keV/nm) for SHI irradiated MoS₂, however, does not include the data point highlighted in green. The argumentation follows the same idea given before (exclusion of blue data point in Fig. 6.6 (c)) and results from the fact SHIs are known to interact more efficiently with matter when their dE/dx is located close the Bragg-peak. The data points shown here in black correspond to ions which all have a dE/dx varying by 8 % or more to their respective dE_{Bragg}/dx . The ion corresponding to the green point deviates by only 3 %. For the sake of comparison this ion type with its respective properties was left unconsidered.

Conclusion of Chapter 6 and Outlook for Chapter 7

Electronic excitation via HCI and SHI irradiation was investigated as a potential tool for controlled defect creation in suspended single-layer MoS₂. The irradiation conditions that were presented allowed a precise adjustment of the pore radius in a range of 0.5 nm to 4 nm. However, even larger defects (approximately 5 nm pore radius with the irradiation facilities that are given) should be accomplishable if experimental conditions are adapted accordingly. Another important observation is the accumulation of Mo atoms next to the pore edge and with it its expected implications on water permeability [33].

The following chapter addresses this aspect and investigates the chemical stoichiometry of MoS₂ in close vicinity to a SHI impact. Since catalytic measurements are a suitable choice to probe defective MoS₂ with respect to its chemical structure, the following chapter is orga-

nized such that a detailed analysis of the chemical modifications in MoS₂ resulting from SHI irradiation is given first before the focus shifts towards the catalytic performance.

7 Chemical Structure of SHI Irradiated MoS₂ for Catalytic Applications

Abstract - The electrochemical generation of hydrogen (H₂) from water via the hydrogen evolution reaction (HER) is one possible solution to address the world's growing energy demand. Usually, platinum (Pt) and its alloys are used as a catalyst for the reaction mainly due to its chemical inertness, high performance, and minimal overpotential to initiate the desired reaction [293–296]. However, the scarcity and high costs of Pt have initiated the search for new and more cost-effective materials. Much attention has been devoted to transition metal and sulfide-based catalysts including MoS₂ [288, 297–300]. Although the basal planes of MoS₂ are rather inert and only show poor performance during HER, its edges or S depleted regions in general (corresponding to under-coordinated Mo atoms) show an increased catalytic activity [301, 302] for a variety of important reactions, *e.g.*, hydrodesulfurization [303, 304] oxygen reduction reaction (OER) [305, 306], and HER [307–310]. The reason for this behavior lies in the crystal structure of MoS₂. While S and Mo atoms located on its basal planes are chemically saturated, Mo atoms located at the edges are under-coordinated and provide potential adsorption places for hydrogen ions. Consequently, the total number of catalytically active sites plays a crucial role by determining the number of reactions that can run simultaneously [52, 311–313]. Investigations towards a controllable and well-understood defect creation approach via SHI in MoS₂ and the activation of otherwise inert basal planes not only opens new ways to modify MoS₂ structurally for an improved HER performance but also sheds light on the chemical stoichiometry of the edges of MoS₂ defects. A profound understanding of the pores' chemistry is equally crucial for tailored catalytic applications as well as for filtration experiments and membrane applications in general.

Parts of the following chapter are an adaptation of ref. [314] and have been reprinted with permission from Madauß, L. *et al.*, Highly active single-layer MoS₂ catalysts synthesized by swift heavy ion irradiation. *Nanoscale* **10**, 22908 (2018), <http://doi.org/10.1039/C8NR04696D>. Published by The Royal Society of Chemistry. Text passages that are reproduced literally are set in quotation marks.

7.1 Investigation of the Mo-S Stoichiometry of SHI Induced Defects in Single-Layer MoS₂

In contrast to the previous chapter which focused on perpendicular irradiation, grazing incidence SHI irradiation (minimal angle between ion beam trajectory and surface) is used here. Even though the size of defects is considerably larger in this case, the responsible defect creation mechanism is still the same and results that will be obtained here can be connected to previous irradiation conditions as well.

To guarantee comparability to the data presented in chapter 6, CVD grown MoS₂ was once again used in this study as shown in Fig. 7.1 (a).¹⁵ Exemplary Raman and photoluminescence spectra of as-grown MoS₂ prior to irradiation are presented in (b) which verify the presence of single-layer MoS₂ by revealing a E_{2g}¹ and A_{1g} mode difference of only 18.5 cm⁻¹ and a high photoluminescence intensity [200]. Due to the harsh acidic environment used during hydrogen evolution reaction measurements (to ensure a sufficient concentration of H₃O⁺ ions for adsorption) SiO₂ with its lacking chemical stability is unsuitable as a substrate demanding an initial transfer onto chemically inert glassy carbon (GC) substrates. Scanning electron microscopy (SEM) images were taken to compare the morphology of transferred flakes on GC before and after irradiation. No defects or fractures of the MoS₂ are observable in (c) whereas various foldings, rifts and even origami-like "3D" structures are formed due to ion impact as shown in (d). Note the bare GC substrate next to the irradiated MoS₂ does not display such features.

It is also known that the substrate material plays an important role for the geometry and length of these surface modifications [315]. In accordance to this, a similar observation has been made here. Even though irradiated MoS₂ monolayer on GC (Fig. 7.1 (e)) reveal comparable features as when supported by SiO₂ (Fig. 7.1 (f)), length and width of the defects do vary though for different support substrates despite identical irradiation conditions (both with respect to the ion type/energy and angle of incidence). Especially the defect width of MoS₂ shows striking differences for the two different support materials. While incisions in GC supported MoS₂ have a width of up to 80 nm or more, modifications in MoS₂ supported by SiO₂ are much narrower. Due to different material properties of SiO₂ and GC (*e.g.*, heat conductance, electron-phonon coupling) the dimensions of the defects certainly differ. Still, considering the resemblance in defect form and structure, it is reasonable to infer that the defect mechanism is the same.

Since previous studies have addressed the catalytic activity of MoS₂ originating from S vacancies as well as the lower displacement threshold energy of S compared to Mo (roughly by a factor of six) [31, 292], the chemical structure and Mo-S stoichiometry close to the ion modified

¹⁵MoS₂ growth was performed by Dr. Meng-Qiang Zhao, Dr. Carl H. Naylor, and Prof. Dr. A. T. Charlie Johnson - Department of Physics and Astronomy, University of Pennsylvania, Philadelphia, USA

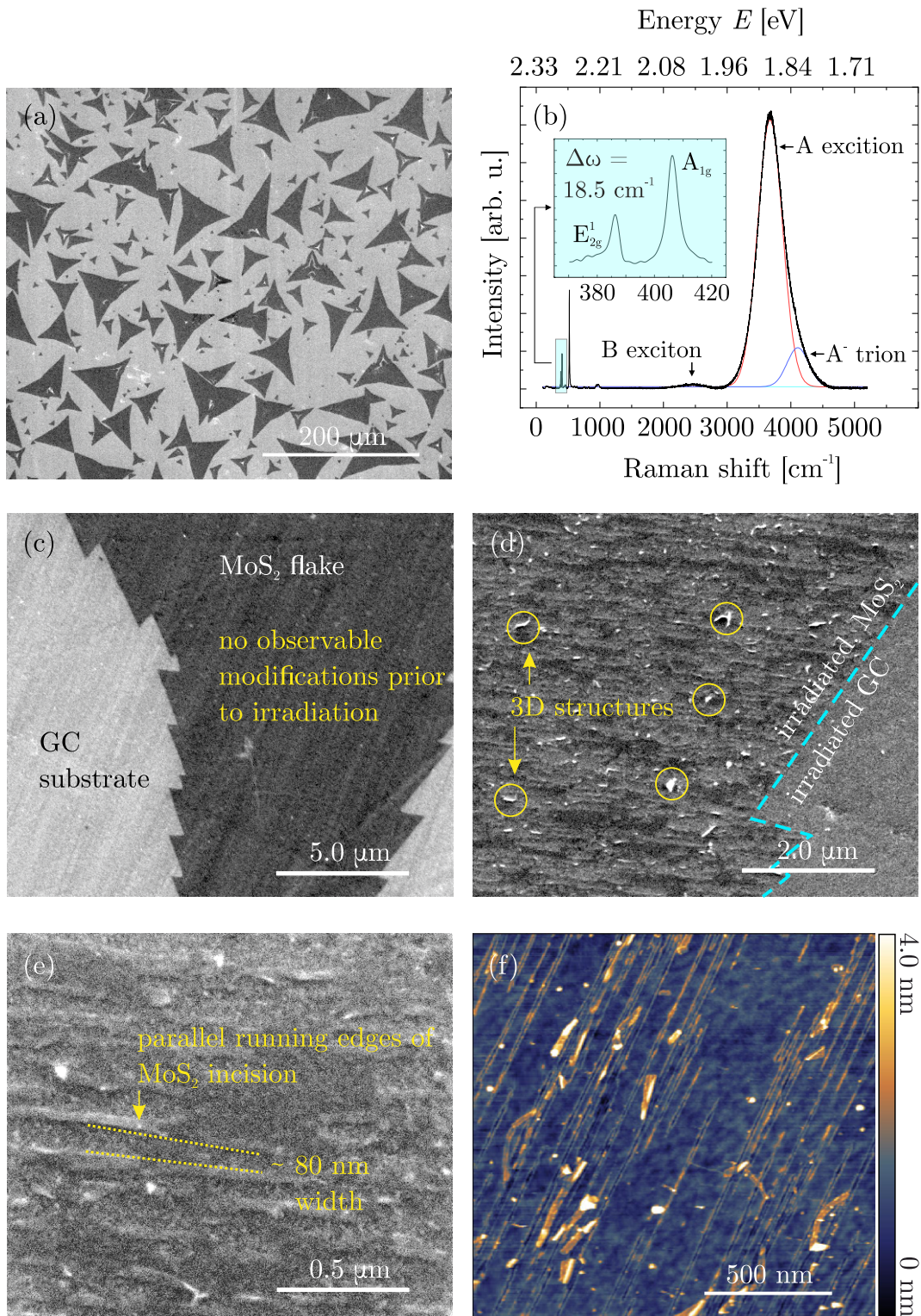


Figure 7.1: (a) SEM image of pristine single-layer MoS₂ on GC. (b) Raman- and photoluminescence spectroscopy measurements of MoS₂ verifying a high crystallinity and presence of single-layer sheets. Noticeable change in morphology of non-irradiated (c) and irradiated MoS₂ (d). Irradiated MoS₂ on GC (e) and SiO₂ (f) show similar defect features, which however differ in size and dimension. Irradiation was performed with 91 MeV Xe ions under grazing incidence at an angle of $\theta = 1^\circ$ with respect to the surface. Reproduced with permission. Published by The Royal Society of Chemistry [100].

track has been investigated by molecular dynamic (MD) simulation, see Fig. 7.2.¹⁶ Irradiation was simulated with the inelastic thermal spike model [316, 317] on unsupported MoS₂ under grazing incidence (1° with respect to the surface) for 91 MeV Xe ions (refer to Supporting Information of ref. [314] for additional information on MD simulation). In agreement to the experiment, MD simulations also predict the formation of a rift with highly amorphous edges along the ion trajectory as shown in (a) and (b). To access under-coordinated Mo atoms visually and correlate catalytic activity to structural changes, the amorphous chains are removed and under-coordinated Mo atoms are color-coded depending on their coordination number (blue = coordination number of 6, green = 5, red = 4), see Fig. 7.2 (c) and (d). According to the MD data nearly 29 % of adjacent S atoms are missing and 28 % of the Mo edge atoms are under-coordinated. To assess the efficiency for creating under-coordinated Mo atoms at 1 ° irradiation, the number of defects along the ion track needs to be calculated. Given an average track length of (400 ± 200) nm for SiO₂ supported MoS₂ (taken from Fig. 7.1 (f)), nearly 1400 S atoms can be calculated missing per ion impact. By tuning the fluence, the defect density can be further increased. However, at too high fluences, tracks will start to overlap so that the achievable S vacancy density will saturate at some stage or even decrease again.

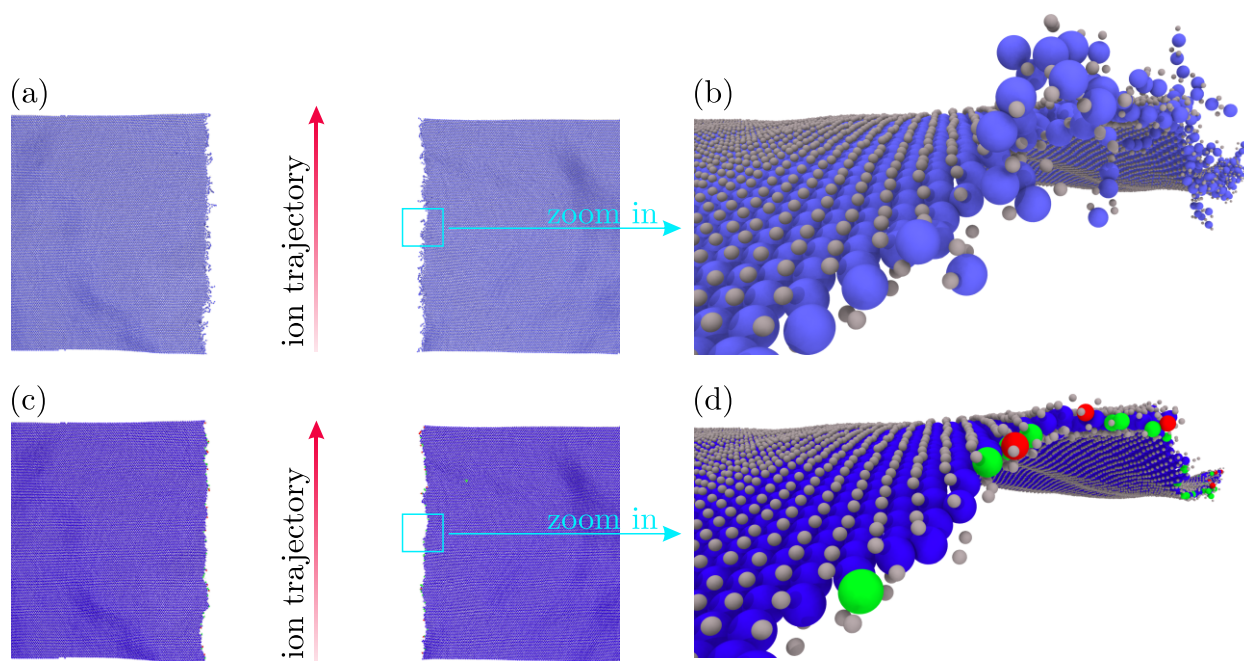


Figure 7.2: MD simulations of a suspended single-layer MoS₂ sheet irradiated with 91 MeV Xe ions under grazing incidence of 1° with respect to the surface. (a), (b) Nano-incision running along the ion trajectory with amorphized edges. (c), (d) Amorphous chains have been removed and coordination numbers of the remaining Mo atoms color coded. Blue: Mo atoms with a coordination number of 6; green: 5, red: 4. Reproduced with permission. Published by The Royal Society of Chemistry [100].

¹⁶MD calculations were performed by Prof. Dr. Flyura Djurabekova and Mr. Henrique Vázquez Muiños - Department of Physics, University of Helsinki, 00014 Helsinki, Finland

Because MD simulations were performed for suspended MoS₂, the actual heat dissipation is expected to behave differently for substrate supported samples. This can lead to an increase in the number of under-coordinated Mo atoms provided that the substrate temperature exceeds the decomposition temperature of MoS₂. The spatial temperature profile of a SiO₂ substrate after 91 MeV Xe irradiation at a grazing angle of 1 ° was therefore investigated using the *Two-Temperature Model* and compared to intrinsic properties of MoS₂.¹⁷ The results are presented in Fig. 7.4 as a side (a) and top (b). The decomposition temperature of MoS₂ is marked as a dotted line along the isotherm of 1458 K [318,319]. MoS₂ located within the area where the thermal spike exceeds its decomposition temperature will provide potential defects for HER afterwards. However, even those parts next to the ion impact where the temperature does not exceed the decomposition temperature of MoS₂ may still have S atoms removed selectively. S has in fact a much lower evaporation temperature than MoS₂ and begins to evaporate from the MoS₂ monolayer crystal at temperatures as low as 500 K [320]. Each ion impact therefore creates under-coordinated Mo atoms located at the edges of the ion rift but also removes S atoms located further away.

To verify the theoretical insight, x-ray photoelectron spectroscopy measurements (XPS) of pristine and irradiated MoS₂ were conducted to obtain information on the elemental composition and chemical state of MoS₂ before and after irradiation.¹⁸ Respective XPS spectra are shown in Fig. 7.4 with the Mo signal originating from MoO₃ (colored in mint green) and Mo bound as MoS₂ (colored in blue). The S peak is shown in yellow. Due to spin orbit coupling, the Mo peaks are split into two separate peaks. Electrons in the 2s orbital of S do not have an angular momentum, hence do not cause a splitting of the signal. Pristine MoS₂ as well as irradiated MoS₂ both show a contribution from the Mo 3d_{5/2} and Mo 3d_{3/2} electrons of MoS₂ and MoO₃. For pristine MoS₂, the MoO₃ contributes ca. 20 % to the overall Mo signal, which can be attributed to oxidized edges and intrinsic defects. This percentage strongly increases for irradiated MoS₂ to nearly 50 % (ion fluence of 15 ions/μm² at a grazing angle of 1° with respect to the surface). The under-coordinated Mo atoms along the ion trajectory oxidize upon exposure to air, hence contributing to the Mo (MoO₃) signal.

Apart from these under-coordinated Mo atoms, TTM simulations also suggest that SHI irradiation creates S vacancies due to the thermal spike after ion impact. The lower sublimation temperature of S compared to Mo will result in a preferential evaporation of S atoms in adjacent rows next to the ion trajectory. Analyzation of the stoichiometry of Mo and S prior and after irradiation using the XPS peak areas and the corresponding relative sensitivity factors (RSFs) [321] reveals an increase in the total Mo(MoS₂+MoO₃):S ratio from 0.56 to 0.88. The larger intensity ratio after irradiation results only from the preferential evaporation of S atoms followed by the oxidation of under-coordinated Mo atoms since the Mo(MoS₂):S ratio remains constant at nearly 50 %.

¹⁷TTM calculations were performed by Dr. Oliver Ochedowski and discussed in ref. [193] for the first time.

¹⁸XPS measurements were performed by Dr. Ulrich Hagemann - University of Duisburg-Essen, CENIDE, ICAN, 47057 Duisburg, Germany

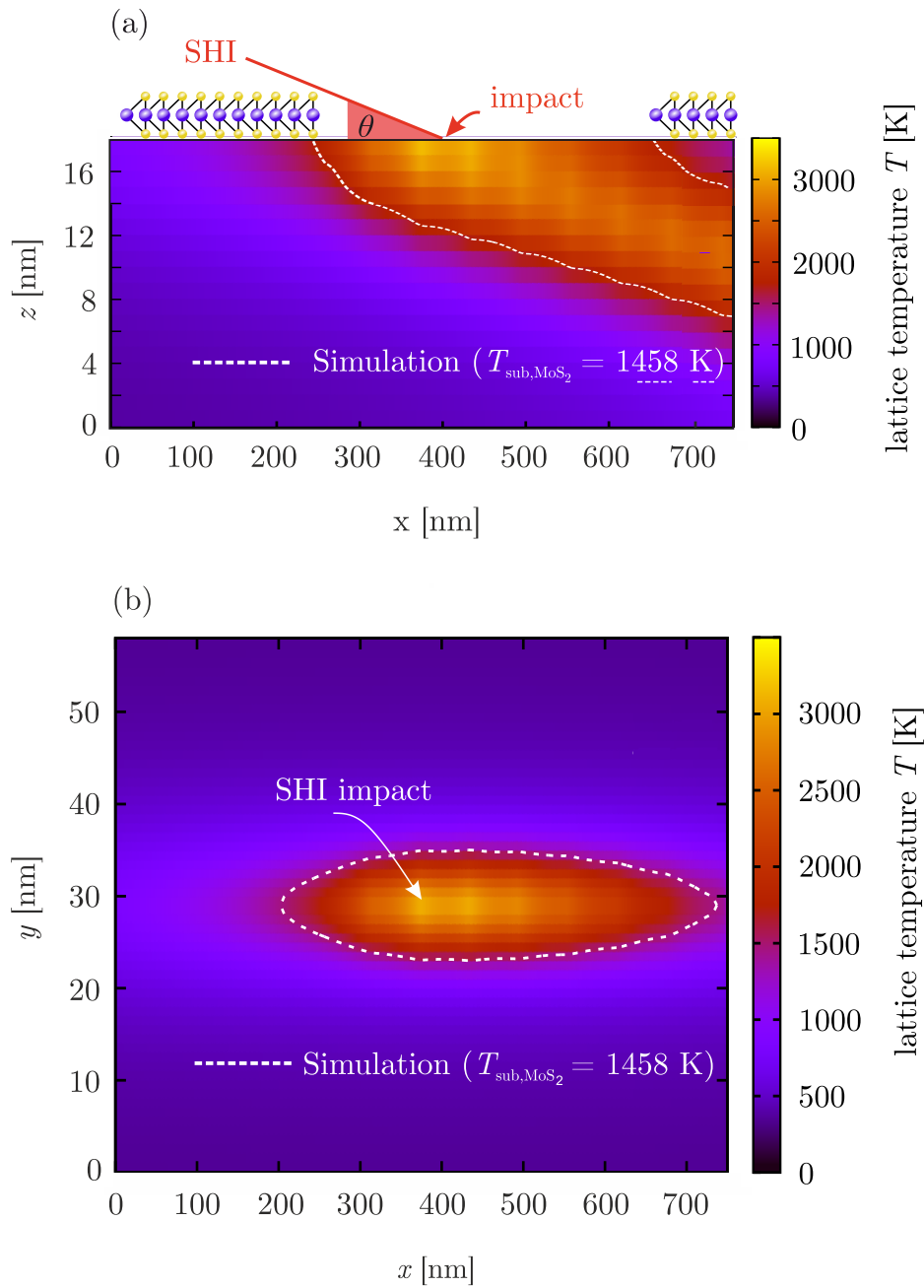


Figure 7.3: Calculated temperature profile as in SiO₂ after irradiation with 91 MeV Xe ions under grazing incidence of 1° with respect to the surface. Temperature profile as a side (a) and top (b) view. The white dotted line depicts the isotherm at the decomposition temperature of MoS₂. Reproduced with permission. Published by The Royal Society of Chemistry [100].

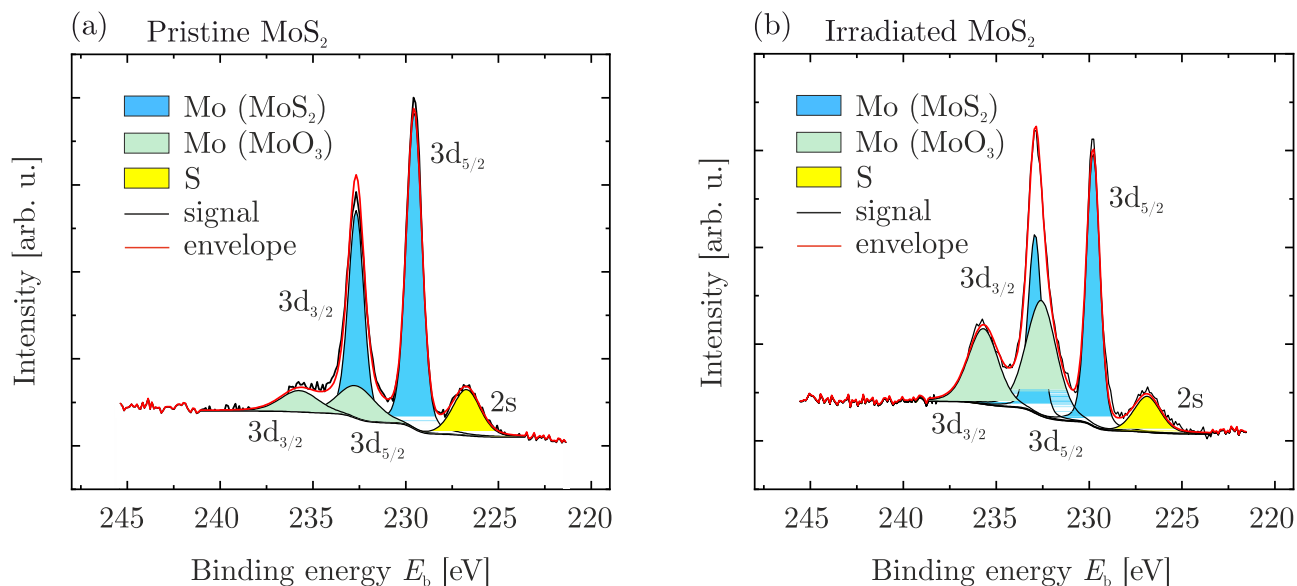


Figure 7.4: XPS spectra of non-irradiated (a) and ion-irradiated (b) single layer MoS₂. Irradiation was performed with 91 MeV Xe ions under grazing incidence of 1° with respect to the surface. Reproduced with permission. Published by The Royal Society of Chemistry [100].

7.2 Hydrogen Evolution Reaction of SHI Generated Defects in Single-Layer MoS₂

Irradiated and pristine MoS₂ on GC substrates were characterized with respect to their catalytic activity during HER which give important information about the chemistry of defects. For this, linear sweep voltammetry (LSV) measurements were performed in an aqueous 0.5 M H₂SO₄ solution as shown in Fig. 7.5 (a).¹⁹ High current densities j at low potentials [V vs. RHE] are desirable as this qualifies the material as a good catalyst. Irradiated MoS₂ shows an almost three times larger current of -35.3 mA cm^{-2} compared to pristine MoS₂ with only 13.3 mA cm^{-2} at an overpotential of -0.6 V vs. RHE .

Aside from its ability to evoke a high current density at low overpotentials, so is a good catalyst characterized by its onset potential, which determines the necessary energy input to initiate the hydrogen evolution. It corresponds to the Gibbs free energy ΔG_{H} of hydrogen ions bonding to the catalyst, which ideally takes a value of zero. Any deviations lead to a too

¹⁹Catalytic measurements were performed by ^aDr. Ioannis Zegkinoglou, ^aYong-Wook Choi, ^aSebastian Kunze, ^{a,b}Prof. Dr. Beatriz Roldan Cuenya - ^aDepartment of Physics, Ruhr-Universität Bochum, 44780 Bochum, Germany and ^bDepartment of Interface Science, Fritz-Haber Institute of the Max Planck Society, 14195 Berlin, Germany.

strong/too poor adsorption, neither of which is convenient for HER as this would lead to an ineffective hydrogen desorption or electron-proton transfer, respectively. Even though an exact value of the onset potential is defined only loosely, the results in (a) (inset) indicate an improved behavior for ion irradiated MoS₂. Comparing the necessary overpotential to obtain a current density of 200 $\mu\text{A cm}^{-2}$, the applied potential for non-irradiated MoS₂ is -300 mV, whereas the potential for irradiated MoS₂ is only -200 mV. A similar observation was previously made by Li *et al.* whose simulations showed a decreasing ΔG_{H} for a increasing amount of S vacancies with a lowest ΔG_{H} of only 200f meV corresponding to a S-vacancy density of 12.5 % [322]. In principle, the same effect was achieved here via SHI irradiation and facilitated by the much lower sublimation temperature of S leading to desulfurized areas as confirmed by TTM simulations and XPS measurements.

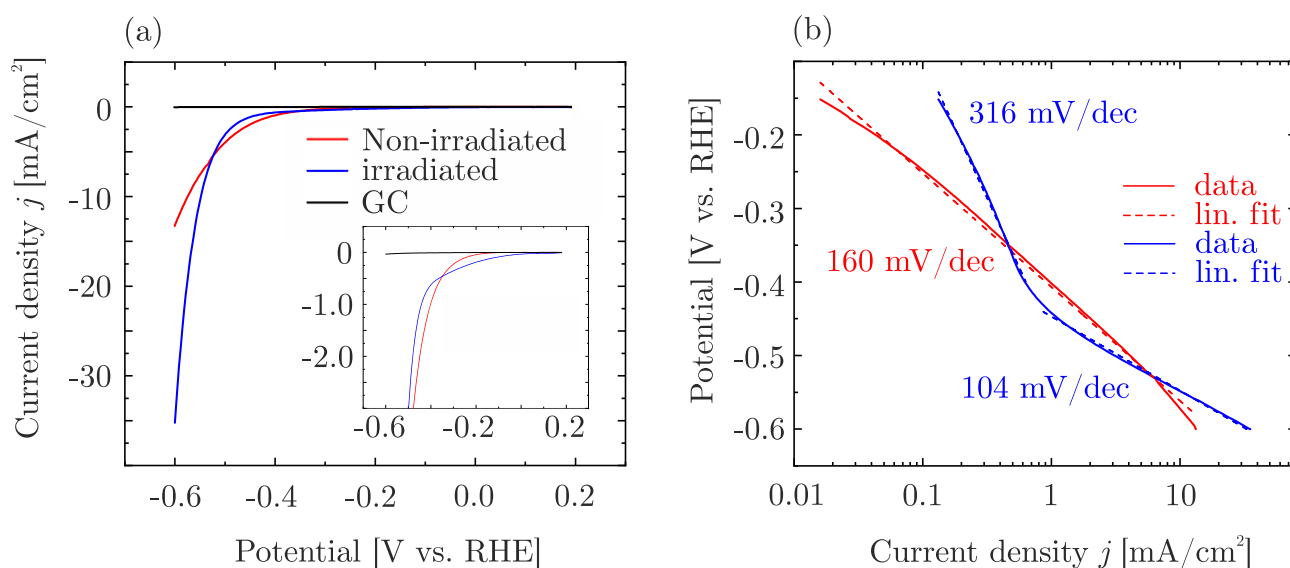
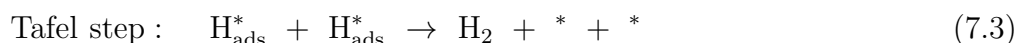
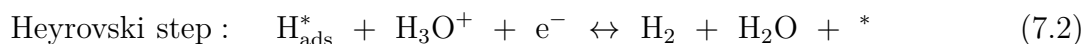
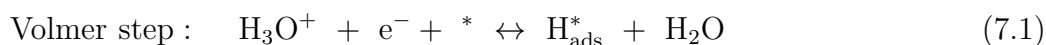


Figure 7.5: HER measurements of non-irradiated (red) and irradiated (blue) MoS₂. Glassy carbon (GC) has been used as a substrate (black). Ion fluence was chosen as 40 ions/ μm^2 . (a) Current density as a function of the potential [V vs. RHE] during linear sweep voltammetry measurements. (b) Tafel plot of respective data in (a). Reproduced with permission. Published by The Royal Society of Chemistry [100].

The measured current can also be related to an interfacial electrocatalytic reaction rate $\nu = jnF$, where n describes the number of electrons being involved in the process and F the Faraday constant. The reaction rate ν may be composed of several individual reaction steps which are shown below in eqs. 7.1, 7.2, and 7.3:



The complete hydrogen evolution reaction can now be described as a combination of either Volmer-Heyrovski or Volmer-Tafel steps. In the former case, a hydronium ion adsorbs at a catalytically active site and is reduced to a neutral hydrogen atom while releasing water (Volmer step). Subsequently, a second reaction involving the adsorbed hydrogen atom and another hydronium ion takes place leading to the generation of hydrogen gas and clearing the initial adsorption sites (Heyrovski step). The latter case describes two Volmer steps occurring one after another and two adsorbed hydrogen atoms being released as hydrogen gas (Tafel step). Due to the different reaction kinetics of Volmer-Heyrovski and Volmer-Tafel, the slope of the measurement curves differs. By plotting the potential [V. vs. RHE] against a logarithmically scaled current density as shown in Fig. 7.5 (b), the Tafel slope b can be obtained by linear fitting according to eq. 7.4 [323–325].

$$\log(-j) = \log(j_0) - \eta/b \quad (7.4)$$

Here, j represents the current density, j_0 is the exchange current density, b is the Tafel slope, and η is the overpotential. In case the Volmer step (which is common to both mechanisms) is the rate determining step, the Tafel slope usually takes a value in the range of 120 mV/dec. If the Heyrovski or Tafel process are rate determining, a slope of 30-40 mV/dec will be obtained [324]. For non-irradiated MoS₂, we measured a Tafel slope of 160 mV/dec which is in good agreement to values reported in literature. Irradiated MoS₂, however, shows two independent regions with different Tafel slopes. Due to the problematic of capacitive effects in the low overpotential regime for $-0.4 \text{ V} < \eta < 0 \text{ V}$, this region shall not be considered further. For a $\eta < -0.4 \text{ V}$, the Tafel slope takes a value of 104 mV/dec, which indicates an improved reaction kinetics and hints towards the Volmer-Tafel process taking place [288, 324–326].

Conclusion of Chapter 7 and Outlook for Chapter 8

The chemical structure of SHI induced defects in single-layer MoS₂ was investigated. MD und TTM calculations suggest the formation of under-coordinated Mo atoms near SHI impact positions as well as a depletion of S atoms right next to and in vicinity of the ion track. XPS measurements have confirmed the outcome of the simulations and allow a fact-based statement that electronic excitation via SHI irradiation (and most likely also via HCl irradiation) create Mo-enriched/S-depleted defects which has been shown to be beneficial for a high water permeabilities through porous MoS₂. Eventually, the catalytic properties of pristine and defective MoS₂ were characterized by linear sweep voltammetry measurements. The hydrogen evolution reaction for SHI modified MoS₂ shows a significantly enhanced activity due to an increased amount of under-coordinated Mo atoms.

In order to further understand the concept of defect formation for SHI modified MoS₂ and

how the defect structures change when irradiation conditions are altered, a closer look is given to the influence of the irradiation angle with respect to the surface, the substrate, and the number of MoS₂ layers.

8 Defect Engineering of MoS₂

Abstract - The introduction of defects via ion irradiation is a well-known and powerful method for controllable and adjustable material modifications. It may be used to boost electrical performance by introducing dopants into the bulk material, to increase chemical reactivity by increasing the number of catalytically active defects or to perforate thin membrane layers for applications in membrane science as has been shown in the previous chapters. It is therefore of particular interest to study different irradiation conditions and their implications on the defect formation in MoS₂. Both the angle of incidence and the layer number will be shown to play crucial roles for the defect introduction in MoS₂ during SHI irradiation. Varying the former parameter turns out to be a practical alternative to adjust pore sizes, whereas the latter one restricts the suitability of multi-layered MoS₂ membranes.

Parts of the following chapter are an adaptation of ref. [31] and have been reprinted with permission from Madauß, L. *et al.*, Defect engineering of single- and few-layer MoS₂ by swift heavy ion irradiation. *2D Mater.* **4**, 015034 (2017), <http://doi.org/10.1088/2F2053-1583/2F4/2F1/2F015034>. Published by IOP Publishing. Text passages that are reproduced literally are set in quotation marks.

8.1 Tuning Defect Modifications in Single-Layer MoS₂ via SHI Irradiation Conditions

Yielding defective 2D TMDCs (here MoS₂) can be realized via several methods. Especially point-like defects can be introduced easily by, *e.g.*, keV-ion [327] and electron [328] irradiation or plasma treatment [329]. As could be shown in previous chapters, SHI irradiation presents a powerful tool to create round-shaped pores in suspended single-layer MoS₂ when perpendicular irradiation is used or extended slit-like defects in substrate supported single-layer MoS₂ in case of grazing incidence irradiation.

The latter irradiation condition can also be used to create extended defect modifications in other materials, *e.g.*, strontium titanate [330], narrow, one-atom deep trenches in silicon carbide [331], or foldings and other defect structures in graphene [32, 332]. How the angle of incidence θ influences the defect length L will be presented in the following. For this, various single-layer MoS₂ flakes on SiO₂ were irradiated and the length of the defects (blue data points) as well as of the bare SiO₂ substrate (green data points) measured by AFM.²⁰ Their length with respect to θ is presented in Fig. 8.1. It is apparent that a decreasing θ leads to longer defects both in the single-layer MoS₂ and the bare substrate. The vanishing difference in defect size dependency on θ for SiO₂ supported MoS₂ and bare SiO₂, however, points towards the substrate as a major driving force for defect creation. The same conclusion is made when fitting the experimental data according to eq. 8.1

$$L = d_{\text{eff}}/\tan\theta, \quad (8.1)$$

with L being the track length, θ representing the angle of incidence, and d_{eff} being a fitting parameter yielding 4.5 nm for MoS₂ and 5.4 nm for SiO₂ data. A schematic visualization of the geometry is given in the inset of Fig. 8.1. Knowing that an SHI deposits energy in a cylindrical volume with a decreasing energy density for larger distances perpendicular to its trajectory, the ion eventually reaches a depth at which the distance to the surface is too great such that surface modifications will no longer be observable (end of track length L). A simple geometrical relation allows to fit the experimental data according to eq. 8.1 such that the effective depths d_{eff} can be obtained. "The key point here, however, is that d_{eff} is considerably larger than the actual thickness of single-layer MoS₂ which is ≈ 1 nm. It is therefore evident that the processes yielding incisions in supported single-layer MoS₂ cannot take place exclusively in the MoS₂ but must occur mainly in the substrate material."

The substrate does play a decisive role, but it is by no means a prerequisite for extended defect creation. STEM-MAADF images from suspended single-layer MoS₂ irradiated with SHI

²⁰Irradiations and measurements of the defect lengths were performed by Dr. Oliver Ochedowski and Dr. Sevilay Akçöltekin for MoS₂ and SiO₂, respectively. MoS₂ rift length dependency was discussed in ref. [193] for the first time.

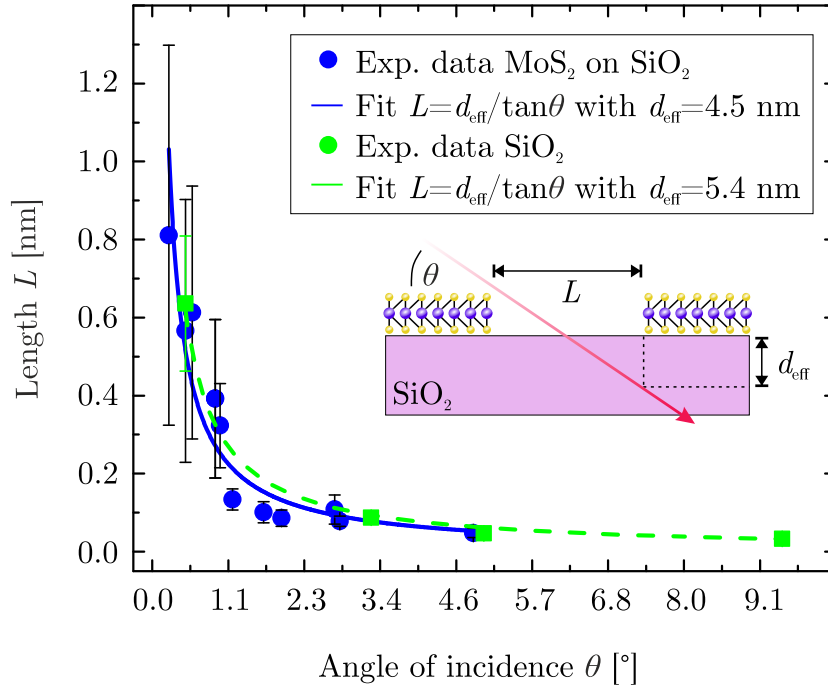


Figure 8.1: Length L of surface modifications in MoS₂ supported by SiO₂ and bare SiO₂ after grazing incidence SHI irradiation. A decreasing angle θ results in longer modifications which are almost equally sized. Reproduced with permission. Published by IOP Publishing [31].

under grazing incidence are presented in Fig. 8.2.²¹ Similar to substrate supported MoS₂, rifts oriented along the direction of the incoming ion beam can be observed in Fig. 8.2 (a). However, they are much shorter compared to rifts in SiO₂ supported MoS₂ (typical length of 100 nm, *i.e.*, about one order of magnitude shorter). "Atomically resolved images (Fig. 8.2 (c)) show that the incisions are extremely narrow (less than 10 nm) and with relatively straight edges on an atomic scale. Surprisingly, the surrounding lattice remains basically undisturbed despite the violent atomic displacements that have taken place inside the ion track core." A similar feature which was discussed in previous chapters are the polycrystalline clusters (bright, round features) that once again have formed after SHI irradiation (with a lattice spacing between 2.8 and 3.2 Å, consistent with them being Mo clusters [333]). The possibility of controlling pore sizes in single-layer MoS₂ by adjusting the angle of incidence can be very beneficial during ion beamtimes as it presents a well-controllable and easy tool to tune pore sizes. The necessity of using SHIs with a large dE/dx in order to create bigger pores may be circumvented by simply varying the angle of incidence. Still, this approach is only feasible when the intent is to increase pore sizes. To obtain smaller defects perpendicular irradiation with an appropriate choice of ion type and properties are inevitable.

²¹STEM images were recorded by Assoc. Prof. Dr. Jani Kotakoski and Dr. Mukesh Tripathi - University of Vienna, Physics of Nanostructured Materials, Boltzmanngasse 5, 1090 Vienna, Austria

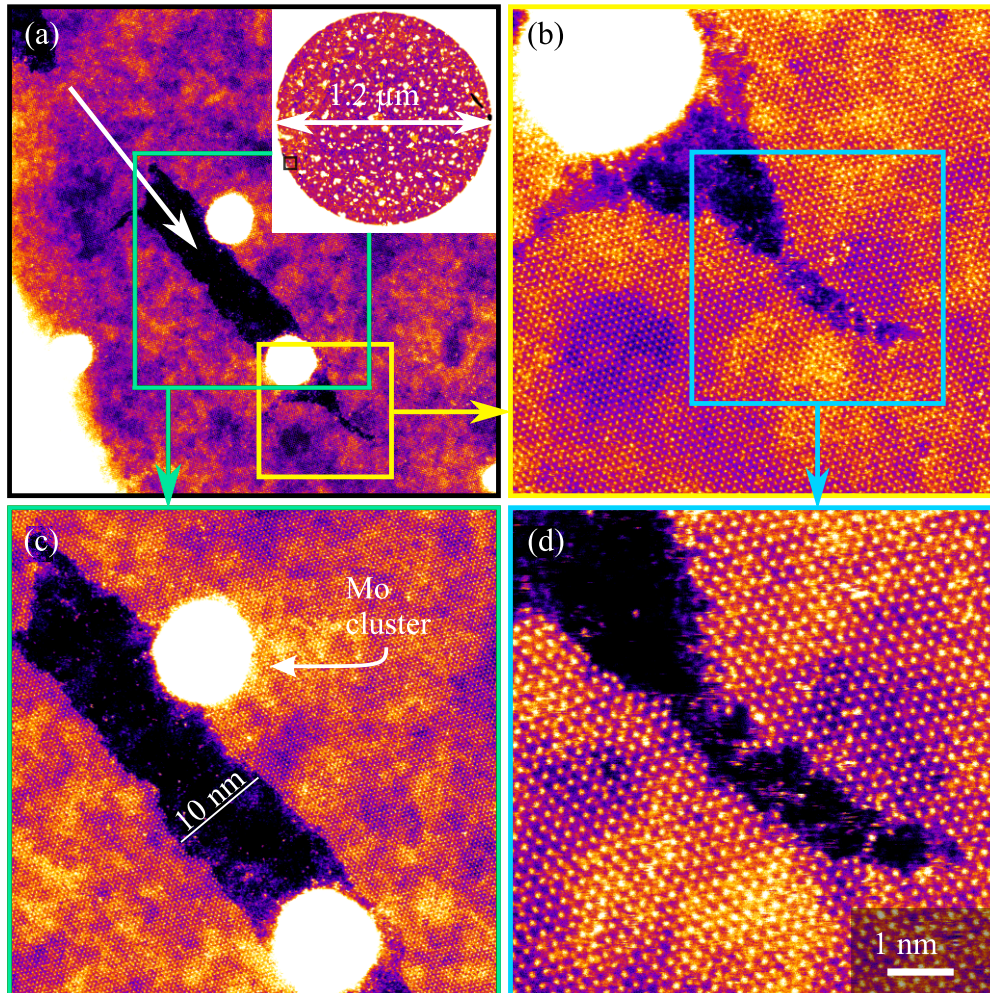


Figure 8.2: STEM-MAADF of irradiated (91 MeV Xe, angle of incidence $\theta \leq 0.2^\circ$) single-layer MoS₂ suspended over 1.2 μm large holes as shown in the inset in (a). The black scratch seen in (a) and (b) is a part of an incision cut into the MoS₂ sheet by the projectile. The part visible in (a) and (b) is roughly 20 nm long. The round white spots are polycrystalline Mo clusters which have formed due to ion bombardment. (b)-(d) Atomically resolved images of the incision show that the MoS₂ lattice outside of the ion track remains intact. Reproduced with permission. Published by IOP Publishing [31].

8.2 Thickness Dependent Defect Types in MoS₂: From Rifts to Hillocks

2D materials utilized as a filter have many advantages over their 3D bulk counterpart. One weak point of them though is the risk of rupture which usually results in a disproportionately large defect. When being supported by a porous support material with much larger pores than the ones in the 2D material, a ruptured or collapsed part of the 2D material represents nothing less than a bypass for the fluid and compromises the suitability of the whole membrane. The risk of rupture can certainly be minimized by reducing the size of the unsupported 2D membrane area to only a few μm^2 , but some applications require hundreds of μm^2 suspended, ultrathin, and porous materials. One possibility to overcome this problem is to use few-layer 2D materials which are mechanically more stable. Their interaction with grazing incidence SHI irradiation will be investigated with the help of exfoliated MoS₂ crystals, which are often conveniently pieced together by several layers of varying thickness and hence more suitable for fundamental research experiments.

Several positions with different layer numbers of the same MoS₂ crystal shown in Fig. 8.3 (a) are analyzed after exposing the sample to ¹²⁹Xe 0.71 MeV/u ions at a constant angle θ of 1° with respect to their surface. Height histograms of the positions marked with red and blue squares in (a) are presented in (b) and (c), respectively. The first height step from the substrate to the first layer accounts for 1.6 nm which deviates from the theoretical value of 0.65 nm but can easily be explained by intercalated water located only between the first layer and the substrate [334, 335]. The other height steps show the expected value of 0.65 nm. More detailed AFM images of different thicknesses (single-, bi-, tri-, multi-layer and bulk MoS₂) and their respective defect structures are presented in (d)-(f).²² It is interesting to note that the form of the defects changes from foldings (for single-layer) to continuous slits (for bi-layer) to discontinuous slits (for tri-layer). Note that foldings in single-layer MoS₂ are not the common defect type but only appear under special irradiation conditions which were coincidentally given for this irradiation [31]. Regular, continuous slits are the usual defect type encountered for single-layer MoS₂ irradiated at grazing angle as well. Further increase of the layer number (4-5 layers in (e)) results in more or less continuous slits with higher nanodots along the trajectory of the ion. These dots (in the following referred to as hillocks) are the dominating feature when dealing with irradiated bulk MoS₂ as shown in (f). Here, the the ion tracks are composed of well-separated and individual hillocks.

²²AFM measurements (a),(d)-(f) were performed by Dr. Oliver Ochedowski and discussed in ref. [193] for the first time.

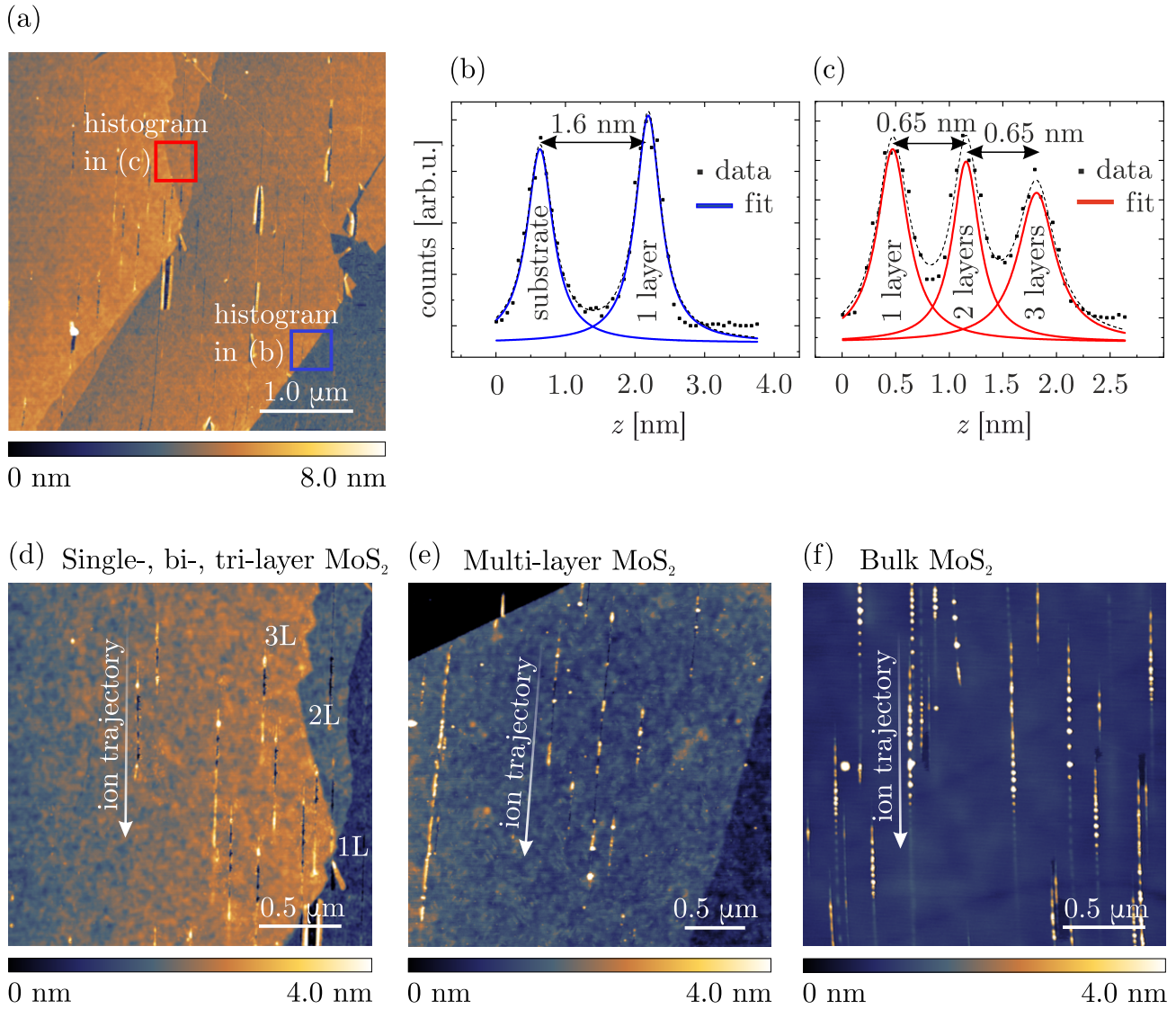


Figure 8.3: Layer thickness dependency of surface modifications in MoS₂ after grazing incidence SHI irradiation. (a) AFM overview image with respective height distributions in (b) for substrate/single-layer and (c) for single-, bi-, and bi-, tri-layer MoS₂. (d) Single-, bi-, trilayer MoS₂, (e) multi-layer MoS₂, and (f) bulk MoS₂ shows incisions/foldings, hillocks/incisions, and hillocks after SHI irradiation, respectively. Reproduced with permission. Published by IOP Publishing [31].

It can be concluded that MoS₂ crystals, which are considerably thicker than four to five layers, are unsuitable for being utilized as a membrane material if the intent is to apply SHI irradiation for perforation. Their layer number is the critical property which will most likely prevent the formation of continuous rifts or defects. Even though results may be turn out differently for perpendicular irradiation conditions, the possibility of obtaining pores similar to those in single-layer MoS₂ is quite unlikely.

Even though bulk MoS₂ does not yield open rifts when irradiated with SHI under grazing incidence, its defect formation is still interesting from a fundamental point of view as it results from an undisturbed interaction of the material and the ion without being influenced or altered by an underlying substrate. It can very well be used as a model system to study the interaction of SHIs with MoS₂ and results can be adapted for thinner layers as well.

8.3 Formation of Hillocks and Blisters in Bulk MoS₂

Exfoliated bulk MoS₂ crystals of several hundreds of nanometer thickness were irradiated with ¹²⁹Xe 0.71 MeV/u ions under grazing angles θ with respect to the sample's surface (θ was changed consecutively between values of 3° and 0.2°). Defect modifications, their sizes and geometries were analyzed by AFM using the PeakForce Tapping[®] mode (refer to section 3.3.2 on p. 48 for information about the measurement technique) and are presented in Fig. 8.4. MoS₂ crystals irradiated at larger θ , *e.g.*, 3° in Fig. 8.4 (a), display rather short incisions along the ion trajectory. With decreasing θ hillocks as the ones shown before in Fig. 8.3 (f) begin to appear. For angles including and below 0.6° with respect to the surface, the point where the ions enters the MoS₂ often results in the formation of a large bulge (in the following referred to as *blister*) followed by a chain of smaller hillocks. A representative AFM image is presented in 8.4 (b). The distance of the hillocks and length of the overall surface modification track further increases with decreasing θ , as shown for MoS₂ irradiated at $\theta = 0.2^\circ$ in Fig. 8.4 (c). The dependency of the hillock distance Δx_{hill} on θ is presented in Fig. 8.4 (d) (blue filled squares). An explanation for this result is that a pronounced interaction between SHI and MoS₂ only occurs in regions with a high electron density, which is only provided within a S-Mo-S layer. Neighboring S-Mo-S layers solely interact via van-der-Waals bonding. By reducing θ , the lateral distance of these passage-points of SHI and dense electron volumes increases. The distance of defects or surface modifications such as the observed hillocks, which are a direct result of the large deposited energy of the ion, will increase accordingly. Comparing the experimental data with theoretical predictions under the assumption that the hillock distance can be calculated via a geometrical relation according to $\Delta x_{\text{hill}} = a * \tan(90 - \theta)$ (see inset in Fig. 8.4 (d)), the respective dependencies for experimental (blue filled squares) and theoretical data (black line) are obtained. Here, a takes a value of 0.65 nm and represents the nominal thickness of

a single-layer MoS₂. Due to a limited accuracy during the experiment (mounting of samples, adjusting ion beam, roughness of samples) θ may vary by $\pm 0.25^\circ$. Assuming an initial offset by $+0.2^\circ$ and plotting every data point adjusted by the same -0.2° (blue hollow squares), the modified experimental data can be described by the geometrical relation quite well.

In accordance to an increase in hillock distance for smaller θ , so can an overall longer track length L be observed as shown in Fig. 8.4 (e). Here, the track length L is defined as the distance of the first surface modification and the last one generated by the same ion (see schematic in Fig. 8.4 (e)). The dependence of L may be described by the same relation which was already used to fit the track length in single-layer MoS₂: $L = d_{\text{eff}} * \tan(\theta)$. The best fit is achieved for a d_{eff} of 4.5 nm. As mentioned before, d_{eff} can be understood as the maximum depth of the SHI inside the material where a modifications can still be visualized at the surface. Likewise in terms of membrane perforation, this value represents the max. thickness of MoS₂ which could theoretically result in a continuous defect structure under grazing incidence irradiation. This consideration presumes that SHIs cannot displace MoS₂ bulk atoms along its trajectory such that something comparable to a hollow channel in the irradiated material is formed but material has to be sputtered off the crystal or ripped apart to result in a continuous defect structure. Given the fact that this analysis was performed with bulk material and that MoS₂ layers, which are supposed to serve as a membrane, are typically suspended, the value of 4.5 nm may turn out larger, since material can then be ejected upwards and downwards.

Still, little is known about the exact nature of these modifications. To investigate their mechanical properties in greater detail, their stiffness and indentation is compared to their topography. As mentioned before in section 3.3.2 on p. 48, PeakForce Tapping[®] can characterize several material properties simultaneously which allows a better comparison of the acquired data without having to deal with inaccuracies or modifications of the sample resulting from multiple individual measurements. Fig. 8.5 presents the (a) topography, (b) stiffness, and (c) indentation of a representative MoS₂ bulk sample after grazing incidence irradiation (stiffness and indentation values have to be viewed as qualitative measures since no calibration of the mechanical properties of the tip was performed prior to the measurements). It is worth noting that blisters show highly reduced stiffness compared to non-irradiated MoS₂ areas despite a constant peak force suggesting a hollow volume underneath the blisters. Equivalently, the blisters' indentation is much larger than that of non-irradiated areas. Further analysis reveals that the indentation of the blisters is nearly twice as large as the height of them. The extreme excitation of the MoS₂ due to SHI irradiation accompanied by a sudden sublimation of the material and an increase in vapor pressure appear to push the material upwards creating these blisters and hillocks with a size of up to 35 nm as shown in the linescan in (d). This observation is supported by the fact that only areas bombarded by SHI show a slightly elevated height compared to pristine parts of the samples as verified by the linescan in (a) whose profile is shown in (e). Even though TMDCs are notorious for having water creeping underneath them which can explain an increase in thickness in certain cases, this assumption is very unlikely to

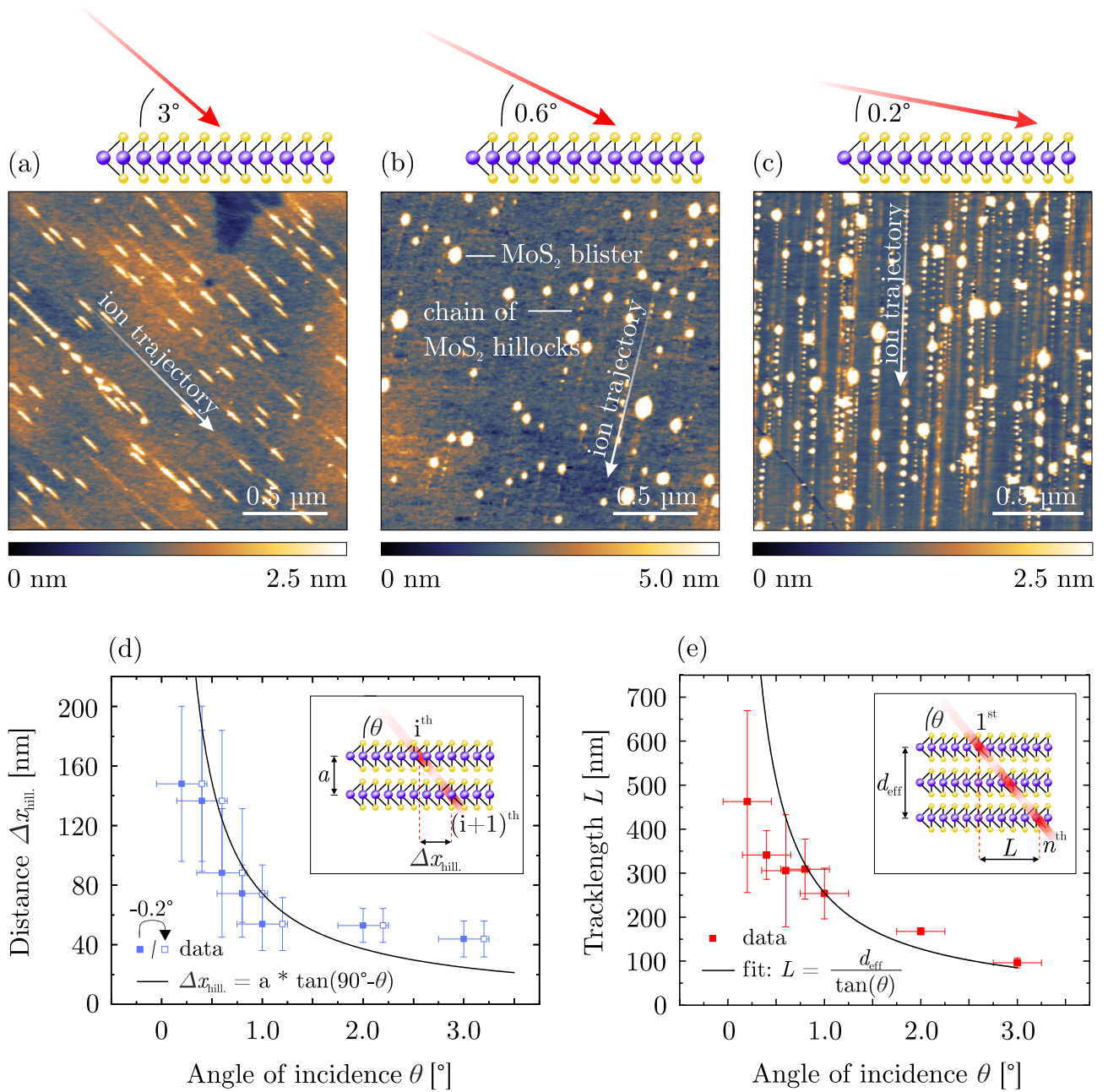


Figure 8.4: AFM images of SHI irradiated bulk MoS₂ under 3° in (a), 0.6° in (b), and 0.2° in (c) with respect to the surface. (d) Evaluation of hillock distance Δx_{hill} as a function of irradiation angle θ . Schematic visualization of Δx_{hill} is shown in the inset of (d). (e) Evaluation of total track length of the hillock chain L as a function of irradiation angle θ . Schematic visualization of L is shown in the inset of (e).

be the reason here. Firstly, previous measurements have shown that the height of single-layer MoS₂ is usually elevated by 1 nm which approximately corresponds to one or two atomic layers of water [336], whereas a step height twice as high was measured here. Secondly, the high density of ion impacts and hence the perforation of the material would promote an area-wide accretion of water underneath the MoS₂ which would not be limited to the immediate proximity of the ion impacts as is the case here.

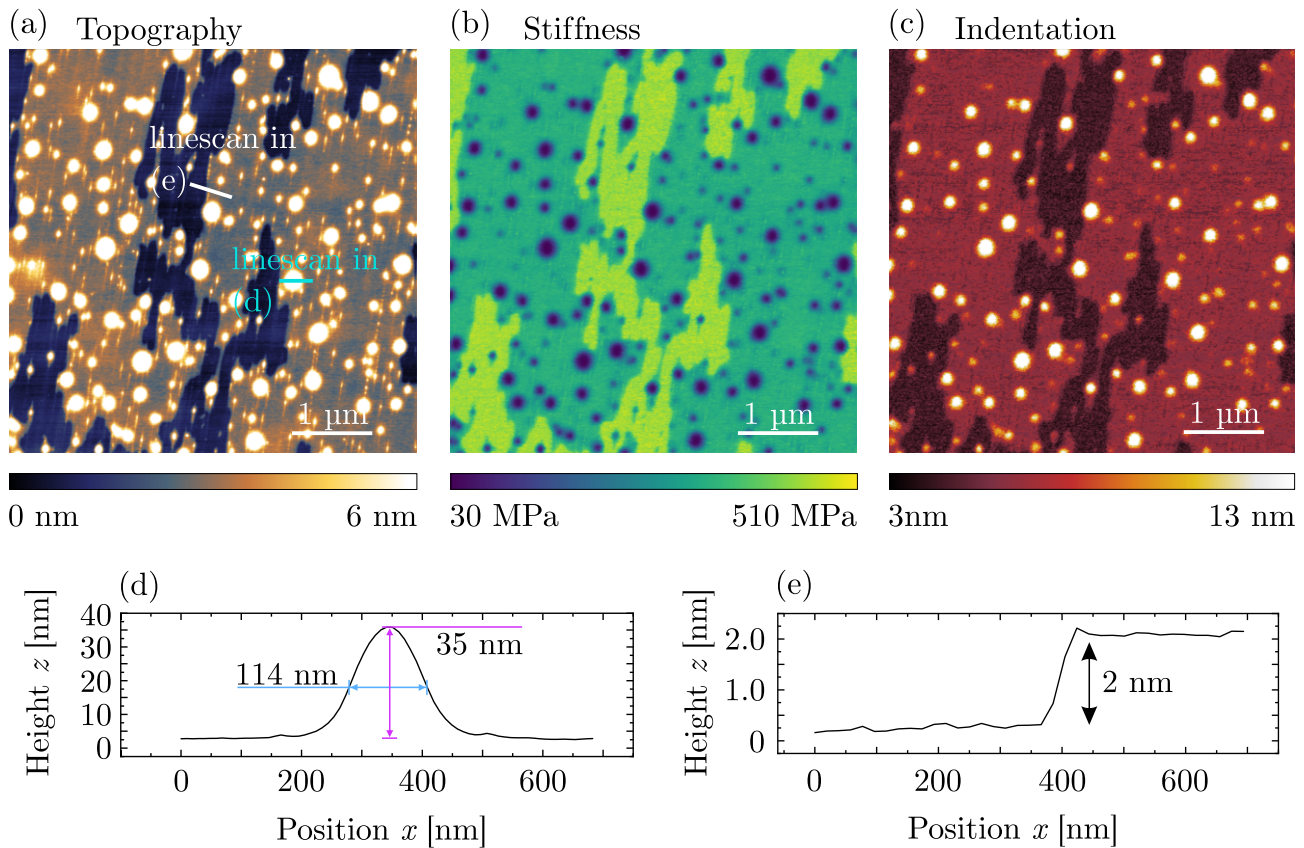


Figure 8.5: AFM analysis of blister formation in bulk MoS₂ after SHI irradiation. Topography, stiffness, and indentation channel shown in (a), (b), and (c), respectively. Linescans in (d) and (e) correspond to marked locations in (a).

Conclusion of Chapter 8

The influence of θ , the presence of a substrate, and the layer thickness of exfoliated MoS₂ on the defect formation during SHI irradiation was investigated. Section 8.1 showed that the length of ion tracks in MoS₂ can be tuned by changing the irradiation angle where smaller angles (with respect to the surface) result in longer defect structures. For substrate supported MoS₂, the dimensions of the modifications are significantly influenced by the underlying substrate but are also observable for suspended material.

Sections 8.2 and 8.3 showed, that increasing the thickness of the MoS₂ results in different defect structures when being irradiated with SHIs. A clear transition from continuous slits to discontinuous slits/hillocks to hillocks only is noticeable for single-layer, few-layer, and bulk MoS₂, respectively. This also limits the possible thickness of multi-layer MoS₂ membranes which are supposed to be perforated by SHI. MoS₂ consisting of significantly more than four to five layers will be difficult to perforate by SHI irradiation. Note that the thickness-dependent experiments were performed with substrate supported MoS₂, which likely behaves differently than unsupported material. Atoms of suspended MoS₂ can be ejected in both directions (upwards and downwards) after SHI impact whereas supported MoS₂ can only sputter upwards. It is not unreasonable to assume that continuous slits or pores are achievable in multi-layer MoS₂ as well if irradiation is performed on suspended MoS₂. However, bulk MoS₂ will most likely behave equally during irradiation whether being supported by a substrate or not.

9 Summary & Outlook - Future of 2D Membranes

The following chapter gives a brief summary of the experiments described in previous chapters and the know-how obtained from those. The focus, however, lies on possible future experiments with respect to 2D membranes which can profit from the progress that has been made during this thesis.

A surface modification technique was introduced in chapter 4, which is based on adsorption of acetate functional groups to the graphene layer by gently pressing an ethylene-vinyl acetate copolymer foil against it. Decorating graphene with these acetate groups results in a reduced interaction of the graphene layer with water during wet-chemical transfer steps allowing a polymer-free transfer and yielding continuous and nearly defect-free graphene free of contaminants. This approach promises more precise pore size and pore creation efficiency studies via TEM in future experiments, especially in terms of ion irradiation studies of graphene as schematically indicated in Fig. 9.1. The improved transfer allows the preparation of cleaner graphene and without the troubling polymer contaminations which have been prohibiting meaningful TEM experiments in the past. Aside from this, the transfer approach may also be used to prepare various porous polymer/graphene composite membranes which can later on be perforated by any method available.

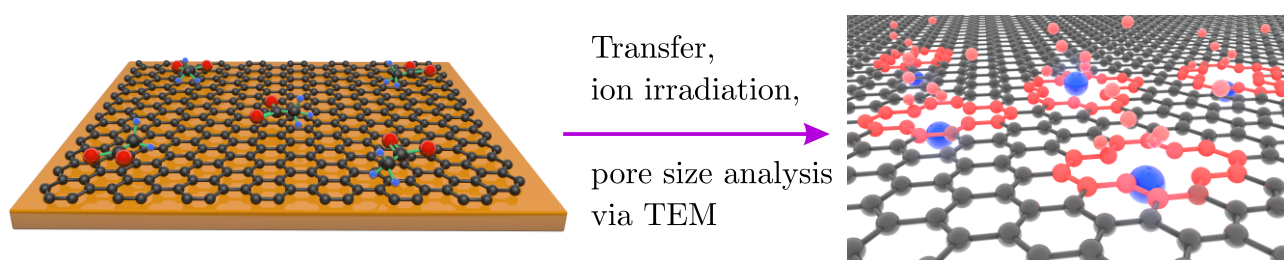


Figure 9.1: Schematic of surface energy modified graphene enabling clean transfer and preparation of suspended graphene for ion irradiation and subsequent TEM analysis.

The thesis then focused on graphene oxide and its applicability to serve as a proton conducting membrane in chapter 5. Hydronium ions showed increased diffusivity over hydroxide ions due to an energetically favored transport via the Grotthuss mechanism and weaker interaction with GO's functional groups. Additionally, the layered structure of GO membranes enables the incorporation of various materials (*e.g.*, nanoparticles or single-layer MoS₂) within its layers [268]. Due to GO membranes' small thickness, both the GO and the integrated material (*e.g.*, single-layer MoS₂), may be modified by SHI irradiation, which would allow to fabricate catalytically active MoS₂ layers already embedded within a membrane structure.

Other 2D materials were recently characterized in terms of their proton conductivity as well. Atomically thin hexagonal boron nitride (hBN) showed exceptional properties during those studies, but measurements were as so often restricted by the small size of exfoliated layers [337]. To overcome this problematic, preliminary experiments addressing the preparation of large-scale CVD hBN were performed during this thesis as well.²³ Fig. 9.2 presents optical (a) and AFM images (b)-(c), as well as XPS measurements of cm²-large hBN. Even though the 13 nm thick multilayer hBN shows increased roughness (RMS value of 2.4 nm), a polymer-free transfer was developed yielding extremely clean hBN as verified by XPS data and allowing first large-scale proton conductivity characterization of CVD hBN in the future.

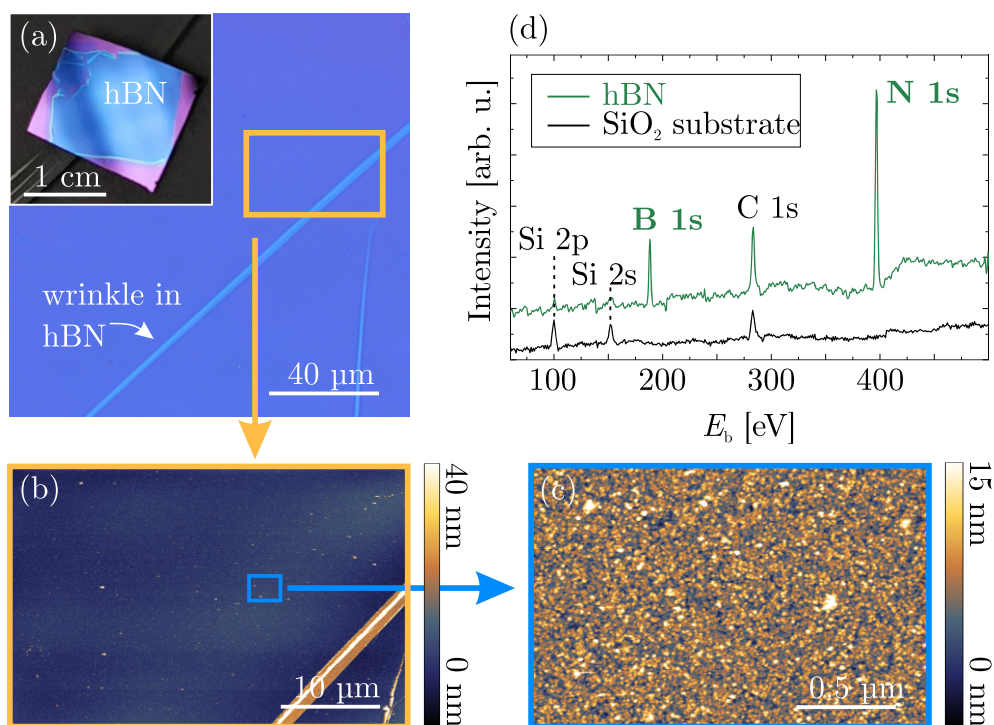


Figure 9.2: (a) Optical image of hBN transferred onto SiO₂ substrate. (b), (c) AFM measurements of hBN. (d) XPS spectrum of hBN on SiO₂ and bare SiO₂.

²³Parts of the data shown in Fig. 9.2 were acquired as part of the M.Sc. thesis *Herstellung großflächiger zweidimensionaler Heterostrukturen mit Hilfe polymerfreier Transfermethoden* by Mr. Lukas Kalkhoff (University of Duisburg-Essen, 2020) who I had the privilege to supervise.

MoS₂ is another interesting candidate for membrane applications. The influence of ion irradiation was studied in chapter 6 and 7 revealing HCI and SHI irradiation to be powerful tools for perforation of suspended single-layer MoS₂. Narrow pore size distributions, customisable pore sizes, Mo-enriched pore edges, and easily adaptable pore densities are realizable. The range of E_{pot} investigated in this thesis resulted in pores with a radius between 0.5 and 2.6 nm. Significant further increase in pore sizes will be hardly achievable with HCI irradiation. Even though a fully ionized Xe⁵⁴ atom with a E_{pot} greater than 200 keV would theoretically be able to create pores with a diameter of 25 nm according to the relation obtained in Fig. 6.6, irradiation times would increase significantly calling for a more efficient and rather industrially constructed HCI source than the one used here (note that these ion sources do exist and are commercially available). SHI irradiation on the contrary is already a commonly used technique for material modification, for example track-etched membranes. Irradiations with very heavy ions (e.g., uranium (U) or lead (Pb)) with a E_{kin} close to their respective Bragg-peak) are not uncommon and used on a regular basis at large irradiation facilities. 1.5 GeV ²³⁸U irradiation for example would yield single-layer MoS₂ pores with a diameter of nine nm. Combining the properties of both ions to perforate 2D materials with *highly-charged-swift-heavy ions* (experimental conditions are given at the GSI) may even further increase the range of obtainable pore sizes and pore creation efficiencies up to 100 %.

Preliminary experiments performed during this thesis aiming for large-area, single-layer MoS₂ membranes are shown in Fig. 9.3. The schematics in (a) and (b) visualize the preparation process. A porous Si₃N₄ grid is covered by MoS₂. The synthesis of continuous MoS₂ was realized with the CVD process presented in section 2.4.2 on p. 27. Raman mappings (intensity of A_{1g} mode shown here) allow an exact quantification of (un-)ruptured MoS₂ revealing potentially uncovered Si₃N₄ pores. The intensity pattern of the Raman map accords with the pore pattern of the substrate indicating a fully covered membrane area of 200 x 100 μm². Future perforation experiments with HCIs or SHIs followed by filtration tests will show whether 2D MoS₂ meets the expectations in terms of permeability and filtration performance.

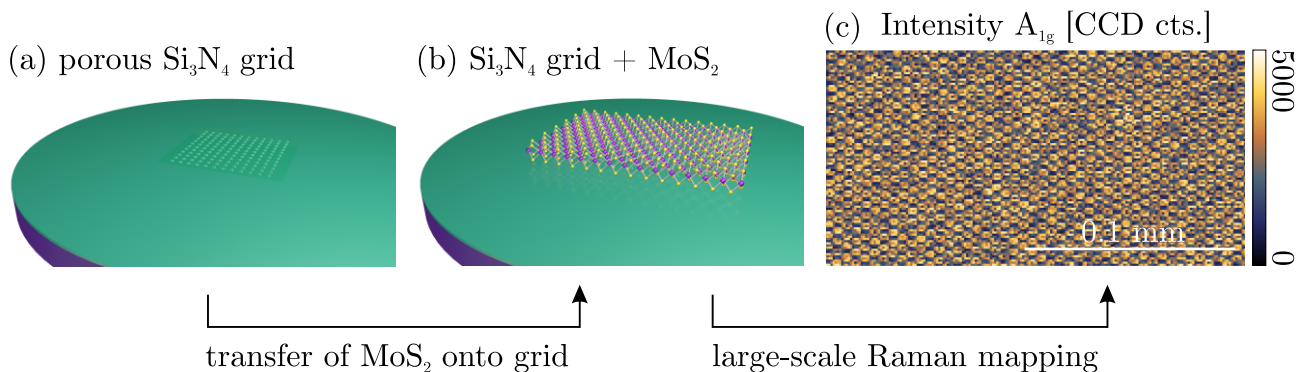
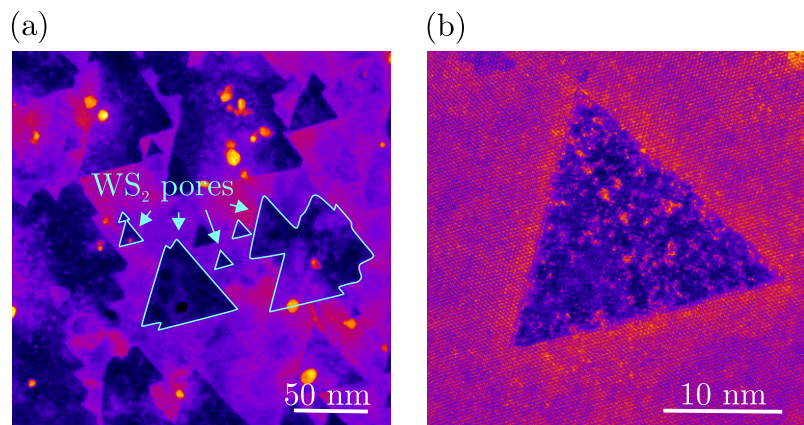


Figure 9.3: (a) Porous Si₃N₄ grids (2.5 μm hole diameter) can be used as support material for single-layer MoS₂. After transfer of MoS₂ onto the material (b), Raman spectroscopy can be used as an effective and precise tool to quantify the coverage (c).

The possibility to alter the geometry of defects in single-layer MoS₂ by tuning the angle of incidence during ion irradiation was found to be a fast and uncomplicated way to adapt pore sizes as shown in chapter 8. SHI perforation, however, should not be used for perforation when dealing with MoS₂ layer thicknesses close to 10 nm.

Aside from MoS₂ other materials may also be investigated in greater detail. HCI irradiation of, *e.g.*, single-layer tungsten disulfide (WS₂) creates considerably larger pores than those observable in single-layer MoS₂. Fig. 9.4 (a) presents a STEM image overview of a Xe³³⁺ perforated 2D WS₂ monolayer.²⁴ Despite an almost equivalent crystal lattice compared to MoS₂ with only the Mo atoms being replaced by W ones, it is intriguing why WS₂ forms triangular pore while pores in MoS₂ are round. The much larger pores which are observable in (a) and display edge lengths of 50 nm or more probably result from double HCI hits and can be avoided by choosing a lower ion fluence. Fig. 9.4 (b) shows the result of a single-ion impact. The pore's edge length is approximately 15 nm and its area easily exceeds those of single-layer MoS₂ even though irradiation was performed with a rather low charge state of only 33+. Additional experiments with varying charge states and other 2D materials could help identify suitable materials with precisely adjustable pores covering a pore size regime beyond what is achievable when utilizing single-layer MoS₂.

Figure 9.4: STEM images of Xe³³⁺ irradiated single-layer WS₂ images. (a) Overview of pores starting to overlap. (b) Single ion impact results in triangular pores.



²⁴STEM images were recorded by Assoc. Prof. Dr. Jani Kotakoski and Dr. Mukesh Tripathi - University of Vienna, Physics of Nanostructured Materials, Boltzmannngasse 5, 1090 Vienna, Austria

Bibliography

- [1] Liu, H. F., Ma, J., Winter, C. & Bayer, R. Recovery and purification process development for monoclonal antibody production. *mAbs* **2**, 480–499 (2010). URL <https://doi.org/10.4161/mabs.2.5.12645>.
- [2] Ronco, C. & Clark, W. R. Haemodialysis membranes. *Nat. Rev. Nephrol.* **14**, 394–410 (2018). URL <https://doi.org/10.1038/s41581-018-0002-x>.
- [3] Stamatialis, D. F. *et al.* Medical applications of membranes: Drug delivery, artificial organs and tissue engineering. *J. Membr. Sci.* **308**, 1–34 (2008). URL <https://doi.org/10.1016/j.memsci.2007.09.059>.
- [4] Lee, A., Elam, J. W. & Darling, S. B. Membrane materials for water purification: design, development, and application. *Environ. Sci.: Water Res. Technol.* **2**, 17–42 (2016). URL <https://doi.org/10.1039/C5EW00159E>.
- [5] Mohammad, A. W., Ng, C. Y., Lim, Y. P. & Ng, G. H. Ultrafiltration in food processing industry: Review on application, membrane fouling, and fouling control. *Food Bioproc* **5**, 1143–1156 (2012). URL <https://doi.org/10.1007/s11947-012-0806-9>.
- [6] Kotsanopoulos, K. V. & Arvanitoyannis, I. S. Membrane processing technology in the food industry: Food processing, wastewater treatment, and effects on physical, microbiological, organoleptic, and nutritional properties of foods. *Crit. Rev. Food Sci. Nutr.* **55**, 1147–1175 (2015). URL <https://doi.org/10.1080/10408398.2012.685992>.
- [7] Garraín, D., Lechón, Y. & La Rúa, C. d. Polymer electrolyte membrane fuel cells (PEMFC) in automotive applications: Environmental relevance of the manufacturing stage. *Smart Grid and Renewable Energy* **02**, 68–74 (2011). URL <https://doi.org/10.4236/sgre.2011.22009>.

- [8] Dziubak, T. & Dziubak, S. D. Experimental study of filtration materials used in the car air intake. *Materials* **13**, 3498 (2020). URL <https://doi.org/10.3390/ma13163498>.
- [9] Vinothkannan, M., Kim, A. R., Gnana kumar, G. & Yoo, D. J. Sulfonated graphene oxide/Nafion composite membranes for high temperature and low humidity proton exchange membrane fuel cells. *RSC Adv* **8**, 7494–7508 (2018). URL <https://doi.org/10.1039/C7RA12768E>.
- [10] Buonomenna, M. G. Membrane processes for a sustainable industrial growth. *RSC Adv* **3**, 5694–5740 (2013). URL <https://doi.org/10.1039/C2RA22580H>.
- [11] Ostadfar, A. *Biofluid Mechanics - Chapter 1: Fluid Mechanics and Biofluids Principles*, p. 32 within chapter (Academic Press, 2016). URL <https://doi.org/10.1016/C2014-0-01583-3>.
- [12] Wang, L. *et al.* Fundamental transport mechanisms, fabrication and potential applications of nanoporous atomically thin membranes. *Nat. Nanotechnol.* **12**, 509–522 (2017). URL <https://doi.org/10.1038/nnano.2017.72>.
- [13] Novoselov, K. S. *et al.* Electric field effect in atomically thin carbon films. *Science* **306**, 666–669 (2004). URL <https://doi.org/10.1126/science.1102896>.
- [14] Novoselov, K. S. *et al.* Two-dimensional gas of massless Dirac fermions in graphene. *Nature* **438**, 197–200 (2005). URL <https://doi.org/10.1038/nature04233>.
- [15] Joshi, R. K. *et al.* Precise and ultrafast molecular sieving through graphene oxide membranes. *Science* **343**, 752–754 (2014). URL <https://doi.org/10.1126/science.1245711>.
- [16] Zhou, K.-G. *et al.* Electrically controlled water permeation through graphene oxide membranes. *Nature* **559**, 236–240 (2018). URL <https://doi.org/10.1038/s41586-018-0292-y>.
- [17] Wen, Q. *et al.* Electric-field-induced ionic sieving at planar graphene oxide heterojunctions for miniaturized water desalination. *Adv. Mater.* **32**, 1903954 (2020). URL <https://doi.org/10.1002/adma.201903954>.
- [18] Andreeva, D. V. *et al.* Two-dimensional adaptive membranes with programmable water

- and ionic channels. *Nat. Nanotechnol.* (2020). URL <https://doi.org/10.1038/s41565-020-00795-y>.
- [19] Shinde, D. B., Vlassiuk, I. V., Talipov, M. R. & Smirnov, S. N. Exclusively proton conductive membranes based on reduced graphene oxide polymer composites. *ACS Nano* **13**, 13136–13143 (2019). URL <https://doi.org/10.1021/acsnano.9b05979>.
- [20] Liu, B. *et al.* A bismuth oxide/graphene oxide nanocomposite membrane showing super proton conductivity and low methanol permeability. *Chem. Sci.* **10**, 556–563 (2019). URL <https://doi.org/10.1039/C8SC03726D>.
- [21] Rimini, E. *Ion implantation: Basics to device fabrication - Chapter 7: Silicon Based Devices*, pp. 259-313, vol. 293 (Springer US, 1967). URL <https://doi.org/10.1007/978-1-4615-2259-1>.
- [22] Kozlov, V. A. & Kozlovski, V. V. Doping of semiconductors using radiation defects produced by irradiation with protons and alpha particles. *Semiconductors* **35**, 735–761 (2001). URL <https://doi.org/10.1134/1.1385708>.
- [23] Schleberger, M. & Kotakoski, J. 2D material science: Defect engineering by particle irradiation. *Materials* **11** (2018). URL <https://doi.org/10.3390/ma11101885>.
- [24] Krasheninnikov, A. V. & Nordlund, K. Ion and electron irradiation-induced effects in nanostructured materials. *J. Appl. Phys.* **107**, 071301 (2010). URL <https://doi.org/doi:10.1063/1.3318261>.
- [25] Aumayr, F., Facsko, S., El-Said, A. S., Trautmann, C. & Schleberger, M. Single ion induced surface nanostructures: a comparison between slow highly charged and swift heavy ions. *J. Phys. Condens. Matter* **23**, 393001 (2011). URL <https://doi.org/10.1088/0953-8984/23/39/393001>.
- [26] Fink, D. *Fundamentals of ion-irradiated polymers* (Springer-Verlag Berlin Heidelberg, 2004), 63 edn. URL <https://doi.org/10.1007/978-3-662-07326-1>.
- [27] Fink, D. *Transport Processes in Ion-Irradiated Polymers: Chapter 4: Ion-Track Etching*, pp. 147-193, vol. 65 (Springer-Verlag Berlin Heidelberg, 2004), 1 edn. URL <https://doi.org/10.1007/978-3-662-10608-2>.
- [28] Chen, C. *et al.* Refractive index engineering through swift heavy ion irradiation of LiNbO₃

- crystal towards improved light guidance. *Sci. Rep.* **7**, 10805 (2017). URL <https://doi.org/10.1038/s41598-017-11358-y>.
- [29] Madauß, L. *et al.* Fabrication of nanoporous graphene/polymer composite membranes. *Nanoscale* **9**, 10487–10493 (2017). URL <https://doi.org/10.1039/C7NR02755A>.
- [30] Ochedowski, O. *et al.* Nanostructuring graphene by dense electronic excitation. *Nanotechnology* **26**, 465302 (2015). URL <https://doi.org/10.1088%2F0957-4484%2F26%2F46%2F465302>.
- [31] Madauß, L. *et al.* Defect engineering of single- and few-layer MoS₂ by swift heavy ion irradiation. *2D Mater.* **4**, 015034 (2017). URL <https://doi.org/10.1088/2053-1583/4/1/015034>.
- [32] Ochedowski, O. *et al.* Folding two dimensional crystals by swift heavy ion irradiation. *Nucl. Instrum. Meth. B* **340**, 39–43 (2014). URL <https://doi.org/10.1016/j.nimb.2014.07.037>.
- [33] Heiranian, M., Farimani, A. B. & Aluru, N. R. Water desalination with a single-layer MoS₂ nanopore. *Nat. Commun.* **6**, 8616 (2015). URL <https://doi.org/10.1038/ncomms9616>.
- [34] Yin, K. *et al.* Generating sub-nanometer pores in single-layer MoS₂ by heavy-ion bombardment for gas separation: A theoretical perspective. *ACS Appl. Mat. Interfaces* **10**, 28909–28917 (2018). URL <https://doi.org/10.1021/acsami.8b10569>.
- [35] Z. F. Cui, Y. Jiang & R.W. Field. Chapter 1 - Fundamentals of Pressure-Driven Membrane Separation Processes, p. 3. In Z. F. Cui, H. S. Muralidhara (Hg.) *2010 – Membrane Technology*, 1–18. URL <https://doi.org/10.1016/B978-1-85617-632-3.00001-x>.
- [36] Baker, R. W. *Membrane Technology and Applications - Chapter 2: Membrane Transport Theory*, pp. 15-17 (John Wiley & Sons, Ltd., 2004), 2 edn. URL <https://doi.org/10.1002/0470020393.ch2>.
- [37] Wijmans, J. G. & Baker, R. W. The solution-diffusion model: a review. *J. Membr. Sci.* **107**, 1–21 (1995). URL [https://doi.org/10.1016/0376-7388\(95\)00102-I](https://doi.org/10.1016/0376-7388(95)00102-I).
- [38] Mehta, A. & Zydney, A. L. Permeability and selectivity analysis for ultrafiltration mem-

- branes. *J. Membr. Sci.* **249**, 245–249 (2005). URL <https://doi.org/10.1016/j.memsci.2004.09.040>.
- [39] Baker, R. W. *Membrane Technology and Applications - Chapter 10 : Ion Exchange Membrane Processes–Electrodialysis*, pp. 393–394 (John Wiley & Sons, Ltd., 2004), 2 edn. URL <https://doi.org/10.1002/0470020393.ch10>.
- [40] Ulbricht, M. Design and synthesis of organic polymers for molecular separation membranes. *Curr. Opin. Chem. Eng.* **28**, 60–65 (2020). URL <https://doi.org/10.1016/j.coche.2020.02.002>.
- [41] Wang, S. *et al.* Advances in high permeability polymer-based membrane materials for CO₂ separations. *Energy Environ. Sci.* **9**, 1863–1890 (2016). URL <https://doi.org/10.1039/C6EE00811A>.
- [42] Baker, R. W. *Membrane Technology and Applications - Chapter 1: Overview of Membrane Science and Technology*, pp. 1–14 (John Wiley & Sons, Ltd., 2004), 2nd edition edn. URL <https://doi.org/10.1002/0470020393.ch1>.
- [43] Akinwande, D. *et al.* A review on mechanics and mechanical properties of 2D materials—Graphene and beyond. *Extreme Mech. Lett.* **13**, 42–77 (2017). URL <https://doi.org/10.1016/j.eml.2017.01.008>.
- [44] Kim J. H., Jeong, Jeong, J. H., Joshi, R. & Lee, G.-H. Mechanical properties of two-dimensional materials and their applications. *J. Phys. D: Appl. Phys.* **52**, 083001 (2018). URL <https://doi.org/10.1088%2F1361-6463%2Faaf465>.
- [45] Lee, G.-H. *et al.* High-strength chemical-vapor deposited graphene and grain boundaries. *Science* **340**, 1073–1076 (2013). URL <https://doi.org/10.1126/science.1235126>.
- [46] Carraher Jr., Charles E., Seymour, R.B. *Structure—Property Relationships in Polymers - Chapter 5: Mechanical Properties of Polymers*, p. 64 (Springer US, 1984), 1 edn. URL <https://doi.org/10.1007/978-1-4684-4748-4>.
- [47] Miranda, A. & Lorke, A. Stability of suspended monolayer graphene membranes in alkaline environment. *Mater. Res. Lett.* **6**, 49–54 (2018). URL <https://doi.org/10.1080/21663831.2017.1390793>.

- [48] Stine, R., Lee, W.-K., Whitener, K. E., Robinson, J. T. & Sheehan, P. E. Chemical Stability of Graphene Fluoride Produced by Exposure to XeF₂. *Nano Lett.* **13**, 4311–4316 (2013). URL <https://doi.org/10.1021/nl4021039>.
- [49] Xue, M., Qiu, H. & Guo, W. Exceptionally fast water desalination at complete salt rejection by pristine graphyne monolayers. *Nanotechnol.* **24**, 505720 (2013). URL <https://doi.org/10.1088/0957-4484/24/50/505720>.
- [50] Lin, L.-C., Choi, J. & Grossman, J. C. Two-dimensional covalent triazine framework as an ultrathin-film nanoporous membrane for desalination. *Chem. Commun.* **51**, 14921–14924 (2015). URL <https://doi.org/10.1039/C5CC05969K>.
- [51] Cohen-Tanugi, D. & Grossman, J. C. Water desalination across nanoporous graphene. *Nano Lett.* **12**, 3602–3608 (2012). URL <https://doi.org/10.1021/nl3012853>.
- [52] Li, W., Yang, Y., Weber, J. K., Zhang, G. & Zhou, R. Tunable, strain-controlled nanoporous MoS₂ filter for water desalination. *ACS Nano* **10**, 1829–1835 (2016). URL <https://doi.org/10.1021/acsnano.5b05250>.
- [53] Zhang, X. & Gai, J.-G. Single-layer graphyne membranes for super-excellent brine separation in forward osmosis. *RSC Adv* **5**, 68109–68116 (2015). URL <https://doi.org/10.1039/C5RA09512C>.
- [54] Gai, J.-G., Gong, X.-L., Wang, W.-W., Zhang, X. & Kang, W.-L. An ultrafast water transport forward osmosis membrane: porous graphene. *J. Mater. Chem. A* **2**, 4023–4028 (2014). URL <https://doi.org/10.1039/C3TA14256F>.
- [55] He, Z., Zhou, J., Lu, X. & Corry, B. Bioinspired graphene nanopores with voltage-tunable ion selectivity for Na⁺ and K⁺. *ACS Nano* **7**, 10148–10157 (2013). URL <https://doi.org/10.1021/nn4043628>.
- [56] Shankla, M. & Aksimentiev, A. Molecular transport across the Ionic liquid–aqueous electrolyte interface in a MoS₂ nanopore. *ACS Appl. Mat. Interfaces* **12**, 26624–26634 (2020). URL <https://doi.org/10.1021/acсами.0c04523>.
- [57] Zhao, S., Xue, J. & Kang, W. Ion selection of charge-modified large nanopores in a graphene sheet. *J. Phys. Chem.* **139**, 114702 (2013). URL <https://doi.org/10.1063/1.4821161>.

- [58] Das, M. P., Thiruraman, J. P., Chou, Y.-C., Danda, G. & Drndić, M. Centimeter-scale nanoporous 2D membranes and ion transport: Porous MoS₂ monolayers in a few-layer matrix. *Nano Lett.* **19**, 392–399 (2019). URL <https://doi.org/10.1021/acs.nanolett.8b04155>.
- [59] Choi, K., Droudian, A., Wyss, R. M., Schlichting, K.-P. & Park, H. G. Multifunctional wafer-scale graphene membranes for fast ultrafiltration and high permeation gas separation. *Sci. Adv.* **4** (2018). URL <https://doi.org/10.1126/sciadv.aau0476>.
- [60] Liu, K., Feng, J., Kis, A. & Radenovic, A. Atomically thin molybdenum disulfide nanopores with high sensitivity for DNA translocation. *ACS Nano* **8**, 2504–2511 (2014). URL <https://doi.org/10.1021/nn406102h>.
- [61] Merchant, C. A. *et al.* DNA translocation through graphene nanopores. *Nano Lett.* **10**, 2915–2921 (2010). URL <https://doi.org/10.1021/nl101046t>.
- [62] Celebi, K. *et al.* Ultimate permeation across atomically thin porous graphene. *Science* **344**, 289–292 (2014). URL <https://doi.org/10.1126/science.1249097>.
- [63] O’Hern, S. C. *et al.* Selective ionic transport through tunable subnanometer pores in single-layer graphene membranes. *Nano Lett.* **14**, 1234–1241 (2014). URL <https://doi.org/10.1021/nl404118f>.
- [64] Surwade, S. P. *et al.* Water desalination using nanoporous single-layer graphene. *Nat. Nanotechnol.* **10**, 459–464 (2015). URL <https://doi.org/10.1038/nnano.2015.37>.
- [65] Boutilier, M. S. H. *et al.* Molecular sieving across centimeter-scale single-layer nanoporous graphene membranes. *ACS Nano* **11**, 5726–5736 (2017). URL <https://doi.org/10.1021/acsnano.7b01231>.
- [66] Landau, L. D. Bemerkungen über Umwandlungstemperaturen. *Helv. Phys. Acta* **7**, 81 (1934).
- [67] Peierls, R. Quelques propriétés typiques des corps solides. *Ann. Inst. Henri Poincaré* **5**, 177–222 (1935).
- [68] Landau, L. D. Zur Theorie der Phasenumwandlungen II. *Phys. Z. Sowjetunion* **11**, 26–35 (1937).

- [69] Mermin, N. D. Crystalline order in two dimensions. *Phys. Rev.* **176**, 250–254 (1968). URL <https://doi.org/10.1103/PhysRev.176.250>.
- [70] Mermin, N. D. & Wagner, H. Absence of ferromagnetism or antiferromagnetism in one- or two-dimensional isotropic heisenberg models. *Phys. Rev. Lett.* **17**, 1133–1136 (1966). URL <https://doi.org/10.1103/PhysRevLett.17.1133>.
- [71] Geim, A. K. & Novoselov, K. S. The rise of graphene. *Nat. Mater.* **6**, 183–191 (2007). URL <https://doi.org/10.1038/nmat1849>.
- [72] Meyer, J. C. *et al.* The structure of suspended graphene sheets. *Nature* **446**, 60–63 (2007). URL <https://doi.org/10.1038/nature05545>.
- [73] Banszerus, L. *et al.* Ballistic transport exceeding 28 μm in CVD Grown Graphene. *Nano Lett.* **16**, 1387–1391 (2016). URL <https://doi.org/10.1021/acs.nanolett.5b04840>.
- [74] Andrzejewski, D., Hopmann, E., John, M., Kümmell, T. & Bacher, G. WS₂ monolayer-based light-emitting devices in a vertical p–n architecture. *Nanoscale* **11**, 8372–8379 (2019). URL <https://doi.org/10.1039/C9NR01573F>.
- [75] Koenig, S. P., Wang, L., Pellegrino, J. & Bunch, J. S. Selective molecular sieving through porous graphene. *Nat. Nanotechnol.* **7**, 728–732 (2012). URL <https://doi.org/10.1038/nnano.2012.162>.
- [76] Moghadam, F. & Park, H. B. 2D nanoporous materials: membrane platform for gas and liquid separations. *2D Mater.* **6**, 042002 (2019). URL <https://doi.org/10.1088/2F2053-1583%2Fab1519>.
- [77] Zhu, J. *et al.* Boundary activated hydrogen evolution reaction on monolayer MoS₂. *Nat. Commun.* **10**, 1348 (2019). URL <https://doi.org/10.1038/s41467-019-09269-9>.
- [78] Sherrell, P. C. *et al.* Large-area CVD MoS₂/WS₂ heterojunctions as a photoelectrocatalyst for salt-water oxidation. *ACS Appl. Energ. Mater.* **2**, 5877–5882 (2019). URL <https://doi.org/10.1021/acsaem.9b01008>.
- [79] Kim, J. H., Jeong, J. H., Kim, N., Joshi, R. & Lee, G.-H. Mechanical properties of two-

- dimensional materials and their applications. *J. Phys. D: Appl. Phys.* **52**, 083001 (2018). URL <https://doi.org/10.1088%2F1361-6463%2Faaf465>.
- [80] Liu, K. & Wu, J. Mechanical properties of two-dimensional materials and heterostructures. *J. Mater. Res.* **31**, 832–844 (2016). URL <https://doi.org/10.1557//jmr.2015.324>.
- [81] Geim, A. K. & Grigorieva, I. V. Van der Waals heterostructures. *Nature* **499**, 419–425 (2013). URL <https://doi.org/10.1038/nature12385>.
- [82] O’Hern, S. C. *et al.* Selective molecular transport through intrinsic defects in a single layer of CVD graphene. *ACS Nano* **6**, 10130–10138 (2012). URL <https://doi.org/10.1021/nn303869m>.
- [83] Madauß, L. *et al.* Fabrication of nanoporous graphene/polymer composite membranes. *Nanoscale* **9**, 10487–10493 (2017). URL <https://doi.org/10.1039/C7NR02755A>.
- [84] Castro Neto, A. H., Guinea, F., Peres, N. M. R., Novoselov, K. S. & Geim, A. K. The electronic properties of graphene. *Rev. Mod. Phys.* **81**, 109–162 (2009). URL <https://doi.org/10.1103/RevModPhys.81.109>.
- [85] Rosłoń, I. E. *et al.* High-frequency gas effusion through nanopores in suspended graphene. *Nat. Commun.* **11**, 6025 (2020). URL <https://doi.org/10.1038/s41467-020-19893-5>.
- [86] Seo, D. H. *et al.* Anti-fouling graphene-based membranes for effective water desalination. *Nat. Commun.* **9**, 683 (2018). URL <https://doi.org/10.1038/s41467-018-02871-3>.
- [87] Heerema, S. J. & Dekker, C. Graphene nanodevices for DNA sequencing. *Nat. Nanotechnol.* **11**, 127–136 (2016). URL <https://doi.org/10.1038/nnano.2015.307>.
- [88] Polsen, E. S., McNerny, D. Q., Viswanath, B., Pattinson, S. W. & John Hart, A. High-speed roll-to-roll manufacturing of graphene using a concentric tube CVD reactor. *Sci. Rep.* **5**, 10257 (2015). URL <https://doi.org/10.1038/srep10257>.
- [89] Bae, S. *et al.* Roll-to-roll production of 30-inch graphene films for transparent electrodes. *Nat. Nanotechnol.* **5**, 574–578 (2010). URL <https://doi.org/10.1038/nnano.2010.132>.

- [90] Kim, K. S. *et al.* Large-scale pattern growth of graphene films for stretchable transparent electrodes. *Nature* **457**, 706–710 (2009). URL <https://doi.org/10.1038/nature07719>.
- [91] Li, X. *et al.* Transfer of large-area graphene films for high-performance transparent conductive electrodes. *Nano Lett.* **9**, 4359–4363 (2009). URL <https://doi.org/10.1021/nl902623y>.
- [92] van Ngoc, H., Qian, Y., Han, S. K. & Kang, D. J. PMMA-etching-free transfer of wafer-scale chemical vapor deposition two-dimensional atomic crystal by a water soluble polyvinyl alcohol polymer method. *Sci. Rep.* **6**, 33096 (2016). URL <https://doi.org/10.1038/srep33096>.
- [93] Leong, W. S. *et al.* Paraffin-enabled graphene transfer. *Nat. Commun.* **10**, 867 (2019). URL <https://doi.org/10.1038/s41467-019-08813-x>.
- [94] Ogata, C. *et al.* All-graphene oxide device with tunable supercapacitor and battery behaviour by the working voltage. *Chem. Commun.* **52**, 3919–3922 (2016). URL <https://doi.org/10.1039/C5CC09575A>.
- [95] Wang, D.-W., Du, A., Taran, E., Lu, G. Q. & Gentle, I. R. A water-dielectric capacitor using hydrated graphene oxide film. *J. Mater. Chem.* **22**, 21085–21091 (2012). URL <https://doi.org/10.1039/C2JM34476A>.
- [96] Wang, L. *et al.* Graphene oxide as an ideal substrate for hydrogen storage. *ACS Nano* **3**, 2995–3000 (2009). URL <https://doi.org/10.1021/nn900667s>.
- [97] Dhakshinamoorthy, A., Alvaro, M., Concepción, P., Fornés, V. & Garcia, H. Graphene oxide as an acid catalyst for the room temperature ring opening of epoxides. *Chem. Commun.* **48**, 5443–5445 (2012). URL <https://doi.org/10.1039/C2CC31385E>.
- [98] Staudenmaier, L. Verfahren zur Darstellung der Graphitsäure. *Berichte der deutschen chemischen Gesellschaft* **31**, 1481–1487 (1898). URL <https://doi.org/10.1002/cber.18980310237>.
- [99] Hummers, W. S., Offeman, R. E. Preparation of graphitic oxide. *J. Am. Chem. Soc.* **80**, 1339 (1958). URL <https://doi.org/10.1021/ja01539a017>.
- [100] Madauß, L. *et al.* Selective proton transport for hydrogen production using graphene

- oxide membranes. *J. Phys. Chem. Lett.* **11**, 9415–9420 (2020). URL <https://doi.org/10.1021/acs.jpcllett.0c02481>.
- [101] He, H., Klinowski, J., Forster, M. & Lerf, A. A new structural model for graphite oxide. *Chem. Phys. Lett.* **287**, 53–56 (1998). URL [https://doi.org/10.1016/S0009-2614\(98\)00144-4](https://doi.org/10.1016/S0009-2614(98)00144-4).
- [102] Li, L., Zhang, X., Qiu, J., Weeks, B. L. & Wang, S. Reduced graphene oxide-linked stacked polymer forests for high energy-density supercapacitor. *Nano Energy* **2**, 628–635 (2013). URL <https://doi.org/10.1016/j.nanoen.2013.07.011>.
- [103] Lyu, J. *et al.* Separation and purification using GO and r-GO membranes. *RSC Adv.* **8**, 23130–23151 (2018). URL <https://doi.org/10.1039/C8RA03156H>.
- [104] Radisavljevic, B., Radenovic, A., Brivio, J., Giacometti, V. & Kis, A. Single-layer MoS₂ transistors. *Nat. Nanotechnol.* **6**, 147–150 (2011). URL <https://doi.org/10.1038/nnano.2010.279>.
- [105] Wang, Q. H., Kalantar-Zadeh, K., Kis, A., Coleman, J. N. & Strano, M. S. Electronics and optoelectronics of two-dimensional transition metal dichalcogenides. *Nat. Nanotechnol.* **7**, 699–712 (2012). URL <https://doi.org/10.1038/nnano.2012.193>.
- [106] Lee, Y.-H. *et al.* Synthesis of large-area MoS₂ atomic layers with chemical vapor deposition. *Adv. Mater.* **24**, 2320–2325 (2012). URL <https://doi.org/10.1002/adma.201104798>.
- [107] Liu, K.-K. *et al.* Growth of large-area and highly crystalline MoS₂ thin layers on insulating substrates. *Nano Lett.* **12**, 1538–1544 (2012). URL <https://doi.org/10.1021/nl2043612>.
- [108] Lee, D. H., Sim, Y., Wang, J. & Kwon, S.-Y. Metal–organic chemical vapor deposition of 2D van der Waals materials—The challenges and the extensive future opportunities. *APL Mater.* **8**, 030901 (2020). URL <https://doi.org/10.1063/1.5142601>.
- [109] Marx, M. *et al.* Metalorganic vapor-phase epitaxy growth parameters for two-dimensional MoS₂. *J. Electron. Mater.* **47**, 910–916 (2018). URL <https://doi.org/10.1007/s11664-017-5937-3>.
- [110] Li, H., Li, Y., Aljarb, A., Shi, Y. & Li, L.-J. Epitaxial growth of two-dimensional

- layered transition-metal dichalcogenides: Growth mechanism, controllability, and scalability. *Chem. Rev.* **118**, 6134–6150 (2018). URL <https://doi.org/10.1021/acs.chemrev.7b00212>.
- [111] Fu, D. *et al.* Molecular beam epitaxy of highly crystalline monolayer molybdenum disulfide on hexagonal boron nitride. *J. Am. Chem. Soc.* **139**, 9392–9400 (2017). URL <https://doi.org/10.1021/jacs.7b05131>.
- [112] Hu, T., Li, R. & Dong, J. A new (2×1) dimerized structure of monolayer 1T-molybdenum disulfide, studied from first principles calculations. *J. Chem. Phys.* **139**, 174702 (2013). URL <https://doi.org/10.1063/1.4827082>.
- [113] Heising, J. & Kanatzidis, M. G. Structure of restacked MoS₂ and WS₂ elucidated by electron crystallography. *J. Am. Chem. Soc.* **121**, 638–643 (1999). URL <https://doi.org/10.1021/ja983043c>.
- [114] Eda, G. *et al.* Coherent atomic and electronic heterostructures of single-layer MoS₂. *ACS Nano* **6**, 7311–7317 (2012). URL <https://doi.org/10.1021/ja983043c>.
- [115] Ries, L. *et al.* Enhanced sieving from exfoliated MoS₂ membranes via covalent functionalization. *Nat. Mater.* **18**, 1112–1117 (2019). URL <https://doi.org/10.1038/s41563-019-0464-7>.
- [116] Wang, Z. & Mi, B. Environmental applications of 2D molybdenum disulfide (MoS₂) nanosheets. *Environ. Sci. Technol.* **51**, 8229–8244 (2017). URL <https://doi.org/10.1021/acs.est.7b01466>.
- [117] Wang, Z. *et al.* Understanding the aqueous stability and filtration capability of MoS₂ membranes. *Nano Lett.* **17**, 7289–7298 (2017). URL <https://doi.org/10.1021/acs.nanolett.7b02804>.
- [118] Sapkota, B. *et al.* High permeability sub-nanometre sieve composite MoS₂ membranes. *Nat. Commun.* **11**, 2747 (2020). URL <https://doi.org/10.1038/s41467-020-16577-y>.
- [119] Feng, J. *et al.* Electrochemical reaction in single layer MoS₂: Nanopores opened atom by atom. *Nano Lett.* **15**, 3431–3438 (2015). URL <https://doi.org/10.1021/acs.nanolett.5b00768>.

- [120] Thiruraman, J. P. *et al.* Angstrom-size defect creation and ionic transport through pores in single-layer MoS₂. *Nano Lett.* **18**, 1651–1659 (2018). URL <https://doi.org/10.1021/acs.nanolett.7b04526>.
- [121] Ghaderzadeh, S. *et al.* Freestanding and supported MoS₂ monolayers under cluster irradiation: Insights from molecular dynamics simulations. *ACS Appl. Mat. Interfaces* **12**, 37454–37463 (2020). URL <https://doi.org/10.1021/acsami.0c09255>.
- [122] Kozbial, A., Gong, X., Liu, H. & Li, L. Understanding the intrinsic water wettability of molybdenum disulfide (MoS₂). *Langmuir* **31**, 8429–8435 (2015). URL <https://doi.org/10.1021/acs.langmuir.5b02057>.
- [123] Allogho, G.-G. & Ashrit, P. V. Wettability and photochromic behaviour of molybdenum oxide thin films. *Thin Solid Films* **520**, 2326–2330 (2012). URL <https://doi.org/10.1016/j.tsf.2011.09.068>.
- [124] Park, J. *et al.* Thickness modulated MoS₂ grown by chemical vapor deposition for transparent and flexible electronic devices. *Appl. Phys. Lett.* **106**, 012104 (2015). URL <https://doi.org/10.1063/1.4905476>.
- [125] Han, G. H. *et al.* Seeded growth of highly crystalline molybdenum disulphide monolayers at controlled locations. *Nature Commun.* **6**, 6128 (2015). URL <https://doi.org/10.1038/ncomms7128>.
- [126] Pollmann, E. *et al.* Molybdenum Disulfide Nanoflakes Grown by Chemical Vapor Deposition on Graphite: Nucleation, Orientation, and Charge Transfer. *J. Phys. Chem. C* **124**, 2689–2697 (2020). URL <https://doi.org/10.1021/acs.jpcc.9b10120>.
- [127] Zhang, X. *et al.* Controllable one-step growth of bilayer MoS₂WS₂/WS₂ heterostructures by chemical vapor deposition. *Nanotechnol.* **29**, 455707 (2018). URL <https://doi.org/10.1088/1361-6528/aaddc5>.
- [128] Cai, Z., Liu, B., Zou, X. & Cheng, H.-M. Chemical Vapor Deposition Growth and Applications of Two-Dimensional Materials and Their Heterostructures. *Chem. Rev.* **118**, 6091–6133 (2018). URL <https://doi.org/10.1021/acs.chemrev.7b00536>.
- [129] Granzier-Nakajima, T., Fujisawa, K., Anil, V., Terrones, M. & Yeh, Y.-T. Controlling nitrogen doping in graphene with atomic precision: Synthesis and characterization. *Nanomaterials* **9**, 425 (2019). URL <https://doi.org/10.3390/nano9030425>.

- [130] Apel, P. Track etching technique in membrane technology. *Radiat. Meas.* **34**, 559–566 (2001). URL [https://doi.org/10.1016/S1350-4487\(01\)00228-1](https://doi.org/10.1016/S1350-4487(01)00228-1).
- [131] Wang, P. *et al.* Ultrafast ion sieving using nanoporous polymeric membranes. *Nat. Commun.* **9**, 569 (2018). URL <https://doi.org/10.1038/s41467-018-02941-6>.
- [132] Rutherford, E. The scattering of α and β particles by matter and the structure of the atom. *Philos. Mag.* **21**, 669–688 (1911). URL <https://doi.org/10.1080/14786440508637080>.
- [133] Sigmund, P. *Stopping of Heavy Ions: A Theoretical Approach - Chapter 5: Electronic Stopping of Point Charges, pp. 29-44; Chapter 10: Nuclear Stopping, pp. 85-94*, vol. 204 (Springer-Verlag Berlin Heidelberg, 2004), 1 edn. URL <https://doi.org/10.1007/b98483>.
- [134] Robinson, M. T. & Torrens, I. M. Computer simulation of atomic-displacement cascades in solids in the binary-collision approximation. *Phys. Rev. B* **9**, 5008–5024 (1974). URL <https://doi.org/10.1103/PhysRevB.9.5008>.
- [135] Wilson, W. D., Haggmark, L. G. & Biersack, J. P. Calculations of nuclear stopping, ranges, and straggling in the low-energy region. *Phys. Rev. B* **15**, 2458–2468 (1977). URL <https://doi.org/10.1103/PhysRevB.15.2458>.
- [136] Bohr, N. II. On the theory of the decrease of velocity of moving electrified particles on passing through matter. *Philos. Mag.* **25**, 10–31 (1913). URL <https://doi.org/10.1080/14786440108634305>.
- [137] Bethe, H. Zur Theorie des Durchgangs schneller Korpuskularstrahlen durch Materie. *Ann. Phys.* **397**, 325–400 (1930). URL <https://doi.org/10.1002/andp.19303970303>.
- [138] Bloch, F. Zur Bremsung rasch bewegter Teilchen beim Durchgang durch Materie. *Ann. Phys.* **408**, 285–320 (1933). URL <https://doi.org/10.1002/andp.19334080303>.
- [139] Lindhard, J., Scharff, M. & Schioett, H. E. Range concepts and heavy ion ranges (Notes on atomic collisions, II). *Kgl. Danske Videnskab. Selskab. Mat. Fys. Medd.* **33** (1963). URL <https://www.osti.gov/biblio/4153115>.

-
- [140] Lifshits, I. M., Kaganov, M. I. & Tanatarov, L. V. On the theory of the changes produced in metals by radiation. *Sov. At. Energy* **6**, 261–270 (1960). URL <https://doi.org/10.1007/BF01479732>.
- [141] Nastasi, M., Michael, N., Mayer, J., Hirvonen, J. K. & James, M. *Ion-solid interactions: fundamentals and applications - Chapter 4: Cross sections*, pp. 71-72 (Cambridge University Press, 1996). URL <https://doi.org/10.1017/CBO9780511565007>.
- [142] Nastasi, M., Michael, N., Mayer, J., Hirvonen, J. K. & James, M. *Ion-solid interactions: fundamentals and applications - Chapter 5: Ion stopping*, pp. 88-90 (Cambridge University Press, 1996). URL <https://doi.org/10.1017/CBO9780511565007>.
- [143] Ziegler, J. F., Ziegler, M. D. & Biersack, J. P. SRIM – The stopping and range of ions in matter (2010). *Nucl. Instrum. Meth. B* **268**, 1818–1823 (2010). URL <https://doi.org/10.1016/j.nimb.2010.02.091>.
- [144] Lindhard, J. & Scharff, M. Energy dissipation by ions in the kev region. *Phys. Rev.* **124**, 128–130 (1961). URL <https://doi.org/10.1103/PhysRev.124.128>.
- [145] Toulemonde, M., Bouffard, S. & Studer, F. Swift heavy ions in insulating and conducting oxides: tracks and physical properties. *Nucl. Instrum. Meth. B* **91**, 108–123 (1994). URL [https://doi.org/10.1016/0168-583X\(94\)96200-6](https://doi.org/10.1016/0168-583X(94)96200-6).
- [146] Wang, Z. G. *et al.* Velocity effect on the damage creation in metals in the electronic stopping power regime. *Nucl. Instrum. Meth. B* **107**, 175–180 (1996). URL [https://doi.org/10.1016/0168-583X\(95\)00851-9](https://doi.org/10.1016/0168-583X(95)00851-9).
- [147] Ruder Boskovic Institute - Retrieved: March 1, 2021. URL <https://www.irb.hr/eng/Divisions/Division-of-Experimental-Physics/Laboratory-for-ion-beam-interactions/Articles/Accelerators>.
- [148] IonBeamCenter.eu - Retrieved: March 1, 2021. URL <https://www.ionbeamcenters.eu/RADIATE-project-partners/cnrs/>.
- [149] DREEBIT GmbH - Electron & Ion Beam Technologies. Ionization Energy Databse. URL <https://www.dreebit-ibt.com/ionization-energy-database.html>.
- [150] Arnau, A. *et al.* Interaction of slow multicharged ions with solid surfaces. *Surf. Sci.*

- Rep.* **27**, 113–239 (1997). URL [https://doi.org/10.1016/S0167-5729\(97\)00002-2](https://doi.org/10.1016/S0167-5729(97)00002-2).
- [151] Burgdörfer, J., Lerner, P. & Meyer, F. W. Above-surface neutralization of highly charged ions: The classical over-the-barrier model. *Phys. Rev. A* **44**, 5674–5685 (1991). URL <https://doi.org/10.1103/PhysRevA.44.5674>.
- [152] Thörner, G. & Borstel, G. Unoccupied surface states and surface barrier in metals. *Appl. Phys. A* **41**, 99–101 (1986). URL <https://doi.org/10.1007/BF00618539>.
- [153] Niehaus, A. Multiple electron capture in slow collisions of highly charged ions with atoms. *Nucl. Instrum. Meth. B* **31**, 359–366 (1988). URL [https://doi.org/10.1016/0168-583X\(88\)90445-4](https://doi.org/10.1016/0168-583X(88)90445-4).
- [154] Kozubek, R. *Analyse von Defektstrukturen in zweidimensionalen Materialien nach der Interaktion mit hochgeladenen Ionen - p. 19*. Dissertation, University of Duisburg-Essen, Duisburg, Germany (2018). URL https://duepublico2.uni-due.de/receive/duepublico_mods_00046404.
- [155] Briand, J. P. *et al.* Production of hollow atoms by the excitation of highly charged ions in interaction with a metallic surface. *Phys. Rev. Lett.* **65**, 159–162 (1990). URL <https://doi.org/10.1103/PhysRevLett.65.159>.
- [156] Winter, H. & Aumayr, F. Hollow atoms. *J. Phys. B* **32**, R39–R65 (1999). URL <https://doi.org/10.1088/0953-4075/32/7/005>.
- [157] Hagstrum, H. D. Theory of auger ejection of electrons from metals by ions. *Phys. Rev.* **96**, 336–365 (1954). URL <https://doi.org/10.1103/PhysRev.96.336>.
- [158] Santra, R., Zobeley, J. & Cederbaum, L. Electronic decay of valence holes in clusters and condensed matter. *Phys. Rev. B* **64**, 263 (2001). URL <https://doi.org/10.1103/PhysRevB.64.245104>.
- [159] Jahnke, T. Interatomic and intermolecular Coulombic decay: the coming of age story. *Nucl. Instrum. Methods Phys. Res. B* **48**, 082001 (2015). URL <https://doi.org/10.1088%2F0953-4075%2F48%2F8%2F082001>.
- [160] Rist, J. *et al.* A comprehensive study of Interatomic coulombic decay in argon dimers:

- Extracting R-dependent absolute decay rates from the experiment. *Chem. Phys.* **482**, 185–191 (2017). URL <https://doi.org/10.1016/j.chemphys.2016.09.024>.
- [161] Wilhelm, R. A. *et al.* Interatomic coulombic decay: The mechanism for rapid deexcitation of hollow atoms. *Phys. Rev. Lett.* **119**, 103401 (2017). URL <https://doi.org/10.1103/PhysRevLett.119.103401>.
- [162] Schwestka, J. *et al.* The role of radiative de-excitation in the neutralization process of highly charged ions interacting with a single layer of graphene. *Nucl. Instrum. Methods Phys. Res. B* **422**, 63–67 (2018). URL <https://doi.org/10.1016/j.nimb.2018.02.022>.
- [163] Stolterfoht, N. *et al.* Multiple-cascade model for the filling of hollow Ne atoms moving below an Al surface. *Phys. Rev. A* **52**, 445–456 (1995). URL <https://doi.org/10.1103/PhysRevA.52.445>.
- [164] Winecki, S., Cocke, C. L., Fry, D. & Stöckli, M. P. Neutralization and equilibration of highly charged argon ions at grazing incidence on a graphite surface. *Phys. Rev. A* **53**, 4228–4237 (1996). URL <https://doi.org/10.1103/PhysRevA.53.4228>.
- [165] Folkerts, L., Schippers, S., Zehner, D. M. & Meyer, F. W. Time scales for charge equilibration of Oq^+ ($3 \leq q \leq 8$) Ions during surface-channeling interactions with Au(110). *Phys. Rev. Lett.* **74**, 2204–2207 (1995). URL <https://doi.org/10.1103/PhysRevLett.74.2204>.
- [166] Hopster, J. *Aufbau einer Ionenstrahlanlage zur Nanostrukturierung von 2D-Materialien mit hochgeladenen Ionen - p. 10*. Dissertation, University of Duisburg-Essen, Duisburg, Germany (2014). URL https://duepublico2.uni-due.de/receive/duepublico_mods_00035210.
- [167] Gruber, E. *et al.* Ultrafast electronic response of graphene to a strong and localized electric field. *Nat. Commun.* **7**, 13948 (2016). URL <https://doi.org/10.1038/ncomms13948>.
- [168] Creutzburg, S. *et al.* Vanishing influence of the band gap on the charge exchange of slow highly charged ions in freestanding single-layer MoS₂. *Phys. Rev. B* **102**, 045408 (2020). URL <https://doi.org/10.1103/PhysRevB.102.045408>.
- [169] El-Said, A. S. *et al.* Creation of nanohillocks on CaF₂ surfaces by single slow highly

- charged ions. *Phys. Rev. Lett.* **100**, 237601 (2008). URL <https://doi.org/10.1103/PhysRevLett.100.237601>.
- [170] Chatterjee, A. & Schaefer, H. J. Microdosimetric structure of heavy ion tracks in tissue. *Radiat. Environ. Biophys.* **13**, 215–227 (1976). URL <https://doi.org/10.1007/BF01330766>.
- [171] Sigmund, P., Matthies, M. T. & Phillips, D. L. Energy deposition and penetration depth of heavy ions in the electronic stopping region. *Radiat. Eff.* **11**, 39–49 (1971). URL <https://doi.org/10.1080/00337577108230466>.
- [172] Fleischer, R. L., Price, P. B. & Walker, R. M. Ion explosion spike mechanism for formation of charged-particle tracks in solids. *J. Appl. Phys.* **36**, 3645–3652 (1965). URL <https://doi.org/10.1063/1.1703059>.
- [173] Seitz, F. & Koehler, J. S. Displacement of atoms during irradiation. *Solid State Phys.: Adv. Res. Appl.* **2**, 305–448 (1956).
- [174] Toulemonde, M., Paumier, E. & Dufour, C. Thermal spike model in the electronic stopping power regime. *Radiat. Eff. Defects Solids* **126**, 201–206 (1993). URL <https://doi.org/10.1080/10420159308219709>.
- [175] Toulemonde, M., Dufour, C., Meftah, A. & Paumier, E. Transient thermal processes in heavy ion irradiation of crystalline inorganic insulators. *Nucl. Instrum. Meth. B* **166-167**, 903–912 (2000). URL [https://doi.org/10.1016/S0168-583X\(99\)00799-5](https://doi.org/10.1016/S0168-583X(99)00799-5).
- [176] Toulemonde, M., Dufour, C. & Paumier, E. Transient thermal process after a high-energy heavy-ion irradiation of amorphous metals and semiconductors. *Phys. Rev. B* **46**, 14362–14369 (1992). URL <https://doi.org/10.1103/PhysRevB.46.14362>.
- [177] Meftah, A. *et al.* Track formation in SiO₂ quartz and the thermal-spike mechanism. *Phys. Rev. B* **49**, 12457–12463 (1994). URL <https://doi.org/10.1103/PhysRevB.49.12457>.
- [178] Osmani, O., Medvedev, N., Schleberger, M. & Rethfeld, B. Energy dissipation in dielectrics after swift heavy-ion impact: A hybrid model. *Phys. Rev. B* **84**, 214105 (2011). URL <https://doi.org/10.1103/PhysRevB.84.214105>.
- [179] Osmani, O., Medvedev, N., Schleberger, M. & Rethfeld, B. Excitation and relaxation

- of swift heavy ion irradiated dielectrics. *e-J. Surf. Sci. Nanotechnol.* **8**, 278–282 (2010). URL <https://doi.org/10.1380/ejssnt.2010.278>.
- [180] Balandin, A. A. *et al.* Superior thermal conductivity of single-layer graphene. *Nano letters* **8**, 902–907 (2008). URL <https://doi.org/10.1021/nl0731872>.
- [181] Wei, X. *et al.* Phonon thermal conductivity of monolayer MoS₂: A comparison with single layer graphene. *Appl. Phys. Lett.* **105**, 103902 (2014). URL <https://doi.org/10.1063/1.4895344>.
- [182] Yan, R. *et al.* Thermal conductivity of monolayer molybdenum disulfide obtained from temperature-dependent Raman spectroscopy. *ACS Nano* **8**, 986–993 (2014). URL <https://doi.org/10.1021/nn405826k>.
- [183] Gandi, A. N. & Schwingenschlögl, U. Thermal conductivity of bulk and monolayer MoS₂. *EPL* **113**, 36002 (2016). URL <https://doi.org/10.1209/0295-5075/113/36002>.
- [184] Hell, S. W. & Wichmann, J. Breaking the diffraction resolution limit by stimulated emission: stimulated-emission-depletion fluorescence microscopy. *Opt. Lett.* **19**, 780–782 (1994). URL <https://doi.org/10.1364/OL.19.000780>.
- [185] Hell, S. W. & Kroug, M. Ground-state-depletion fluorescence microscopy: A concept for breaking the diffraction resolution limit. *Appl. Phys. B* **60**, 495–497 (1995). URL <https://doi.org/10.1007/BF01081333>.
- [186] Abbe, E. Beiträge zur Theorie des Mikroskops und der mikroskopischen Wahrnehmung. *Archiv f. mikrosk. Anatomie* **9**, 413–468 (1873). URL <https://doi.org/10.1007/BF02956173>.
- [187] Helmholtz, H. Die theoretische Grenze für die Leistungsfähigkeit der Mikroskope. *Ann. Phys.* 557–584 (1874).
- [188] G. Binnig & H. Rohrer. Scanning tunneling microscopy. *Surf. Sci.* **126**, 236–244 (1983). URL [https://doi.org/10.1016/0039-6028\(83\)90716-1](https://doi.org/10.1016/0039-6028(83)90716-1).
- [189] Binnig, G., Quate, C. F. & Gerber, C. Atomic force microscope. *Phys. Rev. Lett.* **56**, 930–933 (1986). URL <https://doi.org/10.1103/PhysRevLett.56.930>.

- [190] Voigtländer, B. *Scanning Probe Microscopy: Atomic Force Microscopy and Scanning Tunneling Microscopy - Chapter 11: Forces Between Tip and Sample*, pp. 145-147. NanoScience and Technology (Springer-Verlag Berlin Heidelberg, 2015), 1 edn. URL <https://doi.org/10.1007/978-3-662-45240-0>.
- [191] Voigtländer, B. *Scanning Probe Microscopy: Atomic Force Microscopy and Scanning Tunneling Microscopy - Chapter 13: Static Atomic Force Microscopy*, pp. 177-186. NanoScience and Technology (Springer-Verlag Berlin Heidelberg, 2015), 1 edn. URL <https://doi.org/10.1007/978-3-662-45240-0>.
- [192] Voigtländer, B. *Scanning Probe Microscopy: Atomic Force Microscopy and Scanning Tunneling Microscopy - Chapter 17: Frequency Modulation (FM) Mode in Dynamic Atomic Force Microscopy—Non-contact Atomic Force Microscopy*, pp. 229-252. NanoScience and Technology (Springer-Verlag Berlin Heidelberg, 2015), 1 edn. URL <https://doi.org/10.1007/978-3-662-45240-0>.
- [193] Ochedowski, O. *Modification of 2D materials by swift heavy ion irradiation*. Ph.D. thesis, University of Duisburg-Essen, Duisburg, Germany (2014). URL https://duepublico2.uni-due.de/receive/duepublico_mods_00036835.
- [194] RAMAN, C. V. & KRISHNAN, K. S. A New Type of Secondary Radiation. *Nature* **121**, 501–502 (1928). URL <https://doi.org/10.1038/121501c0>.
- [195] Cançado, L. G. *et al.* Quantifying defects in graphene via Raman spectroscopy at different excitation energies. *Nano Lett.* **11**, 3190–3196 (2011). URL <https://doi.org/10.1021/nl201432g>.
- [196] Ferrari, A. C. & Basko, D. M. Raman spectroscopy as a versatile tool for studying the properties of graphene. *Nat. Nanotechnol.* **8**, 235–246 (2013). URL <https://doi.org/10.1038/nnano.2013.46>.
- [197] Bruna, M. *et al.* Doping dependence of the Raman spectrum of defected graphene. *ACS Nano* **8**, 7432–7441 (2014). URL <https://doi.org/10.1021/nn502676g>.
- [198] Chakraborty, B. *et al.* Symmetry-dependent phonon renormalization in monolayer MoS₂ transistor. *Phys. Rev. B* **85**, 161403 (2012). URL <https://doi.org/10.1103/PhysRevB.85.161403>.
- [199] Rice, C. *et al.* Raman-scattering measurements and first-principles calculations of strain-

- induced phonon shifts in monolayer MoS₂. *Phys. Rev. B* **87**, 081307 (2013). URL <https://doi.org/10.1103/PhysRevB.87.081307>.
- [200] Lee, C. *et al.* Anomalous lattice vibrations of single- and few-layer MoS₂. *ACS Nano* **4**, 2695–2700 (2010). URL <https://doi.org/10.1021/nn1003937>.
- [201] Ferrari, A. C. Raman spectroscopy of graphene and graphite: Disorder, electron–phonon coupling, doping and nonadiabatic effects. *Solid State Commun.* **143**, 47–57 (2007). URL <https://doi.org/10.1016/j.ssc.2007.03.052>.
- [202] Malard, L. M., Pimenta, M. A., Dresselhaus, G. & Dresselhaus, M. S. Raman spectroscopy in graphene. *Phys. Rep.* **473**, 51–87 (2009). URL <https://doi.org/10.1016/j.physrep.2009.02.003>.
- [203] Ferrari, A. C. *et al.* Raman Spectrum of Graphene and Graphene Layers. *Phys. Rev. Lett.* **97**, 187401 (2006). URL <https://doi.org/PhysRevLett.97.187401>.
- [204] Tuinstra, F. & Koenig, J. L. Raman Spectrum of Graphite. *J. Phys. Chem.* **53**, 1126–1130 (1970). URL <https://doi.org/10.1063/1.1674108>.
- [205] Ferrari, A. C. & Robertson, J. Interpretation of Raman spectra of disordered and amorphous carbon. *Phys. Rev. B* **61**, 14095–14107 (2000). URL <https://doi.org/PhysRevB.61.14095>.
- [206] Nemanich, R. J. & Solin, S. A. First- and second-order Raman scattering from finite-size crystals of graphite. *Phys. Rev. B* **20**, 392–401 (1979). URL <https://doi.org/10.1103/PhysRevB.20.392>.
- [207] Verble, J. L. & Wieting, T. J. Lattice mode degeneracy in MoS₂ and other layer compounds. *Phys. Rev. Lett.* **25**, 362–365 (1970). URL <https://doi.org/10.1103/PhysRevLett.25.362>.
- [208] Verble, J. L., Wietling, T. J. & Reed, P. R. Rigid-layer lattice vibrations and van der Waals bonding in hexagonal MoS₂. *Solid State Commun.* **11**, 941–944 (1972). URL [https://doi.org/10.1016/0038-1098\(72\)90294-3](https://doi.org/10.1016/0038-1098(72)90294-3).
- [209] Madauß, L. *et al.* A swift technique to hydrophobize graphene and increase its mechanical stability and charge carrier density. *npj 2D Mater. Appl.* **4**, 11 (2020). URL <https://doi.org/10.1038/s41699-020-0148-9>.

- [210] Liu, J., Vázquez Muñíos, H., Nordlund, K. & Djurabekova, F. Molecular dynamics simulation of the effects of swift heavy ion irradiation on multilayer graphene and diamond-like carbon. *Appl. Surf. Sci.* **527**, 146495 (2020). URL <https://doi.org/10.1016/j.apsusc.2020.146495>.
- [211] H. Vázquez *et al.* Creating nanoporous graphene with swift heavy ions. *Carbon* **114**, 511–518 (2017). URL <https://doi.org/10.1016/j.carbon.2016.12.015>.
- [212] Gammelgaard, L. *et al.* Graphene transport properties upon exposure to PMMA processing and heat treatments. *2D Mater.* **1**, 035005 (2014). URL <https://doi.org/10.1088/2053-1583/1/3/035005>.
- [213] Hallam, T., Berner, N. C., Yim, C. & Duesberg, G. S. Strain, bubbles, dirt, and folds: A study of graphene polymer-assisted transfer. *Adv. Mater. Interfaces* **1**, 1400115 (2014). URL <https://doi.org/10.1002/admi.201400115>.
- [214] Choi, W., Shehzad, M. A., Park, S. & Seo, Y. Influence of removing PMMA residues on surface of CVD graphene using a contact-mode atomic force microscope. *RSC Adv.* **7**, 6943–6949 (2017). URL <https://doi.org/10.1039/C6RA27436F>.
- [215] Mischke, J. *et al.* Direct growth of graphene on GaN via plasma-enhanced chemical vapor deposition under N₂ atmosphere. *2D Mater.* **7**, 035019 (2020). URL <https://doi.org/10.1088/2053-1583/ab8969>.
- [216] Omambac, K. M. *et al.* Temperature-controlled rotational epitaxy of graphene. *Nano Lett.* **19**, 4594–4600 (2019). URL <https://doi.org/10.1021/acs.nanolett.9b01565>.
- [217] Mattevi, C., Kim, H. & Chhowalla, M. A review of chemical vapour deposition of graphene on copper. *J. Mater. Chem.* **21**, 3324–3334 (2011). URL <https://doi.org/10.1039/C0JM02126A>.
- [218] Reina, A. *et al.* Large area, few-layer graphene films on arbitrary substrates by chemical vapor deposition. *Nano Lett.* **9**, 30–35 (2009). URL <https://doi.org/10.1021/nl801827v>.
- [219] Chae, S. J. *et al.* Synthesis of large-area graphene layers on poly-nickel substrate by chemical vapor deposition: Wrinkle formation. *Adv. Mater.* **21**, 2328–2333 (2009). URL <https://doi.org/10.1002/adma.200803016>.

- [220] Kim, H. *et al.* Copper-vapor-assisted chemical vapor deposition for high-quality and metal-free single-layer graphene on amorphous SiO₂ substrate. *ACS Nano* **7**, 6575–6582 (2013). URL <https://doi.org/10.1021/nn402847w>.
- [221] Murdock, A. T. *et al.* Controlling the orientation, edge geometry, and thickness of chemical vapor deposition graphene. *ACS Nano* **7**, 1351–1359 (2013). URL <https://doi.org/10.1021/nn3049297>.
- [222] Xu, X. *et al.* Ultrafast epitaxial growth of metre-sized single-crystal graphene on industrial Cu foil. *Sci. Bull.* **62**, 1074–1080 (2017). URL <https://doi.org/10.1016/j.scib.2017.07.005>.
- [223] Cherian, C. T. *et al.* ‘Bubble-free’ electrochemical delamination of CVD graphene Films. *Small* **11**, 189–194 (2015). URL <https://doi.org/10.1002/smll.201402024>.
- [224] Gao, L. *et al.* Face-to-face transfer of wafer-scale graphene films. *Nature* **505**, 190–194 (2014). URL <https://doi.org/10.1038/nature12763>.
- [225] Kang, J., Shin, D., Bae, S. & Hong, B. H. Graphene transfer: key for applications. *Nanoscale* **4**, 5527–5537 (2012). URL <https://doi.org/10.1039/C2NR31317K>.
- [226] Kim, S. *et al.* Robust graphene wet transfer process through low molecular weight polymethylmethacrylate. *Carbon* **98**, 352–357 (2016). URL <https://doi.org/10.1016/j.carbon.2015.11.027>.
- [227] Lin, W.-H. *et al.* A direct and polymer-free method for transferring graphene grown by chemical vapor deposition to any substrate. *ACS Nano* **8**, 1784–1791 (2014). URL <https://doi.org/10.1021/nn406170d>.
- [228] Lin, Y.-C. *et al.* Graphene annealing: How clean can it be? *Nano Lett.* **12**, 414–419 (2012). URL <https://doi.org/10.1021/nl203733r>.
- [229] Johnson, B. Y., Mazumder, P. & Johnson, K. K. Graphene and polymer-free method for transferring cvd grown graphene onto hydrophobic substrates - patent: C01B 31/04, WO 2016/100418 A1 (2015).
- [230] Lucchese, M. M. *et al.* Quantifying ion-induced defects and Raman relaxation length in graphene. *Carbon* **48**, 1592–1597 (2010). URL <https://doi.org/10.1016/j.carbon.2009.12.057>.

- [231] Alam, A. U., Howlader, M. M. R. & Deen, M. J. The effects of oxygen plasma and humidity on surface roughness, water contact angle and hardness of silicon, silicon dioxide and glass. *J. Micromech. Microeng.* **24**, 035010 (2014). URL <https://doi.org/10.1088/0960-1317/24/3/035010>.
- [232] Abadias, G. *et al.* Volmer-Weber growth stages of polycrystalline metal films probed by in situ and real-time optical diagnostics. *Appl. Phys. Lett.* **107**, 183105 (2015). URL <https://doi.org/doi:10.1063/1.4935034>.
- [233] Mo, Y.-W., Savage, D. E., Swartzentruber, B. S. & Lagally, M. G. Kinetic pathway in Stranski-Krastanov growth of Ge on Si(001). *Phys. Rev. Lett.* **65**, 1020–1023 (1990). URL <https://doi.org/10.1103/PhysRevLett.65.1020>.
- [234] Owens, D. K. & Wendt, R. C. Estimation of the surface free energy of polymers. *J. Appl. Polym. Sci.* **13**, 1741–1747 (1969). URL <https://doi.org/10.1002/app.1969.070130815>.
- [235] Kiselev, A. V. Non-specific and specific interactions of molecules of different electronic structures with solid surfaces. *Discuss. Faraday Soc.* **40**, 205–218 (1965). URL <https://doi.org/10.1039/DF9654000205>.
- [236] Zhang, G. *et al.* Versatile polymer-free graphene transfer method and applications. *ACS Appl. Mater. Interfaces* **8**, 8008–8016 (2016). URL <https://doi.org/10.1021/acsami.6b00681>.
- [237] Park, H. *et al.* Polymer-free graphene transfer for enhanced reliability of graphene field-effect transistors. *2D Mater.* **3**, 021003 (2016). URL <https://doi.org/10.1088/2053-1583/3/2/021003>.
- [238] Vargaftik, N. B., Volkov, B. N. & Voljak, L. D. International Tables of the Surface Tension of Water. *J. Phys. Chem. Ref. Data* **12**, 817–820 (1983). URL <https://doi.org/10.1063/1.555688>.
- [239] Editorial. Renewables get mature. *Nat. Energy* **2**, 17017 (2017). URL <https://doi.org/10.1038/nenergy.2017.17>.
- [240] Seh, Z. W. *et al.* Combining theory and experiment in electrocatalysis: Insights into materials design. *Science* **355** (2017). URL <https://doi.org/10.1126/science.aad4998>.

- [241] Khan, N., Dilshad, S., Khalid, R., Kalair, A. R. & Abas, N. Review of energy storage and transportation of energy. *Energy Stor.* **1**, e49 (2019). URL <https://doi.org/10.1002/est2.49>.
- [242] Yang, Q. *et al.* Ultrathin graphene-based membrane with precise molecular sieving and ultrafast solvent permeation. *Nat. Mater.* **16**, 1198–1202 (2017). URL <https://doi.org/10.1038/nmat5025>.
- [243] Abbasi, R. *et al.* A Roadmap to low-cost hydrogen with hydroxide exchange membrane electrolyzers. *Adv. Mater.* **31**, 1805876 (2019). URL <https://doi.org/10.1002/adma.201805876>.
- [244] Immanuel V. & Dmitri B. Low cost hydrogen production by anion exchange membrane electrolysis: A review. *Renew. Sust. Energ. Rev.* **81**, 1690–1704 (2018). URL <https://doi.org/10.1016/j.rser.2017.05.258>.
- [245] Iulianelli, A., Liguori, S., Wilcox, J. & Basile, A. Advances on methane steam reforming to produce hydrogen through membrane reactors technology: A review. *Catal. Rev.* **58**, 1–35 (2016). URL <https://doi.org/10.1080/01614940.2015.1099882>.
- [246] Burmistrz, P., Chmielniak, T., Czepirski, L. & Gazda-Grzywacz, M. Carbon footprint of the hydrogen production process utilizing subbituminous coal and lignite gasification. *J. Clean. Prod.* **139**, 858–865 (2016). URL <https://doi.org/10.1016/j.jclepro.2016.08.112>.
- [247] Symes, M. D. Just add hot water. *Nat. Energy* **4**, 730–731 (2019). URL <https://doi.org/10.1038/s41560-019-0465-4>.
- [248] Tong, W. *et al.* Electrolysis of low-grade and saline surface water. *Nat. Energy* **5**, 367–377 (2020). URL <https://doi.org/10.1038/s41560-020-0550-8>.
- [249] Chen, X., Shen, S., Guo, L. & Mao, S. S. Semiconductor-based photocatalytic hydrogen generation. *Chem. Riev.* **110**, 6503–6570 (2010). URL <https://doi.org/10.1021/cr1001645>.
- [250] Li, Y. *et al.* Photocatalytic water splitting by N-TiO₂ on MgO (111) with exceptional quantum efficiencies at elevated temperatures. *Nat. Commun.* **10**, 4421 (2019). URL <https://doi.org/10.1038/s41467-019-12385-1>.

- [251] Scanlon, D. O. *et al.* Band alignment of rutile and anatase TiO₂. *Nat. Mater.* **12**, 798–801 (2013). URL <https://doi.org/10.1038/nmat3697>.
- [252] Wu, Q. *et al.* Ultra-small yellow defective TiO₂ nanoparticles for co-catalyst free photocatalytic hydrogen production. *Nano Energy* **24**, 63–71 (2016). URL <https://doi.org/10.1016/j.nanoen.2016.04.004>.
- [253] Nightingale, E. R. Phenomenological theory of ion solvation. Effective radii of hydrated ions. *J. Phys. Chem.* **63**, 1381–1387 (1959). URL <https://doi.org/10.1021/j150579a011>.
- [254] Lehmani, A., Turq, P., Périé, M., Périé, J. & Simonin, J.-P. Ion transport in Nafion® 117 membrane. *J. Electroanal. Chem.* **428**, 81–89 (1997). URL [https://doi.org/10.1016/S0022-0728\(96\)05060-7](https://doi.org/10.1016/S0022-0728(96)05060-7).
- [255] Kraytsberg, A. & Ein-Eli, Y. Review of advanced materials for proton exchange membrane fuel cells. *Energy & Fuels* **28**, 7303–7330 (2014). URL <https://doi.org/10.1021/ef501977k>.
- [256] Yin, C. *et al.* Positron annihilation characteristics, water uptake and proton conductivity of composite Nafion membranes. *Phys. Chem. Chem. Phys.* **19**, 15953–15961 (2017). URL <https://doi.org/10.1039/C7CP03052E>.
- [257] Yin, C. *et al.* Enhancement in proton conductivity and thermal stability in Nafion membranes induced by incorporation of sulfonated carbon nanotubes. *ACS Appl. Mater. Interfaces* **10**, 14026–14035 (2018). URL <https://doi.org/10.1021/acsami.8b01513>.
- [258] Shibahara, Y. *et al.* Effect of humidity and temperature on polymer electrolyte membrane (Nafion 117) studied by positron annihilation spectroscopy. *J. Power Sources* **195**, 5934–5937 (2010). URL <https://doi.org/10.1016/j.jpowsour.2010.02.003>.
- [259] Sun, P., Ma, R. & Sasaki, T. Recent progress on exploring exceptionally high and anisotropic H⁺/OH[−] ion conduction in two-dimensional materials. *Chem. Sci.* **9**, 33–43 (2018). URL <https://doi.org/10.1039/C7SC04019A>.
- [260] Lozada-Hidalgo, M. *et al.* Sieving hydrogen isotopes through two-dimensional crystals. *Science* **351**, 68–70 (2016). URL <https://doi.org/10.1126/science.aac9726>.

- [261] Karnik, R. N. Breakthrough for protons. *Nature* **516**, 173–174 (2014). URL <https://doi.org/10.1038/nature14074>.
- [262] Shiva, K., Ramakrishna Matte, H., Rajendra, H. B., Bhattacharyya, A. J. & Rao, C. Employing synergistic interactions between few-layer WS₂ and reduced graphene oxide to improve lithium storage, cyclability and rate capability of Li-ion batteries. *Nano Energy* **2**, 787–793 (2013). URL <https://doi.org/10.1016/j.nanoen.2013.02.001>.
- [263] Huang, L., Zhang, M., Li, C. & Shi, G. Graphene-based membranes for molecular separation. *J. Phys. Chem. Lett.* **6**, 2806–2815 (2015). URL <https://doi.org/10.1021/acs.jpcclett.5b00914>.
- [264] Bukola, S., Beard, K., Korzeniewski, C., Harris, J. M. & Creager, S. E. Single-layer graphene sandwiched between proton-exchange membranes for selective proton transmission. *ACS Appl. Nano Mater.* **2**, 964–974 (2019). URL <https://doi.org/10.1021/acsanm.8b02270>.
- [265] Bukola, S., Liang, Y., Korzeniewski, C., Harris, J. & Creager, S. Selective proton/deuteron transport through Nafion|graphene|Nafion sandwich structures at high current density. *J. Am. Chem. Soc.* **140**, 1743–1752 (2018). URL <https://doi.org/10.1021/jacs.7b10853>.
- [266] Hu, S. *et al.* Proton transport through one-atom-thick crystals. *Nature* **516**, 227–230 (2014). URL <https://doi.org/10.1038/nature14015>.
- [267] Mogg, L. *et al.* Atomically thin micas as proton-conducting membranes. *Nat. Nanotechnol.* **14**, 962–966 (2019). URL <https://doi.org/10.1038/s41565-019-0536-5>.
- [268] Jin, X. *et al.* Effective separation of CO₂ using metal-incorporated rGO membranes. *Adv. Mater.* **32**, 1907580 (2020). URL <https://doi.org/10.1002/adma.201907580>.
- [269] Raffone, F., Savazzi, F. & Cicero, G. Controlled pore generation in single-layer graphene oxide for membrane desalination. *J. Phys. Chem. Lett.* **10**, 7492–7497 (2019). URL <https://doi.org/10.1021/acs.jpcclett.9b03255>.
- [270] Wang, L. *et al.* Light-driven active proton transport through photoacid- and photobase-doped janus graphene oxide membranes. *Adv. Mater.* **31**, 1903029 (2019). URL <https://doi.org/10.1002/adma.201903029>.

- [271] Zhang, M. *et al.* Molecular bridges stabilize graphene oxide membranes in water. *Angew. Chem. Int. Ed.* **59**, 1689–1695 (2020). URL <https://doi.org/10.1002/anie.201913010>.
- [272] Azizighannad, S. & Mitra, S. Stepwise reduction of graphene oxide (GO) and its effects on chemical and colloidal Pproperties. *Sci. Rep.* **8**, 10083 (2018). URL <https://doi.org/10.1038/s41598-018-28353-6>.
- [273] Lian, B. *et al.* Extraordinary water adsorption characteristics of graphene oxide. *Chem. Sci.* **9**, 5106–5111 (2018). URL <https://doi.org/10.1039/C8SC00545A>.
- [274] Mouhat, F., Coudert, F.-X. & Bocquet, M.-L. Structure and chemistry of graphene oxide in liquid water from first principles. *Nat. Commun.* **11**, 1566 (2020). URL <https://doi.org/10.1038/s41467-020-15381-y>.
- [275] Karim, M. R. *et al.* Graphene oxide nanosheet with high proton conductivity. *J. Am. Chem. Soc.* **135**, 8097–8100 (2013). URL <https://doi.org/10.1021/ja401060q>.
- [276] Liu, C. *et al.* Kinetic modulation of graphene growth by fluorine through spatially confined decomposition of metal fluorides. *Nat. Chem.* **11**, 730–736 (2019). URL <https://doi.org/10.1038/s41557-019-0290-1>.
- [277] Liu, L., Chen, W. & Li, Y. An overview of the proton conductivity of nafion membranes through a statistical analysis. *J. Membr. Sci.* **504**, 1–9 (2016). URL <https://doi.org/10.1016/j.memsci.2015.12.065>.
- [278] Morimoto, N., Kubo, T. & Nishina, Y. Tailoring the oxygen content of graphite and reduced graphene oxide for specific applications. *Sci. Rep.* **6**, 21715 (2016). URL <https://doi.org/10.1038/srep21715>.
- [279] Zheng, S., Tu, Q., Urban, J. J., Li, S. & Mi, B. Swelling of graphene oxide membranes in aqueous solution: Characterization of interlayer spacing and insight into water transport mechanisms. *ACS Nano* **11**, 6440–6450 (2017). URL <https://doi.org/10.1021/acsnano.7b02999>.
- [280] Zhang, M. *et al.* Controllable ion transport by surface-charged graphene oxide membrane. *Nat. Commun.* **10**, 1253 (2019). URL <https://doi.org/10.1038/s41467-019-09286-8>.

- [281] Dahms, F. *et al.* The hydrated excess proton in the zundel cation H_5O_2^+ : The role of ultrafast solvent fluctuations. *Angew. Chem. Int. Ed.* **55**, 10600–10605 (2016). URL <https://doi.org/10.1002/anie.201602523>.
- [282] Agmon, N. The Grotthuss mechanism. *Chem. Phys. Lett.* **244**, 456–462 (1995). URL [https://doi.org/10.1016/0009-2614\(95\)00905-J](https://doi.org/10.1016/0009-2614(95)00905-J).
- [283] Medhekar, N. V., Ramasubramaniam, A., Ruoff, R. S. & Shenoy, V. B. Hydrogen bond networks in graphene oxide composite paper: Structure and mechanical properties. *ACS Nano* **4**, 2300–2306 (2010). URL <https://doi.org/10.1021/nn901934u>.
- [284] Gao, W., Alemany, L. B., Ci, L. & Ajayan, P. M. New insights into the structure and reduction of graphite oxide. *Nat. Chem.* **1**, 403–408 (2009). URL <https://doi.org/10.1038/nchem.281>.
- [285] Chen, M. *et al.* Hydroxide diffuses slower than hydronium in water because its solvated structure inhibits correlated proton transfer. *Nat. Chem.* **10**, 413–419 (2018). URL <https://doi.org/10.1038/s41557-018-0010-2>.
- [286] Cao, Z., Liu, V. & Barati Farimani, A. Why is single-layer MoS_2 a more energy efficient membrane for water desalination? *ACS Energy Lett.* **5**, 2217–2222 (2020). URL <https://doi.org/10.1021/acsenergylett.0c00923>.
- [287] Kozubek, R. *et al.* Perforating freestanding molybdenum disulfide monolayers with highly charged ions. *J. Phys. Chem. Lett.* **10**, 904–910 (2019). URL <https://doi.org/10.1021/acs.jpcllett.8b03666>.
- [288] Kibsgaard, J., Chen, Z., Reinecke, B. N. & Jaramillo, T. F. Engineering the surface structure of MoS_2 to preferentially expose active edge sites for electrocatalysis. *Nat. Mater.* **11**, 963–969 (2012). URL <https://doi.org/10.1038/nmat3439>.
- [289] Han, Grace G. D., Smith, B. D., Xu, W., Warner, J. H. & Grossman, J. C. Nanoporous silicon-assisted patterning of monolayer MoS_2 with thermally controlled porosity: A scalable method for diverse applications. *ACS Appl. Nano Mater.* **1**, 3548–3556 (2018). URL <https://doi.org/10.1021/acsanm.8b00707>.
- [290] Kozubek, R., Ernst, P., Herbig, C., Michely, T. & Schleberger, M. Fabrication of defective single layers of hexagonal boron nitride on various supports for potential applications in

- catalysis and DNA sequencing. *ACS Appl. Nano Mater.* **1**, 3765–3773 (2018). URL <https://doi.org/10.1021/acsanm.8b00903>.
- [291] Yang, Y., Devel, M. & Wang, Z. An atomistic model for the charge distribution in layered MoS₂. *J. Chem. Phys.* **149**, 124102 (2018). URL <https://doi.org/doi:10.1063/1.5045505>.
- [292] Ghorbani-Asl, M., Kretschmer, S., Spearot, D. E. & Krasheninnikov, A. V. Two-dimensional MoS₂ under ion irradiation: from controlled defect production to electronic structure engineering. *2D Mater.* **4**, 025078 (2017). URL <https://doi.org/10.1088/2053-1583/aa6b17>.
- [293] Gray, H. B. Powering the planet with solar fuel. *Nat. Chem.* **1**, 7 (2009). URL <https://doi.org/10.1038/nchem.141>.
- [294] Ge, Z. *et al.* A review of the electrocatalysts on hydrogen evolution reaction with an emphasis on Fe, Co and Ni-based phosphides. *J. Mater. Sci.* **55**, 14081–14104 (2020). URL <https://doi.org/10.1007/s10853-020-05010-w>.
- [295] Cheng, N. *et al.* Platinum single-atom and cluster catalysis of the hydrogen evolution reaction. *Nat. Commun.* **7**, 13638 (2016). URL <https://doi.org/10.1038/ncomms13638>.
- [296] Yin, H. *et al.* Ultrathin platinum nanowires grown on single-layered nickel hydroxide with high hydrogen evolution activity. *Nat. Commun.* **6**, 6430 (2015). URL <https://doi.org/10.1038/ncomms7430>.
- [297] Benck, J. D., Hellstern, T. R., Kibsgaard, J., Chakthranont, P. & Jaramillo, T. F. Catalyzing the hydrogen evolution reaction (HER) with molybdenum sulfide nanomaterials. *ACS Catal.* **4**, 3957–3971 (2014). URL <https://doi.org/10.1021/cs500923c>.
- [298] Kibsgaard, J., Jaramillo, T. F. & Besenbacher, F. Building an appropriate active-site motif into a hydrogen-evolution catalyst with thiomolybdate [Mo₃S₁₃]²⁻ clusters. *Nat. Chem.* **6**, 248–253 (2014). URL <https://doi.org/10.1038/nchem.1853>.
- [299] Ye, G. *et al.* Defects engineered monolayer MoS₂ for improved hydrogen evolution reaction. *Nano Lett.* **16**, 1097–1103 (2016). URL <https://doi.org/10.1021/acs.nanolett.5b04331>.

- [300] Zhu, J. *et al.* Boundary activated hydrogen evolution reaction on monolayer MoS₂. *Nat. Commun.* **10**, 1348 (2019). URL <https://doi.org/10.1038/s41467-019-09269-9>.
- [301] Hinnemann, B. *et al.* Biomimetic hydrogen evolution: MoS₂ nanoparticles as catalyst for hydrogen evolution. *J. Am. Chem. Soc.* **127**, 5308–5309 (2005). URL <https://doi.org/10.1021/ja0504690>.
- [302] Jaramillo, T. F. *et al.* Identification of active edge sites for electrochemical H₂ evolution from MoS₂ nanocatalysts. *Science* **317**, 100–102 (2007). URL <https://doi.org/10.1126/science.1141483>.
- [303] William P. Boone & John G. Ekerdt. Hydrodesulfurization studies with a single-layer molybdenum disulfide catalyst. *J. Catal.* **193**, 96–102 (2000). URL <https://doi.org/10.1006/jcat.2000.2884>.
- [304] Mom, R. V., Louwen, J. N., Frenken, J. W. M. & Groot, I. M. N. In situ observations of an active MoS₂ model hydrodesulfurization catalyst. *Nat. Commun.* **10**, 2546 (2019). URL <https://doi.org/10.1038/s41467-019-10526-0>.
- [305] Zhang, X., Shi, S., Gu, T., Li, L. & Yu, S. The catalytic activity and mechanism of oxygen reduction reaction on P-doped MoS₂. *Phys. Chem. Chem. Phys.* **20**, 18184–18191 (2018). URL <https://doi.org/10.1039/C8CP01294F>.
- [306] Chen, J. *et al.* A computational evaluation of MoS₂-based materials for the electrocatalytic oxygen reduction reaction. *New J. Chem.* **44**, 14189–14197 (2020). URL <https://doi.org/10.1039/D0NJ02621B>.
- [307] Li, G. *et al.* All the catalytic active sites of MoS₂ for hydrogen evolution. *J. Am. Chem. Soc.* **138**, 16632–16638 (2016). URL <https://doi.org/10.1021/jacs.6b05940>.
- [308] Dai, X. *et al.* Co-doped MoS₂ nanosheets with the dominant CoMoS phase coated on carbon as an excellent electrocatalyst for hydrogen evolution. *ACS Appl. Mat. Interfaces* **7**, 27242–27253 (2015). URL <https://doi.org/10.1021/acsami.5b08420>.
- [309] Gao, M.-R., Chan, M. K. & Sun, Y. Edge-terminated molybdenum disulfide with a 9.4-Å interlayer spacing for electrochemical hydrogen production. *Nat. Commun.* **6**, 7493 (2015). URL <https://doi.org/10.1038/ncomms8493>.

- [310] Kong, D. *et al.* Synthesis of MoS₂ and MoSe₂ films with vertically aligned layers. *Nano Lett.* **13**, 1341–1347 (2013). URL <https://doi.org/10.1021/nl400258t>.
- [311] Yin, Y. *et al.* Contributions of phase, sulfur vacancies, and edges to the hydrogen evolution reaction catalytic activity of porous molybdenum disulfide nanosheets. *J. Am. Chem. Soc.* **138**, 7965–7972 (2016). URL <https://doi.org/10.1021/jacs.6b03714>.
- [312] Tsai, C. *et al.* Electrochemical generation of sulfur vacancies in the basal plane of MoS₂ for hydrogen evolution. *Nat. Commun.* **8**, 15113 (2017). URL <https://doi.org/10.1038/ncomms15113>.
- [313] Wang, X. *et al.* Single-atom vacancy defect to trigger high-efficiency hydrogen evolution of MoS₂. *J. Am. Chem. Soc.* **142**, 4298–4308 (2020). URL <https://doi.org/10.1021/jacs.9b12113>.
- [314] Madauß, L. *et al.* Highly active single-layer MoS₂ catalysts synthesized by swift heavy ion irradiation. *Nanoscale* **10**, 22908–22916 (2018). URL <https://doi.org/10.1039/c8nr04696d>.
- [315] Ochedowski, O. *Modification of 2D materials by swift heavy ion irradiation: Chapter 5: Interaction of Swift Heavy Ions with 2D-Materials, p.78 and following*. Ph.D. thesis, University of Duisburg-Essen, Duisburg (2014). URL https://duepublico2.uni-due.de/receive/duepublico_mods_00036835.
- [316] Szenes, G. Comparison of two thermal spike models for ion–solid interaction. *Nucl. Instrum. Meth. B* **269**, 174–179 (2011). URL <https://doi.org/10.1016/j.nimb.2010.11.009>.
- [317] Trautmann, C., Klaumünzer, S. & Trinkaus, H. Effect of stress on track formation in amorphous iron boron alloy: Ion tracks as elastic inclusions. *Phys. Rev. Lett.* **85**, 3648–3651 (2000). URL <https://doi.org/10.1103/PhysRevLett.85.3648>.
- [318] Yang, R., Liu, Z., Wang, Y., Yang, G. & Li, H. Synthesis and characterization of MoS₂/Ti composite coatings on Ti6Al4V prepared by laser cladding. *AIP Adv.* **3**, 022106 (2013). URL <https://doi.org/10.1063/1.4790652>.
- [319] Gordon, J. M. *et al.* Singular MoS₂, SiO₂ and Si nanostructures—synthesis by solar ablation. *J. Mater. Chem.* **18**, 458–462 (2008). URL <https://doi.org/10.1039/B714108D>.

- [320] Donarelli, M., Bisti, F., Perrozzi, F. & Ottaviano, L. Tunable sulfur desorption in exfoliated MoS₂ by means of thermal annealing in ultra-high vacuum. *Chem. Phys. Lett.* **588**, 198–202 (2013). URL <https://doi.org/10.1016/j.cplett.2013.10.034>.
- [321] Wagner, C. D. Sensitivity factors for XPS analysis of surface atoms. *J. Electr. Spectr. Rel. Phen.* **32**, 99–102 (1983). URL [https://doi.org/10.1016/0368-2048\(83\)85087-7](https://doi.org/10.1016/0368-2048(83)85087-7).
- [322] Li, H. *et al.* Activating and optimizing MoS₂ basal planes for hydrogen evolution through the formation of strained sulphur vacancies. *Nat. Mater.* **15**, 48–53 (2016). URL <https://doi.org/10.1038/nmat4465>.
- [323] Liao, L. *et al.* MoS₂ formed on mesoporous graphene as a highly active catalyst for hydrogen evolution. *Adv. Funct. Mater.* **23**, 5326–5333 (2013). URL <https://doi.org/10.1002/adfm.201300318>.
- [324] Murthy, A. P., Theerthagiri, J. & Madhavan, J. Insights on tafel constant in the analysis of hydrogen evolution reaction. *J. Phys. Chem. C* **122**, 23943–23949 (2018). URL <https://doi.org/10.1021/acs.jpcc.8b07763>.
- [325] Fletcher, S. Tafel slopes from first principles. *J. Solid State Electr.* **13**, 537–549 (2009). URL <https://doi.org/10.1007/s10008-008-0670-8>.
- [326] Li, Y. *et al.* MoS₂ nanoparticles grown on graphene: An advanced catalyst for the hydrogen evolution reaction. *J. Am. Chem. Soc.* **133**, 7296–7299 (2011). URL <https://doi.org/10.1021/ja201269b>.
- [327] Mignuzzi, S. *et al.* Effect of disorder on Raman scattering of single-layer MoS₂. *Phys. Rev. B* **91**, 195411 (2015). URL <https://doi.org/10.1103/PhysRevB.91.195411>.
- [328] Komsa, H.-P. *et al.* Two-dimensional transition metal dichalcogenides under electron irradiation: Defect production and doping. *Phys. Rev. Lett.* **109**, 035503 (2012). URL <https://doi.org/10.1103/PhysRevLett.109.035503>.
- [329] Kang, N., Paudel, H. P., Leuenberger, M. N., Tetard, L. & Khondaker, S. I. Photoluminescence quenching in single-layer MoS₂ via oxygen plasma treatment. *J. Phys. Chem. C* **118**, 21258–21263 (2014). URL <https://doi.org/10.1021/jp506964m>.

- [330] Akcöltekin, E. *et al.* Creation of multiple nanodots by single ions. *Nat. Nanotechnol.* **2**, 290–294 (2007). URL <https://doi.org/10.1038/nnano.2007.109>.
- [331] Ochedowski, O. *et al.* Graphitic nanostripes in silicon carbide surfaces created by swift heavy ion irradiation. *Nat. Commun.* **5**, 3913 (2014). URL <https://doi.org/10.1038/ncomms4913>.
- [332] Akcöltekin, S. *et al.* Unzipping and folding of graphene by swift heavy ions. *Appl. Phys. Lett.* **98**, 103103 (2011). URL <https://doi.org/10.1063/1.3559619>.
- [333] Davey, W. P. Precision Measurements of the Lattice Constants of Twelve Common Metals. *Phys. Rev.* **25**, 753–761 (1925). URL <https://doi.org/10.1103/PhysRev.25.753>.
- [334] Shim, J. *et al.* Water-gated charge doping of graphene induced by mica substrates. *Nano Lett.* **12**, 648–654 (2012). URL <https://doi.org/10.1021/nl2034317>.
- [335] Lee, D., Lee, H., Lee, H. & Park, J. Y. Nanotribological effect of water layers intercalated between exfoliated MoS₂ and mica. *J. Phys. Chem. C* **124**, 16902–16907 (2020). URL <https://doi.org/10.1021/acs.jpcc.0c01848>.
- [336] Pollmann, E. *et al.* Apparent differences between single layer molybdenum disulphide fabricated via chemical vapour deposition and exfoliation. *Nanotechnol.* **31**, 505604 (2020). URL <https://doi.org/10.1088%2F1361-6528%2Fabb5d2>.
- [337] Mogg, L. *et al.* Perfect proton selectivity in ion transport through two-dimensional crystals. *Nat. Commun.* **10**, 4243 (2019). URL <https://doi.org/10.1038/s41467-019-12314-2>.

List of publications

1. Sleziona, S.; Rauls, S.; Christen, L.; Pollmann, E.; **Madauß, L.**; Lorke, A.; Wende, H.; Schleberger, M. Towards field-effect controlled graphene-enhanced Raman spectroscopy of cobalt octaethylporphyrin molecules. *Nanotechnol.* (2021), <https://doi.org/10.1088/1361-6528/abde60>
2. Skopinski, L.; Ernst, P.; Herder, M.; Kozubek, R.; **Madauß, L.**; Sleziona, S.; Maas, A.; Königstein, N.; Wucher, A.; Schleberger, M. Time-of-flight mass spectrometry of particle emission during irradiation with slow, highly charged ions. *Rev. Sci. Instrum.* **92**, 023909 (2021), <https://doi.org/10.1063/5.0025812>
3. Ghosh, M.; Junker, M.; van Lent, R. T.; **Madauß, L.**; Schleberger, M.; Lebius, H.; Benyagoub, A.; Wood, J.; Lammertink, R. Charge Regulation at a Nano-porous Two-Dimensional Interface. *ACS Omega* **6**, 2487-2493 (2021), <https://doi.org/10.1021/acsomega.0c03958>
4. Pollmann, E.; Sleziona, S.; Foller, T.; Hagemann, U.; Gorynski, C.; Petri, O.; **Madauß, L.**; Schleberger, M. Large-area, two-dimensional MoS₂ exfoliated on gold: Direct experimental access to the metal-semiconductor interface. submitted
5. **Madauß, L.**; Foller, T.; Plaß, J.; Kumar, P. V.; Musso, T.; Dunkhorst, K.; Joshi, R.; Schleberger, M. Selective proton transport for hydrogen production using graphene oxide membranes. *J. Phys. Chem. Lett.* **11**, 9415-9420 (2020), <https://doi.org/10.1021/acs.jpcclett.0c02481>
6. Roslon, I. E.; Dolleman, R. J.; Licon, H.; Lee, M.; Siskins, M.; Lebius, H.; **Madauß, L.**; Schleberger, M.; Alijani, F.; van der Zant, H. S. J.; Steeneken, P. G. High-frequency gas effusion through nanopores in suspended graphene. *Nat. Commun.* **11**, 6025 (2020), <https://doi.org/10.1038/s41467-020-19893-5>
7. Pollmann, E.; Morbec, J.; **Madauß, L.**; Bröckers, L.; Kratzer, P.; Schleberger, M.

Molybdenum disulphide nanoflakes grown by chemical vapour deposition on graphite: Nucleation, orientation, and charge transfer. *J. Phys. Chem. C* **124**, 2689-2697 (2020), <https://doi.org/10.1021/acs.jpcc.9b10120>

8. **Madauβ, L.**; Pollmann, E.; Foller, T.; Schumacher, J.; Hagemann, U.; Heckhoff, T.; Herder, M.; Skopinski, L.; Breuer, L.; Hierzenberger, A.; Wittmar, A.; Lebius, H.; Benyagoub, A.; Ulbricht, M.; Joshi, R.; Schleberger, M. A swift technique to hydrophobize graphene and increase its mechanical stability and charge carrier density. *npj 2D Mater. Appl.* **4**, 11 (2020), <https://doi.org/10.1038/s41699-020-0148-9>
9. Ghosh, M.; **Madauβ, L.**; Schleberger, M.; Lebius, H.; Benyagoub, A.; Wood, J. A.; Lammertink, R. G. H. Understanding mono and bivalent ion selectivity of nanoporous graphene using ionic and bi-ionic potential. *Langmuir* **36**, 7400-7407 (2020), <https://doi.org/10.1021/acs.langmuir.0c00924>
10. Creutzburg, S.; Schwestka, J.; Niggas, A.; Inani, H.; Tripathi, M.; George, A.; Heller, R.; Kozubek, R.; **Madauβ, L.**; McEvoy, N.; Facsko, S.; Kotakoski, J.; Schleberger, M. A. Turchanin, P.L. Grande, F. Aumayr, and R. A. Wilhelm. Vanishing influence of the band gap on charge exchange of slow highly charged ions in freestanding single layer MoS₂. *Phys. Rev. B* **102**, 045408 (2020), <https://doi.org/10.1103/PhysRevB.102.045408>
11. Pelella, A.; Kharsah, O.; Grillo, A.; Urban, F.; Passacantando, M.; Giubileo, F.; Iemmo, L.; Sleziona, S.; Pollmann, E.; **Madauβ, L.**; Schleberger, M.; Di Bartolomeo, A. Electron irradiation of metal contacts in monolayer MoS₂ field-effect transistors. *ACS Appl. Mater. Interfaces* **12**, 40532-40540 (2020), <https://doi.org/10.1021/acsami.0c11933>
12. Pollmann, E.; **Madauβ, L.**; Schumacher, S.; Kumar, U.; Heuvel, F.; vom Ende, C.; Yilmaz, S.; Güngörmüs, S.; Schleberger, M. Apparent differences between single layer molybdenum disulfide fabricated via chemical vapor deposition and exfoliation. *Nanotechnol.* **31**, 505604 (2020), <https://doi.org/10.1088/1361-6528/abb5d2>
13. Kaupmees, R.; Walke, P.; **Madauβ, L.**; Maas, A.; Pollmann, E.; Schleberger, M.; Grossberg, M.; Krustok, J. The effect of elevated temperatures on excitonic emission and degradation processes of WS₂. *Phys. Chem. Chem. Phys.* **22**, 22609-22616 (2020), <https://doi.org/10.1039/D0CP03248D>
14. Kozubek, R.; Tripathi, M.; Ghorbani-Asl, M.; Kretschmer, S.; **Madauβ, L.**; Pollmann, E.; O'Brien, M.; McEvoy, N.; Ludacka, U.; Susi, T.; Duesberg, G.; Wilhelm, R. A.;

- Krasheninnikov, A. V.; Kotakoski, J.; Schleberger, M. Perforation of freestanding molybdenum disulfide monolayers with highly charged ions. *J. Phys. Chem. Lett.* **10**, 904-910 (2019), <https://doi.org/10.1021/acs.jpcclett.8b03666>
15. Urban, F.; Giubileo, F.; Grillo, A.; Iemmo, L.; Luongo, G.; Passcantando, M.; Foller, T.; **Madauβ, L.**; Pollmann, E.; Geller, M.; Oing, D.; Schleberger, M.; Di Bartolomeo, A. Gas dependent hysteresis in MoS₂ field effect transistors. *2D Mater.* **6**, 045049 (2019), <https://doi.org/10.1088/2053-1583/6/4/045049>
16. Pollmann, E.; Ernst, P.; **Madauβ, L.**; Schleberger, M. Ion-mediated growth of ultra thin molybdenum disulfide layers on highly oriented pyrolytic graphite. *Surf. Coat. Tech.* **349**, 783-786 (2018), <https://doi.org/10.1016/j.surfcoat.2018.05.031>
17. **Madauβ, L.**; Zegkinoglou, I.; Vázquez Muiños, H.; Choi, Y.-W.; Kunze, S.; Zhao, M.-Q.; Naylor, C. H.; Ernst, P.; Pollmann, E.; Ochedowski, O.; Lebius, H.; Benyagoub, A.; Ban-d'Etat, B.; Charlie Johnson, A. T.; Djurabekova, F.; Roldan Cuenya, B.; Schleberger, M. Highly active single-layer MoS₂ catalyst synthesized by swift heavy ion irradiation. *Nanoscale* **10**, 22908 (2018), <https://doi.org/10.1039/C8NR04696D>
18. **Madauβ, L.**, Ochedowski, O.; Lebius, H.; Ban-d'Etat, B.; Naylor, C.; Johnson, A. T.; Kotakoski, J.; Schleberger, M. Defect engineering of single- and few-layer MoS₂ by swift heavy ion irradiation. *2D Materials* **4**, 015034 (2017), <https://doi.org/10.1088/2053-1583/4/1/015034>
19. **Madauβ, L.**, Schumacher, J.; Ghosh, M.; Ochedowski, O.; Meyer, J.; Lebius, H.; Ban-d'Etat, B.; Toimil-Molares, M. E.; Trautmann, C.; Lammertink, R.; Ulbricht, M.; Schleberger, M. Fabrication of Nanoporous Graphene/Polymer Composite Membranes. *Nanoscale* **9**, 10487 (2017), <https://doi.org/10.1039/C7NR02755A>
20. Pollmann, E.; **Madauβ, L.**; Zeuner, V.; Schleberger, M. Strain in single-layer MoS₂ flakes grown by chemical vapor deposition. *Encyclopedia of Interfacial Chemistry: Surface Science and Electrochemistry* **3**, 338-343 (2017), <https://doi.org/10.1016/B978-0-12-409547-2.14175-7>

Danksagung

Im Rahmen meiner Dissertation durfte ich mit vielen Kollegen an unterschiedlichen Projekten und Experimenten arbeiten. An dieser Stelle möchte ich mich bei all jenen bedanken, die mich während dieser Zeit unterstützt und begleitet haben.

An erster Stelle geht mein Dank an Frau Prof. Dr. Marika Schleberger. Die Zeit in der AG, die Möglichkeit, an aktuellen und spannenden Themen arbeiten zu können, und die Freiheiten, die ich im Rahmen meiner Experimente hatte, wusste ich immer zu schätzen und möchte mich ganz herzlich dafür bedanken. Die Kombination aus lockerer und kollegialer Atmosphäre, die eine gelegentlich verlängerte Mittagspause verzeiht, und klaren Zielsetzungen, die man gemeinsam mit dir erarbeiten durfte, empfand ich als extrem angenehm und Ansporn zugleich.

Besonderer Dank gilt auch Herrn Prof. Dr. Mathias Ulbricht. Dank gemeinsamer Forschungsprojekte und Hilfestellungen durfte ich vieles über Polymere und Membranen lernen. Insbesondere der Unterschied zu den sonstigen Themengebieten der Oberflächenphysik und denen meines Studiums der Nano(-opto)elektronik hat mir häufig einen anderen Blickwinkel erlaubt. Ratschläge und Fragen waren stets konstruktiv und haben zum Nachdenken angeregt, wofür ich mich herzlich bedanken möchte.

Viele der in dieser Arbeit durchgeführten Experimente beruhen auf Materialmodifikationen mittels schneller Schwerionen. Ohne die Unterstützung der Mitarbeiter, Wissenschaftler und Techniker vieler Forschungseinrichtungen wären diese Experimente nicht möglich gewesen. Hier sind vor allem Frau Prof. Dr. Christina Trautmann und Frau Dr. Eugenia Toimil Molares zu erwähnen, die mir bereits während meiner Masterarbeit mit GSI- und SHI bezogenen Punkten immer geholfen haben und als meine ersten Kontaktpersonen viele Experimente trotz kurzfristiger Änderungen vor Ort ermöglicht haben.

Gleichermaßen möchte ich Herrn Dr. Henning Lebius und Herrn Dr. Abdenacer Benyagoub vom CIMAP danken. Die Unterstützung vor Ort, sowohl werktags und an Wochenenden, hat das ein oder andere Experiment vor dem Scheitern bewahrt. Die Experimente am GANIL waren immer spannend, die kleinen Plauschs zwischendurch stets mit einem Lacher verbunden und eine willkommene Ablenkung. Das GANIL Gästehaus werde ich allerdings nicht vermissen.

A special thanks goes to Dr. Marko Karlušić and Kristina Tomić Luketić. I always enjoyed working with you and the friendly atmosphere during discussions and conversations.

Many of the measurements presented in this thesis strongly relied on the great cooperation with Prof. Dr. Jani Kotakoski, Dr. Mukesh Tripathi, and Mr. Rajendra Singh. Thank you for our joined experiments and for always agreeing to help us out with (S)TEM analysis.

Vielen Dank auch Herrn Dr. Stefan Facsko and Herrn Dr. Shavkat Akhmadaliev für die kurzfristig eingeschobenen Experimente am Ion Beam Center in Dresden.

Another cooperation I highly appreciated was with Prof. Dr. Rakesh Joshi. I enjoyed our smalltalks during lunch at the Pakistani restaurant, the once-a-year day trips to Sparkasse Essen, as well as the discussions via video conference and I am very grateful for the opportunity to work with you and learn about graphene oxide membranes!

Gleichermaßen möchte ich mich bei Herrn Tobias Foller bedanken. Besten Dank für das Bereitstellen der Graphenoxidmembranen in Spitzenqualität sowie für deine lockere und unkomplizierte Art! Auch wenn ich stets abstreiten werde, sind viele deiner Ideen goldwert. Vor allem aber danke für den Namen des Songs. #Caen2020 #JohannPachelbel #KanonInD-Dur.

Als nächstes richtet sich mein Dank an das Team *AG Schleberger* und dessen Ehemalige. Vorneweg möchte ich mich bei Herrn Erik Pollmann bedanken, den ich bereits bei den Vorkursen zum Studium kennen lernen durfte. Die gemeinsam absolvierten Projekte, die Aufbauten der CVD Öfen und die gemeinsame Promotionszeit haben extrem viel Spaß gemacht und mich in vielerlei Hinsicht weitergebracht. In diesem Sinne: Na sichi, Isi und viel Spaß!

Von Herrn Dr. Oliver Ochedowski durfte ich 2014 die Grundlagen zu 2D Materialien lernen. Vielen Dank für das Anlernen in die verschiedenen Mikroskopietechniken und den damit verbundenen Zeitaufwand! Ebenso bedanke ich mich ganz herzlich bei Herrn Dr. Roland Peschke und Herrn Dr. Philipp Ernst. Viele Experimente mit hochgeladenen Ionen wurden erst durch euch möglich. Zeitintensive Sonderwünsche bei HCI Experimenten meinerseits waren für euch nie ein Problem - danke dafür! Beiden durfte ich ferner die ein oder andere Lektion im Tischfußball erteilen.

Besonderer Dank gilt auch Herrn Lukas Kalkhoff, den ich ebenfalls im ersten Semester unseres Studiums kennen lernen durfte. Auch wenn Experimente uns eher selten in das gleiche Labor führten, habe ich doch die gemeinsamen hBN Arbeiten sehr wertgeschätzt. Die "Runden" mit Zwischenstopp *Cafeteria* waren übrigens immer ein Highlight. Ehre.

Gleichermaßen möchte ich bei den vielen anderen Kolleginnen und Kollegen der *AG Schleberger* bedanken: Bei Frau Lucia Skopinski (und dem dank ihr stetig rauschenden Wasserkocher) und Herrn André ~~Mars~~ ~~Maus~~ Maas für die Unterstützung bei vielen HCI Experimenten und der TEM Analyse;

bei Herrn Stephan Sleziona und Herrn Simon Rauls für die gute, temperaturkontrollierte Büroatmosphäre :) und die Unterstützung im Reinraum und XPS. Gerade zum Ende meiner Promotion durfte ich glücklicherweise vermehrt Experimente mit euch planen und durchführen;

bei Frau Jennifer Schmeink als mehrfache Teamkollegin bei *AG* internen "Mensch-ärger-dich-nicht-Abenden" und deine stete Bereitschaft zu helfen und

bei Frau Christina vom Ende für die zahllosen Stunden am AFM verbunden mit wichtigen

Diskussionen aktueller Serien!

Bedanken möchte ich mich auch bei unserem Techniker-Mechaniker-Reparateur-PostDoc Herrn Dr. Lars Breuer für die Hilfen jeglicher Art technischer oder experimenteller Natur!

Im gleichen Atemzug möchte ich auch Herrn Dr. Andreas Reichert für die gemeinsame Zeit im Schülerlabor, sowie die Unterstützung beim Layout von Postern und Cinema4D Graphiken danken; insbesondere aber für die *meist gelungenen* Wortwitze.

Vielen Dank an Frau Anke Hierzenberger für die netten Gespräche zwischendurch, die vielen Messungen und die vielen vielen hergestellten Proben.

Ebenso geht mein Dank an Herrn Harald Hanulok and Frau Manuela Adam-Skowranek für die Unterstützung bei Bestellungen und dem Paketversand.

Während meiner Promotionszeit durfte ich viele Abschluss- und Projektarbeiten betreuen, was ich immer gerne wahrgenommen habe. Mein Dank richtet sich an die Studierenden: Vanessa Zeuner (M.Sc. NanoEngineering); Simon Schumacher (M.Sc. Energy Science); Andre Maas, Mike Stief, Rahel-Manuela Neubieser (Masterprojekt NanoEngineering); Mike Stief (M.Sc. NanoEngineering); Hazal Elmas (B.Sc. NanoEngineering); Sümeyra Yilmaz, Sümeyra Güngörmüs (Bachelorprojekt NanoEngineering); Osamah Kharsah (B.Sc. NanoEngineering); Yossarian Liebsch (B.Sc. und M.Sc. Energy Science); Jannik Plaß (B.Sc. Energy Science); Lennart Hucht (B.Sc. Energy Science); Maximilian Buchta (M.Sc. Energy Science), Hannah Kohler (B.Sc. Energy Science), Lukas Kalkhoff (M.Sc. NanoEngineering); Katharina Derr (B.Sc. NanoEngineering), Dave Marnold (B.Sc. NanoEngineering); Leonard Christen, Laurenz Kremer (Bachelorprojekt NanoEngineering); Fatih-Can Cakir, Jan Siebenborn, Abdulrahman Amr (Bachelorprojekt NanoEngineering); Stephan Bindarra, Michael Staiger (Bachelorprojekt NanoEngineering).

Vor allem aber möchte ich meinen Eltern, Ursula und Norbert Madauß, und meinem Bruder, Philipp Madauß, für die ständige Unterstützung in jeglichen Lebenssituationen danken.

Eigenständigkeitserklärung

Hiermit versichere ich, dass ich die vorliegende Arbeit selbständig verfasst und ohne unzulässige Hilfe Dritter und ohne Benutzung anderer als der angegebenen Hilfsmittel angefertigt habe. Die verwendeten Hilfsmittel und alle wörtlich oder inhaltlich übernommenen Stellen sind unter Angabe der entsprechenden Quelle gekennzeichnet.

Die Arbeit wurde bisher weder im Inland noch im Ausland in gleicher oder ähnlicher Form einer anderen Prüfungsbehörde vorgelegt.

Der Doktorgrad eines Doktors der Naturwissenschaften (Dr. rer. nat.) wird gemäß §1 Satz 2 der Promotionsordnung angestrebt.

Duisburg, 2. März 2021

Lukas Madauß

DuEPublico

Duisburg-Essen Publications online

UNIVERSITÄT
DUISBURG
ESSEN

Offen im Denken

ub | universitäts
bibliothek

Diese Dissertation wird via DuEPublico, dem Dokumenten- und Publikationsserver der Universität Duisburg-Essen, zur Verfügung gestellt und liegt auch als Print-Version vor.

DOI: 10.17185/duepublico/75000

URN: urn:nbn:de:hbz:464-20211202-103629-4

Alle Rechte vorbehalten.